UTS UNIVERSITY OF TECHNOLOGY SYDNEY

DEVELOPMENT OF NANOSTRUCTURED PHOTOTHERMAL MATERIALS FOR SOLAR DRIVEN WATER EVAPORATION TOWARDS CLEAN WATER PRODUCTION

by Idris Ibrahim

Thesis submitted in fulfilment of the requirements for the degree of

Doctor of Philosophy

under the supervision of Dr. Leonard Tijing, Prof. Hokyong Shon and A/Prof. Andrew McDonagh

University of Technology Sydney
Faculty of Engineering and Information Technology

July 2022

CERTIFICATE OF ORIGINAL AUTHORSHIP

I, *IDRIS IBRAHIM* declare that this thesis, is submitted in fulfilment of the requirements for the award of *Doctor of Philosophy*, in the *School of Civil and Environmental Engineering/ Faculty of Engineering and Information Technology* at the University of Technology Sydney.

This thesis is wholly my own work unless otherwise referenced or acknowledged. In addition, I certify that all information sources and literature used are indicated in the thesis.

This document has not been submitted for qualifications at any other academic institution.

This research is supported by the Australian Government Research Training Program.

Signature:

Production Note:
Signature removed prior to publication.

Date: 07-07-2022

DEDICATION

To my lovely parents and siblings, thank you for your support in all my life.

Without your support I will not reach to this level.

ACKNOWLEDGEMENTS

I would like to thank everyone who contributed to this doctoral study and supported me during this time. Firstly, I would like to thank my principal supervisor Dr. Leonard Tijing for accepting me to join his research group and providing all the support I need to complete this doctoral study. He always encouraged me and guided me to do high-quality work. I also extend my sincere thanks to my co-supervisors Prof. Hokyong Shon, and Prof. Andrew McDonagh, for their consistent support, answering my research questions and advice throughout the project. This doctoral study would not be the same without your support and wise supervision. I would also like to thank the Australian government for giving me a golden opportunity by providing one of the prestigious scholarships International Research Training Program (IRTP) for my doctoral studies.

I cannot forget to thank my family members, especially my parents, siblings, and grandmothers, for their love and support, making me who I am. Without their encouragement, I will not complete my doctoral studies.

I sincerely appreciate our external collaborator from CSIRO, Prof. Avi Bendavid, for his kind support and sharing his knowledge that contributed to my doctoral research. Besides, my sincere appreciation goes to internal collaborators from the faculty of science who trained me , and share their skills. I want to thank Dr. Alexander Angeloski, Dr. Ronald Shimmon, Mr. Geoff McCredie, Dr. Anthea Harris, Dr. Mahmoud El Safadi, Dr. Mark Lockrey, Dr. John Scott, Mr. Herbert Yuan, Mr. Greg Dalsanto, and Dr. Linda Xiao for providing me with essential support during my research studies. I want to acknowledge the contribution of Dr. Katie McBean and Prof. Alaina Ammit for their assistance in using the facilities in Science. I appreciate the assistance from our environmental laboratory staff, Dr. Md Johir, and Dr. Niren Kumar and during my Ph.D.

A special thank you to our school Manager. Van Le, School Academic Officer. Dr. Larissa Koroleva, Senior HDR program officer Reneey Wortley, Responsible Academic Officer. Prof. Hadi Khabbaz and for their kind assistance and support during my candidature. I would like to express my sincere gratitude to Dr. Sherub Phuntsho and Prof. Zhenguo Huang for their valuable comments and suggestions during my candidature assessments 3. I want to acknowledge my best friend, Dr. Kamil Braima, for his kind support, and thanks for always being the shoulder I can always depend on.

Warmly, I would like to acknowledge and thank my colleagues and staff at UTS for their kind assistance along my Ph.D. journey; Dr. Ali Altaee, Madam. Amber Brown, Dr. Piyush Punetha, Dr. Qiang Fu, Mr. Mukit Hossain, Dr. Michael Seo, Dr. MJ Park, Dr. Qiang Hao and Mr. Minh Vu.

Last but not least, I would also like to thank my friends who I met during my Ph.D. journey at UTS, Camilla Gazzana, Dr. Luong N Nguyen, Mr. Zhi Mei Xu, Mr. Ling, Mr. Zhijie Chen, Dr. Naveen Kumar, Dr. Wenkui Dong, and Dr. Syed Muztuza Ali.

TABLE OF CONTENTS

LIST OF PUBLICATIONS, CONFERENCES AND AWARDS

Publications related to the thesis:

- **Idris Ibrahim**, Dong Han Seo, Alexander Angeloski, Andrew McDonagh, Ho Kyong Shon, Leonard Tijing*. 3D nanostructured CuS/Sn_2S_3 microflowers for highly efficient solar steam generation and water purification. Solar Energy Materials and Solar Cells 232 (**2021**): 111377.
- **Idris Ibrahim**, Dong Han Seo, MJ Park, Alexander Angeloski, Andrew McDonagh, Ho Kyong Shon, Avi Bendavid, Leonard Tijing*. A novel robust and scalable plasmonic membrane for a highly efficient solar steam generation under a harsh environment. Chemosphere (2022): 134394
- **Idris Ibrahim**, Dong Han Seo, Andrew M. McDonagh, HoKyong Shon, Leonard Tijing*. Semiconductor photothermal materials enabling efficient solar steam generation toward desalination and wastewater treatment. Desalination 50, Volume 500, 2021, 114853. (**2021**).
- **Idris Ibrahim**, Sayed Mukit Hossain, Dong Han Seo, Andrew McDonagh, Tim Foster, Ho Kyong Shon, Leonard Tijing*. Polydopamine nanostructures decorated a porous nickel foam toward efficient solar harvesting steam evaporator and anti-salt properties. Separation and Purification Technology. (2022): 121054
- **Idris Ibrahim**, Qiang Fu, Andrew McDonagh, Tim Foster, Ho Kyong Shon, Leonard Tijing*.Tannic acid derived multifunctional hydrogel for highly efficient solar evaporator system. (Under review in Desalination).
- **Idris Ibrahim**, Vrushan P, Dong Han Seo, Morteza Afsari, Ho Kyong Shon, Leonard Tijing*. Biomass-based photothermal materials for interfacial solar steam generation: A review. Materials Today Energy. (**2021**), 100716.

Other Publications

- LD Tijing*, JRC Dizon, **Idris Ibrahim**, ARN Nisay, HK Shon, RC Advincula. 3D printing for membrane separation, desalination and water treatment. Applied Materials Today 18, 100486. (**2020**).

- Z Chen, **Idris Ibrahim**, D Hao, X Liu, L Wu, W Wei, D Su, BJ Ni. Controllable design of nanoworm-like nickel sulfides for efficient electrochemical water splitting in alkaline media. Materials Today Energy 18, 100573. (**2020**).
- Wan Jeffrey Basirun, **Idris Mohamed Saeed**, M S Rahman, Shaukat Ali Mazari. Nickel oxides/hydroxides-graphene as hybrid supercapattery nanocomposites for advanced charge storage materials - a review. Critical Review in Solid State and Materials Science 46.6 (2021): 553-586.
- Daoud Khanafer, **Idris Ibrahim**, Sudesh Yadav, Ali Altaee, Alaa Hawari, John Zhou. Brine Reject Dilution with Wastewater for Indirect Desalination: Converting Wastewater Streams to Water Resources. Journal of Cleaner Production, 322, (2021) 129129.
- Sayed Mukit Hossain; **Idris Ibrahim**; Youngwoo Choo; Amir Razmjou; Gayathri Naidu; Leonard Tijing; Jong-Ho Kim. Effective lithium-ion sieve from sludge-generated TiO_2 for lithium resource recovery. Desalination, 525, 115491.
- Dong, W., Li, W., Sun, Z., **Ibrahim, I**., & Sheng, D. Intrinsic graphene/cement-based sensors with piezoresistivity and superhydrophobicity capacities for smart concrete infrastructure Automation in Construction, 133, 103983 (**2022**).
- Luong N.Nguyen, Hang P.Vu, Md Abu Hasan Johir, **Idris Ibrahim**, M. Mofijur ,Leen Labeeuw ,Mathieu Pernice, Peter J.Ralph, Long D.Nghiem. Synthesis and evaluation of cationic polyacrylamide and polyacrylate flocculants for harvesting freshwater and marine microalgae. Chemical Engineering Journal 433 (2022): 133623.
- Minh Vu, Luong N.Nguyen, **Idris Ibrahim**, Md Abu Hasan Johir, Ngoc Bich Hoang, Xiwang Zhang, Long D.Nghiem. Nutrient recovery from digested sludge centrate using
- alkali metals from steel-making slag. Under review in Chemical Engineering Journal, CEJ-D-22-12404.
- Wan Jefrey Basirun, **Idris Mohamed Saeed**, MR Saidur, S Ahmed. Manganese Oxides-Graphene Nanocomposites as Advanced Supercapacitors. In book: Reference Module in Earth Systems and Environmental Science. In book: Reference Module in Earth Systems and Environmental Sciences (Elsevier) DOI:10.1016/B978-0-12-819723-3.00043-3

CONFERENCES AND SEMINARS

Oral Presentations

- 14th International Conference on Challenges in Environmental Science & Engineering, CESE-2021 'Gold nanolayer membrane as solar harvester for efficient solar steam
- generation and seawater desalination' (6th and 7th November 2021, CESE conference series) (Online).
- 2020 VIRTUAL SCHOOL RESEARCH SHOWCASE 'Hierarchical CuS/Sn_2S_3 microflowers for highly efficient solar steam generation and water purification' (5th November 2020, University of Technology Sydney).
- 2021 VIRTUAL SCHOOL RESEARCH SHOWCASE 'Fabrication of a novel solar photothermal membrane for efficient solar seawater desalination' (22nd September 2021, University of Technology Sydney).

AWARDS

- Best Oral Presentation. 2021 VIRTUAL SCHOOL RESEARCH SHOWCASE (22nd September 2021, University of Technology Sydney).
- Best HIRO (Hazard and Incident Reporting Online) FEIT-UTS 2021.

LIST OF ABBREVIATIONS

Full name	Abbreviations
1H,1H,2H,2H-perfluorooctyltrichlorosilane	PFOTS
1H,1H,1H,2H-perfluorodecyltriethoxysilane	PFDTES
Absorption	A
AM 1.5	Air Mass Filter
Anodized alumina Oxide	AAO
Au nanocages	AuNCs
Air-laid paper	ALP
Au nanolayer membrane	Au-PTFE
Bandgap	E_g
Bound water	BW
Carbon nanotube	CNT
Chemical vapor deposition	CVD
Contact angles	CA
Copper sulfide	CuS
Cellulose sponge	CS
Cellulose membrane	CM
Carbon nanotube	CNT
Deionized water	DIW
Energy dispersive X-ray	EDX
Fourier transforms Infrared	FTIR
Free water	FW
Graphene	G

Heterostructure microflowers composed of vertically aligned CuS/Sn_2S_3 nanosheets	3D CSS-NS MF
Hydroxyl groups	-OH
Infrared	IR
Inductive Coupled Plasma-Mass Spectrometer	ICP-MS
Intermediate water	IW
Ion Chromatography	IC
Interfacial solar steam generation	ISSG
Iron sulfate	$FeSO_4.7H_2O$
Localized surface plasmon resonance	LSPR
Mixed cellulose ester	MCE
Magnetic sputtering	MS
Multi-stage flash	MSF
Multi-effect desalination	MED
Membrane distillation	MD
Molybdenum oxide	MoO
Nanoparticles	NPs
Nanocrystals	NCs
Nanowires	NWs
Near-infrared	NIR
Nickel foam	NF
Nitric acid	HNO_3
Photothermal materials	PTMs
Polytetrafluoroethylene	PTFE
Polydimethylsiloxane	PDMS

Poly(p-phenylene benzobisoxazole) nanofibre	PBONF
Poly (vinyl alcohol)	PVA
Polyethylene	PE
Polydopamine	PDA
Polytetrafluoroethylene	PTFE
Potassium Hydroxide	KOH
Reverse osmosis	RO
Reflectance	R
Solar steam generation	SSG
Sulfuric acid	H_2SO_4
Ultraviolet	UV
Visible	vis
Quaternary sulphide, selenide p-type $Cu_2ZnSnSe_4$	CZTSe
Semiconductive hydrogel composed of MnO_2 nanowires/chitosan hydrogel	SPM-CH
Stainless steel	SS
Scanning electron microscopy	SEM
Solar water evaporation	SWE
Sodium chloride	NaCl
Transition metal oxides	TMOs
Tungsten oxide	WO_3
Titanium dioxide	TiO_2
Titanium sesquioxide	Ti_2O_3
Thermal gravimetric analysis	TGA
Tannic acid	TA

Transmittance	T
World Health Organization	WHO
X-ray photoelectron spectroscopy	XPS
X-ray diffraction	XRD

LIST OF SYMBOLS

Symbol	Meaning	Unit
ΔH_{vap}	The specific heat capacity of water	J g^{-1} K^{-1}
ΔT	The temperature variation during water	^{o}C
A	The area of the solar absorber	m^2
A	Absorption	%
C_{opt}	The optical concentration	W m^{-2}
C_p	The specific heat capacity	K)
E_g	The energy difference between the valence band and the conduction band	eV
m	The weight change during water evaporation	Kg m^{-2}
q_{in}	The solar irradiation energy density from the solar simulator	kW m^{-2}
R	Reflectance	%
T	Transmittance	%
t	The irradiation time	h
v_i	The mass loss of water under sunlight	Kg m^{-2}
v_0	The mass loss of water under dark	Kg m^{-2}

LIST OF FIGURES

LIST OF TABLES

ABSTRACT

The lack of access to fresh water is one of the most significant issues the world is facing today. Only a small percentage of the global water source is freshwater, while most (97.5%) exist as saline water. To help address fresh water scarcity, solar steam generation (SSG) has attracted tremendous attention as being scalable, low-cost, and affordable technology. In recent years, increasing interest in SSG for water purification has been mainly due to advancements in photothermal materials (PTMs). This doctoral study focuses on the rational design development of nanostructures PTMs with unique structural properties for high-performance SSG toward seawater desalination applications.

We initially used a single-step solvothermal method to synthesize heterostructure microflowers composed of vertically aligned CuS/Sn_2S_3 nanosheets (3D CSS-NS MF). The structural features are beneficial for effective heat localization through trapping and re-absorbing the heat along with the fast vapor escaping. This resulted in efficient solar-thermal conversion and water evaporation performances. Besides, a stable evaporation was attained using seawater over 10 continuous cycles with a negligible decrease.

Apart from 3D CSS-NS MF, we fabricated a nanoscale gold nanolayer on a polytetrafluoroethylene (PTFE) membrane. Our fabricated membrane displayed a robust mechanical strength and chemical stability arising from the adhesiveness of the thin film Au on the PTFE membrane. More remarkably, good reusability was observed in seawater and high salinity brine, even under severe chemical conditions.

Despite the outstanding anti-salt performances of Au-PTFE membrane, there is still a drawback with the low evaporation performance. For that reason, a scalable *in situ* oxidative polymerization approach was developed to fabricate polydopamine nanowires uniformly growing on 3D porous nickel foam. Notably, by taking advantage of the PDA containing

abundant hydrophilic hydroxyl groups, exceptional durability and stability were obtained using seawater and high brine salinity.

Lastly, we reported a facile method for preparation of hydrogel composed of polyvinylalcohol matrix and ferric-tannate. The prepared hydrogel possesses a rough surface, and diffusion-confined nanochannels. These features are beneficial for solar-thermal conversion, facilitate rapid vapor escape, and anti-salt properties. A stable performance was achieved for 3 consecutive days at seawater and high brine salinity. Moreover, the little salt formed on hydrogel surface during day gradually dissolve and back to the bulk saline water at night condition through the rich nanochannels. In summary, our innovated PTMs in this doctoral study provide insight into development of PTMs which might be promising for large scale solar evaporators towards seawater desalination applications.

CHAPTER 1

INTRODUCTION

1.1 Research background

It is forecast that by 2050 around four billion people will be affected by freshwater scarcity due to rising population and industrialization [1]. Almost 80% of human diseases result from unsafe water and sanitation [2] and so improving water quality is necessary to improve the general well-being of the population. Seawater desalination processes are reliable technologies that meet the growing demand for freshwater. Global desalination capacity is currently ~70 million m^3day^{-1} and is increasing [3]. Highly efficient thermally-driven desalination technologies are often used, though processes such as multi-effect desalination (MED) and multi-stage flash (MSF) are still economically and geographically impractical for small-scale applications [4]. Pressure-driven membrane desalination processes, in particular seawater reverse osmosis (RO) technology, currently dominate the desalination market due to simple operation, ability to produce high-purity water, low upfront capital investment and operating costs compared to thermally driven processes [5]. However, concentration polarization effects limit the overall recovery of RO water to less than 50% and reduce energy efficiency in further recovery of water [6]. Additionally, RO membranes require frequent cleaning or replacement due to scaling and fouling phenomena, which increases the operation costs.

An alternative renewable energy driven sustainable clean water production method is solar water evaporation, also known as solar steam generation (SSG). SSG utilizes sunlight to evaporate the water and condense it to generate a high purity water [3, 7-14]. This technology also has potential in industrial wastewater purification as well as water desalination with low CO_2 emission and energy consumption [15]. Traditional solar evaporator mostly possess low solar photothermal conversion efficiencies of 30-45% arising from poor solar-light absorption and massive heat losses, which makes it an impractical approach to generate large quantities of clean water [14, 16, 17]. Thus, there is a need for more effective light-absorbing materials, new device designs, and modules for highly efficient SSG devices. Recently, novel light-

absorbing nanomaterials have attracted immense attention. Some nanomaterials exhibit solar-to-thermal conversion efficiencies of close to 100% and consequently increase the solar water evaporation performance [14, 18-21].

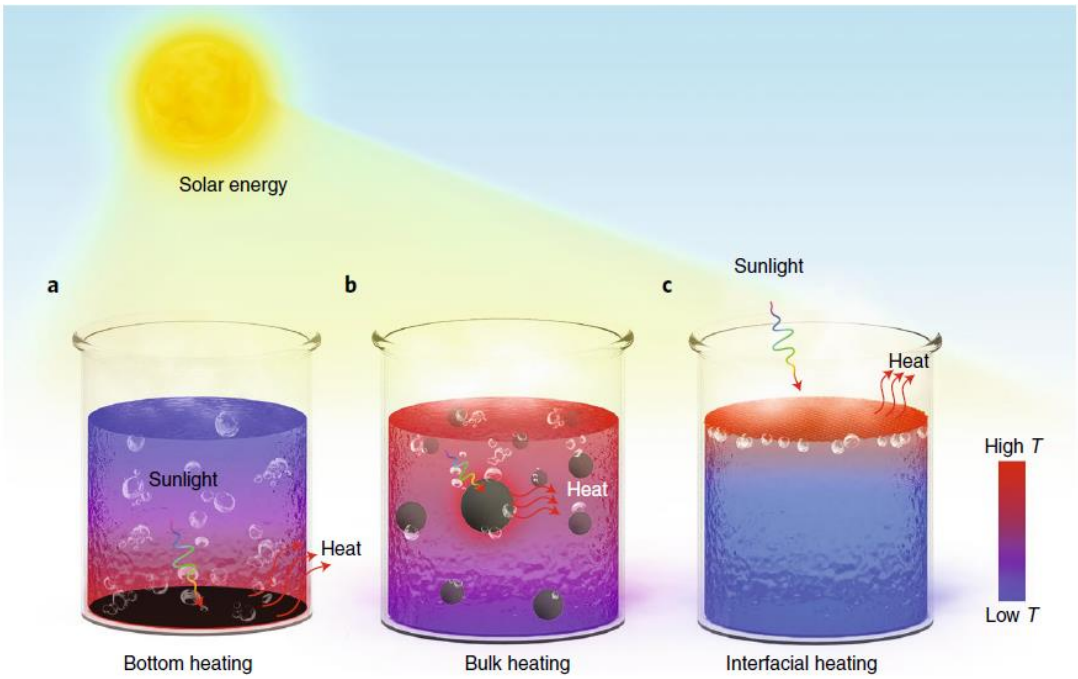

Figure 1.1 Solar-driven evaporation system configurations: (a) bottom heating, (b) volumetric heating (dispersed case), and (c) interfacial heating [9].

SSG systems are categorised into three configurations depending on the place of the PTMs (see **Figure 1.1)**: (i) PTM layer fixed at the bottom of the device, (ii) volumetric systems where PTMs are dispersed, and (iii) interfacial systems where PTMs float on the water surface [18]. In the first two systems PTMs fixed at the bottom and volumetric systems) display low photothermal conversion efficiency due to the slow heat accumulation process where large quantities of water need to be heated before efficient evaporation can take place [18]. For systems where the PTM layer is at the bottom (**Figure 1.1 a)**, light must travel through the bulk water before reaching the solar absorber. Consequently, the intensity of sunlight is reduced as it reaches the bottom solar absorber. At the same time, this creates difficulties in raising the water temperature and evaporation. [22] In the dispersed configuration case, controlling the

optimum amount of PTM particles to be dispersed inside the water is critical as non-optimum amounts will either lead to insufficient and slow heat generation or reduced photothermal efficiency due to PTM shading (**Figure 1.1 b**). For the "fixed at the bottom" and volumetric systems, the evaporation efficiency is usually low which is attributed to three factors: (i) reduced solar absorption corresponding to reduced intensities and scattering of the light within the water, (ii) substantial thermal energy loss, and (iii) heat loss to the bulk water that is not involved in steam generation due to thermal diffusion [23, 24].

On the other hand, a newer configuration based on floating the PTM layer on top of the water surface (interfacial design, **Figure 1.1** c). This system was reported to provide outstanding photothermal conversion efficiencies even exceed the theoretical limit (> 100%) [25-28]. The lower thermal conductivity of air compared to water significantly reduces heat dissipation [29]. In the interfacial system, light absorbed by the PTM is converted into heat, which induces localized heating of water at the water-air interface to enable evaporation. Heat losses can be additionally reduced by placing the porous thermal insulators at the bottom of the absorber. Also, wick materials is added to supply the water to the heated region [4, 30]. The floating SSG configuration (interfacial system) is the most promising configuration in terms of photothermal conversion efficiencies and water production rates.

1.2 Research Objectives and scope

The development of advanced PTMs is critical for enhancing solar light harvesting across the entire solar spectrum and light-to-thermal conversion efficiency. Such materials may also possess salt-resistant properties and long term reusability and stability leading to effective solar evaporator toward seawater desalination applications. These properties can be achieved by tailoring and control of structural morphologies, sizes and porosity of the PTMs at nanoscale level. This doctoral research aims to synthesize and develop a series of nano/microstructure

PTMs with unique structural properties for high-performance solar-driven water evaporators with anti-salt properties.

The specific objectives of this study are as follows:

1. To implement a scalable approach to synthesize PTMs with unique nano/microstructure for excellent solar thermal conversion and high water evaporation performance.
2. To prepare highly stable PTMs with robust mechanical strength and chemical stability to tolerate harsh environmental conditions.
3. To investigate the stability and durability of the PTMs under seawater and high salinity brine.
4. To explore the capability of the designed PTMs derived solar evaporator to reject seawater salt ions.

1.3 Research significance

This research provides feasible and scalable approaches for developing efficient solar PTMs for high-performance solar evaporators, with the goal of demonstrating their capability for salt ion rejections and good reusability and stability over multiple cycles. Novel 3D CuS/Sn_2S_3 microflowers composed of vertically aligned nanosheets demonstrated their efficiency for water evaporation performance for water purifications. In addition, to achieve PTMs with robust mechanical strength and chemical stability, nanoscale gold thin film coated PTFE membrane was demonstrated with good performances under harsh conditions. Furthermore, a novel solar evaporators are presented consisting of PTMs of porous structural materials, including PVA/TA-Fe hydrogel and PDA decorated nickel foam, which are a suitable choice to improve water evaporation with anti-salt performance. Overall, these results provide clear guidance for evaluating the potential of PTMs with unique structural morphology for solar-driven water purification fields.

1.4 Thesis structure

The thesis outline is illustrated in **Figure 1.2** and the details of each chapter is provided below.

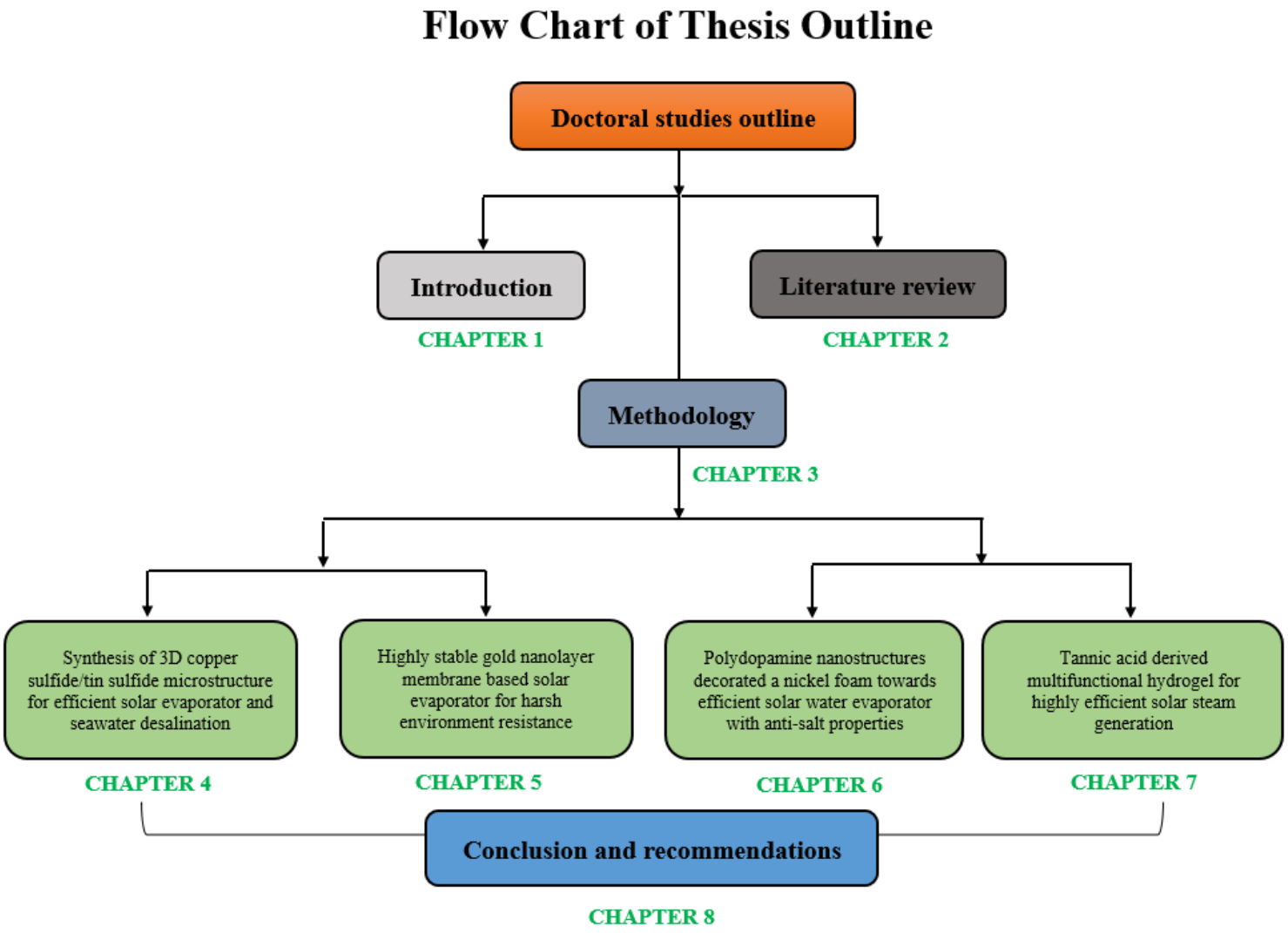

Figure 1.2 Thesis outline

Chapter 1: INTRODUCTION

This chapter presents a brief background on the research topic, including the principle of solar steam generation and PTMs. The research motivation, objectives, and the significance of this work are illustrated.

Chapter 2: LITERATURE REVIEW

This chapter reviews the research development of solar steam generation including the classes of PTMs used in SSG, the development of SSG, and the applications in seawater desalination

Chapter 3: MATERIALS AND METHODS

The materials used and methodology is given in this chapter, which includes the raw materials used, synthesis method, materials characterization, SSG device fabrication, thermal management, SSG performance, and water purifications. The characterizations of the synthesized and fabricated PTMs were conducted using various instruments including; scanning electron microscopy (SEM) with an EDS detector, X-ray diffraction (XRD), X-ray photoelectron spectroscopy (XPS), Fourier-transform infrared spectroscopy (FTIR), Thermogravimetric analysis (TGA) and Brunauer, Emmett and Teller (BET) surface area. The surface wettability was measured using a contact angle. The optical properties were measured using the Universal Measurement Spectrophotometer (UMS), heat management was visualized on a Fluke E6 Infrared Camera (Fluke, USA). The mass change of the solar evaporator was measured using an electronic balance which is connected to a labtop. A custom-built device designed for condensation and collection of evaporated salt water. Ion concentrations of salted and desalinated water were analyzed using the inductively coupled plasma mass spectrometer (ICP-MS).

Chapter 4: SYNTHESIS OF 3D COPPER SULFIDE/TIN SULFIDE MICROSTRUCTURE FOR EFFICIENT SOLAR EVAPORATOR AND SEAWATER DESALINATION

A hierarchical structure of copper tin sulfide microflowers composed of vertically aligned nanosheets using a single-step solvothermal method is described. The gaps between microflowers structures and the abundant nanocavities between the vertically aligned nanosheets are beneficial for efficient sunlight harvesting over the solar spectrum, thermal heat localization, and utilizations through trapping and re-absorbing the emitted heat and allowing fast escape of water vapor. The synthesized materials werer deposited on a mixed cellulose ester membrane, then coated with hydrophobic silane material. The resulted membrane could achieve excellent water evaporations of 1.42±0.04 kg m^{-2} h^{-1}, corresponding to an efficiency of 82.9% under one sun irradiation. Good anti-salt performance can obtain with a stable evaporation performances over ten continuous cycles under an actual seawater.

Chapter 5: HIGHLY STABLE GOLD NANOLAYER MEMBRANE BASED SOLAR EVAPORATOR FOR HARSH ENVIRONMENT RESISTANCE

In this chapter, a novel thin-film gold nanolayer was sputtered on polytetrafluoroethylene (PTFE) membrane using a magnetron sputtering technique (named as; Au-PTFE). Au-PTFE membrane exhibited strong adhesiveness of on PTFE fibrous surface. This resulted in enhancing the mechanical strength of the PTFE membrane. Additionally. Excellent chemical stability can be achieved under harsh chemical conditions (acidic, basic, and oxidized). The prepared solar evaporator of Au-PTFE on cellulose sponge resulted in excellent salt ions rejection, meeting the required standard for drinking water. Furthermore, exceptional reusability and stability are demonstrated in natural seawater, high salinity brine (150 g/L NaCl), and harsh chemical conditions. In addition, auto-cleaning properties can be obtained by placing 2.5 g of NaCl on the Au-PTFE surface, which could dissolve back to the water within 150 minutes via advection and diffusion process.

***Chapter 6**: POLYDOPAMINE NANOSTRUCTURES DECORATED A NICKEL FOAM TOWARDS EFFICIENT SOLAR WATER EVAPORATOR WITH ANTI-SALT PROPERTIES*

This chapter reports *in situ* PDA NWs decorated on 3D porous nickel foam substrate. This unique structure results in boosted light absorption by the nickel foam. The synthesized material exhibited unique hierarchical nanostructures, superhydrophilicity, and high porosity resulting in excellent solar light absorption and thermal conversion. A simple solar evaporator was made of polystyrene foam, and the cotton cloth resulted in a fast water supply to the evaporator and exceptional heat localizations. The design solar evaporator resulted in high water evaporation performance and anti-salt capability even at high salinity solutions (75g/L). The small amount of salt formed on the PDA NWs-NF surface can be re-washed through immersing in di-ionized water. This is attributed to the merits of the coated PDA, which contains rich hydrophilic hydroxyl groups, resulting in a weak adhesion of salts on the PDA NWs -NF surface.

Chapter 7: TANNIC ACID DERIVED MULTIFUNCTIONAL HYDROGEL FOR HIGHLY EFFICIENT SOLAR STEAM GENERATION

This chapter reports the designing and fabrication of porous PVA hydrogel using TA-Fe complex as cross-linker and solar absorber and utilized for solar steam generations and seawater desalination. The designed hydrogel has features of confined nanochannel uniformly distributed on the hydrogel surface, with superhydrophilicity properties. Consequently, excellent water evaporation performance can be obtained of 2.35±0.11 kg m^{-2} h^{-1}, corresponding to an efficiency of 94.6 %. Additionally, excellent remarkable anti-salt capability was realized with stable performance over 3 consecutive days under high brine salinity (75 g/L NaCl). At the end of each day's performance, we observed formations of salt layer on the hydrogel surface and the salt redissolved at night (dark conditions) into the bulk

saline water. The nanochannels on the hydrogel surface allowed water supply from the cellulose sponge.

Chapter 8: CONCLUSION AND RECOMMENDATIONS

This chapter describes the results and the outcomes of the entire body of work and addresses future research and perspectives.

CHAPTER 2

LITERATURE REVIEW

Parts of this chapter are based on the following publications:

Idris Ibrahim, Dong Han Seo, Andrew M. McDonagh, HoKyong Shon, Leonard Tijing*. Semiconductor photothermal materials enabling efficient solar steam generation toward desalination and wastewater treatment. Desalination 50, Volume 500, 2021, 114853. (**2021**).

Idris Ibrahim, Vrushan P, Dong Han Seo, Morteza Afsari, Ho Kyong Shon, Leonard Tijing*. Biomass-based photothermal materials for interfacial solar steam generation: A review. Materials Today Energy. (**2021**), 100716

2.1 Introduction

Safe drinking water is essential for the human population and has remained a significant challenge. The World Health Organization estimated that more than one billion people suffer from a lack of clean drinking water [31]. In addition, unsafe drinking water can cause serious water-borne diseases such as diarrhea, respiratory infections, and cholera [31-34]. These issues are often more severe in remote or rural areas where it is challenging to implement traditional clean water production systems and processes [35]. Solar energy is a highly accessible and renewable energy resource providing huge amounts of energy has attracted significant attention to obtain clean water [18]. The ancient Greek philosopher Aristotle noted the relationship between water and energy as follows [29]:

"*Now the sun moving, as it does, sets up processes of change and becoming and decay, and by its agency the finest and sweetest water is every day carried out and is dissolved into vapor and rises to the upper regions, where it is condensed again by the cold and so returns to the earth*"

From this point, numerous designs for building solar stills for solar seawater desalination were developed. Solar desalination systems that consume solar energy are classified as direct or indirect systems [11, 36]. A system that absorbs sunlight directly and converts it into heat to generate vapor inside the solar collector is called a direct system. Meanwhile, the system that collects the sunlight and generates heat in a system and combined with conventional desalination technology like membrane distillation (MD) or forward osmosis (FO) is called an indirect system [11]. The indirect system experienced a high-cost, low water production efficiency per unit area compared to the traditional fossil-fuel-based technology making it impractical for large scale [37]. Hence, more scholars and industry attention have been shifted towards the direct system to design small-scaled devices suited in rural areas where water is scarce, and the sunlight is abundant. In the mid-1950, the basin solar still reported as a

promising technology for solar desalination. But systems still suffer from low thermal efficiency and low water production 1-4 L/m^2/day [37]. The nano-enabled SSG has attracted tremendous attention as cost-effective, scalable, and affordable technologies to overcome the fresh water scarcity issues [38]. This technology is mainly based on PTMs to harvest solar energy and convert it into heat for water vapor generation [38, 39]. In the first study, Halas' demonstrated a dispersed gold nanoparticles (NPs) system in SSG, where water vapor is generated through boiling mechanisms, achieving 80% efficiency [40]. Later on, Chen's group initiated a new approach to utilize heat and suppress the losses. In their proposed design, the solar absorber part was separated from the bulk water using a thermal insulator in a system called ISSG [41]. They employed exfoliated graphite as a solar absorber coated on hydrophilic porous carbon foam (thermal insulator), which results in water evaporation efficiency of ~85%. Later on, a number of groups have tried to improve the efficiency of solar evaporator by using different solar absorbers and system designs. To design a highly-efficient SSG system for desalination, it needs to satisfy four main criteria: (i) use of PTMs with excellent optical properties; (ii) the solar absorber (i.e., PTM and substrate) should possess low thermal conductivity to localize the generated heat; (iii) the system should possess fast water transport channels [42-47], and; (iv) the absorber should exhibit anti-salt crystallization properties when evaporating saline feedwater [42, 48].

2.2 Strategies for achieving efficient interfacial solar evaporator

2.2.1 Fabrication of efficient solar-thermal (Photothermal) conversion materials

Solar irradiance at the earth's surface on a sunny day is approximately 1 kWm^{-2} (equivalent to one Sun) at sea level [49]. The solar spectrum consists of ~7% ultraviolet (UV) light (300-400 nm), ~43% visible (vis) light (400-700 nm), and ~50% near-infrared (NIR) light (700-2500 nm) [50, 51]. An optimal semiconductor PTMs for SSG can capture all the wavelengths of the incident sunlight (UV-Vis-NIR) and efficiently convert the absorbed light into heat. To achieve the maximum light-to-heat conversion, the PTMs must absorb sunlight with low reflection and transmittance and avoid heat loss during the photothermal conversion process [52].

2.2.1.1 Nano-microstructure semiconductor photothermal materials

Semiconducting materials excited by photons with energies greater than or equal to their bandgap generate electron-hole pairs. As excited electrons relax, energy can be released in the form of heat or vibrations by energy transfer to the material lattice (i.e., non-radiative relaxation via phonons). When the phonons encounter defects in the lattice of the material with poor thermal conductivity, heat dissipates into the surroundings, which establishes a temperature distribution depending on the optical absorption and their recombination characteristics [18, 23]. Semiconductor PTMs with narrow bandgap (E_g) can achieve excellent photothermal conversion efficiencies as most of the solar spectrum can be utilized for heat generation. Large bandgap PTMs exhibit limited optical absorption, which results in low photothermal conversion efficiencies. Besides regulating the bandgaps, nano/microstructure semiconductor PTMs contribute to excellent light absorption through sunlight reflection and trapping. Various strategies have been exploited to narrow the bandgap for enhancing the light absorption of semiconductor PTMs. Strategies, examples, and perspectives are discussed in the next sections in detail. A summary of the methods materials preparation and SSG performance of various semiconductor-based PTMs is illustrated in **Table 2.1** a. Plasmonic materials with localized

surface plasmon resonance (LSPR) are capable of absorbing a broad light spectrum up to the NIR region, which is beneficial for remarkable light harvesting within a extensive range of the solar spectrum. The increase in the valence band leads to a plasmonic resonance peak shift to higher frequencies [53]. The LSPR can be obtained and tuned by two main methods: (i) free carriers (holes) formed through cation vacancies due to the presence of a defect or doping [53, 54] and ; (ii) use of low bandgap materials to boost the absorption to cover the whole solar spectrum. The structure compositions and morphology could also play a vital role in improving light absorption [55]. Traditional noble metals have been widely used to generate the LSPR effect. However, high cost limits their practical applications, especially in solar steam generation. Interestingly, LSPR semiconductor materials with low bandgap open a new avenue as alternative candidates to noble metals. This is attributed to their relatively lower cost (precursors cost as well as fabrication cost) and potential to be synthesized at large-scale.

Metal chalcogenides

Non-stoichiometric p-type semiconductor $Cu_{2-x}S$ is a well-known plasmonic semiconductor PTM in solar steam generation. It can exhibit different bandgaps through varying the crystal structures via controlling the stoichiometric (x) in $Cu_{2-x}S$ [53]. The stoichiometric and morphologies can be varied by controlling the synthesis parameters or precursors types. This has a significant influence on photothermal conversion efficiency [56]. For instance, Zhang et al. fabricated high-quality Cu_7S_4 nanocrystals (NCs) with different shapes via heat controlled reactions with sulfur in 1-octadecene for SSG [56]. At one sun irradiation, water evaporation efficiencies of 60.5%, 51.6%, 53.1%, and 47.8% were achieved for monodisperse disk-like, monodisperse spherical, polydisperse disk-like, and polydisperse spherical Cu_7S_4 NCs, respectively. The highest performance was achieved by monodisperse disk-shaped NCs as they possess the strongest LSPR effect and have high electron (hole) carriers. Quaternary p-type

Cu_2ZnSnX_4 (X=S or Se) has received considerable attention as an effective solar absorber due to its low and tuneable bandgap [57]. For example, Cu_2ZnSnS_4 was investigated as an efficient solar absorber due to its narrow direct energy bandgap and a very high optical absorption coefficient (> 10^4 cm^{-1}) [58, 59]. Mu et al. synthesized 3D Cu_2ZnSnS_4 nanosheet as an efficient solar absorber for SSG applications [60]. The strong surface plasmon resonance caused by high carrier concentration results in low bandgap and the incident light trapped between the microstructure leads to excellent light absorption properties of 92.25% at the entire solar spectrum. This results in a remarkable solar evaporation rate and efficiency of 1.46 kg^{-1} m^{-2} h and 84.5%, respectively, under 1 sun irradiation. Similar to the quaternary sulfide, selenide p-type $Cu_2ZnSnSe_4$ (CZTSe) with narrow bandgap (E_g = 0.88 to 1.2 eV) has been demonstrated as potential solar absorber [61]. This quaternary p-type displays excellent light absorption, and more research on this direction can be considered. For example, Yang et al. demonstrated CZTSe nanocarambolas and irregular shapes for highly efficient SSG [62]. The optical properties of quaternary p-type display strong LSPR that covers the full solar spectrum. The high free carrier (hole) density of the nanocarambolas and the unique assembled nanoporous structure hence achieve a strong LSPR effect in the IR region. Hence, excellent photothermal conversion in the absorber layer to evaporate the water layer at the interface and exhibit a high-water evaporation rate of 1.52 kg m^{-2} h^{-1}, at one sun irradiation. On the other hand, the irregular shape displayed a weak LSPR effect, resulting in a lower water evaporation rate of 1.412 kg m^{-2} h^{-1}. However, despite the exceptional performance, the high toxicity of selenium added during the synthesis process remains a challenge that could hinder the applications of these materials for SSG application. Previous works revealed that metal chalcogenides possess excellent light absorption characteristics. Among reported metal chalcogenides PTMs, copper sulfides feature merits of the low-cost, easy synthesis process. They can be formed in various morphologies and sizes, making it easy to be integrated with several types of substrates for

enhancing the optical properties. So far, this unique class is the most promising semiconductor PTMs due to its excellent solar water evaporation performances. In contrast, in the case of binary metal chalcogenides, despite the excellent display performance, more investigations are required regarding the structure compositions and morphology regulations.

Oxygen deficient metal oxides

Transition metal oxides (TMOs), such as tungsten oxide (WO_3) or molybdenum oxide (MoO_3), have attracted considerable attention as excellent PTMs mainly ascribed to their excellent thermal stability [63-65] and their unique characteristics of the free outer-d valence electrons. Their bandgap can be regulated through phase transitions, as the occupancy level of its 5d orbitals varies with lattice distortion [66]. Oxygen-deficient metal oxides possess high charge carrier density, which is necessary for achieving the LSPR effect. This also acts as a defect for phonon propagation, leading to expected enhancement in photothermal conversion efficiency in SSG application. Additionally, introducing oxygen vacancy results in the appearance of defect energy levels and reducing the gap between the valence band and the defect level [67, 68]. Tungsten oxide, WO_{3-x} (e.g., $WO_{2.72}$, $WO_{2.83}$ WO, and $W_{19}O_{49}$) with oxygen defects is an attractive LSPR candidate for SSG. Amorphous WO_3 possesses large lattice distortion and displays a wide bandgap of E_g= 3.4 eV; while the monoclinic crystalline phase exhibits E_g=2.6 eV [66, 69]. After introducing the oxygen vacancy, nonstoichiometric WO_{3-x} displays strong broad light absorption in the NIR region due to intervalence charge transfers, LSPR of free electrons, small polariton absorption and narrower bandgap [70]. Sun et al. reported the phase transition from semiconductor metallic WO_3 to quasi-metallic through a hydrogenation process, delivering excellent light absorption characteristics of 90.6% [71]. Furthermore, ab initio calculation showed a narrower bandgap of $WO_{2.9}$ compared to WO_3, consequently extending the range of light absorption wavelengths from UV to Vis to NIR region. Additionally, the band structure of $WO_{2.9}$ shows that both the upper valence band and lower

conduction band is partially occupied, with its Fermi energy level shifted nearer to the conduction band. Fang et al. designed and fabricated a flexible, self-floating $W_{18}O_{49}$ nanowires/carbon foam composite through a hydrothermal and annealing process using melamine foam as a raw precursor for carbon-based support [72]. During the annealing process, the melamine foam was converted into carbon foam with a highly porous net structure, which contributed to the scattering and trapping of the light. In addition, the total amount of reduced $W_{18}O_{49}$ (W^{5+} or W^{4+}) was increased from 16.7% to 45%. This results in intensive oxygen vacancy and enhances the light absorption characteristics. For this reason, a high-water evaporation rate of 1.694 kg m^{-2} h^{-1} was obtained under one sun irradiation. The flexible features of the composite make it reusable for several cycles with stable performance. Chang et al. demonstrated a flexible solar steam generator composed of nonstoichiometric $W_{18}O_{49}$ mesocrystals wrapped with PDMS on PTFE membranes [73]. The mesocrytals materials consist of high oxygen vacancies, leading to strong LSPR, and broadband light absorption with a bandgap of 2.7 eV. As consequence, water evaporation rate of 1.15 kg m^{-2} h^{-1}, and efficiency of 80.7% under one sun irradiation. MoO_x is another example of oxygen-deficient metal oxides with strong LSPR properties, making it promising PTMs for SSG applications. For example, Lu et al. employed an oxygen-deficient MoO_x flower-like structure composed of atomically thick nanosheets [74]. The light absorption of ~ 90% was obtained, corresponding to a bandgap of 1.82 eV. The material was loaded onto the PTFE membrane and applied as a solar steam generator where a water evaporation rate of 1.255 kg m^{-2} h^{-1} and an efficiency of 85.6 % were achieved. Guo's group presented the work on using MoO_{3-x} quantum dots as PTM, where its absorption band closely matched with the solar spectrum [67]. The oxygen vacancy was introduced by the hydrothermal method utilizing chitosan as both reducing and capping agent. After loading the materials into cellulose acetate membrane and coated with fluoroalkylsilane, a water evaporation rate of 4.95 kg m^{-2} h^{-1} and an efficiency of 62% were demonstrated under

5 sun irradiation. Oxygen deficient metal oxides are good materials with a lower bandgap of and strong LSPR effect for achieving excellent light absorption for solar water evaporation. To increase the solar absorption capability for water evaporation performance, advance research is required, such as; tailoring morphology control (e.g., porous, size and diameter) or nanocomposite design.

Size, concentrations, and other parameters

An effective approach to adjust bandgap is to tailor the material size with a narrow size distribution. Taking titanium dioxide (TiO_2) as an example, it exists in different crystal phases (i.e., anatase, rutile, brookite) and exhibits wide E_g (3-3.2 eV). As a result, the optical absorption is limited to the UV region (< 400 nm), accounting for a total of <7% of the solar spectrum [75, 76]. Wang et al. reported nanoscale titanium sesquioxide (Ti_2O_3) NPs (size ~400 nm) using a ball milling process and obtained a very small bandgap of 0.1 eV. The corresponding bandgap mechanism is illustrated in **Figure. 2a** [77]. The light absorption characteristics are compared to the commercial bulk Ti_2O_3. The bulk one shows less light absorption capability (85.4%) compared to nanosize Ti_2O_3 NPs (92.5 %), due to the less efficient light scattering of bulk particles (**Figure. 2b**). To investigate the effect of NP size, they reduced the size to 350 nm and resulted in 1% increase in the light absorption. Also, the materials demonstrated a 100% conversion of the entire absorbed light into heat. After loading Ti_2O_3 NPs on cellulose membranes, a remarkable water evaporation rate of 1.32 kg $m^{-2}h^{-1}$ under one sun irradiation was obtained. Besides the size, the concentration of semiconductor PTMs display a vital role in enhancing the optical characteristics. For example, Tao et al. investigated the impact of the plasmonic CuS concentrations in light absorption [78]. They incorporated different amounts of CuS (1 to 12 mg) into the PVDF membrane. The light absorption was increased with increasing the amounts of CuS concentrations reaching to a

maximum (12 mg) absorption of >90% in the UV-vis and >96% in the NIR region (**Figure. 2c**). With excess amounts of CuS (16 mg), they found no difference to the optimum loading case (12 mg) as it reaches the saturation level. 12 mg-CuS-PVDF produces a water evaporation rate of 1.43 kg m^{-2} h^{-1}, 2.91 kg m^{-2} h^{-1}, and 5.93 kg m^{-2} h^{-1} under 1 sun, 2 suns, and 4 suns irradiation, respectively (**Figure. 2d**). In contrast, Chen et al. presented a MoS_2 nanoflower structure with an external diameter of 1 μm composed of nanosheets deposited on air-laid paper (ALP) as efficient PTMs. They realized that by changing the concentration of MoS_2 into the ALP layer, the light absorption efficiency also varies until no change is observed [79]. Yang et al. reported the hybrid composite material of MoS_2 nanosheets with single-walled CNTs by controlling the thickness of nanosheets from 2 to 6 nm, the solar absorption was enhanced from 82% to 95% [80]. The surface roughness cause in multi-scattering and trapping of incident solar irradiation that enhances light absorption [81]. For instance, CuS/PE composite membrane was also prepared to feature rough 3D surface and open porous channels, leading to light absorption of ~ 93%, low transmittance of ~2.5%, and reflectance of ~4% [82]. The growing semiconducting PTM on a rough membrane or 3D supports, such as metal foams, would be a desirable SSG application approach. Through regulating the thickness and concentrations of semiconductor PTMs not only impact on the light absorption but also the water evaporation efficiency. It is also recommended to investigate the effects of the PTM thicknesses and concentrations on light absorptions and water evaporation efficiency.

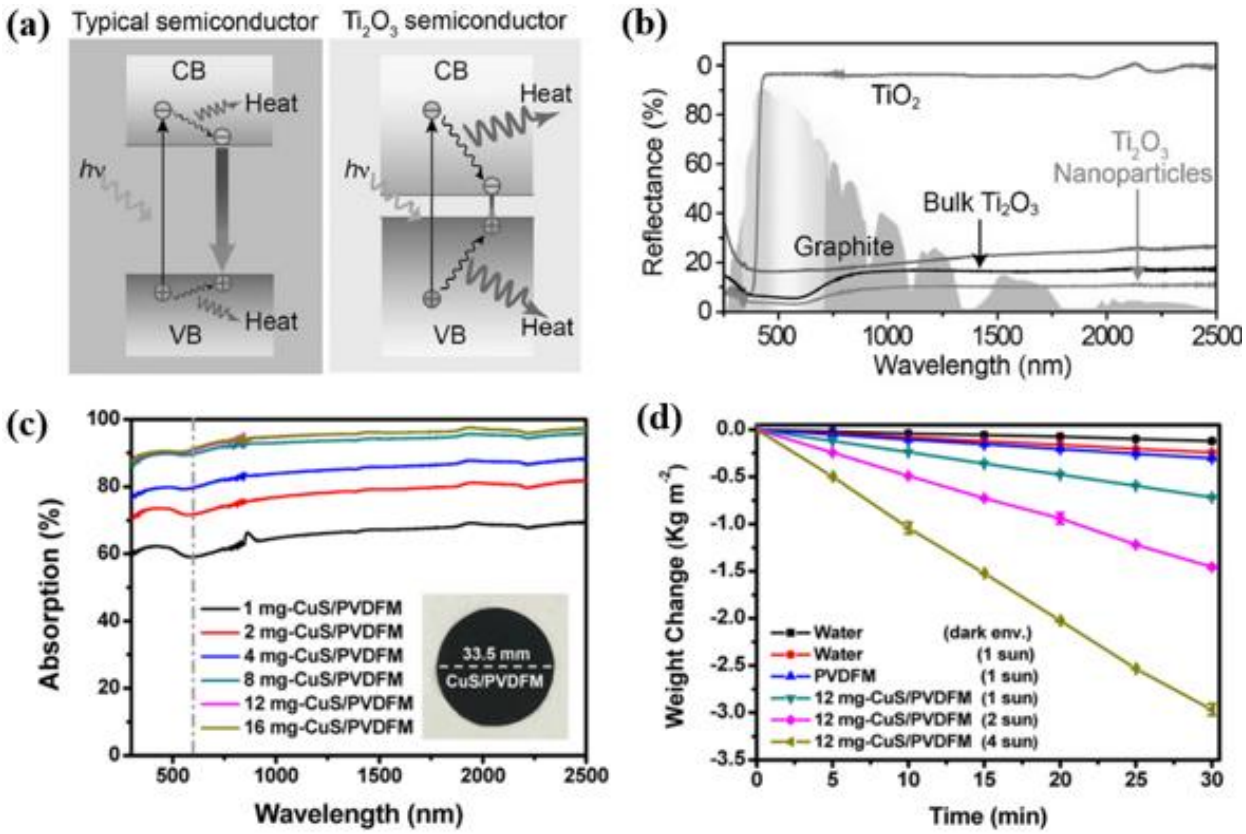

Figure 2.1 (a) Schematic Illustration of typical electron-hole generation and relaxation in a typical semiconductor (left) and narrow bandgap Ti_2O_3 (right), (b) solar reflectance spectra of Ti_2O_3 NPs [77], (c) UV−vis−NIR absorption spectra of different amount CuS/PVDFMs, and (d) water evaporation rate of 12 mg-CuS/PVDFM under increasing solar intensities irradiation [78].

2.2.1.2 Noble metals based photothermal materials

Noble metal-based nanostructures (e.g. Au, Ag, Pd) have been widely reported as PTMs in SSG. This is ascribed to their stability under harsh environmental conditions (acidic, basic conditions) [83-85]. The light absorption mechanism caused by localized surface plasmon resonance (LSPR) which broadened the absorption and extended to the infra-red regions. The plasmon-assisted photothermal effects occur when metal nanoparticles are illuminated at their resonant wavelengths, which causes oscillation of the electron cloud. Rather than through radiative emission, the decay of these hot electrons through electron-electron scattering redistributes the hot electron energy, which can rapidly increase the localized surface

temperature of metal particles [86, 87]. Several strategies have been implemented to develop effective PTMs for solar water evaporations. This can be done by tailoring the size and shapes of the PTMs or by using an effective substrate that contributes to the light and heat localizations. **Table 2.1** b gives summary of the preparation and SSG performances of different types of noble metals based PTMs.

The effect of Size and Morphology

It has been reported that the morphology of the noble metals has a strong influence on the resonant frequency position of the plasmon absorbance. For that reason, researchers have tried to synthesize different types of nanostructures (nanoparticles, nanocage, nanocylinders) with varied LSPR in the UV-ViS-NIR regions. Several researchers investigated au nanoparticles (NP) with solid centers and quasi-spherical shapes. However, their LSPR were limited to the UV region (250-800 nm). Au NPs with increasing diameters between 3 and 40 nm and red shift from 520 to 530 nm are still limited to the UV region [88]. AuNP with hollow structures (e.g., cages, boxes and shells) or with anisotropic structures (e.g., stars, multipods and rods) can exhibit LSPR peaks tuneable to the entire visible and NIR regions [29]. For instance, Wu *et al* designed and fabricated Au nanocages (AuNCs) with hollow interiors and porous walls, followed by electrospinning with PVDF [29]. They indicated that the LSPR mechanism could be explained by its absorption rather than scattering. Besides the morphology, the size of nanostructures can impact light absorption. The Au nanocages peaks can be shifted from 400-1200 nm by controlling the wall thickness and porosity of the walls [29]. The floated AuNCs/PVDF could generate an efficiency of 79.8 % under the natural sun.

Effect of the substrates used

The substrate also plays a vital role in improving the light absorption or the plasmonic enhancement properties. Therefore, different types of substrates were integrated with noble metals nanoparticles, including; AAO [89, 90], Wood [91] and diatomite [92], and bio-inspired

systems. For instance, Zhu's group proposed that the depositing of noble metals NPs into porous open channels substrates such as Anodized alumina Oxide (AAO) was found to be an efficient method to minimize light reflections. AAO is nanoporous template material with sizes ranging from 20-400 nm, which can be fabricated via anodization of alumina foil at high voltage (-40 V) [93]. The straight and open channels with loaded Au NPs can further enhance the light absorption properties. Based on this principle, Jia Zhu et al., applied Anodized alumina Oxide (AAO) into an SSG [89]. AAO is nanoporous template material with sizes ranging from 20-400 nm, which can be fabricated via anodization of alumina foil at high voltage (-40 V). The straight and open channels with loaded Au NPs can further enhance the light absorption properties. The absorption shifts from ViS to NIR by tuning the pore diameters and the deposition parameters. For the first time, Zhu's group demonstrated the controlled fabrication of AuNC morphology via manipulating the pores diameter of AAO nanoporous template (***D:*** 50 nm, 100 nm and 200 nm). The mechanism can be described by the assembling of close-packed NPs around the inner sidewall of the pore, creating random particles with different sizes in large quantity and the plasmon hybridization effect, which is an agreement with their previous report [94]. Additional nanotubes are arranged in a photonic crystal-like structure, which dominates the infrared absorption cut-off feature. Au nanoparticles are redshifted with the increasing AR, indicating the broadband absorption mechanism of LSPR hybridization. However, the intrinsic resonance of Au nanotubes is blue-shifted with an increasing thickness (t), which suggests the cut-off point of the nanotube-built photonic-crystal-like geometry [89]. Despite the good performance of AAO substrates, it is still suffering from high cost, deposition of NPs into the channels is more complicated, weak mechanical stability and some toxicity issues [95]. To overcome this issue, bio-inspired substrates have been considered as a good substrate for plasmonic noble metals derived PTMs SSG [24, 95-97]. For example, Sheng et al. designed ring shapes natural bamboo (thickness of ~1 cm) and deposited Au NPs uniformly

on the vessels of the bamboo [97]. Bamboo consists of vertically oriented vessel microchannels that provide water capillary force, resulting in excellent water transport. It exhibited a high absorption capability of 99% over the UV–Vis–NIR because of the strong LSPR and the internal reflection and trapping through the microchannel. The plasmonic bamboo maintains low thermal conductivity at a wet state with a slight increase from 0.30 W/m/k (for bamboo) to 0.35 W/m/k, thus providing excellent insulating properties. SSG efficiency of 87% was obtained under 10 suns irradiation. Deng groups proposed Au NPs coated air-laid paper via incubating aqueous Au NPs solution on (ALP) overnight with the assist of formic acid which allowed the diffusion of Au NPs (**Figure 2.2 a)** [24]. The optical properties display that the prepared Au NPs/ALP possess higher light absorption of 87% compared to the free standing Au NP film 64% (**Figure 2.2 b)**. This result confirm the beneficial of the microporous ALP for enhancing the light absorption of the plasmonic Au NPs through multiple scattering. The solar evaporation performance was conducted under 4.5 sun irradiation, the resulted showed that a an evaporation efficiency of 77.8% for Au NPs/ALP which is relatively higher than free standing Au NP film 47.7%. The solar evaporator and schematic of the evaporation mechanism of Au NPs/ALP is shown in **Figure 2.2 c.** Bioinspired plasmonic membrane composed of filter paper coated with gold NPs was reported by Wang and his co-workers [96]. The fabrications process involved the preparation of colloidal Au NPs followed by vacuum deposition of the dispersed gold on filter paper which pre-treated initially with poly(diallyl dimethyl ammonium chloride). A good light absorption of 87.7% was achieved along the whole solar spectrum regions. This resulted in a water evaporation of 12.18 and an efficiency of 85% at 10 sun irradiation. Chen et al. investigated the influence of substrates on the light absorption (Au NPs) with as-prepared poly(p-phenylene benzobisoxazole) nanofibre (PBONF) [98]. The commercial filter paper exhibited low light absorption of 6.7% compared to the 34.7% of PBONF, which corresponded to the vibration modes in the π-conjugated structure that is

stimulated by excitation of optical transition. The light absorption of 67.4% was obtained in Au NPs/PBONF system. Upon-sun light irradiation, the designed Au NPs/PBONF can achieve a good solar thermal conversion with a surface temperature increase of 9 ^{o}C from the initial temperature. This resulted in a water evaporation rate of 1.42 kg m^{-2} h^{-1}. Fang et al. made further steps toward improving plasmonic metals' performance by depositing Ag nanoparticles into micrometer size-diatomite via chemical plating mainly composed of silica [92]. During the water evaporation, the water is absorbed through the cavity and multi pores of diatomite, which could also reduce the heat loss. Meanwhile, Ag NPs act as solar absorbers by harvesting the light and converting it into heat. This resulted in a water evaporation rate of 1.39 kg m^{-2} h^{-1}, corresponding to an efficiency of ~92.2% were demonstrated.

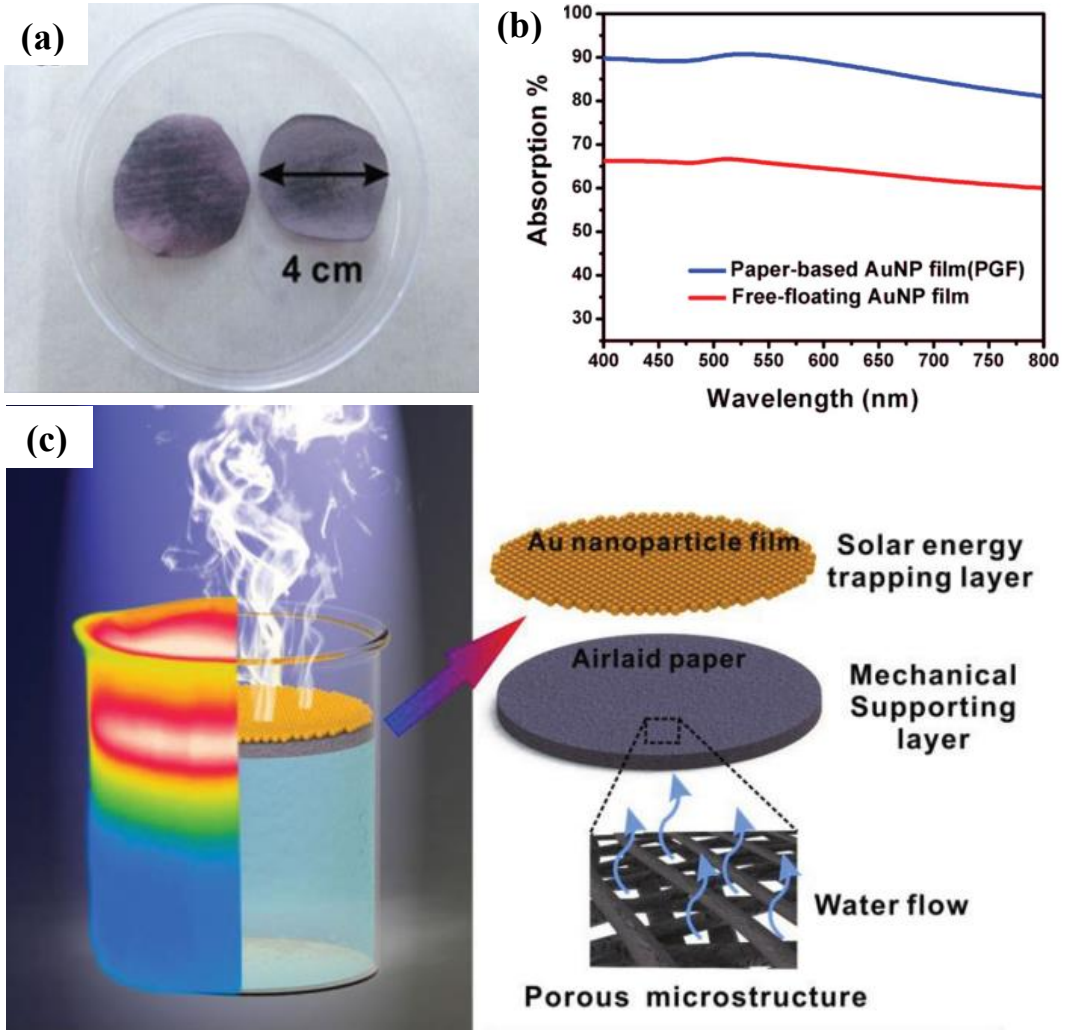

Figure 2.2 (a) Photograph of the prepared Au NP/ALP. (b) The optical characteristics of Au NP/ALP in comparison to the free standing Au NP. (c) Schematic lustration of the composition of Au NP/ALP and the working mechanism during solar water evaporation [24].

2.2.1.3 Nanostructured polydopamine based photothermal materials

A conjugated polymer such as Polydopamine (PDA) has been widely investigated and displays good performance in SSG applications. This is attributed to its unique features of the straightforward fabrication process and excellent light absorption caused by strong π-electron localization [39, 99-104]. In addition, the materials exhibit high stability when attached to various types of substrates, making it ideal PTMs. In 2017, Jiang et al. fabricated a flexible bilayer interfacial evaporator composed of spherical PDA (diameter ~1 μm) loaded into 3D open microporous bacterial nanocellouse matrix (BNC) [104]. This resulted in excellent light absorption of 98% across the solar spectrum region. The floated PDA/BNC bilayer can achieve high solar thermal conversion with a surface temperature that can reach up to 43 ^{o}C under one sun and 72 ^{o}C under 3 suns. This resulted in solar water evaporation and efficiency of 1.13 kg m^{-2} h^{-1} and 3.47 under 3 suns, respectively, under one sun irradiation. Later on, Xu et al. prepared a PDA-coated pinewood through the self-polymerization process at room temperature [105]. The functionalization of wood morphology and pore channel size remains unchanged. This results in maintaining the mechanical and physical properties of biomass, greatly assisting in enhancing the water transport channels. The superhydrophilicity of wood-PDA, due to the abundance of hydroxyl groups (–OH) from PDA, resulted in continuous and fast water transport. Besides, PDA acts as an excellent solar absorber for sunlight absorption. As a result, a water evaporation rate of 1.38 kg m^{-2} h^{-1}, corresponding to the photothermal conversion efficiency of 87% under 1 sun irradiation, was obtained. Zou et al. demonstrate PDA integrated into cellulose aerogel for SSG applications [106]. The as-prepared PTMs exhibited a rough and porous surface structure with good thermal insulation properties. This resulted in good dollar light absorption ~90% matching the solar spectrum region. Besides, efficient solar-thermal conversion can be realized with a surface temperature that can reach up to 40 ^{o}C within 10 min from the initial temperature of 22 ^{o}C. Consequently, a water evaporation rate up to 1.36 kg m^{-}

^{2} h^{-1} with an efficiency of 86%. Zhang et al. suggested the use of semi-coke coated with PDA as self-floating PTMs [107]. The synergistic effect of the interaction between semi-coke and the coated PDA PTMs enhanced results in a stable rough micro-nanostructure and excellent solar-thermal effects. This results in excellent optical characteristics with light absorption of ~99% in the 250-1200 nm wavelength range. Additionally, a water evaporation rate of 1.41 kg m^{-2} h^{-1} with a photothermal efficiency of 90.56% was obtained. The above-mentioned results confirm the promising applications of PDA as effective PTMs for SSG applications. However, there is a huge scope for the decorations of PDA with porous metal substrates which have not investigated yet. This could be a promising methods specially for the salt-resistance applications in solar desaliantion applications. **Table 2.1** c display the preparation method of PDA and their perfoemance in SSG.

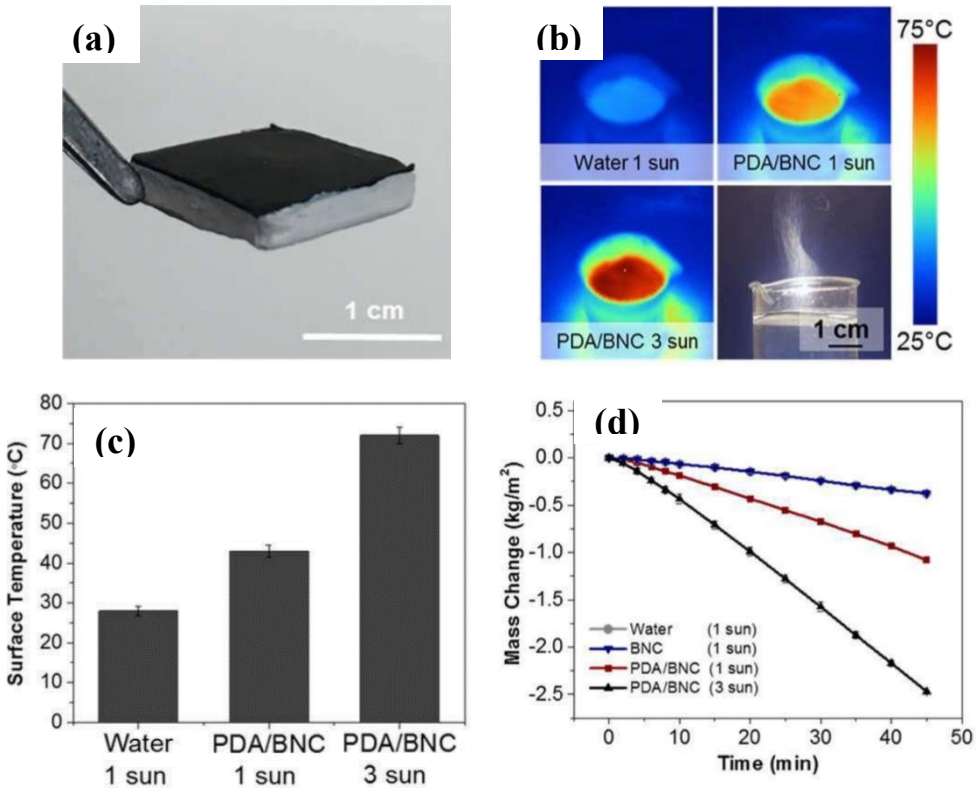

Figure 2.3 (a) Photograph of PDA/BNC. (b,c) IR images and corresponding temperature of the generated heat on the surface of PDA/BNC and water based solar evaporator at irradiation of 1 sun and 3 suns. (d) The mass change during water evaporation of PDA/BNC and water based solar evaporator at irradiation of 1 sun and 3 suns [104].

2.2.1.4 Hydrogel based photothermal materials

Hydrogel constitutes a group of polymeric materials with a hydrophilic structure with high porosity endows them with a capability to absorb large amounts of water within the 3D networks [108-111]. These merits extended the applications of these materials in solar-driven water evaporations. It can meet all the criteria for efficient solar evaporator for solar harvester, excellent solar-to-thermal conversion, and allowing fast water escaping. The hydrogel can integrate with various nanostructured materials such as integrations with other materials to form composite hydrogel graphene [112], Metal-organic framework [113], organic polymers [114, 115]. The hydrogel can be formed through chemical cross-linking in where the hydrogen bonding is substituted with the covalent bonding that inhibits the dissociation in water. Or physical cross-linked (also called non-covalent bonding) where physical entanglements including hydrogen bonding, hydrophobic interactions and electrostatic [110, 116]. In this literature review, we classified hydrogel based on the origin of the polymer as Poly (vinyl alcohol) (PVA) derived hydrogel and polymer beyond PVA with the integration with nanostructure PTMs.

PVA hydrogel derived nanostructure photothermal materials

PVA is known as synthetic polymer contains abundance (-OH) functional groups with advantages of being hydrophilic, biodegradable and biocompatible and good mechanical strength properties [110, 117]. All these merits attracted scholars' attention to utilizing PVA-derived hydrogels for SSG applications. The PVA-derived hydrogel can be formed through various crosslinking methods classified as (a) chemical cross-linked, (b) physical cross-linked, and (c) irradiation chemical cross-linked. This method is usually combined with other techniques to enhance the porosity, such as freeze-drying, freeze-thawing to enhance the porosity and surface properties (**Figure 2.4 a**) [110]. For example, Yu et al. reported a tree-inspired hydrogel with a vertically aligned channel adding MXene as a solar harvester, mainly

fabricated by a directional freeze-drying process [118]. It formed through the incorporation of a given concentration of PVA and MXene in Teflon mold. This was followed by placing the Teflon mold on a copper cylinder and immersing it in liquid nitrogen for freeze casting. This process results in the formation of vertically aligned channels, which is highly beneficial in solar light absorption-thermal conversion. The as-designed hydrogel possesses features of fast water transport and escaping. The interaction between the hydrophilic PVA-MXene and water molecules resulted in a low heat required for water vapor generations. Taking advantage of the above-mentioned merits resulted in a high evaporation rate up to 2.71 kg m^{-2} h^{-1} and thermal conversion efficiency (90.7%) at one sun irradiation. In a recent study, Liu et al. demonstrated a novel strategy by designing PVA functionalized graphene hydrogel as an effective solar thermal convertor for high-performance water evaporation [112]. They used NMP solvent, which formed a complex with PVA that acts as the cross-linker in the gel network. The graphene was dispersed well after being added to the PVA-NMP complex. The proposed method resulted in hierarchical structure hydrogel with a porous network structure, which is an advantages for enhancing solar harvesting and thermal conversion through multiple internal reflections within the pores (**Figure 2.4 b**). This resulted in superior solar absorption up to ~ 97% across the whole solar spectrum. As result, a water evaporation rate of 1.77 kg m^{-2} h^{-1} with efficiency of 91.6% can be achieved under one sun irradiation. In most recent studies, Hao et al. designed and developed PVA with sodium lignosulfonate (SLS), and combined with carbon nanotube as solar absorber, as effective hydrogel PTMs [119]. The added SLS has an advantages of rich hydroxyl groups that cross-linked network with PVA. In addition to that, it can form hydrogen bonding with water which improve the content of intermediate water. The resultant hydrogel achieve a light absorption of 95% in the (UV-vis-NIR; 300 to 2500 nm), which attributed to the presence of CNT. The solar thermal conversion result confirm that a temperature up to 47.1 ^{o}C can be obtained under one sun irradiation. Due to the above

mentioned advantages, a good water evaporation rate of 2.09 kg m^{-2} h^{-1} was obtained under one sun irradiation. **Table 2.1** d highlight the hydrogel preparation, characteristics and SSG performances. The advantages, drawbacks, and enhancing approaches of different classes of PTMs reported in this thesis are presented in **Table 2.2.**

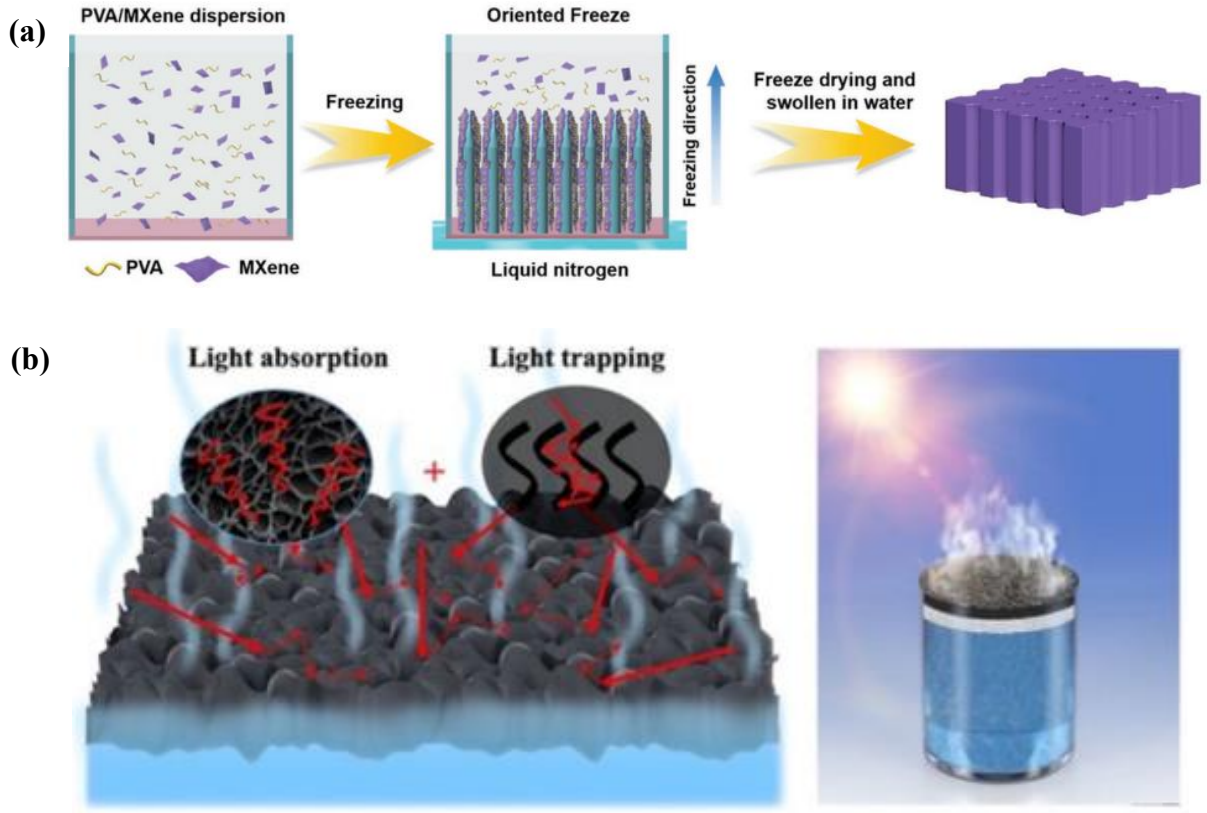

Figure 2.4 **(a)** Schematic illustration of the preparation process of PVA/MXene hydrogel with vertically aligned channels [118]. **(b)** A schematic illustration of hierarchical PVA-Graphene hydrogel which offer a synergistic effect in light absorption and trapping and the designed solar evaporator [112].

Other polymeric derived hydrogel nanostructure photothermal materials

Besides PVA, other researchers tried to discover other materials beyond PVA to improve the water vaporization enthalpy. Such as using starch derived hydrogel [120], chitosan derived hydrogel [121, 122], alginate [115], double network hydrogel poly-(ethylene glycol) diacrylate-polyaniline [123], Starch with rich hydrophilic (-OH) hydroxyl groups identified as a suitable superabsorbent hydrogel for solar steam evaporator [110, 120, 124]. For instance, in the most recent study, Xu et al. used a simple strategy using a starch-derived hydrogel incorporated carbon nanotube as a high-performance solar evaporator system [120]. They used a simple gelatinization followed by a freeze-thawing process for 10 continuous cycles. The starch-derived hydrogel resulted in an internal porous structure, which contributes to the rapid water transport and lowers the enthalpy evaporation resulting in reduced energy consumption for water evaporation. Meanwhile, carbon nanotube (CNT) with network structure act as a solar harvester. As a result, an efficient solar harvester can obtain ~92% in the wavelength range of 300–2500 nm, which higher than the pure starch hydrogel (without CNT) 36 %. For solar water evaporation, PS foam was placed below the starch/CNT hydrogel to act as a heat localizer. Under one sun irradiation, a solar water evaporation of 2.77 kg m^{-2} h^{-1} with an evaporation efficiency of ~88% was achieved. Later on, Guo et al. developed hybrid hydrogel by combining the mechanical strength of PVA and the water absorption of rich hydroxyl groups starch [125]. After the gelatinization of PVA with starch, small amounts of polyethylene foam were added to enhance the floating of the evaporator on the water. Then, carbon black nanoparticles coated cellulose nanofiber were overlaid on nonwoven fabric and introduced to the hydrogel, followed by subjecting to freeze (-20 ºC) and thawing (25 ºC) for 3 cycles. The designed hydrogel achieved excellent solar to thermal conversion with a temperature that can reach up to 52.0 °C. A water evaporation rate of 1.08 kg m^{-2} h^{-1} corresponding to an efficiency of ~88%, was reported under one sun irradiation. Li et al. suggested that the copolymerization

of vinyl monomers resulted in incorporating the nanomaterials, which usually act as radical scavengers that impede the polymerization [126]. They proposed the combination of poly(ionic) hydrogel with a solar harvester of polypyrrole-silver nanoparticles to the solar thermal hydrogel. In detail, they used 1-vinyl-3-ethylimidazolium bromide, N,N′-methylene-bis-acrylamide as cross-linker and ammonium persulfate as initiator. The prepared hydrogel was subjected to a freezing-thawing process repeated 10 times. This followed by in-situ polymerization and spray coating to prepare a top polypyrrole-silver nanoparticle which acts as a solar harvester, and bottom poly(ionic) hydrogel acting as supporter and water supply to the top PTM. This results in excellent light absorption of 96% across the whole solar spectrum region.

Challenges and prospects in hydrogel derived photothermal materials

Despite the advantages of the reported study in hydrogel-driven solar evaporators, many studies are still needed. Three main points are needed to be addressed to bring the hydrogel-derived PTMs to practical applications. (1) The cost of the nanocomposite incorporated with the hydrogel must be considered before the fabrication process. (2) More straightforward and less complicated methods need to be developed. (3) The mechanism of the incorporated nanocomposite with the hydrogel needs to be further explored to understand their effectiveness in enhancing the porosity and water absorptivity. PVA display perfect superabsorbent for solar-driven hydrogel materials. However, more research is needed to propose a strategy to lower vaporization enthalpy and understand the interactions of nanostructures PTMs and the hydrogen bonding in the perfect superabsorbent hydrogel.

Table 2.1 Summary of the design and SSG performances of different classes of PTMs

Materials and design				Performance		Ref.
Photothermal materials	**Supporter/ Thermal insulator**	**Synthesis Method**	**Morphology and Structures**	**Light Absorption (%) (UV-ViS-)**	**Water Evaporation rate/ Pure water**	
a. Semiconductor						
Multifunctional CuO NWs mesh	EPE	Immersion + Alcohol burner	Nanowires on Cu mesh	93	1.42	[127]
CuS/PVDF	Self-float	Hydrothermal + Phase inversion	Hierarchical nanostructure ***T:*** 85 nm/	95	1.43	[78]
CuS/SCM nanoflower	Self-float	Hydrothermal	3D covellite nanoflower composed of nanosheets/ ***D:*** ~2 µm/	-	1.09	[128]
Porous CuS NPs	PE hybrid membrane/ Self-float	Single-layer Solvothermal	CuS NPs ***D:*** ~40 nm/ PE ***PS:*** ~73.9 µm, ***T:*** 112 µm	93	1.02	[129]
3D-plasmonic covellite CuS /PVDF	/ Self-float	Hydrothermal + Phase inversion	Hierarchical nanostructure ***T:*** ~85 nm	>90 UV-vis	1.43	[130]

				>96 NIR		
Cu_xS	MCE/ PU foam	Solvothermal + Vacuum assisted deposition	CuS particles embedded in porous MCE	85	1.12	[131]
CuPO on PDMS composite	Self-floated	Hydrothermal	Hierarchical flower microstructured composed of nanosheet/ ***D:*** 2-5 µm	41.8	1.85	[132]
Cotton-CuS aerogel	PS foam	Casting method + Freeze-drying	Yolk-shell NCs-agarose Shell wall ***T:*** 40–70 nm	94–95.5	1.63	[133]
CuS films/MCE	PU foam	Solvothermal	Particles embedded into porous MCE	85	1.12	[134]
Cu_xS/Cu foam	PS foam	Solution based method	3D hierarchical Nanorods structure	96.3	1.96	[135]
Cu_2SnSe NS array	PU foam	Re-flask + Vacuum assisted deposition	NS array/ ***D:*** 200-300 nm	97	1.657	[136]
$Cu_2ZnSnSe$ NS array/CEM				95.5	1.643	
$Cu_{12}Sb_4S_{13}$ NPs/CAM	Self-float	Reflask + Vacuum deposition	NPs/ ***S:*** 30-70 nm	-	6.6	[137]

$CuCr_2O_4/SiO_2$ Composite	Quartz glass fibers	Impregnation + Calcination	Nonwoven fibrous membrane	57 (Dry) 53 (Wet)	1.32	[138]
$Cu_{2-x}S$ NWs/Melamine foam	Self-floated	Polyol method	Ultralong nanowire/ ***D:*** ~50 nm and ***L:*** tens of micrometers	-	-	[139]
Oxygen-Defected MoO_x Nanostructure	EPE	Hydrothermal	Hierarchical flower like structure composed of nanosheet/ ***S:*** 1 um/	97	1.255	[74]
MoS_2 nanosheets	BNC hydrogel	Chemical exfoliated +	Nanoshee/ Bilayer	96	0.81/0.76 Sun	[98]
MoS_2/C-PU Composite	Self-floated	Hydrothermal	3D spoke-like structure	98	1.95	[140]
MoS_2	Cotton cloth/ PS foam	Hydrothermal	Nanoflower hierarchical	90	1.3	[141]
MoS_2	EPE	Hydrothermal	Nanoflower composed of numerous nanosheets	96.15	1.27	[142]
b. Plasmonic metals						
Pt/Au/TiO_2-decorated Plasmonic Wood Carbon	Self-floated	Calcination	Nanoparticles/ ***S:*** 500 nm	-	90.4 /10 sun	[143]

Au-ZnO/MCE	Self-floating	Sonication + Chemical reduction + Vacuum deposition	Hedgehog-like hierarchical ZnO particles /Au nanoparticles	-	8.70	[144]
Pd@Bamboo	Self-floating	Carbonization+ solution based	Ordered and porous structure and nano-Pd layer was firmly coated on the inner surface of the vessel	>99	12.8/ 10 suns	[145]
Au/Au NPs@Cotton	Self-floating	Surface treatment + Chemical Reduction	Au/Au NPs with ***S:*** 70 to 100 nm are uniformly distributed on the fibers	-	1.4	[83]
Thin-film black Au membranes	Self-floating + they surrounded the system with styrofoam	Anodization + Sputtering	Self-aggregated nanowire bundles with irregular three 3D patterns coated with Au ***T:*** 40 nm	91	0.67	[146]
Al NPs/AAO membrane	Self-floating	Anodic oxidation + Al NPs deposition	Anodized Alumina oxide with ***D:*** ~300 nm, Al NPs with ***T:*** ~85 nm	>96	0.92	[147]

Au/PVDF	Self-floating	Chemical reduction + Filtration	Top surface with spherical structure an bottom surface with flower like structure and ***PS***: 0.36 µm	~90	1.03	[148]
Au NPs/ALP	Self-floating	Chemical reduction + Deposition	AuNPs (***D:*** 17.4 ± 0.3 nm) and AuNPs film is attached on the paper fibers	87 (UV-Vis)	~7 g/h at 4.5 sun	[24]
c. Polydopamine						
Bilayer of PDA/BNC	Self-floating	In situ polymerization + Dispersion in bacteria growth media + Freeze-drying	Thin BNC (~100 µm) with a dense entangled layer of cellulose fiber network and PDA in spherical shape with ***D:*** 1 µm	98 (Vis)	1.13	[104]
PDA/Wood	Self-floating	Surface treatment+ Self polymerization	Perforative channels interconnected by staggered walls with ***PD:*** 30 ~ µm	-	1.38	[105]

PDA filled cellulose aerogel		Chemical Cross-linking + Freeze-drying + In situ polymerization coating	Rough and porous structure	90	1.36	[106]
Semi-coke/PDA@melamine sponge	Self-floating	In situ polymerization + Co-precipitation	Melamine sponge with 3D porous network structure coated with a rough surface Semi-coke, and PDA were adhered to the surface	>99	1.41	[107]
PDA/Natural rubber sponge	PS foam	In situ polymerization+ coating	3D porous structure with a rough surface, ***PS:*** tens to hundreds µm	-	1.35	[149]
d. Hydrogel						
Mxene/PVA	PS foam	Directional Freezing	Vertically aligned channels hydrogel and the size of the coated Mxene nanosheets of 1-2 µm	>97	2.71	[118]

Graphene/PVA	PS foam	Chemical cross-linking	Hierarchical structure with porous network	97	1.77	[112]
PVA/Sodium alginate/CNT	Self-floating	Gelation+ Freeze-drying	Porous structure with ***PS***: of 10–60 μm	95	2.09	[119]
CNT/Starch	PS foam	Gelation+ Freeze-thawing	Micrometre-sized pores and CNT with network structure are nested	92	2.77	[120]
CB deposited nonwoven fabric	PVA@starch	Vacuum filtration + Gelation + Freeze-thawing	Dense layer of CB with interconnected and neatly arranged	-	1.08	[125]
Ag/PPy-PMBA-BrILs	Self-floating	Chemical Cross-linking + Freeze (by liquid nitrogen) and thawing (in distilled water) + in-situ polymerization + spraying	Smooth and wrinkled surface with abundance holes of PMBA-BrILs coated with small particles of Ag/PPy	96	1.37	[126]

MnO_2 NWs/Chitosan Hydrogels	Self-floating	In-situ polymerization	Vertically aligned microchannel with ***PS:*** ~ 0.5 µm and the MnO_2 NWs are distributed on the surface	94	1.78	[121]
p-PEGDA-PANi hydrogel	EPE foam	Solvent casting/salt leaching method+ oxidative polymerization	Interconnected microporous structure (***PD:*** 270-325 µm)	98.5	1.40	[123]

S: Size, PS: pore size, PD: Pore diameter, T: Thickness, D: Diameter, L: Length, NPs: Nanoparticles, NWs: Nanowires, NCs: Nanocages, NS: Nanospheres, EPE: Expandable polyethylene, EPS: Expandable polystyrene, PE: Polyethylene, PDMS: Polydimethylsiloxan, PDA: Polydopamine, PS: Polystyrene, PU: Polyurethane, PANi: Polyaniline, CEM: Cellulose ester membrane, CM: Cellulose membrane, AAM: Anodized alumina membrane, p-PEGDA: poly(acrylamide-co-poly(ethylene glycol), PMBA: poly(N,N'-methylenebis(acrylamide), PTFE: Polytetrafluoroethylene, PVDF: poly(vinylidene fluoride), PVA: Polyvinyl alcohol, BNC: Bacteria nanocellulose, AAO: Anodized Aluminium Oxide, CNT: Carbon nanotube, CB: Carbon Black.

Table 2.2 Advantages, drawbacks, and enhancing approaches of different classes of PTMs

Materials	Advantages	Drawbacks	Enhancing approaches
Polydopamine	• Biodegradable. • Easier fabrication process. • It can grow on various substrates.	✓ Moderate solar light absorption. ✓ Hard to exist in various morphologies.	○ Exploring a unique Structural morphology. ○ The incorporation of PDA into metal foam substrate.
Plasmonic	• Good chemical stability even under high environmental conditions.	✓ Complicated fabrication process. ✓ Poor solar light absorption. ✓ High cost.	○ Using a straightforward method to fabricate large-scale materials. ○ Enhancing solar light absorption.
Semiconductor	• Excellent solar light absorption. • It can exist in various structures and morphologies.	✓ The fabrication process can be complicated as it requires hazardous solvents.	○ Fabrication of microstructures materials.
Hydrogel polymer	• Low cost. • More straightforward fabrication process and does not require complicated equipment. • Excellent solar light absorption. • It can be integrated with various classes of PTMs.	✓ The anti-salt stability under high salinity remains a challenge.	○ Investigating the effect of porosity and structural morphologies on overall performances. ○ Integrating the hydrogel polymer with a new type of PTMs

2.2.2 Thermal management and interfacial solar evaporator systems

Thermal management is critical for the adequate performance of an interfacial SSG system. In an ideal case, all generated heat is utilized to evaporate the water, but heat losses are unavoidable due to interfacial SSG configuration. Heat is lost by conductive and radiative processes from the solar absorber to the water beneath it and by convective and radiative processes to the surroundings [4, 150]. For example, the conventional design of a hydrophobic solar absorber attached on top of a hydrophilic porous floating support exhibits inherent thermal loss issues. The adjacent water can fill the gaps in the hydrophilic support layer, replacing air voids and increasing conductive thermal losses as water has higher thermal conductivity than air [41] improvements to the interfacial SSG system design are classified into 2D and 3D solar water evaporator configurations.

2.2.2.1 2D solar steam generation system

Earlier studies on 2D interfacial SSG systems were based on thin hydrophobic layers of solar absorber directly floating on the water. There were high thermal losses due to direct contact with water. To minimize the heat losses, a supporting layer to act as both a thermal insulator and floating material is usually added [41]. This also isolates the solar absorber from the bulk water forming a common interfacial 2D SSG design. This strategy has attracted increased interest from many research groups as such design improved the water evaporation rate. Polymeric materials are usually used for this insulating support layer. For example, Ques's group demonstrated the use of MXene membrane with external polystyrene foam as a thermal insulator [151]. Their design enabled heat localization with less conduction heat loss leading to a more stable temperature on the evaporation surface (~ 39 ^{o}C). Some researchers have opted to modify the supporting substrate to mitigate the heat loss drawback. For example, metal foam substrates have also been utilized as they possess high porosity and low thermal conductivity.

Xu et al. fabricated CuO nanowires on a copper foam with low thermal conductivity of 0.02 W m^{-1} K^{-1} using a solution-based flame treatment method [152]. For SSG application, they designed a device consisting of external expandable polyethylene EPE foam with low thermal conductivity underneath the CuO layer; consequently, the heat losses considerably reduced. Upon solar irradiation under one sun, the light was converted into heat by the CuO nanowires with a temperature of 32.5 ºC. Furthermore, they observed a negligible increase in bulk water temperature (~1 ºC) after 30 min of light irradiation under one sun. This displayed insignificant heat conduction from the solar evaporation surface to the bulk water. Consequently, a water evaporation rate of 1.45 kg m^{-2} h^{-1} with an efficiency of 84.4% was achieved. A substrate with 3D interconnected microstructure such as natural wood, hydrogel, and PU sponge substrates display low thermal conductivity and excellent heat localization. Besides, air with low thermal conductivity passes along with the vapor and provides additional thermal insulation. These distinctive features make it a suitable substrate for high-efficiency semiconductor PTMs devices. For example, environment-friendly natural wood possessing mesoporous structures and open microchannels have been utilized with semiconductor PTMs [63, 153, 154]. Liu et al. combined $CuFeSe_2$ NPs (E_g ~ 0.45 eV) into the microporous channel in the wood substrate [153]. At 1 sun irradiation, the surface temperature of the black wood increased from 20.1 ºC to 62 ºC at the dry state and 30.1 ºC at the wet state. On the other hand, the blank raised to 41.7 ºC at the dry state and a negligible increase in the wet state. The solar-to-heat conversion results indicated that incident light is being effectively converted to heat. Therefore, a water evaporation efficiency of 67.7% and 85.2% under 1 and 5 suns irradiation, respectively, which is attributed to the good thermal insulation provided by the wood substrate.

Nevertheless, recently hydrogel derived solar evaporator has been demonstrated as effective superabsorbent materials with excellent heat localizers and fast water evaporator which could exceed the water evaporations value. Irshad et al, proposed semiconductive hydrogel composed

of MnO_2 nanowires/chitosan hydrogel (named as SPM-CH) with vertically aligned macropore ~ 0.5 µm which is beneficial for solar thermal conversion and heat localizations [121]. Upon sunlight irradiation, the surface temperature of the hydrogel rose from 22.3 °C to 40.6 °C after 30 min of sunlight irradiation, which demonstrates the capability of the evaporator for solar energy harvesting is highly beneficial for water evaporation performances **Figure 2.5 a.** The excellent solar thermal conversion is attributed to the high structural porosity and swelling ratio, which resulted in perfect solar thermal conversion with negligible downward heat losses. Additionally, it will allow sufficient water supplying which is beneficial for high-water evaporation. **Figure 2.5 b**. illustrate the mechanism for heat localization and its utilization for vapor generation. As a result, excellent water evaporations of 1.7 kg m^{-2} h^{-1} with an efficiency of 90.6% can obtain under one sun irradiation.

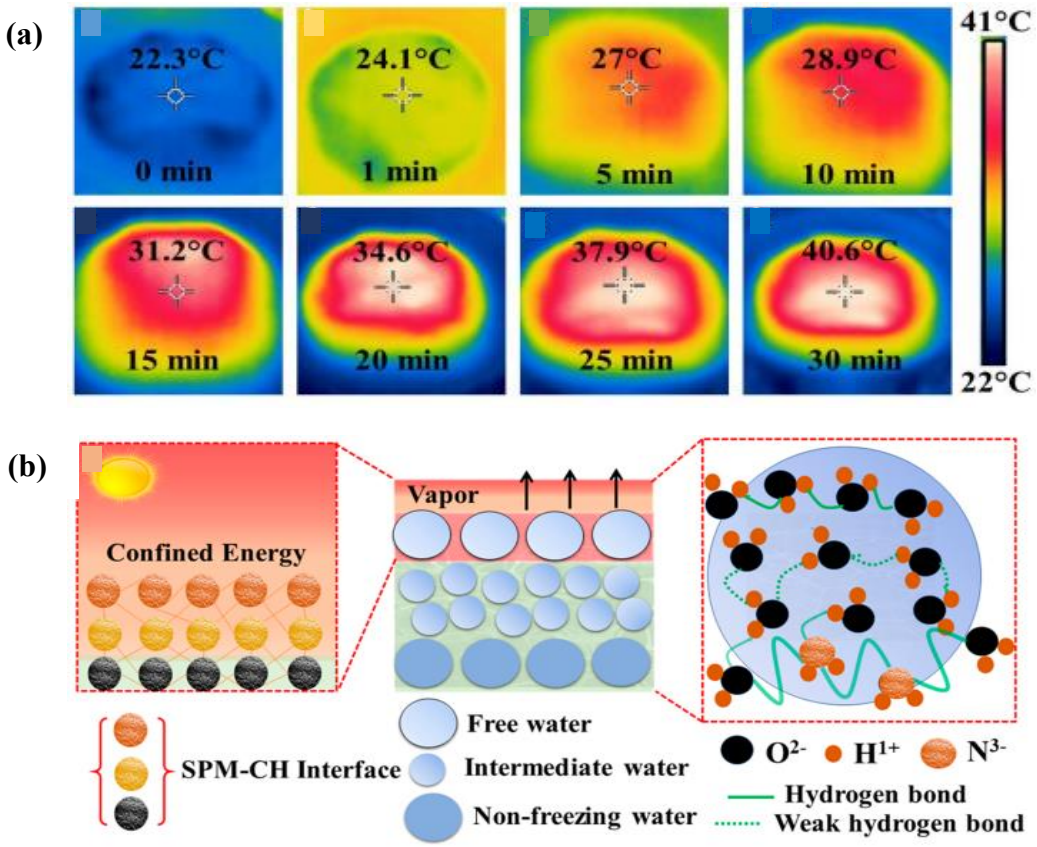

Figure 2.5 (a) Infra-red images of semiconductive in-situ polymerized SPM-CH under one sun irradiation. (b) Schematic illustration of energy confinement and its utilization for vapor generation [121].

2.2.2.2 3D solar steam generation system

To improve SSG device performances, researchers came up with 3D modular structures that enhance the photothermal conversion and minimize heat losses. This can exceed the theoretical solar evaporation limit in some reports [26, 155]. The system proves to overcome the convection and radiation issues of some 2D design configurations, such as flat membranes-based solar steam generations. Furthermore, the system could recover or reabsorb the energy lost and harvest energy from the environment [156, 157] or reduce the downward heat loss through the air gap, which acts as an insulating barrier [157]. For instance, Peng et al. developed a unique 3D cup-shaped solar absorber coated with $CuFeMnO_4$ pigment. They found that the diffuse reflectance and thermal radiation energy can be recovered, which was not observed in the 2D disk [155]. This is attributed to the 3D design: (i) recover the diffuse light reflectance and radiated heat from the bottom of the cup through the cup wall; (2) gain energy or heat capture from the external environment result through the heat exchange. As a result, a remarkable water evaporation rate and efficiency of ~100% and 2.04 kg m^{-2} h^{-1} were achieved, respectively, under one-sun irradiation. Huang et al. presented a novel approach for designing an SSG device [157]. The authors prepared dual-phase $Cu_{2-x}S$ on Cu foam with 3D hierarchical branch architecture with a synergistic increment of the LSPRs and the bandgap absorption (**Figure 2.6 a**). **Figure 2.6 b** reveals the proposed design bridge shape with an air-gap below the top absorber part, acting as a thermal insulator barrier beside PS foam to suppress the downward heat loss. Also, the as-designed 3D system allows the energy from the environment to contribute. The two tails serve as a water pathway channel (**Figure 2.6 d)**. Under one-sun irradiation, radiation and convection heat losses of 4.4% and 1.6%, respectively, were detected by IR images visualizing the heat distribution on the top and side of the device (**Figure 2.6 e**). This caused an impressive water evaporation rate and efficiency of 1.96 kg m^{-2} h^{-1} and 94.5%, respectively (**Figure 2.6 c**). These fruitful findings in 3D semiconductor SSG devices revealed

the critical role of the device design for achieving exceptional water evaporation rate/efficiency. Despite the good performances of the 3D solar evaporator systems. But, there are a lot of questions regarding the amount of raw materials required. In addition to that, the water supply remains a challenge as most of the part of the photothermal evaporator surface is not exposed to enough water, unlike in the case of porous hydrogel materials. Notwithstanding these accomplishments, the research on these directions is not investigated enough. Therefore, future studies are needed regarding the above-mentioned challenges.

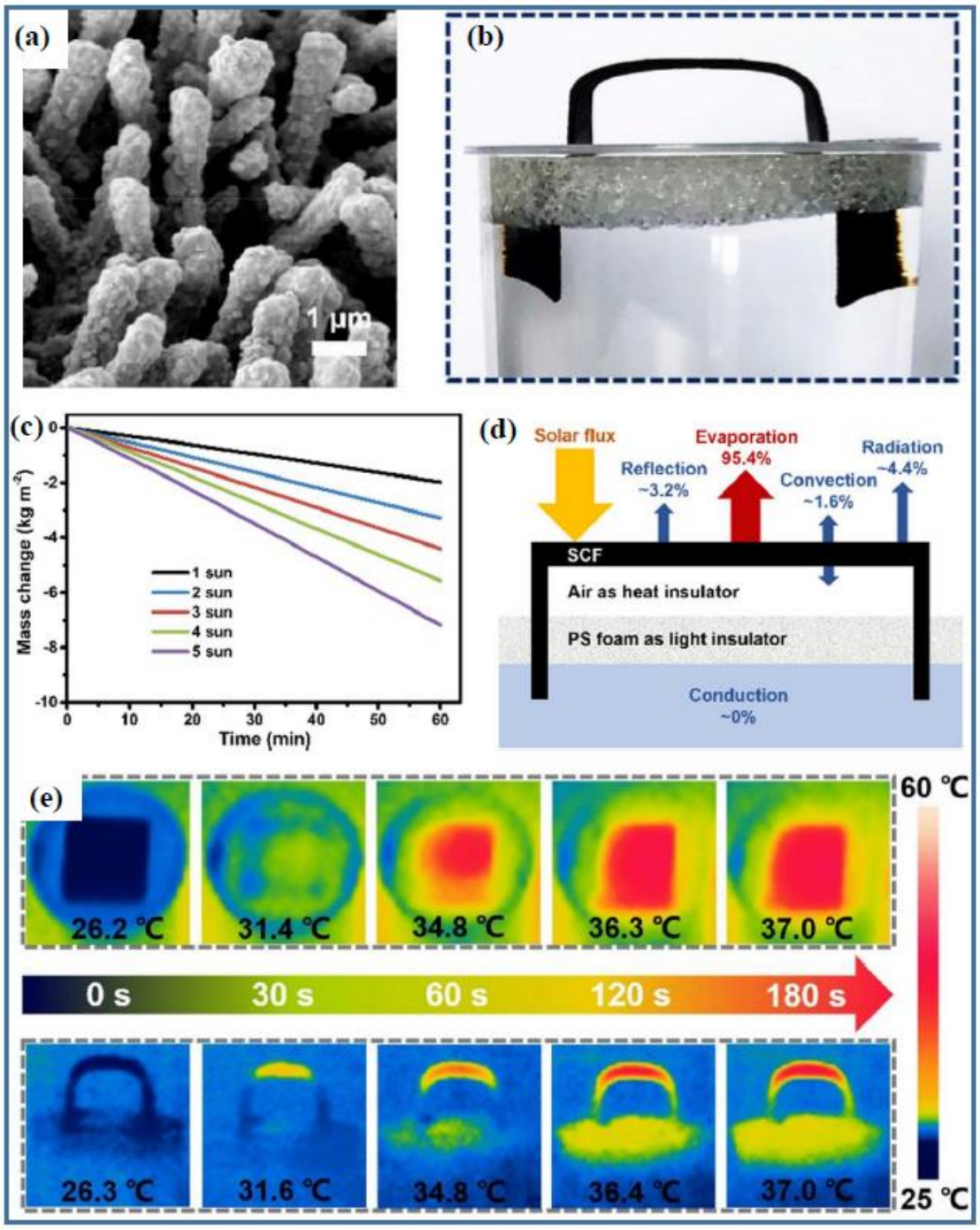

Figure 2.6 (a) SEM images of 3D hierarchical branch architecture Cu_xS/Cu foam, (b) photograph of the device fabricated with the bent Cu_xS/Cu foam, (c) water evaporation under different light intensities for Cu_xS/Cu foam, (d) energy balance and heat loss diagram of Cu_xS/Cu foam under 1 sun irradiation, and (e) IR thermal images of top-view and side-view of the water-wetted Cu_xS/Cu foam under 1 sun irradiation [157].

2.2.3 Water supply pathway

The water supply from the bulk water to the upper part of the solar absorber region through capillary actions is a core component for highly efficient interfacial SSG systems. The substrate plays a vital role in supplying water to the solar absorber part. The bottom substrate should possess a hydrophilic and porous structure for water permeation to the solar absorber part through capillary action [158]. However, low wettability restricts the heat-to-water evaporation efficiency due to insufficient water supply [159]. Various substrates such as cellulose membrane (CM) [62, 67, 77, 134, 151, 160], air-laid paper [79], PVDF [78, 161, 162], semipermeable collodion membrane [53], and polyethylene have been used to provide both as insulating support and water pathway [82]. Wicking pathways are specially designed within or around the insulating support or as a fully isolated system from the solar absorber, directly not in contact with bulk water, while a free-air gap exists between them. Moreover, 1D and 2D capillary water channels are added in the system connecting the absorber part and feed-water to enable the fast wicking of water to the solar absorber. For example, Chen et al. used air-laid paper to wrap around an expandable polystyrene support layer to act as 2D water transport channel towards hydrophilic MoS_2 absorber. The excellent water capillary actions and wettability leads to a water evaporation rate of 1.27 kg $m^{-2}h^{-1}$ [79]. On the other hand, Wu et al. employed a photothermal-water contactless system composed of CuS-agarose aerogel as PTM, insulator foam as a thermal insulator, and cotton rod as a 1D water channel to transport the water to the PTM part (evaporation area) [133]. A new approach has been suggested by using substrates with 3D interconnected microchannels such as biomass wood, PU foams, and hydrogels structure, which have the ability to absorb a large amount of water with heat localization effects. This design also does not require additional wicking materials or thermal insulators. Sun et al. reported the efficiency of macroporous polyacrylamide hydrogel with copper sulfide as a highly efficient water transport system. The macroporous hydrogel is

capable of absorbing a sufficient amount of water and allow water vapor to escape, while copper sulfide absorbs the incident light, which is trapped through the macroporous hydrogel structure, resulting in a water evaporation efficiency of 92%. Researchers also utilized biomass materials such as wood and cotton as a natural water pathway. Wood composed of cellulose, rich in hydroxyl group, prevents the detachment and agglomeration of the $CuFeSe_2$ NPs from the substrate [153]. In addition to that, the porous microchannel structure of the wood facilitates water transport to the absorber part. As a result, water evaporation efficiency of 67.7% and 85.2% was achieved under 1 and 5 suns, respectively. Other factors such as absorbers' surface porosity and roughness, concentration, and the distance from the absorber to the bulk water are significant factors affecting the water evaporation performance. For example, CuS NPs attached to polyethylene (PE) membrane with open, microporous channels of ~73.9 μm generated sufficient capillary forces to replenish water to the CuS/PE membrane the water evaporates from the absorber regions [82]. Chen et al. observed that after increasing the concentration of MoS_2, the evaporation rates were also increased [79]. However, after reaching an optimum MoS_2 concentration, the heat exchange velocity reduced, leading to a slightly lower water evaporation rate [163, 164]. Yao et al. investigated the effect of the absorber-to-water surface distance using SnSe/NF and found that 1 mm (tested between 1, 5, and 10 mm) distance produced the highest evaporation rate [81]. Despite the excellent water transport, the design of the supporting layer is an aspect that needs further investigation to improve the efficiency of the SSG device.

2.2.4 Strategy to mitigate salt crystallization

Salt crystallization is one of the main issues in water desalination for SSG. Therefore, it is essential to prevent or minimize it to allow the reusability and stability of the as-designed devices. The salt crystallization takes place when the water travels towards the PTMs and its supporting structures. The salt ions can migrate along with vapor and crystalize on the solar absorber layer [165]. The accumulation of salts on the solar absorber will have a detrimental effect on water evaporation especially when a high concentration of salts is crystallized. This leads to dramatically low solar-thermal conversion and water evaporation rate [166-169]. As a result, numerous methods have been proposed to enable anti-salt crystallization capability for the solar absorber system, and distinct improvements have been achieved. This includes coating the solar absorber with a superhydrophobic layer [151, 170], fabricating a Janus type membrane [171-174], and using hydrophilic porous polymer architecture [168, 175].

2.2.4.1 Hydrophobic PTMs as salt blocking materials

Fabrication of hydrophobic PTMs have been reported as a direct and effective strategy to prevent and repeal the salt ions crystallizations on the surface of the solar evaporators. Besides, it possesses self-cleaning salt properties making it applicable PTMs, especially for saturated brine solutions [176]. For instance, Xu et al. demonstrated an effective strategy for preparing copper foam coated with aluminum oxide NPs and decorated with carbon black and modified with the solution of 1H,1H,2H,2H-perfluorooctyltrichlorosilane as adequate hydrophobic salt tolerance PTM [176]. They designed a solar evaporator composed of the designed PTM and underneath leaf as water lily and vascular bundles to act as water path to supply the water to the water lily. As a result, water evaporation rates of 1.31 kg m^{-2} h^{-1} and 1.28 kg m^{-2} h^{-1} under water and brine (10%) were obtained under one sun irradiation. The surface remains clean after 8 hours of continuous solar irradiations using 10% brine solution. Howver, the hydrophobic PTMs prevent and lower the water supplying during solar thermal conversion which result in

lowering water evaporations performance. Meanwhile, Hydrophilic nanostructured photothermal membranes display a drawback of salt crystallizations during solar seawater desalination, hence hindering its practical applications [160]. To overcome this defects, one approach is to treat the surface with a hydrophobic layer at the top, and, commonly, silane treatment is employed [170, 177-179]. This design is similar to Janus structures and prevents the formation of a hydration salt layer on the surface; thus, salt deposition is diminished [160, 180]. For example, Ye et al. modified TiO_x-coated on stainless steel (SS) meshes with 1H,1H,2H,2H-perfluorooctyltrichlorosilane (PFOTS) through vapor deposition and produced a superhydrophobic surface with a contact angle of 150^o [181]. The modified hydrophobic membrane surface exhibited a stable, non-fouled surface after solar irradiation for days. Ye et al. modified TiO_x-coated on stainless steel (SS) meshed with 1H,1H,2H,2H-perfluorooctyltrichlorosilane (PFOTS) through vapor deposition and produced a superhydrophobic surface with a contact angle of 150^o [181]. The modified hydrophobic membrane surface exhibited a stable, non-fouled surface after solar irradiation for four days. Que and his co-workers observed that salts crystallized and accumulated on hydrophilic Cu_2SnSe_3/cellulose membrane resulting in a lower water evaporation rate (**Figure 2.7 a-c**) [160]. On the other hand, the hydrophobic $Cu_2SnSe_{3/}$ hydrophilic cellulose membrane surface maintains clean and unclogged even after 10 hours of operation, with continuous and stable water evaporation through the channels made by interconnected nanospheres (**Figure 2.7 d-f**). The proposed mechanism of salt rejections and water evaporation with the simulated curve is illustrated in **Figure 2.7 (g-i).**

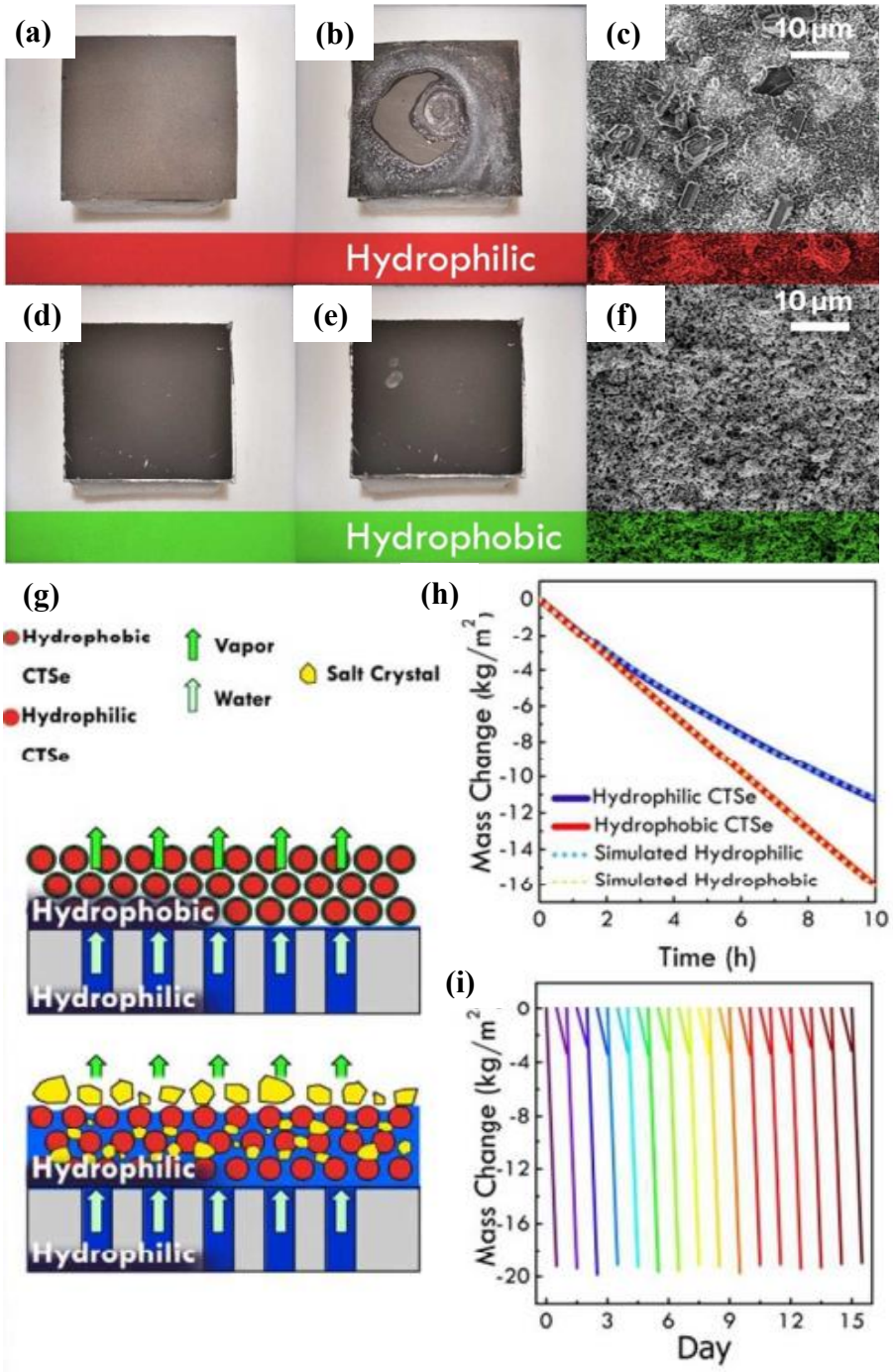

Figure 2.7 Photo-image of hydrophilic and hydrophobic membranes (a and d) before solar desalination (b and e) after 10 h solar desalination. SEM images of the membranes after 10 h solar desalination (c) hydrophilic (f) hydrophobic. (g) Schematic illustration of the mechanism for salt rejections of hydrophilic and hydrophobic membranes (h,i) Mass change of the hydrophilic and hydrophobic membranes with the corresponding simulated decay curves [160].

2.2.4.2 Porous structural PTMs

Porous structural PTMs have been demonstrated as practical solutions for salt-resistance solar evaporators with long-term durability and stability. It has been shown through this method the PTMs can be reused through simple zero-liquid discharge or through day reflow-and night reflow approaches [182]. An example following this strategy includes designing; porous metal-based PTMs, biomass-based PTMs, and hydrogel-based PTMs. Metals foam-driven solar PTMs is another strategy that has been proposed not to improve the solar-thermal conversion characteristics but also to achieve excellent anti-salt PTMs. This is attributed to its 3D porous interconnected structures that allow more water to pass through during the evaporations and achieve excellent self-cleaning properties [183]. For example, Wang's group reported 3D oxygen vacancy-rich WO_{3-x} composed of nanorod array grown on nanosheet array coated Ni foam substrate as effective solar evaporator and anti-salt properties [183]. They demonstrated an evaporation rate of 1.50 kg m^{-2} h^{-1} under one sun irradiation, with an efficiency of 88%. Using natural seawater, they showed excellent stability for up to 10 continuous cycles (1 h/cycle) under one sun irradiation (**Figure 2.8 a)**. Also, they have noticed no salt formed on the surface, as further confirmed by the SEM images (**Figure 2.8 b)**. In addition, they evaluated the salt resistance of the evaporator anti-salt properties. Furthermore, they conducted the self-cleaning properties by placing a certain amount of salt on the top of the evaporator surface, which could deliver an excellent anti-salt characteristic, and no slats were noticed on the surface of the evaporator after 11 minutes of exposure to sunlight irradiation. Later on, Cui's group proposed hydrophobic NF PTMs consisting of graphene (G) and MoO_{3-x} decorated on NF using both facile chemical vapor deposition (CVD) followed by hydrothermal methods [184]. They demonstrated that the hydrophobic property (contact angle ~113°) of the designed solar evaporator could be beneficial for reducing the salt accumulations on the surface. Ren et al. used plasma-enhanced chemical vapor deposition to fabricate hierarchical graphene on NF

as an effective solar evaporator with excellent anti-salt. They realized a reduction in evaporation rate after short-term under 5 sun irradiation. Then they demonstrated the salt on the surface can be removed by dip rinsing in water [185]. **Figure 2.6 c-g,** illustrated the evaporation performance using simulated seawater and the SEM images with elemental mapping before and after performances.

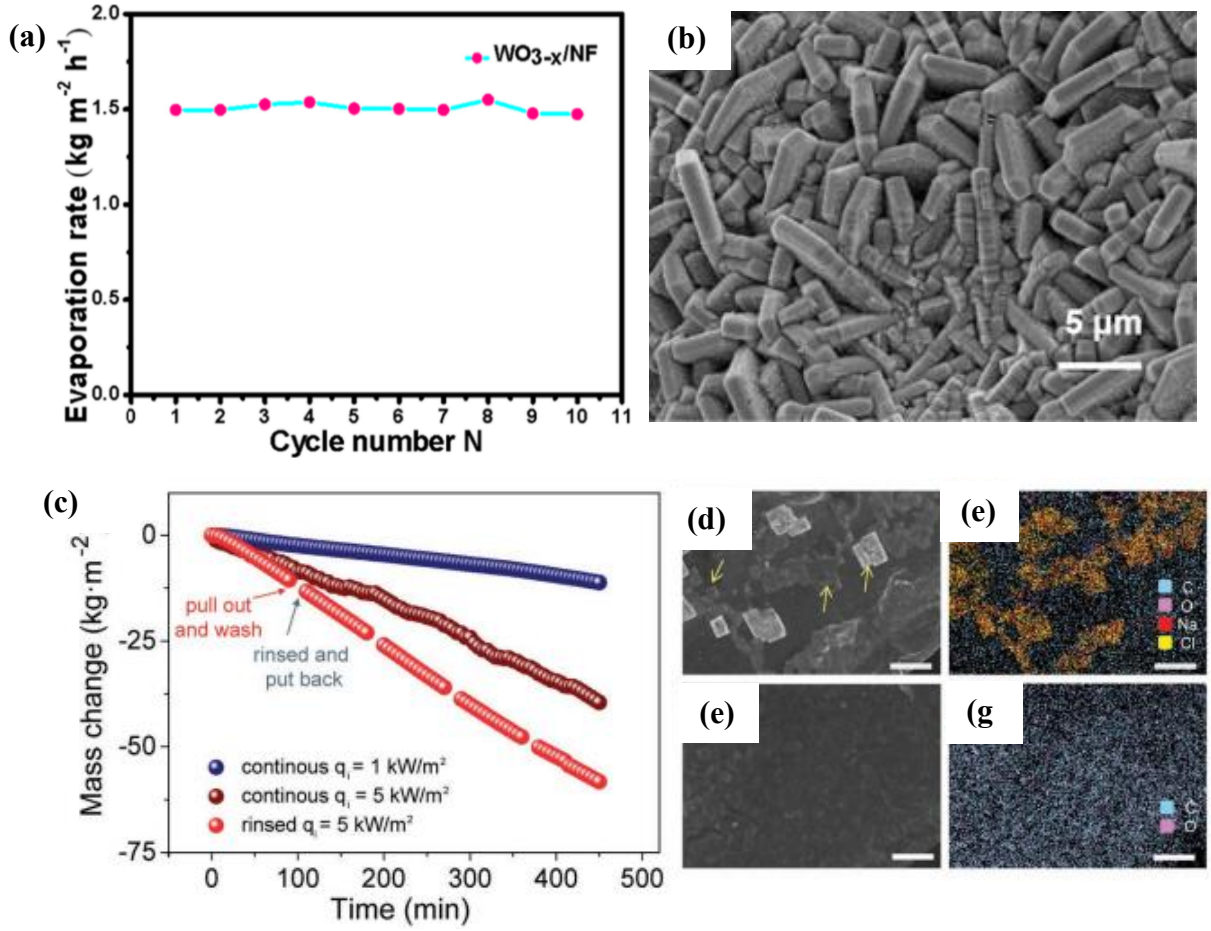

Figure 2.8 (a) Cycle stability of WO_{3-x} /NF demonstrated a stable evaporation performance over ten continuous cycles at one sun irradiation. (b) SEM images after ten cycles revealed no salt formed on the surface [183]. (c) Long time continuous desalination test of hierarchical graphene foam under the illumination of 1 kW m^{-2} (blue dots) and 5 kW m^{-2} (wine-red dots). (d, e) SEM images and elemental mapping revealed the salt formations (NaCl) on the hierarchical graphene foam after 240 min under solar illumination of 5 kW m^{-2} (f, g). The images display no salt formations after dip immersing on the water [184].

Porous hydrogel PTMs another promising strategy for designing highly and effective PTMs for seawater desalination. This ascribed to its high porous channels with efficient water supply, resulting in fast salt crystals exchange [111]. This strategy will prevent the salts from accumulating for the long term on the hydrogel surface. Xu et al. demonstrated CNT/Starch as effective anti-salt solar steam generators. Their designed hydrogel was stable for up to 5 continuous days under natural seawater with evaporation rates ranging from 2.52 and 2.62 kg m^{-2} h^{-1} under one sun irradiation. The excellent stability due to the day-and night flow self-cleaning which help to recover the solar evaporator and result in long-term durability. Furthermore, they examined the anti-salt properties by placing 1 g of NaCl on the evaporator surface. They noticed salt was gradually disappeared, and no salt found after 7 hours of solar irradiation [120]. In another example, Yu's group developed a novel hybrid biomass-based hydrogel as a highly efficient solar steam generator [113]. It consists of biomass and konjac glucomannan incorporated with Fe-based metal-organic framework NPs (diameter of ~35 nm) with polyvinyl alcohol. The hydrogel and PVA presence's internal structure of micropores (~ 10 μm) leads to rapid water transport and a high evaporation rate. The as-designed hydrogel displayed high resistance against salt crystallization formation after placing some NaCl for 30 min. The self-cleaning function in hydrogel-based PTM occurs through an equilibrium established through water transport-induced salt ions absorption and diffusion that enabled salt ion discharge processes. Besides, biomass substrates have been suggested as an efficient substrate to mitigate salt accumulation. It happens through self-cleaning via the hydrophilic porous microchannels with a large diameter, allowing continuous water evaporation and dissolution of the formed salt to the bulk water [165, 186, 187]. For instance, He et al. investigated the anti-salt crystallization of bimodal porous balsa wood and found it to lessen salt crystallization and maintain a stable water evaporation rate [166]. As revealed in **Figure 2.9b**, the brine solution diffuses to the large vessel channel surroundings, contributing to salt

exchange with the brine bulk. This salt exchange process can effectively prevent salt crystallization and accumulation in the solar absorber region. To prove the phenomena of vessel channel contribution on the anti-crystallization, they conducted additional experiments by blocking the vessel channel with polydimethylsiloxane (PDMS). The results revealed salt accumulation on the surface when one channel was blocked, as shown in **Figure 2.9a,b**, confirming the vital role of the vessel channel in the anti-salt crystallization strategy. Recently, Li et al. reported a unique device to alleviate salt crystallization issues while enabling fast water transport [165]. As described in **Figure 2.9c,** the device consists of carbonized green algae as a solar absorber with added cotton thread as an anti-salt crystallizer. They observed that salt crystallization occurred only in the cotton thread regions rather than the carbonized algae region during the evaporation process. This can be explained by the stronger adhesion of salts on cotton threads than cohesion. Additionally, the cotton-aided device plays a significant role for anti-salt crystallization as no salt is observed on the solar absorber part for up to 15 days of operation. The studies mentioned above reveal that porous structural PTMs exhibit excellent salt crystallization through unique internal structures. The exploration of different anti-salt crystallization effects induced by various porous materials are required. **Table 2.3** presents the numerous methods proposed in the literature to enable anti-salt crystallization capability for the solar absorber system.

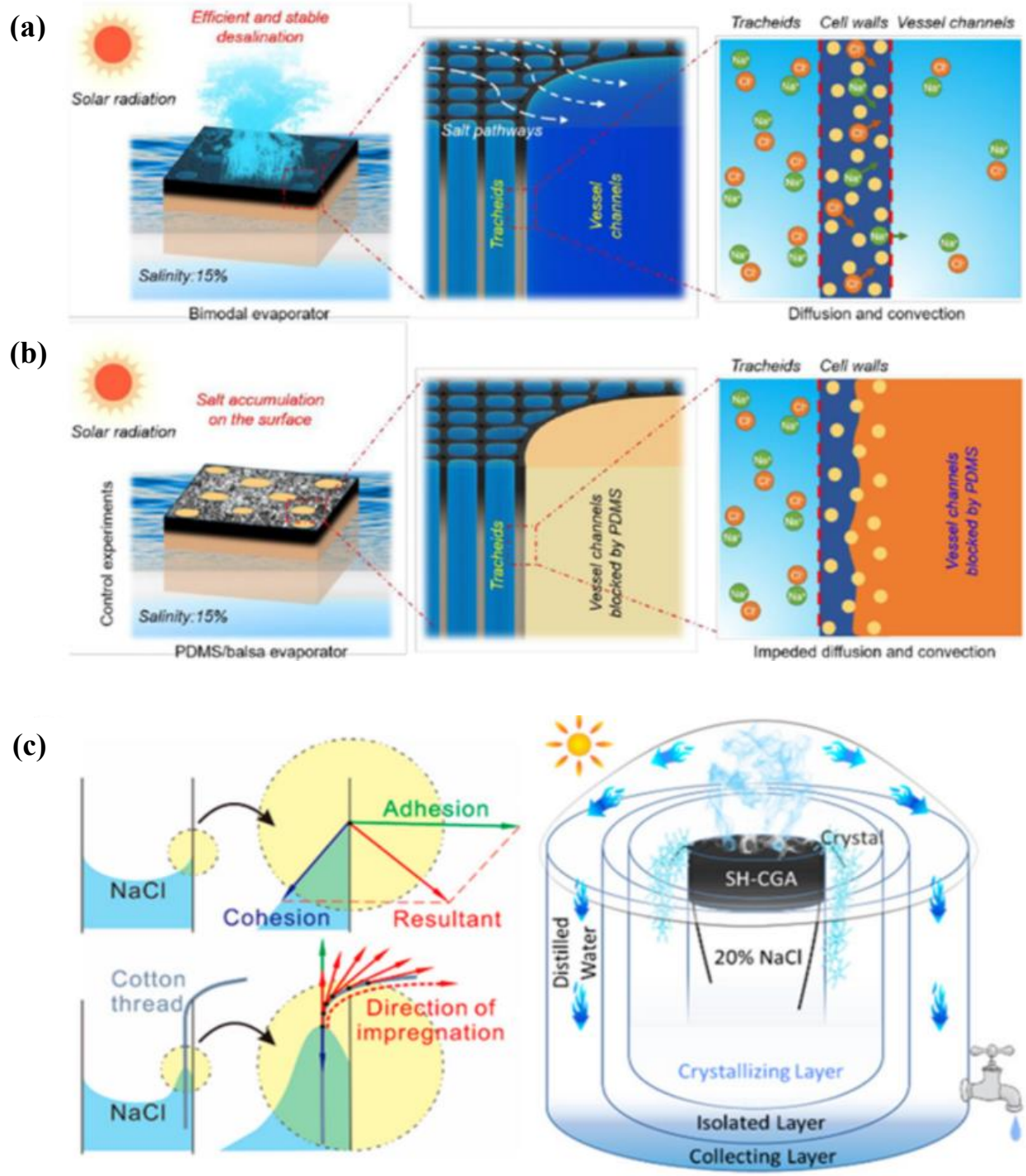

Figure 2.9 Anti-salt accumulation and crystallization. (a) Schematic illustration of the ionic composition of simulated seawater and distilled water from superhydrophilic carbonized green algae [165]. (b),(c) Schematic illustrating the mechanism of the bimodal porous balsa wood for anti-salt crystallization and fouling mechanism [166].

Table 2.3 Comparison of strategies used for anti-salt crystallization in solar steam generation.

Classifications	**Process**	**Drawbacks**	**Ref**
Hydrophobic salt blocking	Fabricating hydrophobic PTMs	Low-water evaporations	[182]
	Through spray coating or vacuum depositions with silane layer on hydrophilic PTM	Physical interactions of silane with PTM result to instability issues	[151, 188]
Porous PTMs	Superhydrophilicity and macroporous structure, a fast dissolution of salt which may crystallize within pores of materials and transfer back to saline solution could be achieved	Complicated fabrication process	[168, 175, 189]
	Introduction of ionic liquid moiety caused repulsion effect on cations in salt solution and has a salt resistant capability	More research investigations are required	[175, 189]
	Hydrophilic substrates composed of micro-aligned channels contributing in self-cleaning of accumulated salt	-	[27, 113, 165, 166]

2.3 Summary and research gaps in the literature

In recent years, there has been increasing interest in SSG for water purification. This has been mainly due to the advancements in PTMs, better understanding and approach for thermal management, and newer system and process configurations. This review has thoroughly discussed the contribution of PTMs for solar steam generation applications, including various synthesis approaches, techniques for improving their photothermal properties, thermal management strategies, and their utilization for desalination and wastewater treatment. Nevertheless, there are still some existing challenges that should be addressed. These include:

Nanostructured photothermal materials

- There is a need to develop innovative nano-microstructure semiconducting PTMs. Synthesizing a heterostructures semiconductor PTMs with the creation of microstructures or with structural aligned could enhance the light absorption, localize the heat and facilitate vapor escaping. This could result in excellent water evaporation performances.
- The complicated fabrications process and high cost of noble-metals-based PTMs might hinder its practical applications. Therefore, it is crucial to discover and explore cost-effective and scalable methods to fabricate noble metals-based PTMs with high chemical stability and robust mechanical strength.
- PDA dopamine nanostructures have been reported as excellent PTMs which can be grown on various types of substrates. Based on the literature study, the integration with porous metal foam and understanding the coating uniformity effects could be a good study for SSG applications.
- Furthermore, more research on the understanding mechanism of integrated nanocomposite within the hydrogel network and its effect on the structural morphology and water evaporations needs to be conducted.

Anti-salt solar photothermal materials

The salt crystallization on the solar evaporator's surface has been considered one of the significant challenges for bringing solar evaporator for applications in solar desalination. Therefore, research studies on anti-salt solar evaporators are still ongoing. In this doctoral study, we focus on the structural properties of the PTMs to tackle this issue.

- Combining the features of the adhesiveness of the PTMs on the substrate and designing substrate with functionality hydrophilic groups can mitigate the salt crystallizations and achieve self-cleaning properties.
- Literature studies demonstrated that preparing nanostructure PTMs with zero-liquid discharge and corrosion resistivity can be a good option for long-term stability. This ensures using a simple physical method for washing the PTMs without causing any damage to the PTMs. Thus, more research directions are required for designing washable PTMs based solar evaporators.
- Designing nanostructure PTMs with the richness of the porosity can result in salt crystal dissolving through diffusion and advection processes. This effective solution will ensure excellent reusability and long-term stability.

CHAPTER 3

MATERIALS AND METHODS

3.1 Overview

In this research study, various PTMs were synthesized for efficient solar-driven water evaporation for seawater desalination. The experimental studies are illustrated **in Figure 3.1.** Firstly, synthesis and fabrication of PTMs were conducted using techniques including solvothermal, magnetic sputtering, solid-state reactions, vacuum depositions, and spray coating. Secondly, the synthesized PTMs were characterized using X-ray diffraction (XRD), X-ray photoelectron spectroscopy (XPS), scanning electron microscopy (SEM), energy dispersive X-ray (EDX), and BET surface area to determine their formation and investigate their structural morphology and surface properties. Light absorption characteristics of synthesized PTMs were measured using a spectrophotometer (UV-vis-NIR). The materials characterization through morphological and structural properties are essential factors for understanding the capability of the materials for light absorption, water evaporation, salt ions rejections, and its reusability. Thirdly, after synthesizing PTMs and characterizing them, a simple solar evaporator was fabricated to study the solar light-thermal-vapor generations. An infrared (IR) camera was used to visualize the surface temperature of the PTMs and the side of the solar evaporator device. In contrast, a thermocouple device was used to measure the bulk water temperature. Lastly, the solar water evaporation performances were measured using the weight change of water over time. A custom-built device was fabricated for water condensation and collection. This was followed by the analysis of the salt ions before and after rejections using Inductive Coupled Plasma-Mass Spectrometer (ICP-MS) and Ion Chromatography (IC).

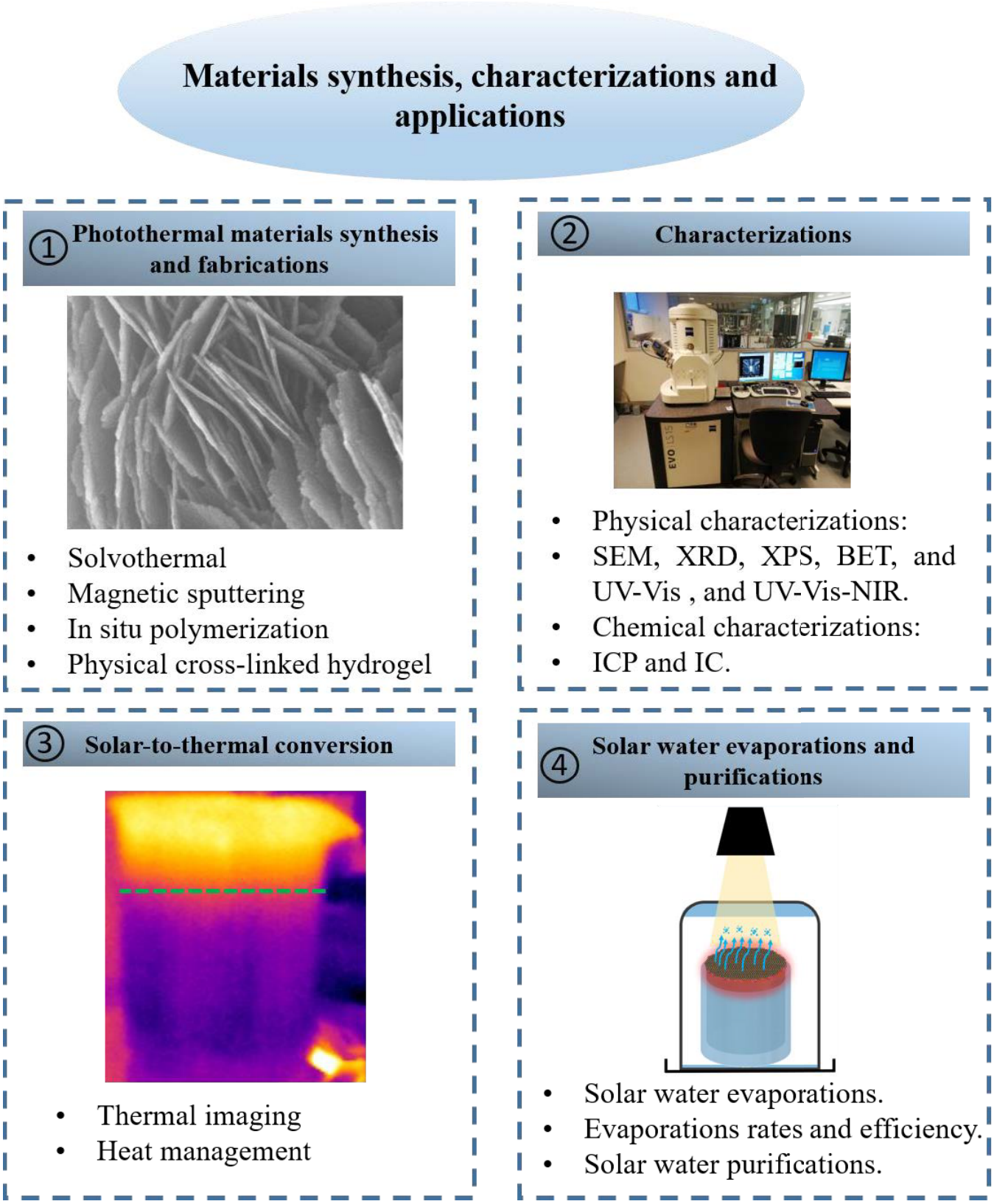

Figure 3.1 Schematic of experimental strategies used in this study.

3.2 Materials

Chemicals and substrates used in this study are described in **Table 3.1 and 3.2.**

Table 3.1 List of chemicals used in this study

Chemical	**Formula**	**Molecular weight (g/mol)**	**Purity (%)**	**Suppliers**
Copper nitrate trihydrate	$Cu(NO_3)_2.3H_2O$	241.6	98.5	Chem-Supply
Tin chloride dihydrate	$SnCl_2.2H_2O$	225.64	99	Univar Solution
Iron(II) sulfate hydrate	$FeSO_4.7H_2O$	278.02	97	Sigma Aldrich
Gold Target	Au	196.9	>99.9%	AJA DCXS-750, Scituate, MA, USA
Thiourea	CH_4N_2S	76.12	≥99.0	Sigma Aldrich
Ethanol	CH_3CH_2OH	46.07	95%	Chem-Supply
Ethylene Glycol	$C_2H_6O_2$	62.07	99.8	Sigma Aldrich
Acetic acid	CH_3COOH	60.05	≥99.7	Sigma Aldrich
Polyvinyl alcohol	$(C_2H_4O)_x$	89,000-98,000hydrolyzed	99+%	Sigma Aldrich
Tannic acid	$C_{76}H_{52}O_{46}$	1701.2	98%	Riedel-de Haen
Tris-HCl	$NH_2C(CH_2OH)_3.HCl$	57.60	>99%	Sigma Aldrich

1H,1H,1H,2H-perfluorodecyl-triethoxysilane (PFDTS)	$C_{16}H_{19}F_{17}O_3Si$	610.38	98%	Sigma Aldrich
Hydrochloric acid (32%)	HCl	36.458	99.9%	Chem-supply
Nitric acid (70%)	HNO_3	63.01	99.9%	Sigma Aldrich
Sulfuric acid	H_2SO_4	98.079	98.0%	Sigma Aldrich

Table 2. List of substrates used in this study

Substrate	**Formula**	**Properties**	**Suppliers**
Nickel foam	NF	**Thickness:** 1.6 mm **Surface area:** 346 g m^{-2}	MTI, USA
Polytetrafluoroethylene membrane	PTFE	**Pore size:** 1 µm	Ningbo
Mixed cellulose ester membrane	MCE	**Pore size:** 0.45 µm	Sterlitech

3.3 Synthesis and Fabrication methods

3.3.1 Solvothermal method

The solvothermal reactions were conducted in organic solvents such as ethanol and isopropanol. This method is a common and straightforward method to synthesize

nanostructures with different morphologies. Precursors and solvents are dispersed and transferred into a Teflon-lined vessel, then lined with autoclave metal and placed in an oven. The Teflon-lined vessels are protected with external stainless steel used as a protector to form a pressure to make the reaction occurred. A single-step solvothermal method was used to synthesize 3D microflowers copper sulfide/tin sulfide heterostructures composed of vertically aligned nanosheets. Detailed discussions are provided in Chapter 4.

Figure 3.2 Image of the Teflon-lined vessel reactor used in this study

3.3.2 Magnetron sputtering method

Gold thin films nanolayer were sputtered (deposited) on PTFE membrane surface using a magnetron sputtering system equipped with a 75 mm Au diameter target and power supply (AJA DCXS-750, Scituate, MA, USA). The target purity was 99.99%. The distance between the target and the substrate was 70 mm. The substrate used was a PTFE membrane (pore size: 0.45 μm). The deposition system was equipped with rotary and cryogenic pumps and a controlled gas introduction system. Argon gas was introduced into the chamber before the deposition process. A base pressure of $1x10^{-4}$ Pa was reached in the chamber before the sputtering started. The deposition pressure could be set independently of the gas flow by adjusting a throttle valve. The deposition pressure was adjusted to be 1.0 Pa. The DC power was set at 100 W. The sputtering method was used to deposit thin films gold nanolayer on PTFE membranes, as discussed in Chapter 5. The deposition time was 4 min, and the thickness of deposition nanolayer thin film was 50 nm [190]. The change in the mass loading of the PTFE membrane after the gold nanolayer deposition was 45 $\mu g/cm^2$.

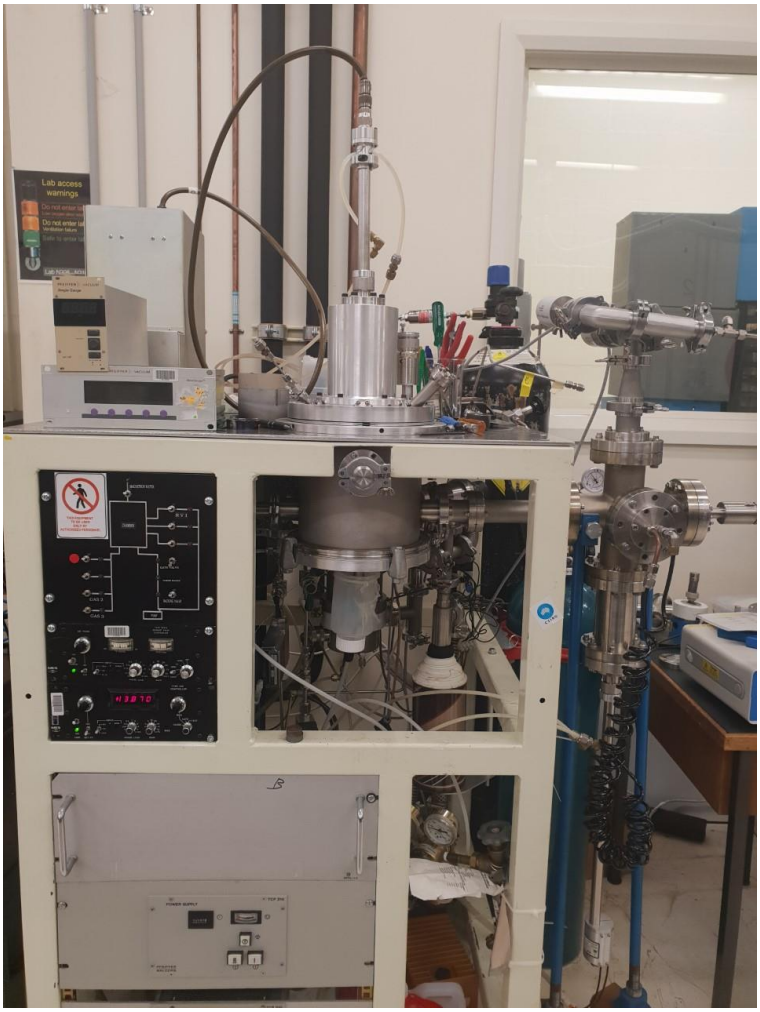

Figure 3.3 Image of the magnetron sputtering system used in this study.

3.3.3 Preparation of physically cross-linked hydrogel

Hydrogel is a highly porous three-dimensional hydrophilic material that absorbs and holds water within the polymer structures [191, 192]. The interaction between the polymer and water takes place through hydration or capillary force, causing the expansion of the polymer [192]. The formations of hydrogel through physical cross-linked is one of the standard methods used to form the hydrogel. It is formed through hydrogen bonding, hydrophilic or hydrophobic interactions, metal coordination formation, and π–π stacking [193]. In this study examines hydrogels formed through hydrogen bonding and metal coordination, composed of polyvinyl alcohol (PVA) cross-linked tannic acid (TA)-iron coordination complex. Details of the formation of the multifunctional hydrogel are discussed in Chapter 7.

3.3.4 In situ synthesis of polydopamine nanoparticles

Polydopamine can be coated on various substrates, making attractive materials for broad applications. PDA synthesis is straightforward by adding dopamine.HCl in aqueous alkaline solutions for a specific time. The reactions usually occur via *in situ* oxidative polymerization of dopamine under magnetic stirring utilizing the air from the atmosphere as an oxygen source. The oxidation of dopamine-quinone undergoes a nucleophilic intramolecular cyclization reaction leading eventually to the formation of 5,6-dihydroxyindol [194, 195]. In this study, we used *in situ* methods to synthesize polydopamine nanostructure on nickel foam (Chapter 6).

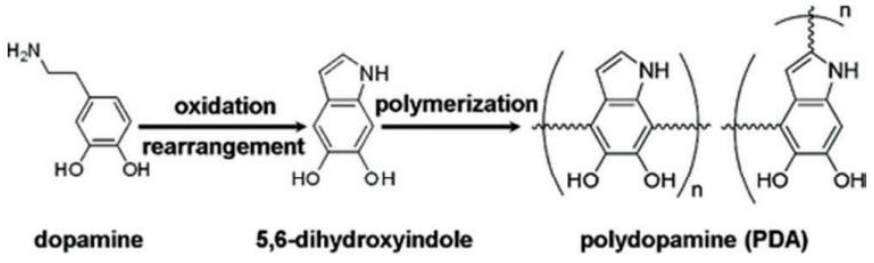

Figure 3.4 Michael oxidation reaction for the formations of PDA [194].

3.4 Materials Characterization

3.4.1 Scanning Electron Microscopy (SEM)

Scanning Electron Microscopy is the most applicable instrument for investigating structural morphology and chemical composition characterizations. The light source replaced with a high-energy electron beam enables a highly magnified image and provides information about the morphology and chemical composition of the material. The electron gun produces an electron beam with a high current and adjustable energy. The electrons produced to interact with the atoms that make up the sample produce signals containing information about the structure and chemical compositions [196]. In this study, field emission scanning electron microscopy FE-SEM (Zeiss Supra 55VP). The accelerated voltage was an essential factor for obtaining high magnification images. Before SEM analysis, the poor conductive PVA@TA-Fe hydrogel was sputtered-coated with Au-Pd with a thickness of 10 nm using Leica EM ACE600 Sputtering (Chapter 7).

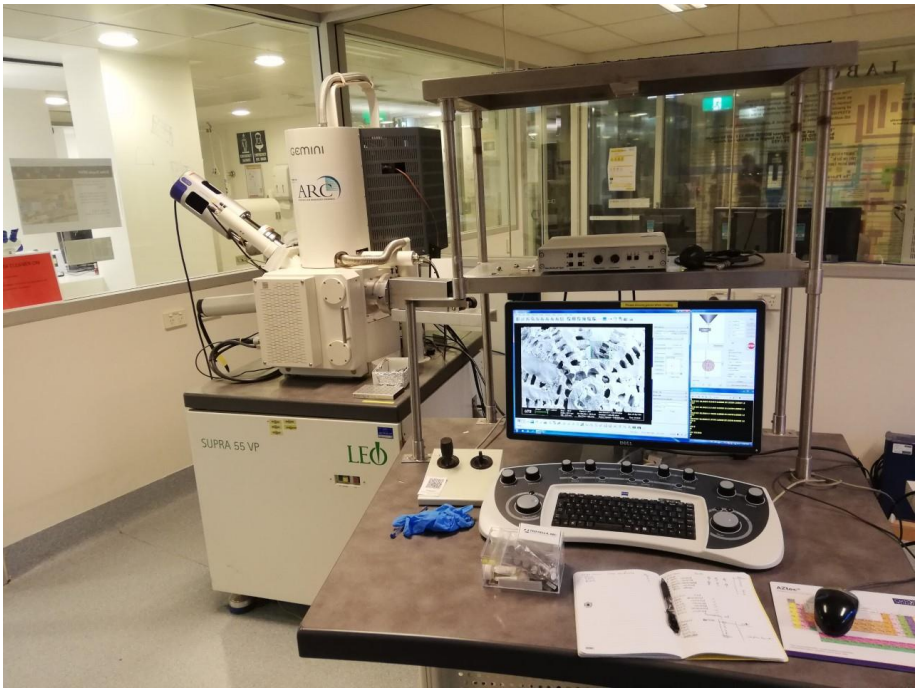

Figure 3.5 photo-Image of the Scan Electron Microscopy (SEM) used in this study.

3.4.2 X-ray diffraction (XRD)

X-ray diffraction (XRD) is an advanced instrument used to study the crystal structures and phases of the materials. X-ray diffractometers are composed of a sample holder, an X-ray tube, and an X-ray detector [197]. During the process, X-rays are produced by interactions of electrons (voltage) generated by heating a tungsten filament that act as a cathode ray tube. The further heat increases at the filaments result in accelerating high voltage towards a positive anode. The bombarding of the target material results in x-ray generations [198, 199]. The conversion of the diffraction peaks to d-spacings identify the possible matching of structures of materials because each material has a set of unique d-spacings [198]. Characteristically, this is realized by comparing d-spacings to the corresponding standard reference patterns. The diffractions only take place when Bragg's law meets the conditions of constructive interference, the Bragg's law:

$n\lambda = 2d\sin\theta$

where n is an integer, λ is the wavelength of the X-rays, d is the interplanar spacing generating the diffraction, and θ is the diffraction angle. In this research, we use a Bruker D8 Discovery X-ray diffractometer with Cu Kα radiation. The measurement was performed with a scan range (20-80), and a scan speed of 2 deg/min. XRD was used to determine the crystal phase and structures of CuS/Sn_2S_3, which are presented in Chapter 4.

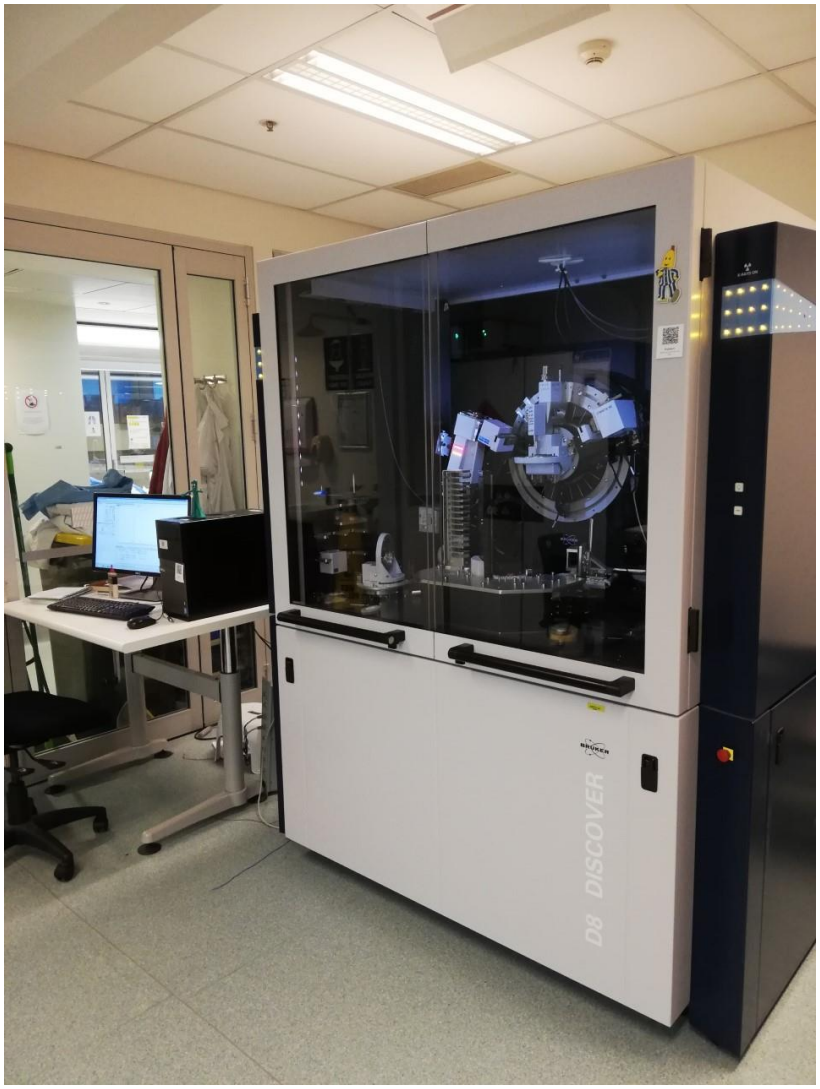

Figure 3.6 Image of the X-ray diffraction (XRD) used in this study

3.4.3 X-ray photoelectron spectroscopy (XPS)

X-ray photoelectron spectroscopy *(*XPS) is a powerful technique used to investigate the surface compositions of materials, including composition and electronic states of elements. The working phenomenon behind XPS is the electron emissions from surfaces after light irradiations. During the analysis, electrons within a sample surface absorb photons of (beam of x-rays). At the same time, the emission occurred only when the energy gained through the electron in a sample surpasses the lowest energy required for it to release from the surface [200, 201]. The kinetic energy analysis of the emitted electrons from the sample surface (1-10 nm) results in information on the electronic states of atoms in the sample surface area [202]. The XPS has been used in this doctoral study to investigate the surface compositions of CuS/Sn_2S_3 microflowers, (Chapter 4). In this study, Thermo Fisher scientific K-Alpha+ XPS, consists of a monochromatic Al X-Ray source (1.486 eV) was used. The collection of angle-dependent XPS with depth resolution of ~ 1-10 nm.

Figure 3.7 Image of the X-ray photoelectron spectroscopy (XPS) used in this study.

3.4.4 Thermal gravimetric analysis (TGA)

TGA analysis is a thermal analysis system where the mass changes of the samples are measured over time as a function of temperature at a given rate. The analysis can occur either under inert atmosphere N_2 or in an air O_2 atmosphere [203]. In this Ph.D. study, TGA instrument Simultaneous TG-DTA (SDT 2960) was used for the analysis. The analysis was conducted under N_2 gas, with heating rate 10ºC/min. Before the analysis, the baseline corrections are made by taring a TGA pan on an empty alumina crucible. After that, ~20 mg of the samples is placed on an alumina crucible subjected to a temperature started from room temperature and up to 1000 ºC. In this doctoral study, TGA analysis was used to measure the amount of the PDA NWs on the nickel foam surface, as described in Chapter 6. Also, the analysis was carried out to measure the amount of iron in the PVA@TA-Fe hydrogel, as described in Chapter 7.

Figure 3.8 Photo-Image of the thermal gravimetric analysis (TGA)

3.4.5 N_2 sorption/desorption measurement

The specific surface area analysis was carried out using Brunauer-Emmette Teller (BET) (Quantachrome Instrument). During the analysis, the sample was first weighed and outgassed by applying a vacuum at an elevated temperature. This step is vital to remove any gases and contaminants for obtaining precise results. The physical adsorption occurs by introducing nitrogen gas molecules into the solid adsorbent surface, forming relatively weak van der Waals forces. The amount of adsorbed gases are associated with the specific surface area of the sample. With the continuous gas applied, the adsorbent surface will form a thin layer covering the entire surface [204]. Brunauer-Emmette-Teller (BET) theory was used to calculate the surface area and pore size of CuS/Sn_2S_3 microflowers, (Chapter 4). The pressure range 0.03 to 0.5 P/P_o. The degassing was under vacuum conditions. (Autosorb iQ model, Quantachrome, USA) was used to determine N_2 sorption/desorption isotherms at 77 K.

Figure 3.9 Photo-Image of the BET device used in this study.

3.4.6 Water contact angle

The contact angles (CA) is a quantitative method used to investigate surface wettability. Wettability is how a liquid droplet spreads out on a solid substrate after depositions to form boundary surfaces with solid states. Theta Lite 100 (Attension) following the sessile drop method was used in this work. During the analysis, a water droplet of around 5-8 ml was released from a needle tip onto the substrate surface. The water droplet behavior was recorded using a motion camera with a rate of 12 frames per second. Then, contact angles value were measured through OneAttention software [205]. In this doctoral study, we used the contact angle to measure the surface wettability and investigate the water's speed penetrating within the surface. Water penetration speed is an essential criterion for escaping vapor during solar evaporation.

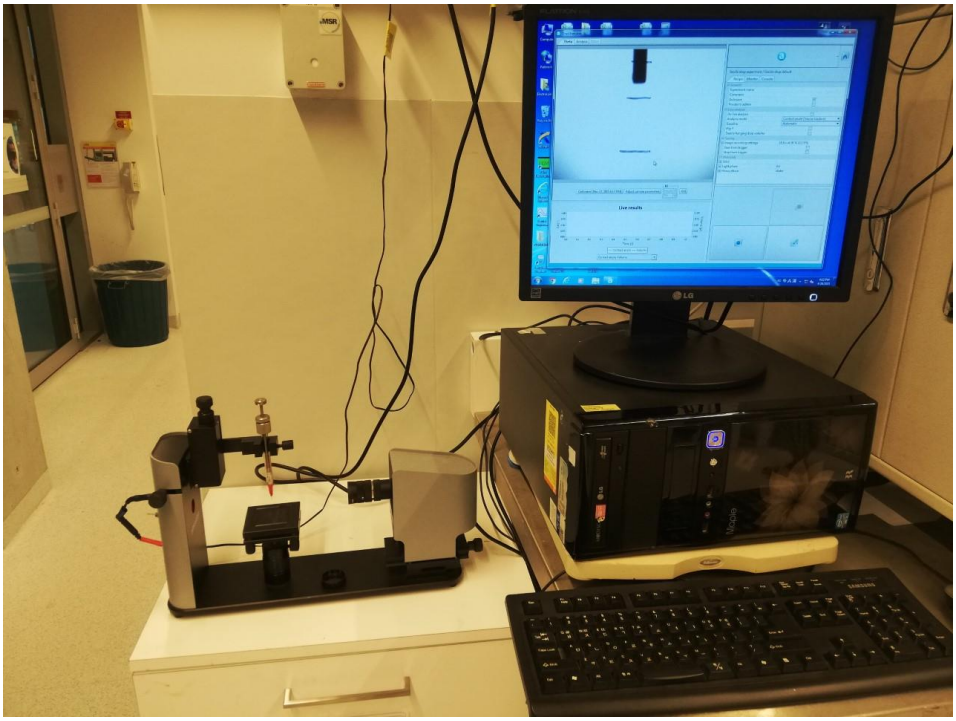

Figure 3.10 Photo-Image of the Contact angle device used in this study

3.4.7 Inductive Coupled Plasma-Mass Spectrometer (ICP-MS)

Inductively coupled plasma is one of the critical quantitative instruments used to investigate the trace-multi elements at the ppm-level. During the analysis, the samples are sprayed into the plasma source, which decomposes samples into constituent elements. The benefit of plasma is that the ionization source occurs in a chemically inert environment, thus preventing oxidation reaction. Then, the positively charged ions pass by a differentially pumped interface into a vacuum system housing a quadrupole mass spectrometer (MS). The MS is an effective detector to provide details about the qualitative and quantitative composition of complex mixtures. In this study, we used (Agilent 7900 ICP-MS) to quantify the positively charged ions of seawater concentrations (K^+, Na^+, $Mg^{2+,}$ and Ca^{2+}) before and after desalination.

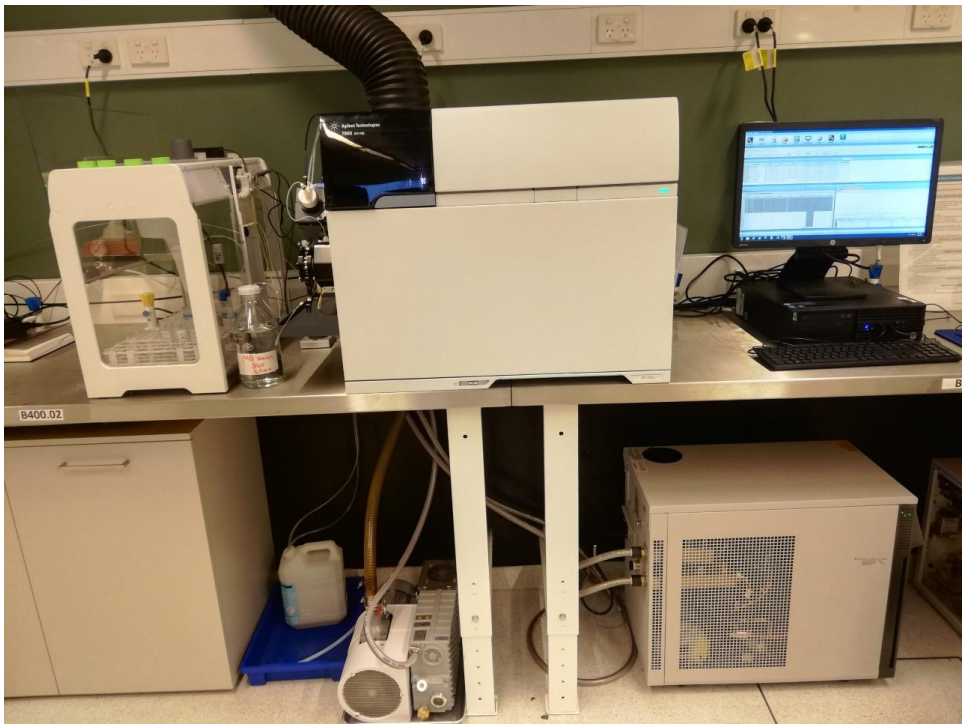

Figure 3.11 Photo-Image of Inductive Couple Plasma-Mass Spectrometer (ICP-MS) used in this study.

3.4.8 Ion Chromatography (IC)

Ion chromatography is one of the essential analytical tools for quantifying inorganic elements. The IC system used (Thermo Fisher, Australia), equipped with a Dionex AS-AP autosampler and a Dionex Ion Pac IC column (4 µm pore size, 4 mm diameter, and 250 mm length). During the analysis process, the solutions are injected (with injection volume was 10 µL) and passed through pressurized column ions. The solutions are separated through interaction with the resin, which acts as stationary phase, and the eluent acts mobile phase. In this study, we use used it to analyze the negatively charged ions (NO_3^-, Cl^-, and SO_4^{-2}) of the purified water at various pH conditions (see Chapter 5).

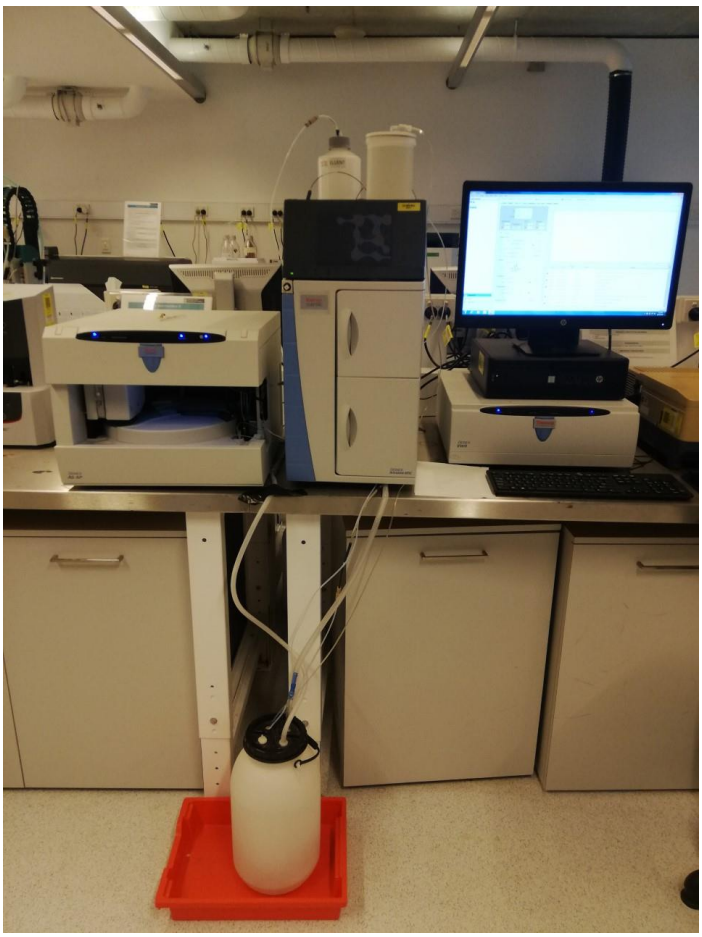

Figure 3.12 Photo-Image of Ion Chromatography (IC) used in this study.

3.4.9 Raman and FTIR spectroscopy

Raman and Kirshnan first established the theory of inelastic scattering of light in 1928, who observed it experimentally since the theory has been known as Raman. When a material interacts with light, the generated photon might be absorbed and scattered. Then, after the molecules are absorbed, it will promote from a low energy excited state to a higher energy excited state. The absorption spectroscopy can be measured from the loss of that energy from the radiation light. There is also a possibility that photons interact with the vibrational molecule and then scatter from it, with no energy required for the photon to match the energy levels difference. The wavelength change is usually small, and it will be observed by using monochromatic. And the interaction of the monochromatic light with the sample, a slight shift in the wavelength can be obtained, called: the Raman effect, where it can be used to get information on the sample [206].

In Fourier transforms Infrared (FTIR), infrared radiations pass through the vibrational molecules are absorbed, resulting in an absorbance spectrum [207]. In this doctoral study, FTIR spectroscopy was used to investigate the bonding water interactions with the hydrogel structures PVA@TA-Fe. Raman and FTIR were used to investigate the functional groups of the hydrogel (Chapter 7). The FTIR measurments were carried on using (ATR-FTIR, IRAffinity-1 FTIR equipped with MIRacle 10 single reflection ATR accessory, Shimadzu). The measurments were carried at room temperature and a wavenumber range of 500 to 4000 cm^{-1} with 64 scans at a resolution of 4 cm^{-1}. The Raman spectra were conducted using A Renishaw inVia Raman spectrometer system (Gloucestershire, UK) equipped with a Leica DMLB microscope (Wetzlar, Germany) and a laser power 633 nm renishaw helium neon laser source. The measurement was taken place at room temperature with wavenumber range of 3000 to 4000 cm^{-1} .

Figure 3.13 Photo-Image **of** Fourier transforms Infrared (FTIR)

3.5 Solar water evaporations experiments and applications

3.5.1 Solar light absorption

The light absorption characteristics of the fabricated PTMs was measured via a spectrophotometer equipped with an integrating sphere (950 PerkinElmer Lambda) at wavelengths (300-2500 nm; Ultraviolet-Visible-Near-Infrared). Firstly, Baseline corrections are made with an integrating sphere placed at the reflections part while leaving the transmittance part empty. This step is vital for accounting for any effect coming from the scattered light in the sample or instrument noise. During the process, the transmittance is obtained by allowing the incident light to pass through the sample compartment and hit a mirror reflected over the sample sitting at the entrance of the sphere. Then, the transmitted light is reflected off the diffuse surface of the integrating sphere and ultimately travel via a third aperture where the detector is installed. Meanwhile, the reflectance amounts are measured by

locating the sample at backporting of the integrating sphere. **Figure 3.14** describes the diffuse reflectance and transmittance measurements. The absorbance of the samples can be determined using the equation ($A = 100 - R - T$), A is absorption, R is reflectance, T is transmittance [208].

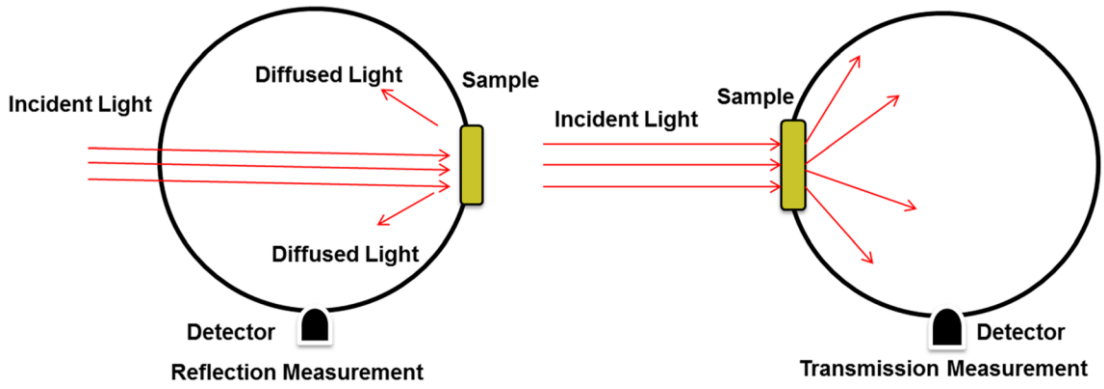

Figure 3.14 Total diffuse reflectance and transmittance measurement using the integrating sphere [209].

3.5.2 Fabrication of solar evaporation system

To evaluate the solar-to-heat-to-vapor generations of the prepared PTMs. First, a solar evaporator was fabricated mainly consisting of 3 main components; (1) PTMs which can absorb the sunlight over the Full solar spectrum regions efficiently (wavelength from 250 to 2,500 nm): ultraviolet (UV) region (UV), visible (vis) region, and the near-infrared (NIR) and efficiently convert it into heat. (2) thermal insulator is placed underneath of the PTMs and separate it from the bulk water act as heat localizer at the air/water interface and minimized the downward heat losses, and (3) capillary channel to supply an abundant amount of water rapidly from the bottom bulk water to the upper part PTMs.

In this study, a solar simulator (Beijing perfect light: PLS-SXE300) was used as a sunlight source operated under controlled solar irradiation. The solar light intensity was measured using

a calibrated optical power meter (PM100D, THORLABS, USA). An aperture with a hole size matching the size of the solar evaporator was applied to prevent the extra light from exposure to the outer surface. The light-to-heat conversion of the evaporation surfaces was monitored by visualizing the heat at the solar absorber surface after irradiation under controlled solar intensity infrared camera using IR camera (FLIR, E6). The surface temperature with PTMs and without (bulk water and control samples) were also examined and compared. In addition, the temperature variations of the bulk water during the solar evaporation process was monitored using a thermocouple (RS PRO: RS172TK) (**Figure 3.15)**

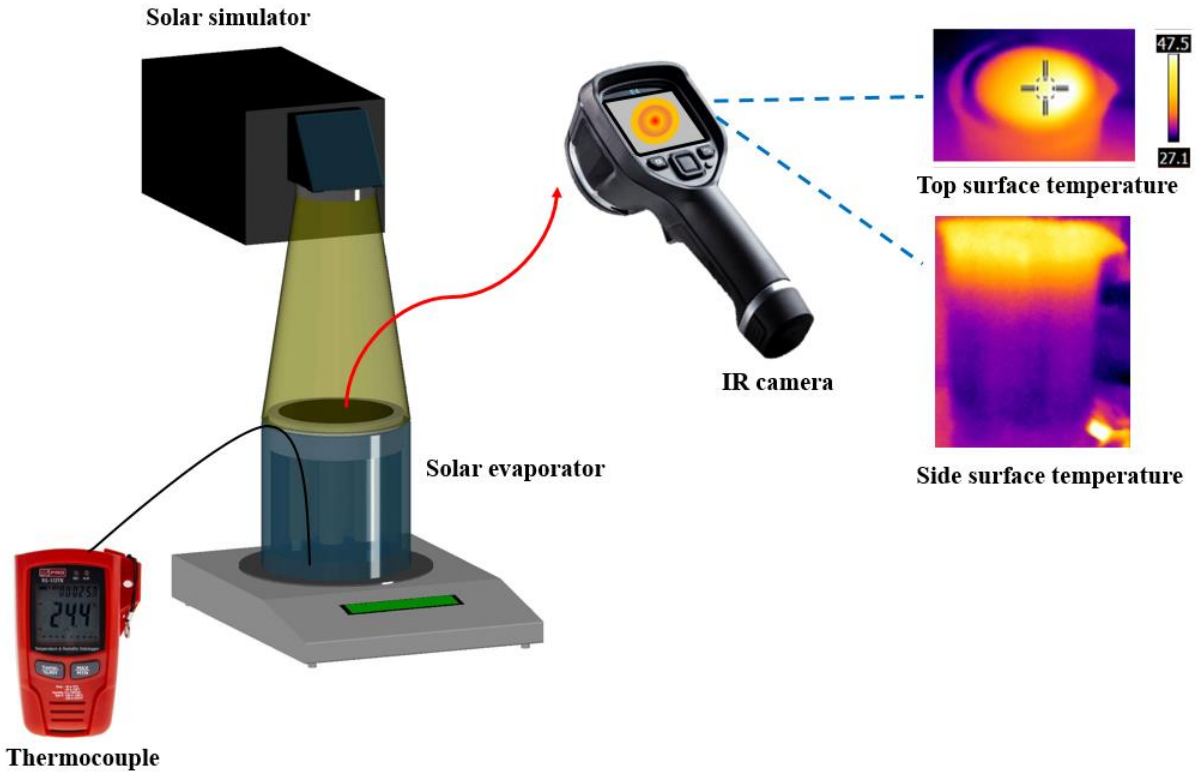

Figure 3.15 Schematic diagram of measuring of the surface temperature of solar evaporator system and bulk water temperature

3.5.3 Solar heat-to vapor generations

To evaluate the water evaporation performances. A system was designed which consists of;

(1) Interfacial solar evaporator; PTMs to absorb sunlight and generate heat where the vapor escapee through the nanostructure design and the porous substrate. Thermal insulator for heat localizations and wick materials acting as water supply channels.

(2) A solar simulator; is a sunlight source where light is irradiated under controlled irradiation one sun (1 kWm^{-2}), equivalent to the natural sunlight hitting the earth on a cloudless day.

(3) High precision electronic balance (Ohaus-IC-PX84/E) with accuracy 0.1 mg, connected to the laptop, was used to measure the weight change of the feedwater. The experiment duration for solar water evaporation is 60 minutes for each sample test. The whole solar evaporator was placed on the electronic balance. After irradiating the sunlight, the measurement was recorded at one interval every 4 minutes. The environmental temperature and humidity during tests were measured.

(4) The errors were calculated during solar water evaporation by repeating the experiments three times for each water evaporation test. The average results were reported, and the standard deviations were calculated and presented in the graphs.

(5) Aperture with a hole identical to the solar evaporator was used to concentrate the light on the PTMs part and prevent heating the surrounding region **Figure 3.16**.

The water evaporation rate is calculated as (Eq. 3.1) [53, 210, 211]:

$$v = \frac{m}{A\,t} \tag{3.1}$$

Where m is the weight change during water evaporation (kg), A is the area of the solar absorber (m^2), and t represents the irradiation time (h).

Water evaporation efficiency is then obtained using the following (Eq. 3.2) [156, 210-212]:

$$\eta = \frac{\Delta m\ H_e}{C_{opt}\ q_{in}} \tag{3.2}$$

where $\Delta m = (m_i - m_o)$, m_i is the mass loss of water under sunlight and m_o is mass loss under dark, H_e is the total vaporization enthalpy of the water-steam phase change (2260 kJ kg^{-1}), C_{opt} represents the optical concentration, and q_{in} is solar irradiation energy density from the solar simulator (kW m^{-2}).

In this doctoral study, various solar water evaporators were designed, and the details are provided in **Chapter 4**, **Chapter 5**, **Chapter 6** and **Chapter 7**.

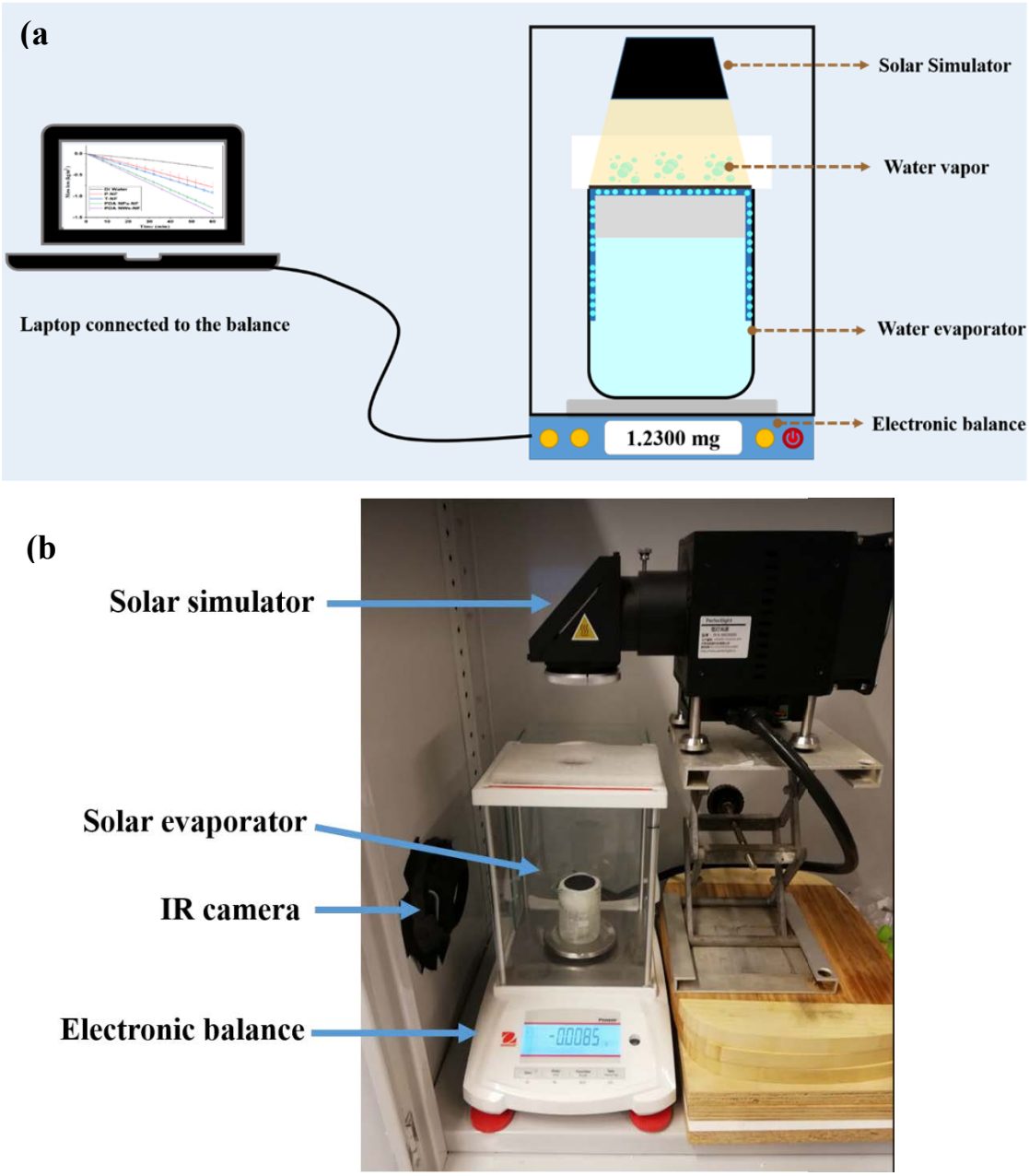

Figure 3.16 (a) Schematic illustration of the experimental set-up for solar steam generations. **(b)** Photo-image of the experimental set-up.

3.5.3.1 The stability and reusability of PTMs

Designing PTMs with good recyclability and stable water evaporation performance is an essential factor in developing commercial and practical SSG devices. The harsh feedwater environment accelerates the potential degradation of BPTMs. Therefore, BPTMs with good stability, recyclability, and durability are essential for the long-term, large-scale implementation of these devices in real-world applications. Numerous studies investigated the stability of BPTMs in various feedwater environments, including acidic, neutral, and alkaline conditions. The recyclability and durability of the PTMs were also evaluated under harsh environmental conditions, under acidic (0.1 M H_2SO_4), basic (0.1 M KOH), and oxidizing conditions (0.1 M HNO_3), respectively [213]. We also used similar protocols as mentioned in sections **3.4.3** and **3.4.4**.

3.5.3.2 Solar seawater desalination

After performing the water evaporation experiments, the optimized PTMs with the highest water evaporation performance were selected for solar water desalination. The test was performed using actual seawater and high brine salinity. After sunlight irradiations, the evaporated water was condensed and collected using a simple custom-built device (**Figure 3.17**). The device consists of a solar evaporator covered with a larger beaker (250 mL) at the top and petri-dish placed at the bottom. It consists of a solar evaporator, a glass collector basin, and a glass cover that serves as the condenser. Solar light from the solar simulator is illuminated at the top part, passing through the transparent glass cover, and heat up the black photothermal material that is floated on the source water inside a beaker to induce evaporation. Water vapor escapes from the absorber and reaches the inside surface of the glass cover, and is condensed into liquid water. The liquid water then slides down towards the collecting basin at the bottom. Samples were taken from the feed water and the collected pure water and the representative ions are then measured using ICP-MS. This design facilitates water collection through the condensation process. The condensed water was collected, and the salt ions (Na^+, K^+, Ca^+, and Mg^+) concentrations (ppm) were analyzed before and after using ICP-MS. The concentrations of the collected water of the designed solar evaporator should meet the standard level of drinking water required by the World Health Organization (WHO) and the U.S. Environmental Protection Agency (EPA), > Na^+ (200 mg/L), Ca^{2+} (75 mg/L), K^+ (12 mg/L), and Mg^{2+}(50 mg/L) [214, 215].

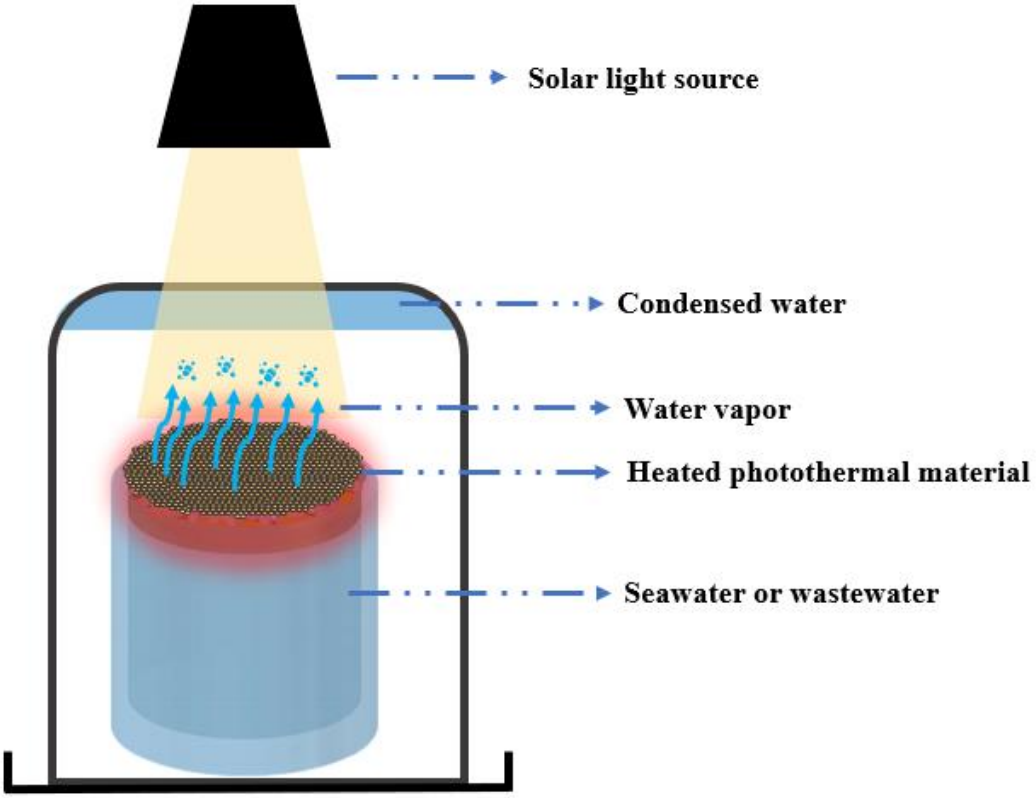

Figure 3.17 custom-built device for water condensation and collection

CHAPTER 4

SYNTHESIS OF 3D COPPER SULFIDE/TIN SULFIDE MICROSTRUCTURE FOR EFFICIENT SOLAR EVAPORATION AND SEAWATER DESALINATON

This chapter is based on our publication: **Idris Ibrahim**, Dong Han Seo, Alexander Angeloski, Andrew McDonagh, Ho Kyong Shon, Leonard Tijing*. 3D nanostructured CuS/Sn_2S_3 microflowers for highly efficient solar steam generation and water purification. Solar Energy Materials and Solar Cells 232 (2021): 111377

4.1 Introduction

Nano/microstructure semiconductor materials display great potential as PTMs. This is due to the relatively low cost, ease of fabrication, effective photothermal conversion efficiency, and the range of possible morphologies and structures (e.g., crystal structure, dimension, and porosity) [188]. To exploit such advantages of nanostructured semiconductor-based PTMs, manipulation of the PTMs' morphologies or intrinsic properties should be examined to improve the SSG device performances. For example, Lu et al. demonstrated the synthesis of 1D-O doped MoS_{2-x} ultrathin nanosheets that generated nano-confined channels for effective water evaporation. Such confined nanochannels effectively reduced the vaporization enthalpy and improved the water evaporation performance [216]. A remarkable water evaporation rate of 2.50 kg m^{-2} h^{-1} under one-sun irradiation was reported, corresponding to solar-to-vapor efficiency of 89.6%.

Copper sulfide (CuS) has attracted researchers attention as a promising PTM for high-efficient solar evaporator due to its low-cost, strong light absorption in the near-infrared (NIR) arising from a tunable, localized surface plasmon resonance (LSPR), and excellent photothermal conversion efficiency [99, 217]. As mentioned above, various forms of copper sulfide nano/microstructures have been reported, such as nanoparticles [218], nanorods [157], nanosheets [219]), shapes [56], and phases [157]. After designing effective PTMs, solar seawater desalination and wastewater treatment applications have been considered for practical applications. During seawater desalination, salt accumulation on the surface of the evaporator is a common issue. Several strategies have been reported to resolve this problem or at least to minimize the salt formation, such as the Janus absorber [171, 220], hydrophobic absorber [221], polymer-based salt-resistant [175, 222], and hydrogel structure [46, 223].

In this work, we report a single-step solvothermal synthesis of 3D microflowers CuS/Sn_2S_3 heterostructure consisting of vertically aligned ultrathin nanosheet assemblies (3D CSS-NS

MF). The 3D CSS-NS MF PTMs were deposited on a hydrophilic mixed cellulose ester (MCE) membrane and coated with hydrophobic silane layer at the top to reduce the salt formation. Our prepared 3D CSS-NS MF/CA exhibited high photothermal conversion which result in excellent performances in solar seawater desalination with good durability over 10 continuous cycles under natural seawater. We believe that this work possesses a promising application for solar thermal conversions for various applications.

4.2 Experimental Section

4.2.1 Materials

Copper(II) nitrate trihydrate ($Cu(NO_3)_2 \cdot 3H_2O$) and ethanol were purchased from Chem-Supply. Tin(II) chloride dihydrate ($SnCl_2.2H_2O$) was purchased from Univar Solution. Thiourea, 2-propanol, acetic acid, ethylene glycol, methylene blue (MB), 1H,1H,1H,2H-perfluorodecyl-triethoxysilane (PFDTS), and Rhodamine B (RhB) were purchased from Sigma-Aldrich. Mixed cellulose ester (MCE) membrane membranes (pore size 0.45 μm, diameter 47 mm) were purchased from Sterlitech. All materials were used without any further purification.

4.2.2 Synthesis of 3D microflowers CuS/Sn_2S_3 heterostructure

The 3D CSS-NS MF was prepared using a facial, scalable and low-temperature solvothermal method. A growth solution was prepared by dissolving copper nitrate trihydrate (0.483g, 2 mmol), tin (II) chloride dihydrate (0.225 g, 1 mmol), thiourea (0.228 g, 3 mmol) into a beaker containing ethylene glycol (30 ml) and ethanol (10 mL) in a 50 mL Teflon vessel. The solution was stirred vigorously at room temperature for 1 hour. The vessel was then transferred to an autoclave, sealed, and heated at 180 ^oC for 10 h. The product was then washed several times with deionized water and once with ethanol by centrifugation. The collected product was dried in a vacuum oven at 50 ^oC for 4 hrs.

4.2.3 Fabrication of photothermal membranes

Photothermal membranes containing the 3D CSS-NS MF/MCE PTM were prepared by dispersing 3D CSS-NS MF (20, 30, 40 and 60 mg) in a mixture of water (38 mL) and ethanol (2 mL) and sonicated for a period of 10 mins to obtain a stable suspension. The suspension was deposited onto a MCE membrane (diameter of 47 mm) by vacuum filtration. The diameter of the area loaded with 3D CSS-NS MF is 35 mm (see **Figure 4.1).** The membrane was then dried at 60 ^{o}C for 4 hours. A hydrophobic layer was deposited on the 3D CSS-NS MF/MCE membrane using a spray coating process. In brief, a silane solution consisting of 2.0% 1H,1H,1H,2H-perfluorodecyltriethoxysilane (PFDTES), 0.5% acetic acid, and 97.5% isopropanol was prepared according to literature [151, 224]. The solution was transferred into an airbrush spray coater and sprayed on the top surface of the 3D CSS-NS MF/MCE membrane for 10 seconds. After the coating process, the membrane was left to dry overnight at ambient temperature.

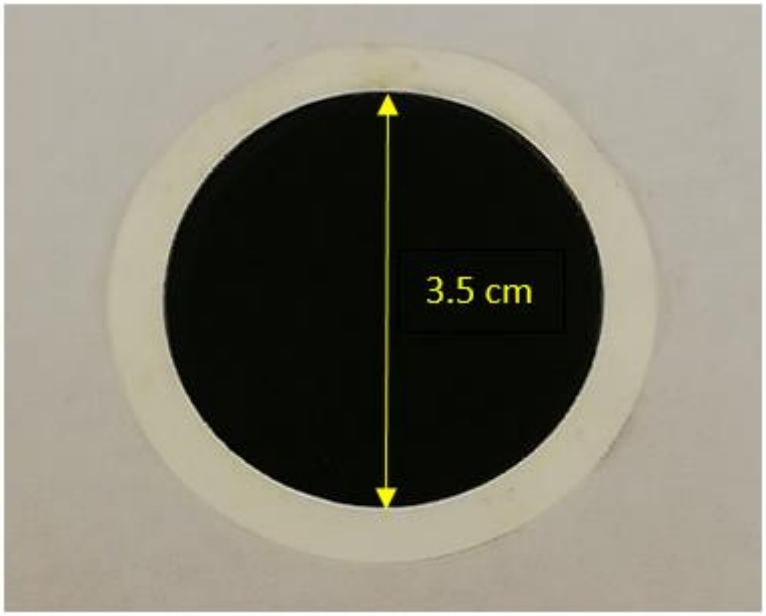

Figure 4.1 3D CSS-NS MF on mixed cellulose ester (MCE) membrane.

4.2.4 Characterization

The morphologies of the as-synthesized materials were analyzed using scanning electron microscopy (SEM) (Zeiss Supra 55VP, Germany) at an acceleration voltage of 5.0 kV. EDS spectra were acquired using a Zeiss EVO SEM equipped with an EDS detector and an acceleration voltage of 10.0 kV. Powder X-ray diffraction (pXRD) patterns were collected using a Bruker D8 Discover powder X-ray diffractometer. Cu Kα radiation (40 KV and 40 mA) was used, and the scans were acquired between 20°- 80° 2θ with a step size of 0.02°. Surface properties were measured using an X-ray photoelectron spectroscopy (XPS) (Thermo Fisher Scientific K-Alpha+). The specific surface area analysis was carried out using Brunauer-Emmette Teller (BET) (Quantachrome Instrument). Water contact angles were determined using Attension Thured eta Lite 100 (Biolin Scientific). Infrared (IR) images and surface temperatures were recorded on a Fluke E6 Infrared Camera (Fluke, USA). Optical transmittance and reflectance between 300 and 2500 nm were measured using a PerkinElmer Lambda 950 with an integrating sphere (UV-Vis-NIR). The ion concentrations of collected evaporated waters were measured using an inductively coupled plasma mass spectrometer (Agilent 7900 ICP-MS). Dye concentrations of Methylene blue (MB) and Rhodamine B (RhB) in the polluted and purified water were analyzed using Ultraviolet-Visible spectroscopy (Agilent UV Cary 60).

4.2.5 Solar steam generation experiments

A solar evaporator was prepared consisting of CuS/Sn_2S_3 microflowers loaded on a MCE membrane and air-laid paper wrapped on polystyrene foam placed in a 100 mL beaker filled with 70 mL de-ionized water. The evaporator was irradiated using a solar simulator (PLS-SXE300, Beijing Perfect Light, China) equipped with a xenon lamp (300 W) and AM 1.5G filter. The output solar irradiation was controlled with a variable voltage source, and the light intensity was measured using a solar power meter (PM100D, THORLABS, USA). The SSG

experiments were conducted at a temperature of 21-23 ºC and humidity of 48-55%. An analytical balance (Pioneer, IC-PX84/E), connected with a laptop, was used to measure the weight loss of evaporated water as a function of time. The water evaporation measurements were repeated three times to determine an average mass loss. The heat distribution on the system was visualized using an IR camera, which imaged the top and side surfaces of the illuminated device. The experiments were conducted at different solar irradiation of 1, 1.5, and 2 suns. A schematic and photograph of the experimental design set-up is shown in **Figure. 4.2**.

4.2.6 Solar seawater desalination experiments

For solar desalination experiments, seawater was collected from Rose Bay Beach, Sydney, Australia. The seawater was filtered using a coarse filter, followed by a 5-micron bag filter, then treated with UV light before use. The primary ion concentrations (Na^+, Mg^{2+}, K^+, and Ca^{2+}) of saline and desalinated seawater were measured.

4.3 Results and discussions

4.3.1 Morphology and structure

Advanced nano/microstructure semiconductor PTMs are highly desirable for SSG applications due to their high photothermal conversion efficiencies, which are greater than those with bulk microstructures. To achieve superior solar thermal conversion and high water evaporation rate, it is necessary to regulate the size, morphologies, and structures of semiconductor PTMs [38]. In this work, we synthesized 3D CSS-NS MF with unique morphology using a single-step solvothermal method. The presence of crystalline phases within the 3D CSS-NS MF was assessed using XRD. The diffraction patterns showed the crystalline phases to be covellite (CuS) and orthorhombic (Sn_2S_3), which were indexed using JCPDS no. 06-0464 and JCPDS no. 14-0619, respectively (**Figure 4.2a)** [225, 226]. The presence of these phases demonstrates the ability to straightforwardly form complex mixed metal sulfide nanomaterials using

solvothermal decomposition of Cu(II) and Sn(III) solutions. Furthermore, the amount of the added precursor copper ions, which is twice the amount of the tin ions, plays a significant role in forming rich covellite phase CuS. The energy-dispersive spectroscopy (EDS) analysis indicates the co-existence of 3D CSS-NS MF consisting of Cu, Sn, and S (**Figure 4.2b**). Elemental mapping analysis revealed the co-existence and a homogeneous distribution of Cu, Sn, and S in the microflowers. (**Figure 4.2c**).

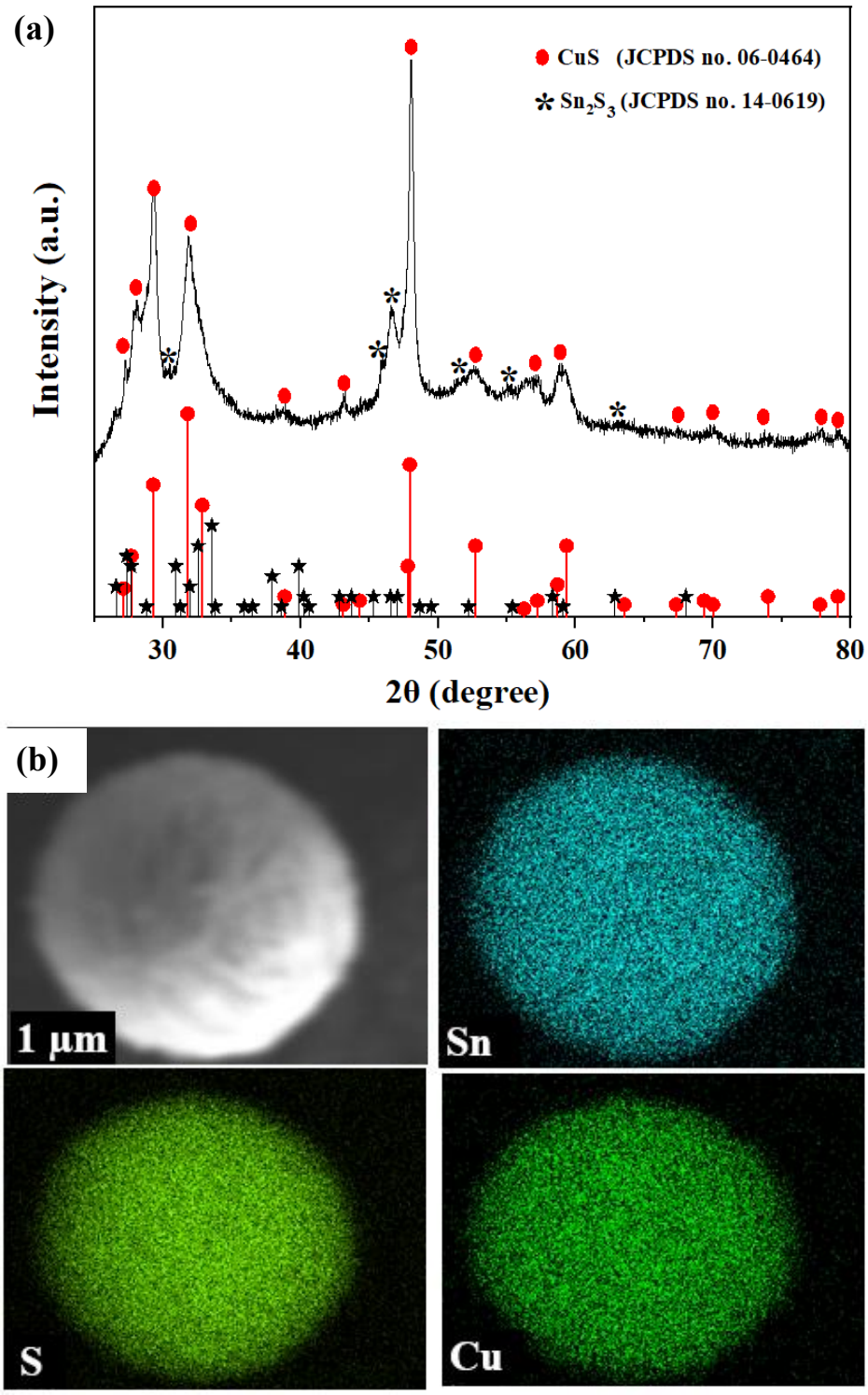
(a)
CuS (JCPDS no. 06-0464)
Sn2S3 (JCPDS no. 14-0619)
Intensity (a.u.)
30
40
50
60
70
80
2θ (degree)
(b)
1 μm
Sn
S
Cu

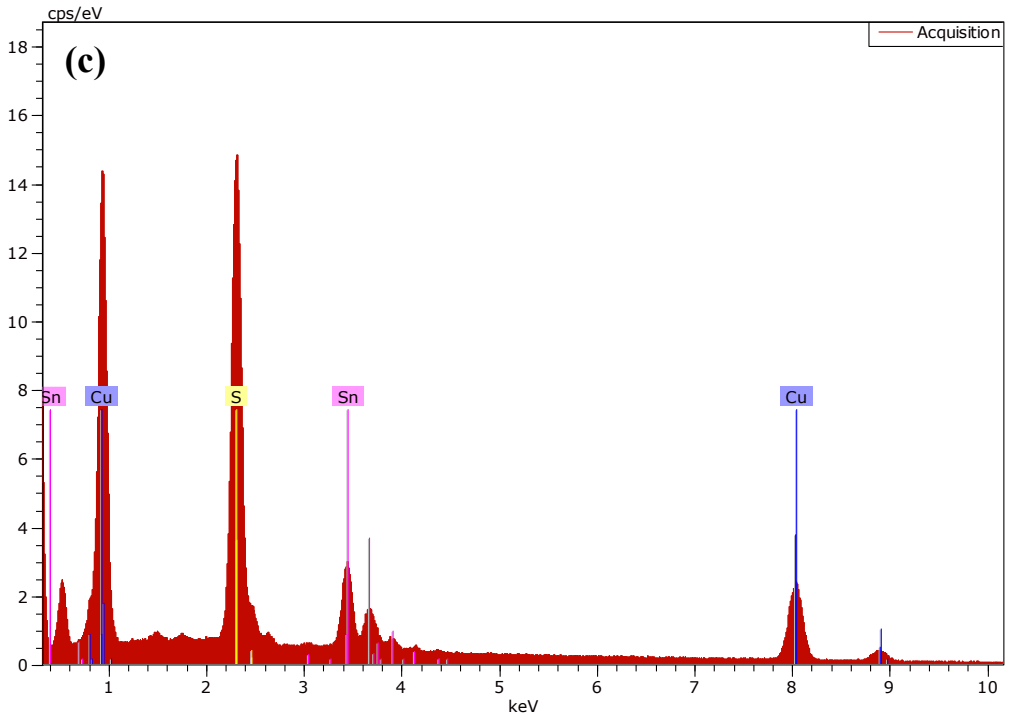

Spectrum: Acquisition

El	AN	Series	unn. C [wt.%]	norm. C [wt.%]	Atom. C [at.%]	Error (1 Sigma) [wt.%]
S	16	K-series	16.67	25.35	42.84	0.61
Cu	29	K-series	38.28	58.21	49.65	1.25
Sn	50	L-series	10.81	16.44	7.51	0.35
Total:			65.76	100.00	100.00	

Figure 4.2 (a) Powder XRD pattern corresponding to covellite CuS and orthorhombic Sn_2S_3. The diffraction peaks at 2θ = 27.12°, 27.68°, 29.27°, 31.78°, 38.84°, 43.10°, 47.94°, 52.72°, 57.21°, 59.35° and 67.30°, 70.13°, 73.64, 77.78°, and 79.12° correspond to the covellite CuS planes (100), (101), (102), (103), (105), (106), (110), (108), (202), (116), (118), (207), (208), (212) , and (213). Peaks at 46.52°, 30.74°, 46.21°, 46.5°, 51.9°, 55.49°, and 62.92° are assigned to the (111), (310), (430), (170), (080), (530), and (600) plane of orthorhombic Sn_2S_3. **(b)** Elemental mapping result showing the distribution of Cu, Sn, and S. **(c)** EDS analysis and elemental composition of 3D CSS-NS MF.

Furthermore, XPS was used to investigate and confirm the chemical composition of 3D CSS-NS MF. The full survey XPS spectra reveal the existence of Cu, Sn, and S elements, which is consistent with EDS analysis (**Figure 4.3a**). **Figure 4.3b-d** displays the resolution spectra of Cu 2p**,** , S 2P, and Sn 3d. The peaks at 162.0 eV, and163.0 eV (**Figure 4.3b**) are ascribed to the S^{-2} $2p_{3/2}$ and S^{-2} $2p_{1/2}$ in CuS and Sn_2S_3, respectively [227, 228]. While the peaks at 487.3 eV and 495.7 eV correspond to the Sn^{-2} $3d_{5/2}$ and Sn^{-2} $3d_{3/2}$, respectively **(Figure 4.3c)** [227]. In **Figure 4.3d,** two major peaks with binding energies at 932.1 eV and 952.18 are observed, corresponding to the Cu^{2+} $2p_{3/2}$ and Cu^{2+} $2p_{1/2,}$ respectively (**Figure 4.3c)** [228]. Thus, XPS spectra analysis confirms the formation of CuS/Sn_2S_3 heterostructure in the synthesized composite, as evident from chemical structural analysis.

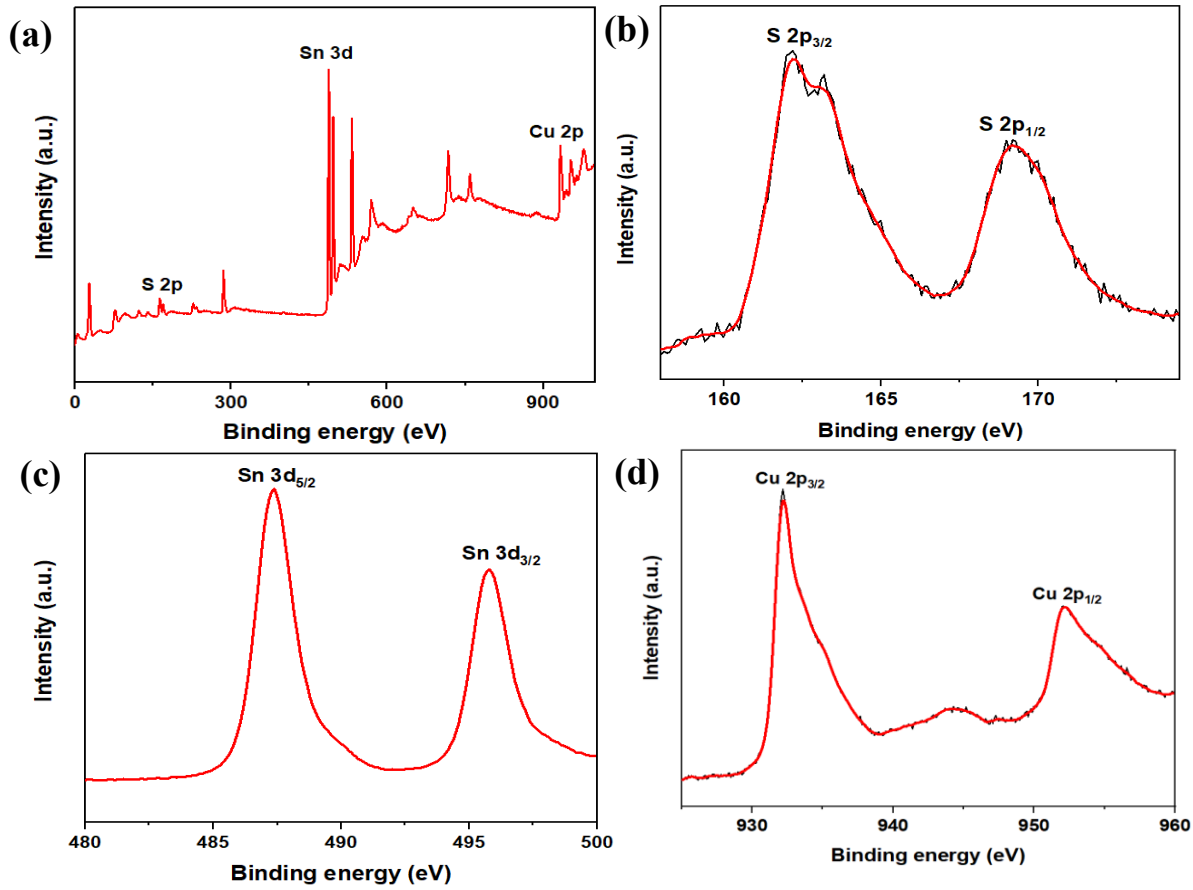

Figure 4.3 XPS spectra of the as-prepared 3D CSS-NS MF (a), XPS survey (b) S 2p, (c) Sn 3d and (d) Cu 2p.

The surface morphology and structure of the as-synthesized 3D CSS-NS MF was examined using SEM. The SEM images reveal uniform hierarchical microflower-like structures with sizes of ~1.5-5 μm **(Figure 4.4a).** Individual microflowers are composed of nanosheets with thicknesses of ~25 nm and contain cavities (holes) (**Figure 4.4b**). Furthermore, the non-aqueous environment provided by ethylene glycol and ethanol plays a critical role in this reaction where it provides an environment for the crystal growth, hence preventing any agglomeration and resulting in uniform, crystalline nanostructures [229]. Nitrogen adsorption-desorption isotherm analysis revealed the 3D CSS-NS MFs possess a relatively high surface area of 53 m^2 g^{-1} (**Figure 4.4c**). From the Barrett-Joyner-Halenda (BJH) method, the pore size is 0.069 cm^3/g. Furthermore, the curves of 3D CSS-NS MFs display a type IV isotherm confirming that the adsorbent possesses a mesoporous nature. The structural morphology clearly shows the as-synthesized 3D CSS-NS MF exhibited unique structural features such as densely packed vertically-aligned ultrathin nanosheets and the presence of numerous channels formed by these nanosheets. These properties are favourable for efficient solar absorption, heat localization and to facilitate vapor escaping for high-performing solar water evaporation materials.

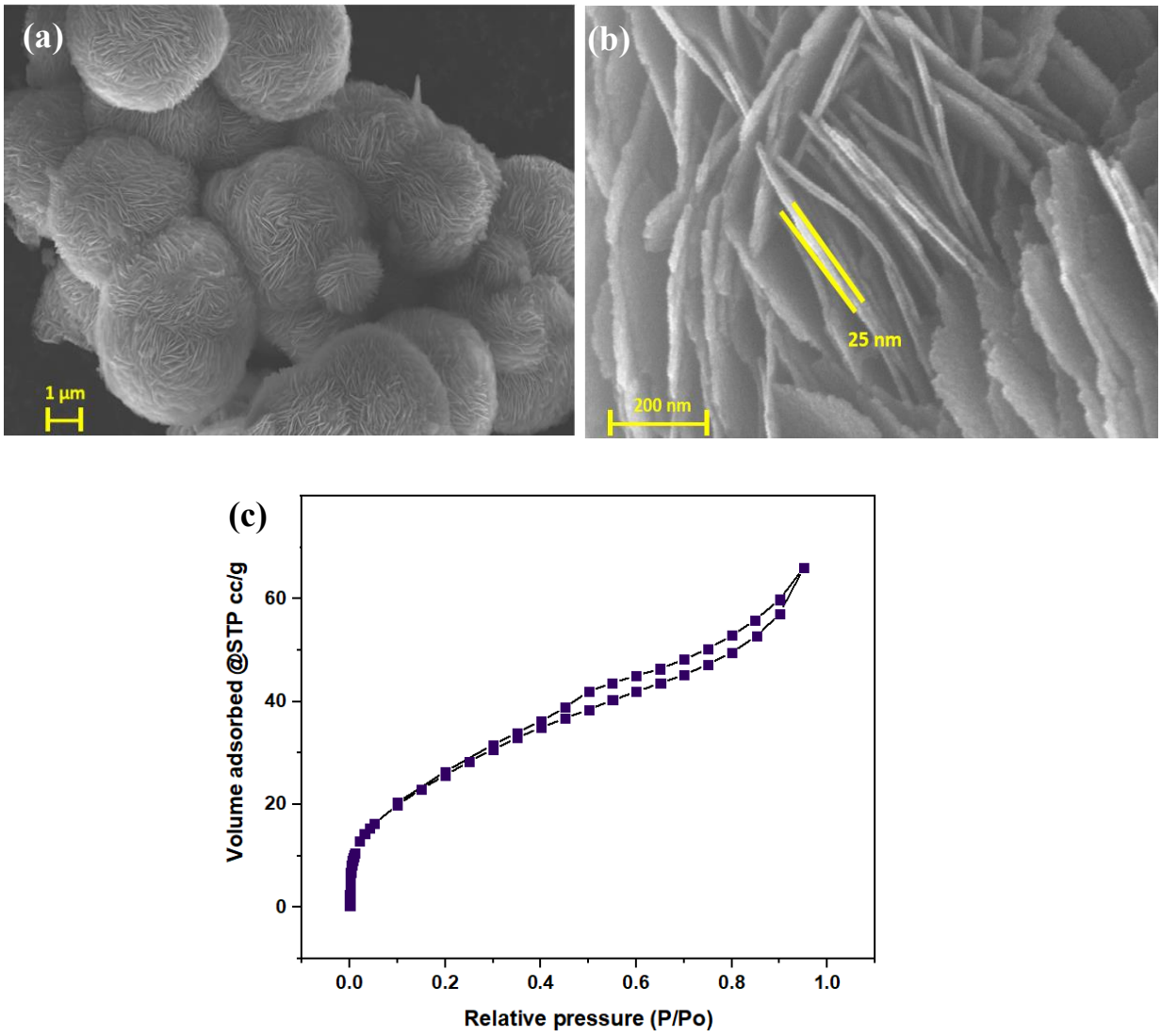

Figure 4.4. Low (a) and high (b) magnification SEM images of the synthesized 3D CSS-NS MF. (c) Nitrogen adsorption-desorption isotherms analysis

4.3.2 Fabrication and properties of photothermal membranes

Figure 4.5a illustrates the morphology of the support MCE membrane showing pore sizes of about 0.45 µm. **Figure 4.5b** reveals the top surface structure of a 3D CSS-NS MF/MCE membrane, where 3D CSS-NS MFs are uniformly distributed on the membrane surface. A hydrophobic surface layer of 1H,1H,1H,2H-perfluorodecyltriethoxysilane (PFDTES) was deposited on top of the membrane using a spray-coating process to enhance the anti-fouling and anti-salt crystallization properties. As shown in **Figure 4.5c**, the contact angle was significantly increased from 0° (MCE membrane and 3D CSS-NS MF-40 loaded on the MCE

membrane) to 142° after the hydrophobic surface layer coating process, and the SEM image indicates that the structural morphology of 3D CSS-NS MF-40 was maintaining after the coating process. The hydrophobic modifications of hydrophilic semiconductor PTMs are widely used to prevent salt accumulation on the solar absorber surface. Such hydrophobic surface modification provides long-term stability for PTMs without obvious decay in water evaporation performances, leading to enhanced solar evaporator recyclability.

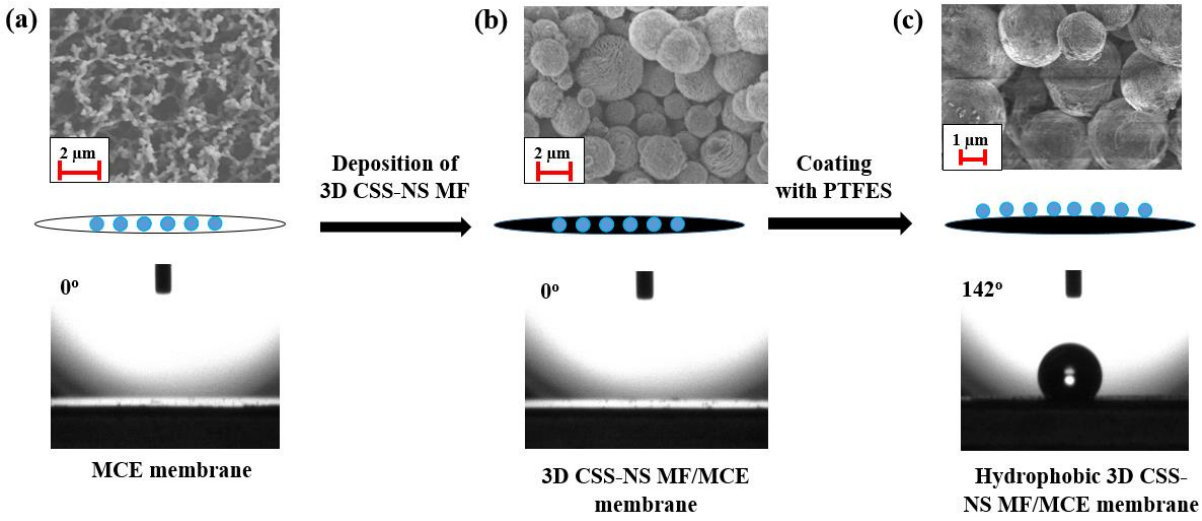

Figure 4.5 Fabrication of hydrophobic 3D CSS-NS MF on MCE membrane. (a) Hydrophilic cellulose acetate membrane with pore size of 45 µm; (b) 3D CSS-NS MF deposited on a MCE membrane; the SEM image indicates uniform deposition of 3D CSS-NS MF on the membrane and the water contact angle shows the hydrophilic nature of composite membrane; (c) The water contact angle showing the successful coating of PFDTES to achieve a hydrophobic 3D CSS-NS MF/MCE membrane; SEM image after the coating process.

4.3.3 Solar-to-thermal conversion and management

Effective solar light absorption is essential for high solar vapor generation performances. The effect of 3D CSS-NS MF-*x* concentrations was examined using different amounts of 3D CSS-NS MF (*x*: 20, 30, 40, and 60 mg) loaded onto the MCE membrane covering a diameter of 4 cm. The pristine MCE membrane displayed negligible light absorption across the solar spectrum. After the loading of 3D CSS-NS MF on a MCE membrane, superior light absorption was obtained covering the whole solar spectrum (92-94%) (**Figure 4.6a**). 3D CSS-NS MF-40 revealed the highest light absorption compared with 3D CSS-NS MF-20, 3D CSS-NS MF-30, and 3D CSS-NS MF-60 samples. An excellent light absorption was demonstrated with an absorbance of ~92% within ultraviolet and visible, and ~98% of the near-infrared regions. This is attributed to the microscale surface roughness, which more effectively captures diffuse light reflections, while the rough surface revealing more reflectance [230, 231]. The light absorption ability had reached saturation at 3D CSS-NS MF-40, and we did not observe further improvement at 3D CSS-NS MF-60. The excellent broadband light absorption is attributed to the presence of nanocavities between the vertically aligned nanosheets in 3D hierarchical microflowers as well as compacted structure 3D microflowers that lead to internal light scattering and trapping, contributing to effective light-harvesting efficiency [232, 233]. Moreover, the localized surface plasma resonance (LSPR) induced by the collective oscillation of a high density of holes is beneficial in extending the light absorption to the NIR regions [62, 157, 234]. In order to evaluate the effect of water on the solar absorber part during evaporation, light absorption was measured in the wet state. The pristine MCE membrane displayed increased light absorption compared to the corresponding value in the dry state (**Figure 4.6b**). Similarly, 3D CSS-NS MF-40 in the wet state demonstrated an increase in light absorption within ~98% within ultraviolet and visible, and slight increase ~98.6% in the of the near-infrared region. These results suggest that when water occupies the pores of the pristine

membrane and the spaces in the microflower structures in CSS-NS MF, the amount reflected light is reduced [138]. This trend has been observed in other studies [138, 159, 233] .

An excellent solar thermal conversion efficiency is another important aspect for achieving highly efficient interfacial SSG devices [39, 99, 176, 235]. In semiconductor PTMs, after absorption of sunlight by the PTMs, excited electron-hole pairs are formed by incident photons with energy higher than that of the bandgap of the PTMs. This indirect excitation of electrons then leads to relaxation to the band edge and then releases the irradiative energy into heat. This heat creates a temperature distribution depending on the absorption and surface characteristics [38, 217, 236]. Hence, as-synthesized 3D CSS-NS MF indicated good sunlight harvesting across the solar spectrum. We further investigated solar-thermal conversion using different solar light irradiations (1 sun, 1.5 suns, and 2 suns) over 15 minutes, recording the temperature variations at the 3D CSS-NS MF surface-based solar evaporator using an infrared (IR) camera, as shown in **Figure 4.6c** and **Figure 4.6d.** Test reproducibility of temperature ingredient was ensured by repeating the experiments three times. Upon 1 sun irradiation, the surface temperature of 3D CSS-NS MF-40 rapidly increased from 20 to 41 ^{o}C within 90 s, and reached 42 ^{o}C within 360 s. In contrast, the water surface lacking 3D CSS-NS MF/MCE membrane coverage displayed a slight increase in temperature from 19 ^{o}C to 25 ^{o}C**.** The excellent light-to-heat conversion efficiency may be attributed to the presence of nanocavities between the nanosheets of the microflower structure that play a vital role in enhancing light absorption and enabling heat localization and recovery of emitted heat [232]. In addition, the dense surface of the compact microflowers distributed on the membrane surface is also beneficial for localizing the heat in the solar absorber region. The mechanism of the solar-to-thermal conversion process of 3D CSS-NS MF is illustrated in **Figure 4.6e.** The obtained interlayer temperatures are comparable to other studies such as 1D O-doped MoS_{2-x} nanosheets that could reach surface

temperatures of 39 ºC [216], copper-zinc-tin selenide nanocarambolas with a surface temperature of 39 ºC [62], and Cu_2ZnSnS_4 nanosheets with a temperature of 41.7 ºC [188].

To further understand the photothermal conversion process, the static surface temperature was investigated under various sunlight irradiations at 1 sun (1 kW m^{-2}), 1.5 sun, and 2 suns. Correspondingly, with an increase in the sunlight irradiation from 1 sun to 1.5 suns and 2 suns, the surface temperature of 3D CSS-NS MF-40/MCE membrane was further increased from 22 ºC to 48 ºC at a power irradiation of 1.5 suns, and to 53 ºC at 2 suns, respectively, after 15 mins of solar irradiation. The change in bulk water temperature beneath the steam generation device at a 5 cm depth was low with an increase of ~1.3 ºC, and the side-view IR image is given in **Figure 4.6f**. This demonstrates that the as-designed 3D CSS-NS MF-40/MCE membrane and the system configuration (PS foam as insulator below the solar absorber) effectively suppressed the downward heat transmission to the bulk water and enhanced heat localization and conversion at the air-water interface.

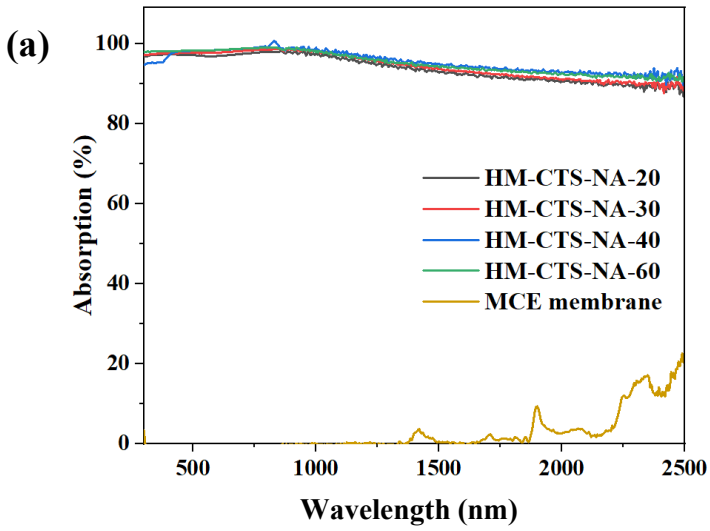
(a)
Absorption (%)
Wavelength (nm)
HM-CTS-NA-20
HM-CTS-NA-30
HM-CTS-NA-40
HM-CTS-NA-60
MCE membrane

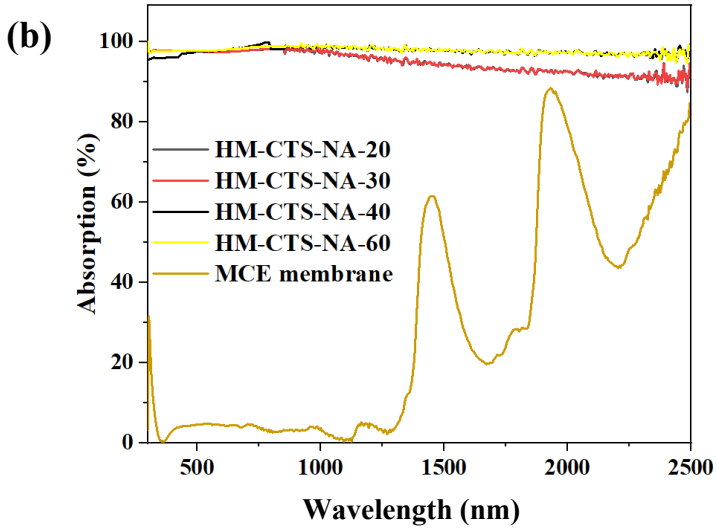
(b)
Absorption (%)
Wavelength (nm)
HM-CTS-NA-20
HM-CTS-NA-30
HM-CTS-NA-40
HM-CTS-NA-60
MCE membrane

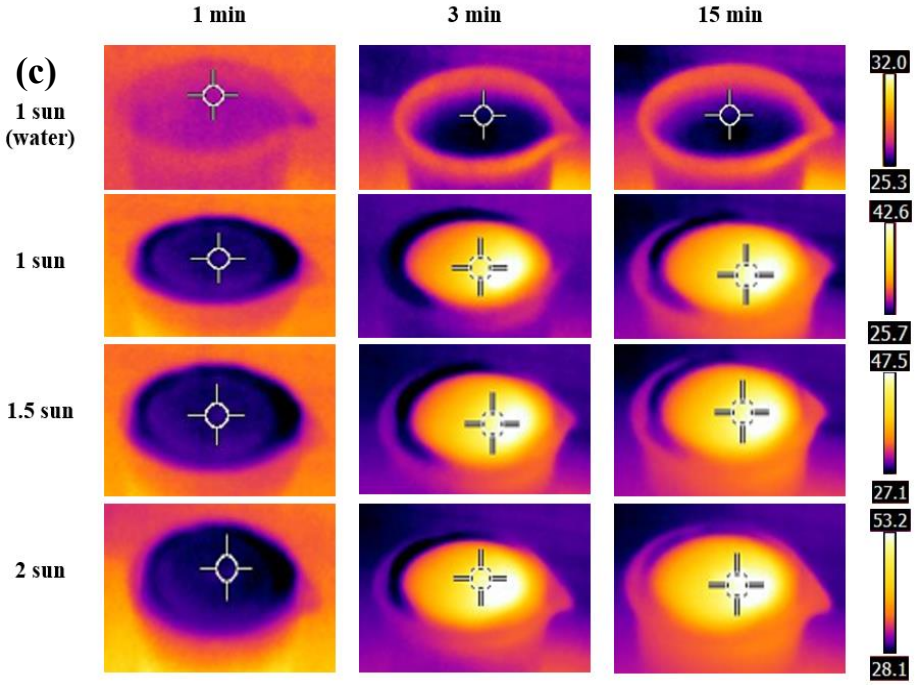
(c)
1 min
3 min
15 min
1 sun (water)
1 sun
1.5 sun
2 sun
32.0
25.3
42.6
25.7
47.5
27.1
53.2
28.1

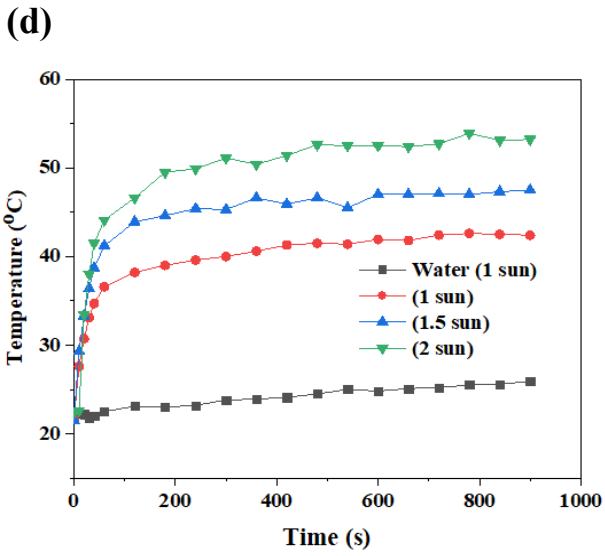
(d)
Temperature (°C)
Time (s)
Water (1 sun)
(1 sun)
(1.5 sun)
(2 sun)

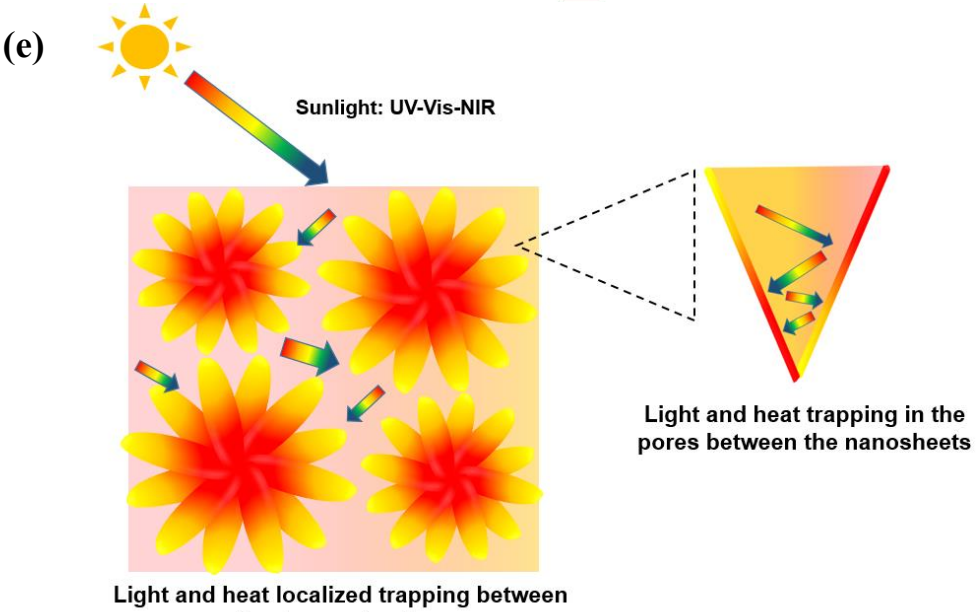
(e)
Sunlight: UV-Vis-NIR
Light and heat trapping in the pores between the nanosheets
Light and heat localized trapping between the dense structure

(f)

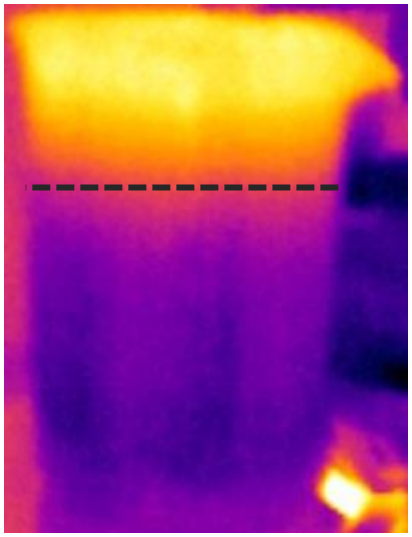

Figure 4.6 (a) Absorbance spectrum of pristine MCE membrane and a 3D CSS-NS MF/MCE membrane at loadings of 20 mg (black), 30 mg (red), 40 mg (blue), and 60 mg (green) at dry state, (b). At wet state. (c) Temperature variations at the top surface of the 3D CSS-NS MF-40/ MCE. (d) IR images of an interfacial 3D CSS-NS MF/MCE membrane show the temperature distribution and heat localization from 0 to 900 s (1-sun irradiation). (e) The mechanism of the solar-to-heat and heat-to-vapor generation process of CTS. (f) Infra-red image displaying the efficiency of the as-designed device in localizing the heat and minimizing the downward heat losses, after 10 min of solar irradiation under 1 sun.

4.3.4 Water evaporation performance

Water evaporation experiments were conducted at different concentrations of 3D CSS-NS MF at various light intensities (1, 1.5, and 2 suns). The water evaporation rate was measured by the mass change from the device over the testing duration at intervals of 4 mins (1 hour evaporation for each test). The water is transported from the bulk water to the solar absorber area (3D CSS-NS MF/CA membrane) through the hydrophilic air-laid paper (ALP). Upon solar illumination, the water continuously evaporates from the 3D CSS-NS MF/MCE membrane. **Figure 4.7 a and b** illustrate the schematic of the designed solar evaporator in this study.

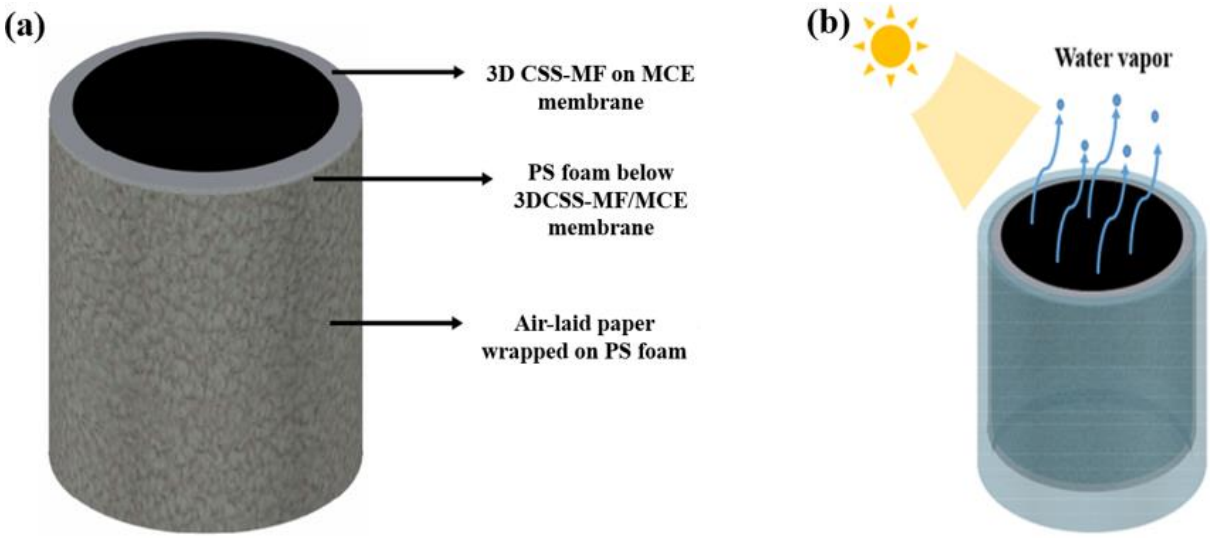

Figure 4.7 Schematic illustration of (a) 3D CSS-NS MF/MCE based solar evaporator. (b) The water evaporation process showing the vapor escaping through the top photothetmal 3D CSS-NS MF/MCE membrane.

The water evaporation rate is calculated based on Eq. 3.1. After irradiating the wet 3D CSS-NS MF under one sun irradiation, 3D CSS-NS MF-40 displayed the highest water evaporation rate of 1.42±0.04 kg m^{-2} h^{-1}. This value is 4.9 times higher than pure water (0.29 kg m^{-2} h^{-1}). The water evaporation rates of the other samples showed evaporation rate of 1.32±0.07 kg m^{-2} h^{-1} for 3D CSS-NS MF-20, 1.36±0.02 kg m^{-2} h^{-1} for 3D CSS-NS MF-30, and 1.29±0.07 kg m^{-2} h^{-1} for 3D CSS-NS MF-60, respectively (see **Figure 4.8 a,b)**. The above results indicate that the water evaporation rate increases with an increase in the concentration 3D CSS-NS MF until it reaches the highest evaporation rate at 3D CSS-NS MF-40. The increase of deposition amount of 3D CSS-NS MF was found to enhance the evaporation rate. However, excess amounts of 3D CSS-NS MF-60 resulted in a low water evaporation rate. We attribute this to the excess amount of deposited 3D CSS-NS MF leading to a high density of the compact microflowers, which could weaken the water transport channels. As a result, slow and impeded water transport and vapor release. The water evaporation performances under different intensities were also examined. An increase in solar intensities increased the water evaporation

rate to 2.24 kg m^{-2} h^{-1} under 1.5 sun and to 2.97 kg m^{-2} h^{-1} under 2 sun conditions, as shown in **Figure 4.8c.** These data indicate that with increasing light intensity speed up the water vapor release and escape [237].

The evaporation rate in a dark environment was calculated with values of 0.089 kg m^{-2} h^{-1} for blank water, 0.096 kg m^{-2} h^{-1} for 3D CSS-NS MF-20, 0.098 kg m^{-2} h^{-1} for 3D CSS-NS MF-30, 0.099 kg m^{-2} h^{-1} for 3D CSS-NS MF-40, and 0.086 kg m^{-2} h^{-1} for 3D CSS-NS MF-60 (**Figure 4.8d)**. Based on Eq 3.2, the evaporation efficiency without the solar absorber (water only) was calculated to be 13% under solar irradiation of 1 sun. With the solar absorber (3D CSS-NS MF on MCE membrane), the solar-to-vapor conversion efficiency was found to be 86.3 % for 3D CSS-NS MF-20, 87.8 % for 3D CSS-NS MF-30, 92.6% for 3D CSS-NS MF-40, and % 84.4% for 3D CSS-NS MF-60 (**Figure 4.8e**). It can be noted that the water evaporation rate and the solar-to-vapor conversion efficiency of 3D CSS-NS MF-40 were among the highest values. Such outstanding water evaporation performance can be explained by several features, including the controlling of the 3D CSS-NS MF concentrations, resulting in effective photothermal conversion within the pores of the nanosheet microflowers. Moreover, the high surface area induced by the nanocavities formed by the vertically aligned nanosheets in the microflowers facilitated the vapor transport from the absorber part without a significant interface. In addition, the continuous water supply induced by the air-laid paper to the solar absorber (3D CSS-NS MF/MCE membrane) resulted in continuous water evaporation [79] (**Figure 4.8f**). It is worth noting that the evaporation performance in this study is superior compared to some reported values (**Table 4.1**).

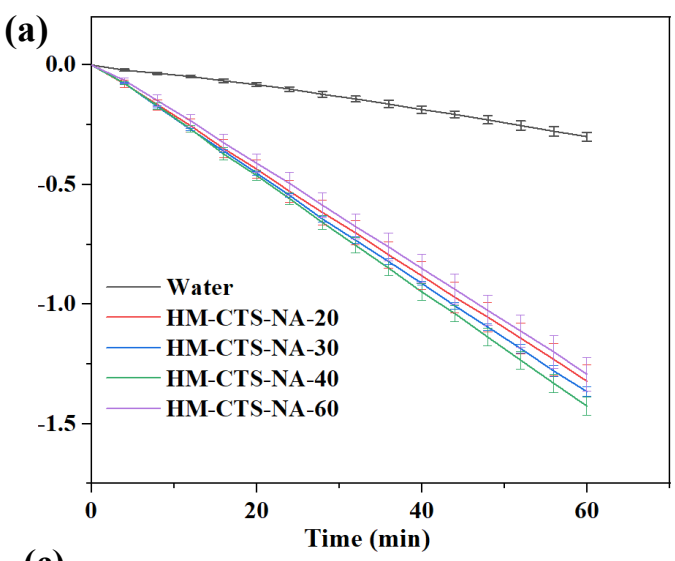
(a)
0.0
-0.5
-1.0
-1.5
0
20
40
60
Time (min)
Water
HM-CTS-NA-20
HM-CTS-NA-30
HM-CTS-NA-40
HM-CTS-NA-60

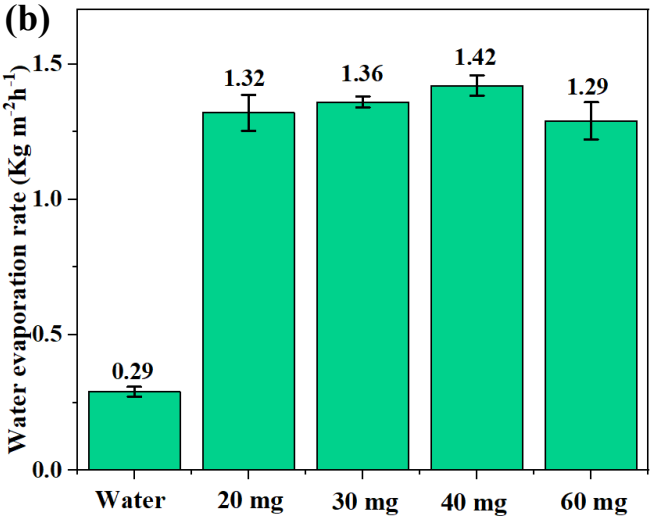
(b)
Water evaporation rate (Kg m-2h-1)
1.5
1.0
0.5
0.0
0.29
1.32
1.36
1.42
1.29
Water
20 mg
30 mg
40 mg
60 mg

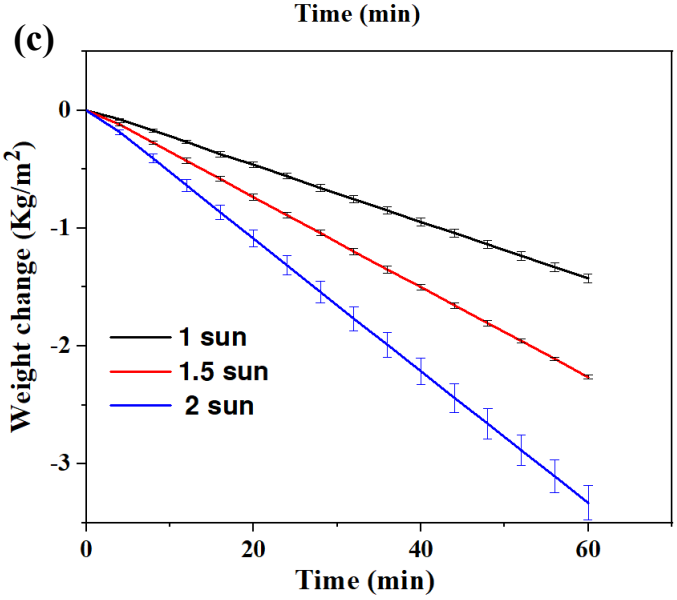
(c)
Weight change (Kg/m2)
0
-1
-2
-3
0
20
40
60
Time (min)
1 sun
1.5 sun
2 sun

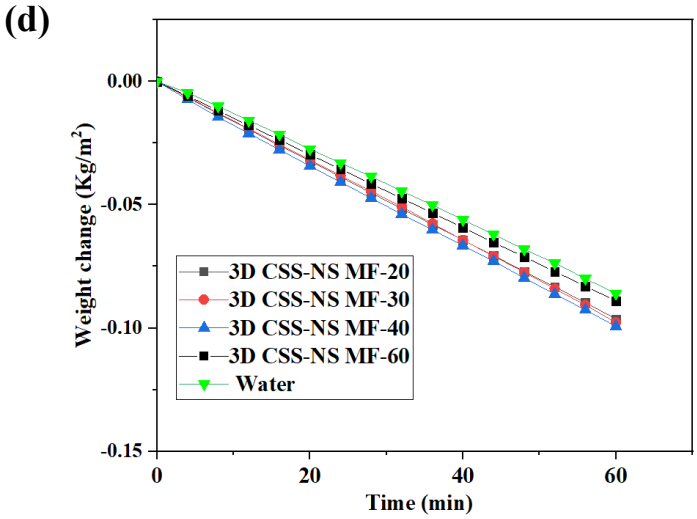
(d)
Weight change (Kg/m2)
0.00
-0.05
-0.10
-0.15
0
20
40
60
Time (min)
3D CSS-NS MF-20
3D CSS-NS MF-30
3D CSS-NS MF-40
3D CSS-NS MF-60
Water

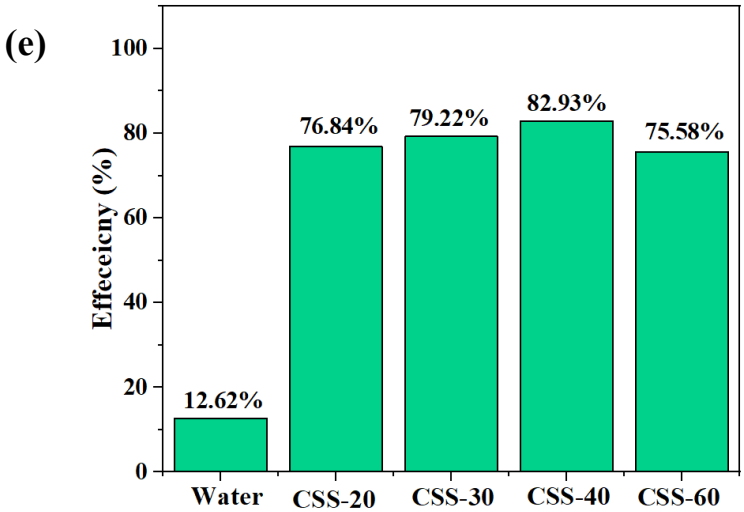
(e)
Effeceicny (%)
100
80
60
40
20
0
12.62%
76.84%
79.22%
82.93%
75.58%
Water
CSS-20
CSS-30
CSS-40
CSS-60

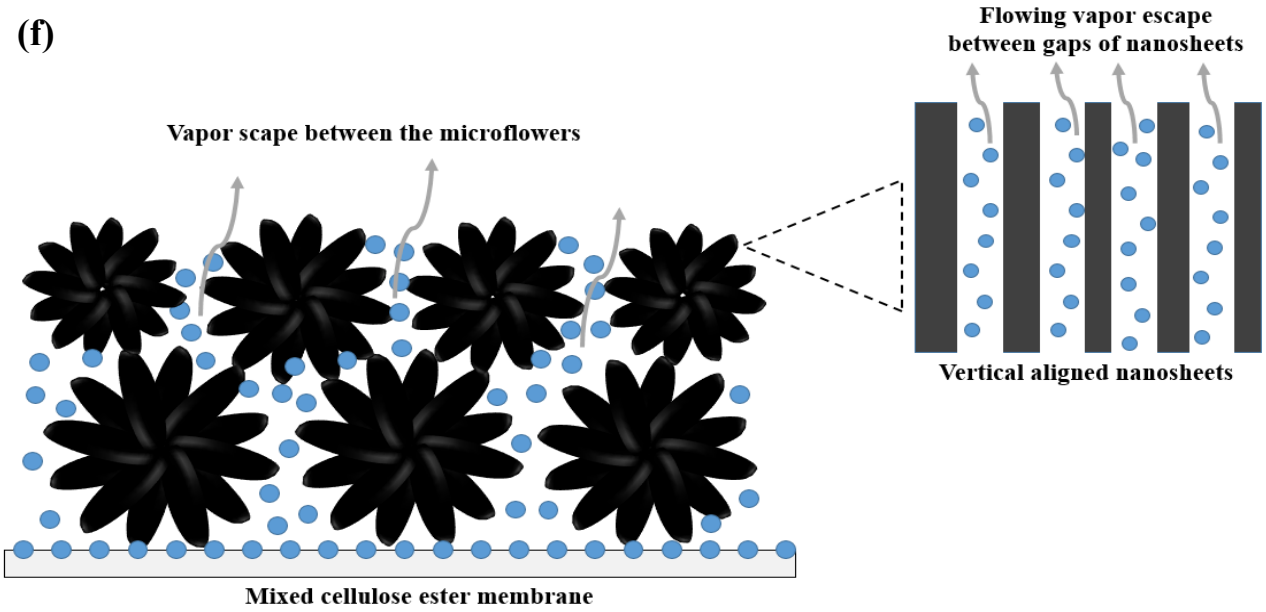

Figure 4.8 (a) Water evaporation rate with different loadings of 3D CSS-NS MF (20 mg to 60 mg) on MCE membrane, and (b) corresponding water evaporation rate. (c) Water evaporation rate of 3D CSS-NS MF-40 at different solar irradiations (1 sun, 1.5 sun, and suns). (d) Water evaporation performance at dark condition. (e) Solar-to-vapor conversion efficiency of 3D CSS-NS MF (20 mg to 60 mg). (f) The water transport mechanism of 3D CSS-NS MF-40/CA through the nanocavities of the vertically aligned nanosheets and the gaps between the microflowers.

Table 4.1 Comparison of solar water evaporation performance with some reported works on semiconductor-based PTMs

Photothermal materials	**Water Evaporation rate ($Kg\ m^{-2}\ h^{-1}$) under one sun**	**Ref.**
Multifunctional CuO nanowire mesh	1.42	[127]
3D-plasmonic covellite CuS hierarchical nanostructure /PVDF	1.43	[78]
CuS nanoflower	1.09	[128]
Single-layer CuS/PE membrane	1.02	[129]
Cu NPs / C- TiO_2	1.5	[238]
Cu_xS film	1.12	[131]
Cotton-CuS yolk-shell nanocage-agarose aerogel	1.63	[133]
3D CSS-NS MF-40	1.42±0.04	This work

4.3.5 Water desalination and durability performance

For the water desalinatin test, a home-made device was used for collecting the evaporated water from the feedwater. **Figure 4.9 a,b** illustrates the designed device used for the test. In this study, we used a real seawater obtained from Rose Bay Beach, Sydney. The major ion concentrations of (Na^+, Mg^{2+}, K^+, and Ca^{2+}) were measured before and after the solar desalination. The ICP-MS analysis indicated the concentrations of the ions were significantly reduced from 7506.3, 698.4, 513.6, and 356.3 mg L^{-1} to 0.391, 0.104, 0.322, and 0.203 mg L^{-1} (**Figure 4.9c**). The result demonstrated that the quality of the distillate met the standards of drinking water quality set out by the World Health Organization (WHO) [214, 215]. The mass changes of seawater were close to deionized water with a water evaporation rate of 1.41±0.03 and 1.42±0.04 kg m^{-2} h^{-1}, respectively, under 1 sun irradiation (**Figure 4.9d**)

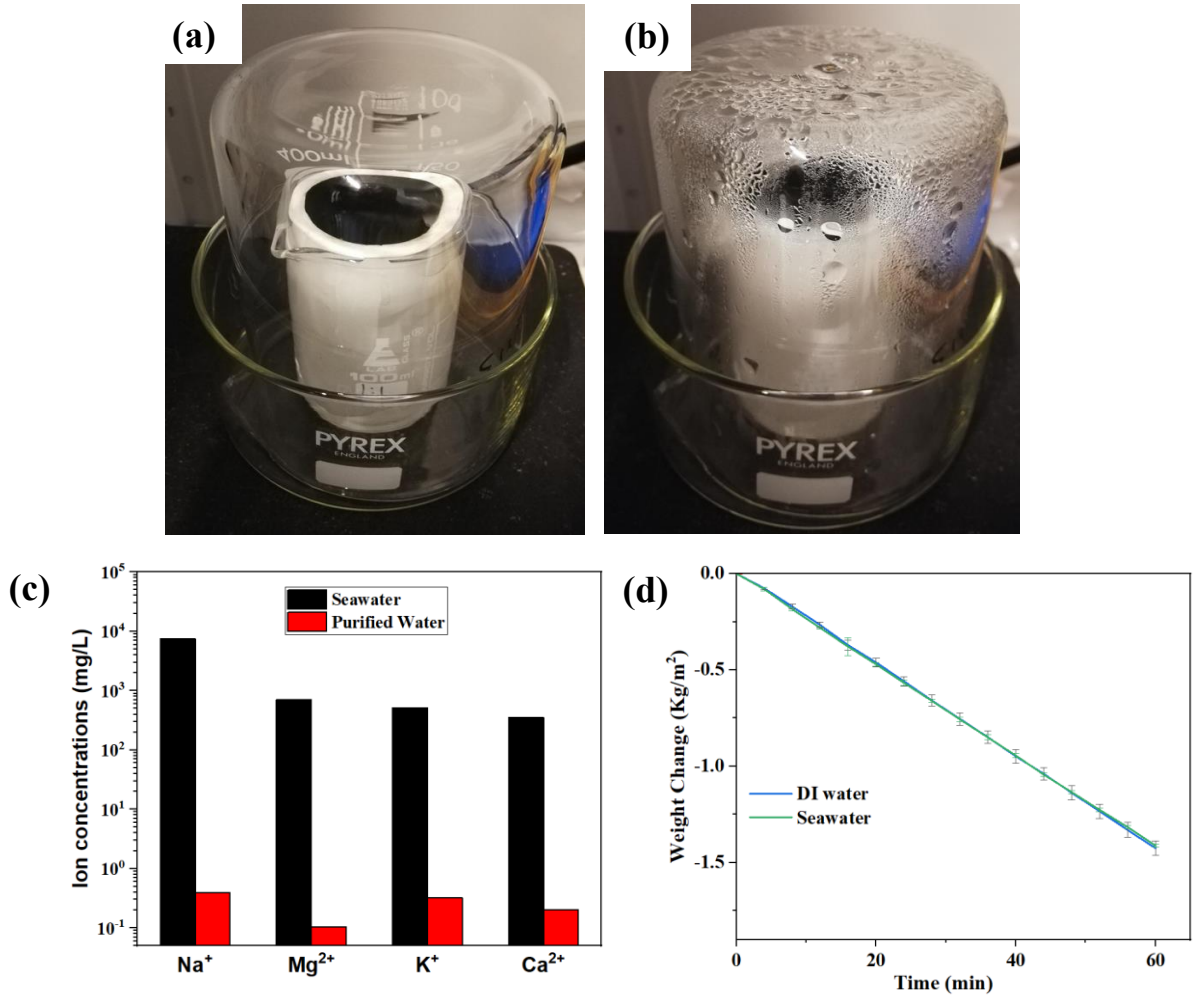

Figure 4.9 Photo-image of the home-made device for water collections through condensation process; (a) Before solar irradiations, (b) after solar irradiations (1 sun irradiation). (c) ICP analysis showing ion concentrations of seawater and the desalinated water (ion concentrations are lower than WHO and EPA standards). (d) Water evaporation data for DI water and natural seawater.

Furthermore, the stability test of the 3D CSS-NS MF PTMs based evaporator under similar seawater was performed continuously with 10 cycles (1-hour evaporation per cycle) under 1 sun irradiation. An excellent reusability performance was observed with stable evaporation rates to the 5^{th} cycle (1.40 kg m^{-2} h^{-1}), and then there was a slight decrease (1.35 kg m^{-2} h^{-1}) until the 10^{th} cycles (**Figure 4.10a**). The slight decreases was attributed to the formations of tiny salts on the black 3D CSS-NS MF, which was observed visually after 10 h of cycling test. SEM images of the solar absorber after the cycling test confirmed the salt migration and formation on the surface. The imaging on the clean part (black area) on 3D CSS-NS MF/MCE reveals the clean and the uniformity of the microflowers on the surface of the membrane (**Figure 4.10b**). This could facilitate solar light absorption and allowing continuous vapor generation [174]. On the other hand, the imaging on the tiny form salts confirmed the salt migration and formation on the microflower surface (**Figure 4.10c and d**). This cause in clogging some of the surface pores and decreased the solar evaporation area thereby reducing slightly the evaporation rate lower light absorption and reduce the water escape on that spot.

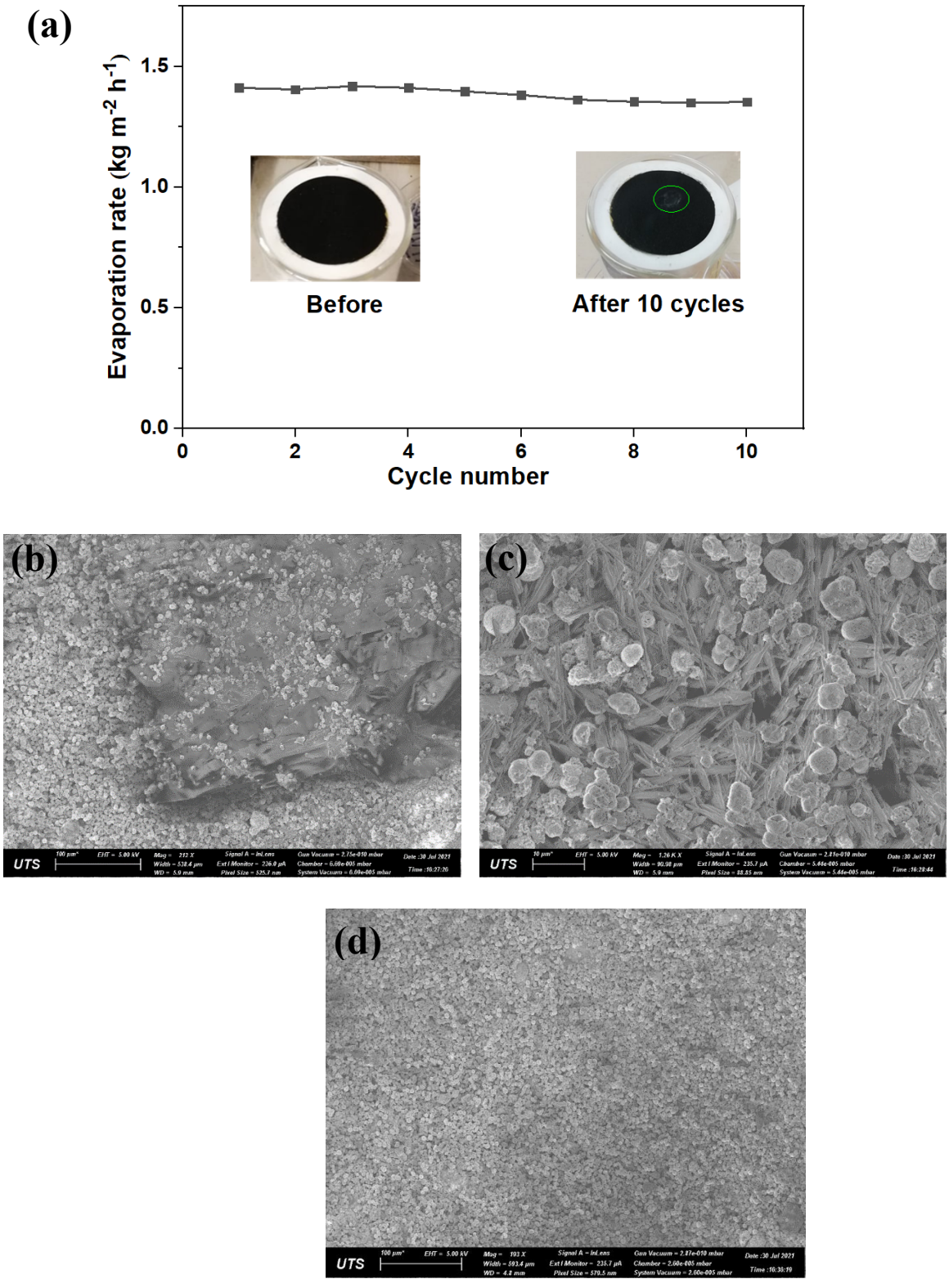

Figure 4.10 (a) Solar seawater evaporation performance for the 3D CSS-NS MF-based evaporator over 10 cycles, the inset images display the salt formation (green circle). SEM image of 3D CSS-NS MF/CA membrane surface after 10 hours (10 cycles) solar desalination. The salted form spot (b and c) (the images display the salt formations). (d) black part (the image indicates the presence and uniformity of 3D CSS-NS MF).

4.4 Conclusion

In conclusion, 3D CSS-NS MF has been synthesized as an efficient photothermal material for SSG applications. The rich nanocavities between the vertically aligned nanosheets and the compact microflowers were beneficial for high light absorption, excellent heat localization, thermal management, and fast vapour escaping. As a result, a high water evaporation rate of 1.42±0.04 kg m^{-2} h^{-1}, corresponding to the solar to vapour conversion efficiency of 82.93%, was obtained under 1 sun irradiation. Furthermore, 3D CSS-NS MF based evaporator demonstrated its effectiveness in salt rejection that met WHO drinking water standards. This study demonstrates the importance of controlling structural morphologies and sizes of the PTMs for high-efficiency solar steam generation devices.

CHAPTER 5

HIGHLY STABLE GOLD NANOLAYER MEMBRANE BASED SOLAR EVAPORATOR FOR HARSH ENVIRONMENT RESISTANCE

This Chapter is based on our revised manuscript: **Idris Ibrahim**, Dong Han Seo, MJ Park, Alexander Angeloski, Andrew McDonagh, Ho Kyong Shon, Avi Bendavid, Leonard Tijing A novel robust and scalable plasmonic membrane for a highly efficient solar steam generation under a harsh environment. Chemosphere (2022): 134394.

5.1 INTRODUCTION

Noble metals such as gold nanoparticles have been used as firstly reported by Hala's group in 2013 [40] and have since attracted broad interest, which led to an increase in research activities related to SWE. Noble metals are known to exhibit excellent chemical stabilities under harsh environments such for evaporation of sources water with highly acidic and basic conditions [83-85]. Previous studies on noble metals-based PTMs utilized either complicated or small-scale synthesis strategies [150]. Furthermore, the mechanical strength of their fabricated PTMs remains a challenge, hence hindering their practical implementation. Thus, a scalable strategy to allow the fabrication of nanoscale noble metals-based PTMs with excellent mechanical stability is essential for practical application in SWE. Magnetron sputtering (MS) is a promising technique that enables the deposition of nanoscale thin film on various substrates [239]. The method provides a cost-effective thin film coating at relatively low temperatures and can produce uniform thin film layers on large substrate areas with excellent adhesion [240, 241]. Based on the advantages of MS technique in forming an effective nanoscale thin film on a substrate surface. In the present study, a well-designed Au nanolayer on PTFE membrane surface by MS technique for SWE is demonstrated. Benefitting from the strong adhesiveness of the Au nanolayer on PTFE membrane surface, it results in a robust mechanical strength, excellent chemical stability even under harsh environments. The light absorption capability of our fabricated membrane covers the whole solar spectrum region. The designed solar evaporator of Au nanolayer-PTFE on cellulose sponge resulted in excellent salt ion rejection, meeting the required standard for drinking water. Furthermore, exceptional reusability and stability are demonstrated in natural seawater and harsh chemical conditions. Our findings reveal the novelty of magnetron sputtering methods for scaling up highly stable PTMs with excellent salt resistance for long-term durability solar evaporators.

5.2 Materials and methods

5.2.1 Materials

Gold targets (Au >99.9% purity) were purchased from Kurt J. Lesker company. A commercial polytetrafluoroethylene (PTFE, 0.45 μm pore size) membrane was obtained from Ningbo and used it as substrate for forming nanoscale thin film Au. A commercial cellulose sponge was purchased from a local supermarket, utilized as the insulator and floating support for the Au nanolayer membrane. Potassium hydroxide (KOH) was purchased from Merck; hydrochloric acid was bought from Chem-Supply, and sulfuric acid and nitric acid were received from Sigma Aldrich**.**

5.2.2 Fabrication of Au nanolayer membrane

The fabrication process of gold nanolayer membrane is described in section 3.3.2.

5.2.3 Characterization

The structure and the morphology of pristine PTFE and Au nanolayer membrane was investigated using field emission scanning electron microscopy (FE-SEM, Zeiss Supra 55VP) at an accelerated voltage of 10 kV. The surface wet ability of the samples was investigated by Theta Lite 100 (Attension) using a sessile drop method. A volume of 10 μL water droplet was vertically dropped on the substrate surface. The light absorption characteristics of the pristine PTFE and Au nanolayer membranes were measured at wavelength ranges (300-2500 nm; Ultraviolet-Visible-Near-Infrared regions) using a spectrophotometer equipped with an integrating sphere (950 PerkinElmer Lambda). Infrared (IR) images and surface temperatures were recorded on Infrared Camera (FLIR, E6). The concentrations of the positively charged ions (K^+, Na^+, $Mg^{2+,}$ and Ca^{2+}) in seawater before and after purification were measured using an inductively coupled plasma mass spectrometer (ICP-MS, Agilent 7900), while the

negatively charged ions (NO_3^-, Cl^-, and SO_4^{-2}) were measured using ion chromatography (IC) (Thermo Fisher, Australia).

5.2.4 Solar water evaporation test

The SWE set-up consisted of a solar simulator (PLS-SXE300) with a standard AM 1.5G filter, a precision analytical weighing balance (IC-PX84/E, Ohaus, 0.1 mg accuracy) connected to a computer, an infrared camera (FLIR E6), and Type-K thermocouples (RS PRO: RS172TK). The solar evaporator of Au/PTFE membrane (diameter = 4.5 cm) on cellulose sponge a thickness of 1.3 cm (under water) (**Figure 5.1**), floated at the air-water interface on a 100 ml beaker filled with 80 mL deionized water (DIW). During the experiment, simulated sunlight at irradiation of 1 sun = 1 kW m^{-2} was illuminated on the solar evaporator which was placed on the entire electronic balance. The change in weight with respect to time was continuously recorded at 4 min interval, with each evaporation experiment lasting for 1 h. Changes in membrane surface temperature were measured by an IR camera at various intervals, and a thermocouple was used to measure the bulk water temperature changes. SWE experiments at dark condition (without simulated light) was also carried out. Pristine PTFE membrane without gold thin film was also checked for its SWE performance, which served as the control for comparison. All experiments were carried out at room temperature of 22 ± 2 ºC and humidity ~ 52.5%.

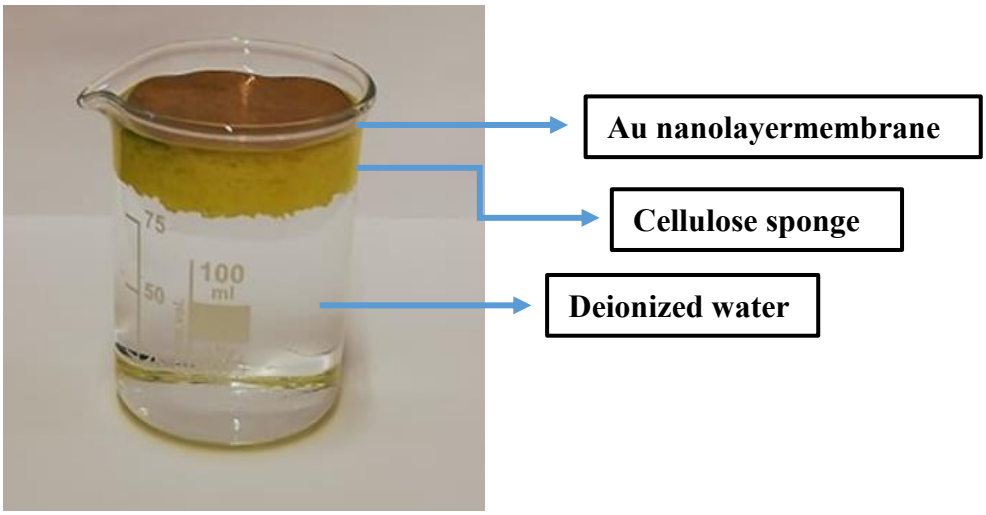

Figure 5.1 (a) photo-image of the designed plasmonic membrane based solar evaporator.

5.2.5 Solar water desalination and stability test under harsh environment

The potential of our Au nanolayer membrane for water desalination was evaluated by treating a real seawater collected from Cronulla Beach, Sydney, Australia and similar protocols for SWE were followed. In addition, a high salinity brine solution of NaCl (at 150 g/L) was prepared. The stability of the gold PTMs was evaluated under a harsh environment utilizing acidic (0.1 M H_2SO_4), basic (0.1 M KOH), and oxidizing conditions (0.1 M HNO_3) [213], with respective ionic strengths (*I*) of 0.3 M, 0.1 M, and 0.1 M. During the water purification tests, the evaporated water was collected and analyzed using ICP and IC techniques to measure the ions of the feedwater and the collected water. In addition, cycling stability tests (10 cycles) were demonstrated.

5.3 Results and discussion

5.3.1 Characterizations of Au nanolayer -PTFE membrane

Figure 5.1. shows the pristine PTFE and fabricated Au nanolayer films coated PTFE membranes. A magnetron sputtering process was used to uniformly coat thin films of gold onto PTFE membranes. The duration of the coating process was 4 min with film thickness of 50 nm. This type of coating process ensures quick, highly scalable, and uniform deposition of materials in a single step without the use of chemicals, making it a practical fabrication approach. This technology enables the fabrication of Au nanolayer membranes in large areas, which is vital for practical applications. A PTFE membrane was chosen as the substrate due to its good mechanical strength, flexibility, chemical stability, and high-temperature resistance [242]. During the magnetron sputtering process, strong physisorption was expected between the partially ionized Au particles and the modified PTFE membrane surface which led to their good adhesion with each other [243]. As illustrated in **Figure 5.1 a-c,** after deposition of the Au nanolayer, the circular white membrane top surface (inset of **Figure 5.1 a**) acquired a gold color, signifying the successful coating of the Au nanolayer. The coated membranes display strong adherence of the thin-layer Au to the PTFE membrane. The modified membranes can easily be folded and returned to their original state without detachment of the coating or membrane damage (**Figure 5.1 d**). These features are beneficial for the development of scalable and effective PTM for solar water evaporators.

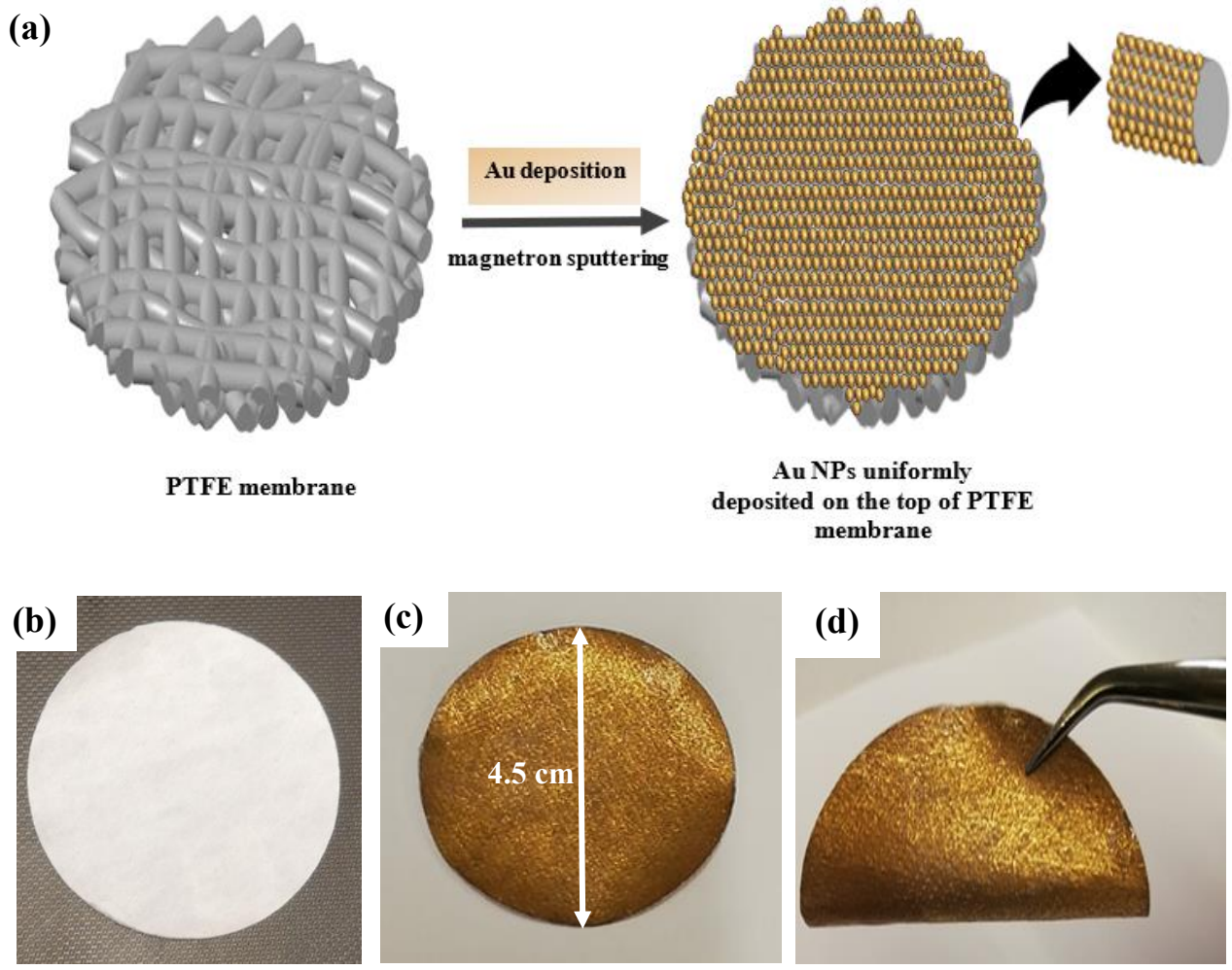

Figure 5.2 (a) Schematic illustration of gold deposition on a pristine PTFE membrane substrate. (b) Image of a pristine PTFE membrane. (c) Image of a gold-coated PTFE membrane. (d) Image showing the flexibility of the Au-PTFE membrane.

The structural morphology, elemental compositions, surface analysis and wettability of the fabricated Au nanolayer were examined. SEM images reveal that the surface morphology of the pristine PTFE contains unequal-length extended holes with open and distributed channels (**Figure 5.3a**). After gold deposition, a homogeneously distributed gold layer with a thickness ~50 nm was observed on the PTFE fiber surfaces **(Figure 5.3b** and **2c)**. The surface structure and porosity of the PTFE were maintained after the coating process. This structure is favorable for fast and extensive vapor diffusion and can facilitate good water evaporation performance [74]. Elemental mapping (**Figure 5.3d**) and Energy-Dispersive X-ray Spectroscopy (EDS)

analysis (**Figure 5.3e**) confirm the existence and the distribution of Au nanolayer homogeneously on the PTFE membrane surface.

(a)

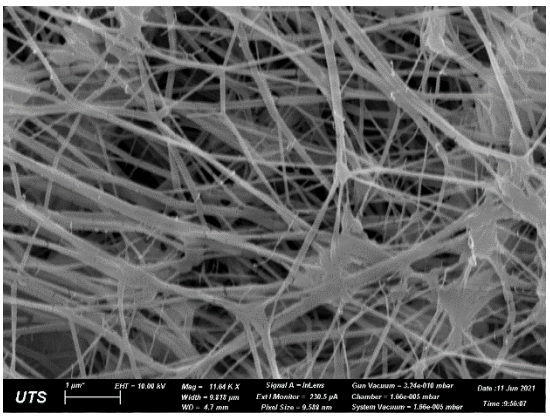
UTS

(b)

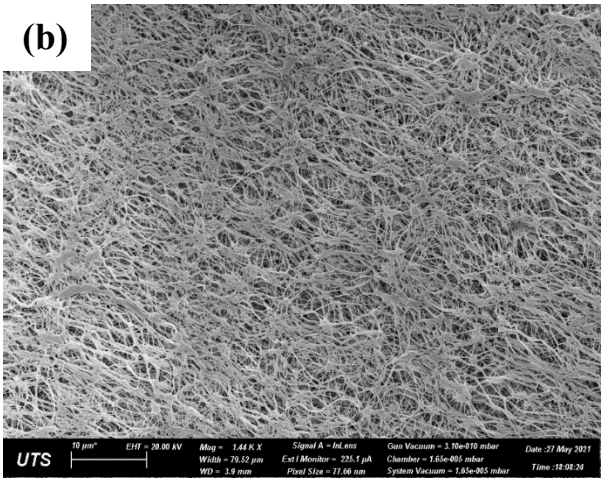
UTS

(c)

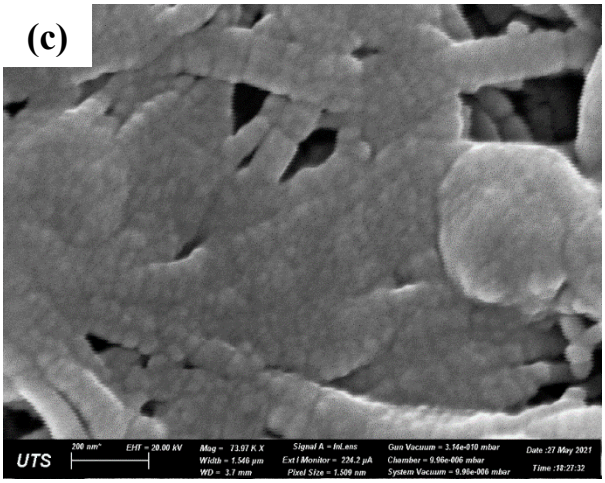
UTS

(d)

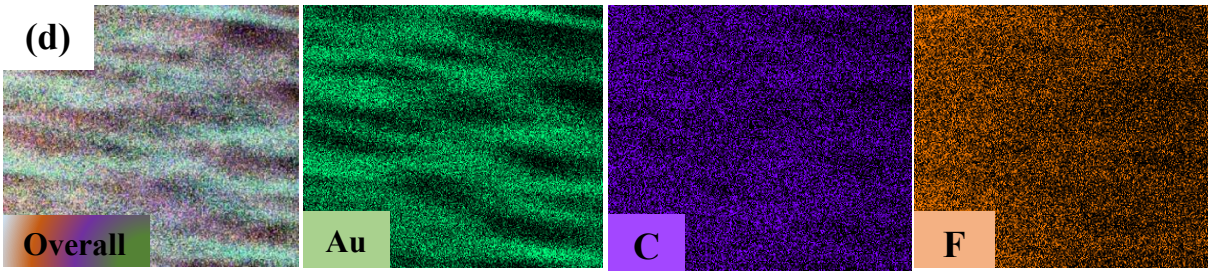
Overall
Au
C
F

(e)

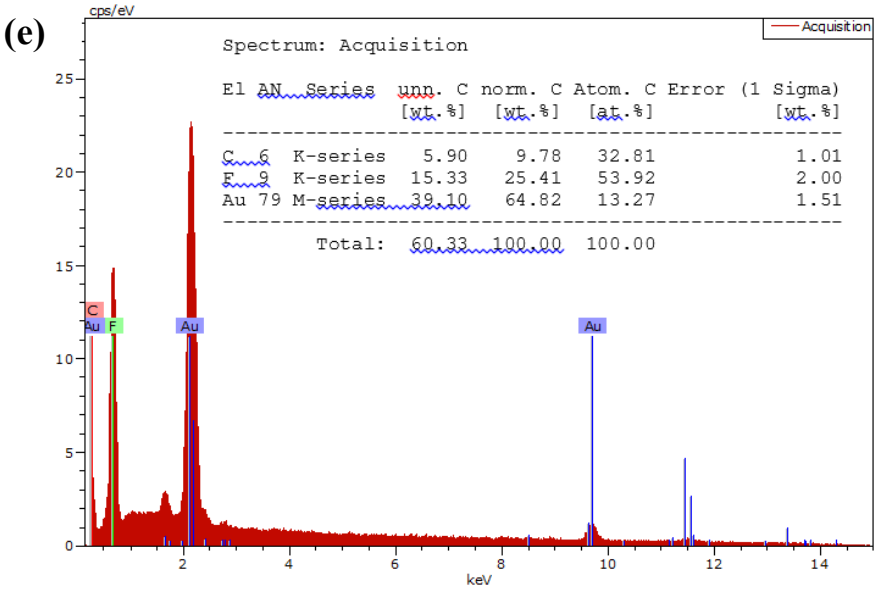
cps/eV
Acquisition
Spectrum: Acquisition
El AN Series unn. C norm. C Atom. C Error (1 Sigma)
[wt.%] [wt.%] [at.%] [wt.%]
C 6 K-series 5.90 9.78 32.81 1.01
F 9 K-series 15.33 25.41 53.92 2.00
Au 79 M-series 39.10 64.82 13.27 1.51
Total: 60.33 100.00 100.00
C
Au
F
Au
Au
keV

Figure 5.3 (a) SEM images of the pristine PTFE membrane. (b) low and (c) high magnification SEM images of the photonic membrane, (d) Elemental mapping results confirm the Au nanolayer distribution on the PTFE membrane surface. (e) EDS analysis of the Au/PTFE membrane

Additionally, XPS analysis was conducted to investigate the elemental composition and electronic structure of the Au nanolayer on PTFE membrane surface. The XPS survey spectrum confirms the presence of Au, C, F and O (**Figure 5.4 a)**. High-resolution XPS analysis revealed narrow doublet peaks of Au $4f_{5/2}$ (84.12 eV) and Au $4f_{7/2}$ (87.75 eV), separated by 5 eV (**Figure. 5.4 b)**. The peaks at 680 eV, 284.59 eV match F 1s, and C 1s, respectively, [83, 244]. The weak peaks of F 1s, and C 1s suggest the successful Au nanolayer coating and uniformity on the PTFE membrane surface.

The surface wettability plays a vital role in the anti-salt properties of PTMs for solar seawater desalination [39]. The dynamic wetting of water droplets on the pristine PTFE and gold deposited PTFE membrane were measured using a contact angle measurement (tensiometer) apparatus. The pristine PTFE membrane surface showed a water contact angle of 145±3°, indicating that it is almost superhydrophobic (**Figure 5.4 c)**. The thin layer of gold on the PTFE surface has drastically increased its wettability, with a water contact angle of 100±4° (**Figure 5.4 d)**. The hydrophobic behavior supported the self-floating ability of the membrane on water. In addition, it can act as an anti-salt property by repealing the salt ion crystallization on the evaporator surface, which is beneficial for the long-term durability of solar desalination.

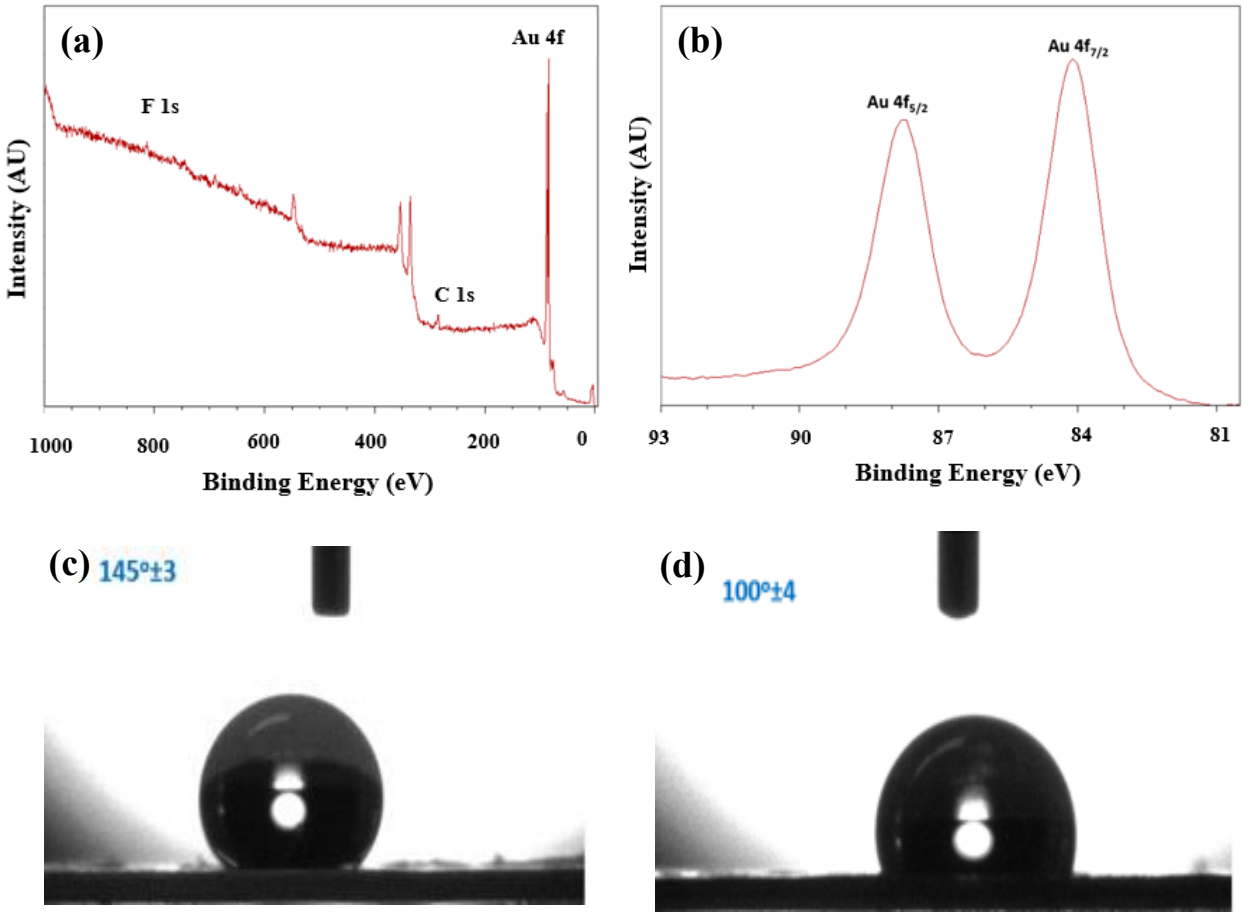

Figure 5.4 (a) Spectra Survey of x-ray photoelectron spectra (XPS) of Au-PTFE membrane (b) High resolutions XPS spectra confirming the existence of the Au 4f. (c,d) Surface wettability test of PTFE membrane and Au nanolayer membrane displays hydrophobic properties, and reduction in hydrophobicity being observed after the gold nanolayer deposition.

5.3.2 The stability of Au nanolayer-PTFE membrane

PTMs with chemical stability and robust mechanical strength of are essential for practical applications in SWE. The tensile strength and percentage strain results indicated that for pristine PTFE membrane, i.e., without the thin film gold coating, only 6.71 MPa, and 33.9%, were obtained, respectively. After the coating process, the values have increased to 8.09 MPa, and 36.48%, respectively. This phenomenon can be explained by the strong adhesiveness of the coated Au nanolayer to the membrane, enhancing its mechanical properties. The gold layer did not detach or fall off from the surface of PTFE membrane. Furthermore, the chemical

stability was assessed by heating the Au-PTFE membrane under acidic, basic, and oxidizing conditions at a temperature of 40 ^{o}C for 30 hours. In addition, we subjected the Au-PTFE membrane under sonication for 40 minutes. The EDS analysis revealed that the gold on the treated membranes maintained similar composition as with the original samples (**Figure 5.5-5.8**), even after exposure to these harsh environments. This signifies that our designed Au nanolayer has not been corroded under harsh conditions. This signifies that the magnetron sputtering method could be superior technique to fabricate Au nanolayer-based solar absorber compared to those techniques reported in the literature, such as electrospinning [29] and dip-coating [91]. The obtained results demonstrated that the magnetron sputtering method resulted in nanolayer gold formation with a remarkable adhesiveness membrane surface. This could be a promising strategy for the fabrication of a stable photothermal membrane for solar-driven water purification.

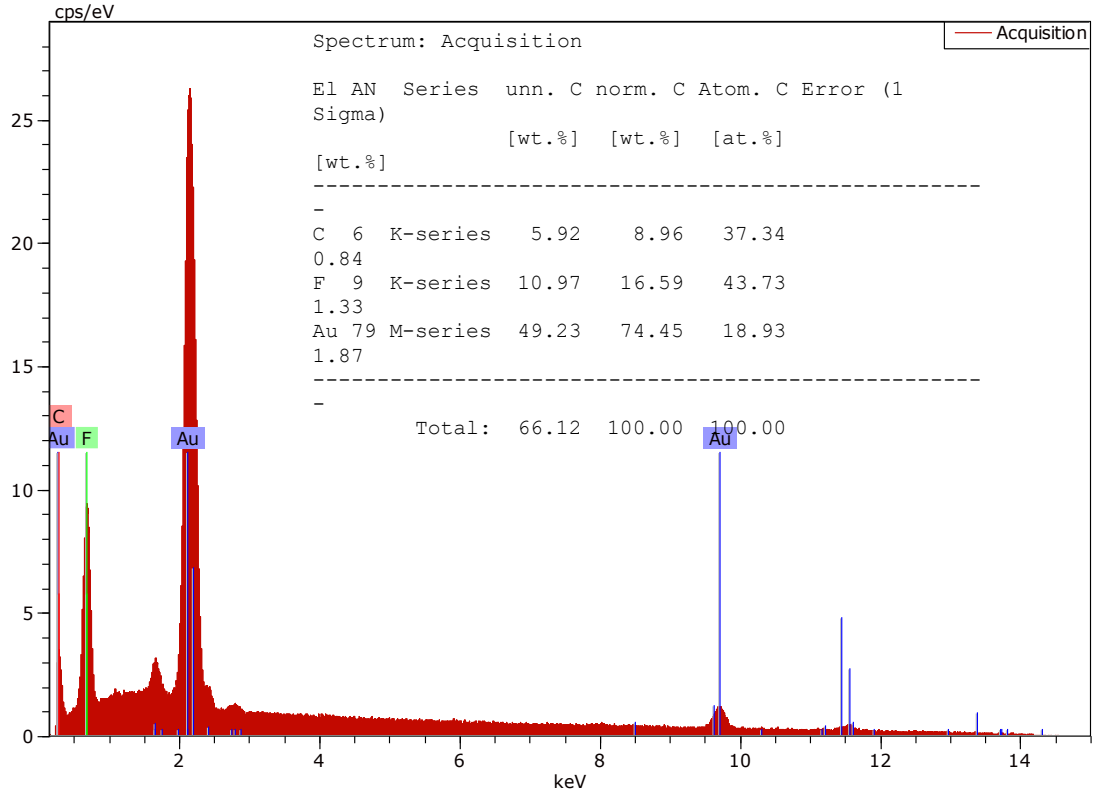

Figure 5.5 EDS analysis of the Au/PTFE membrane after treated under H_2SO_4 for 30 hours at a temperature of 40 ºC.

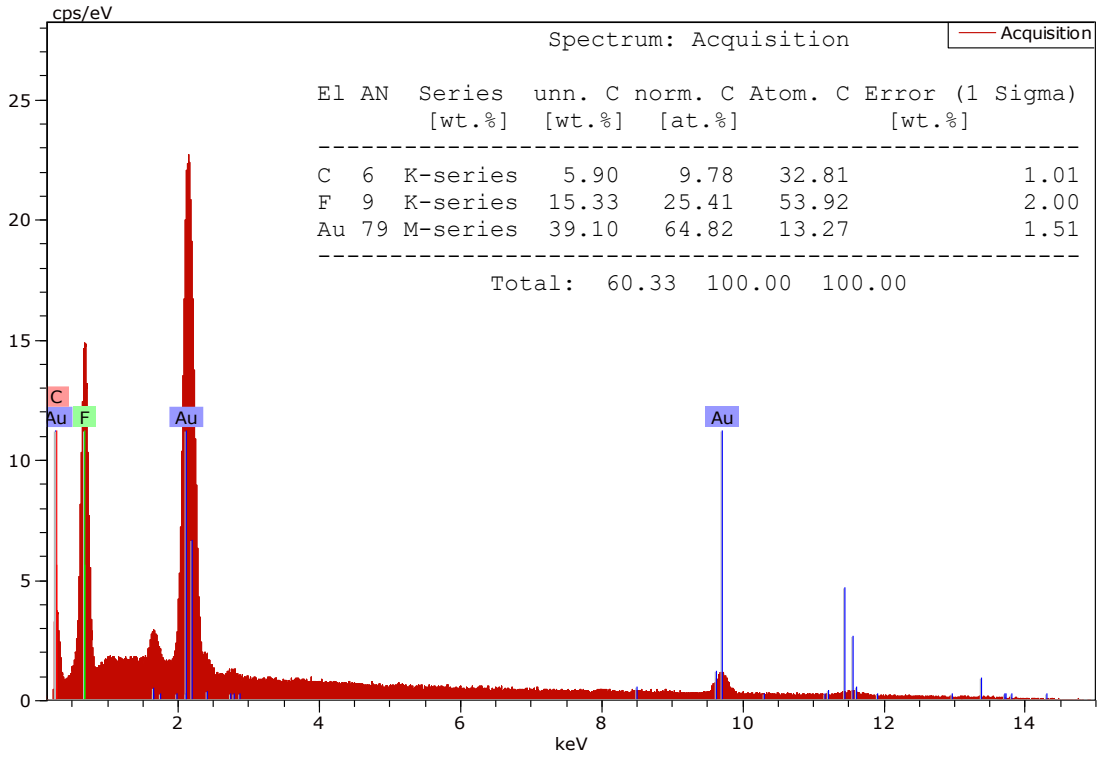

Figure 5.6 EDS analysis of the Au/PTFE membrane after treated under KOH for 30 hours at a temperature of 40 ºC.

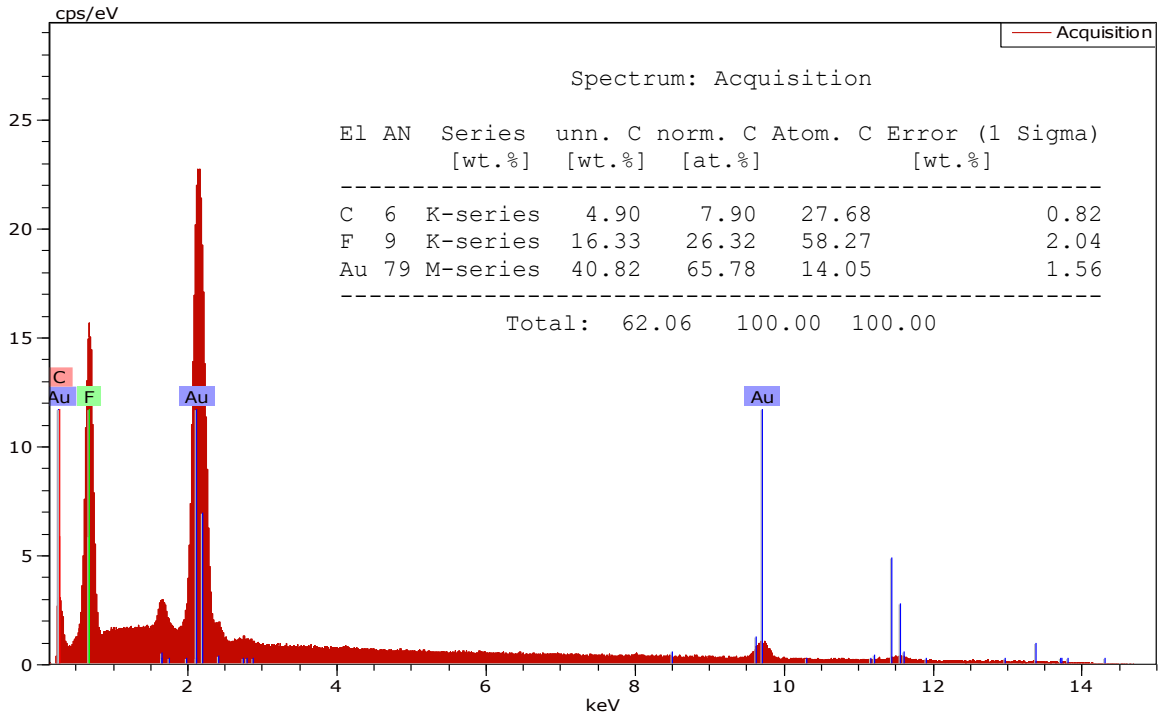

Figure 5.7 EDS analysis of the Au/PTFE membrane after treated under HNO_3 for 30 hours at a temperature of 40 ºC.

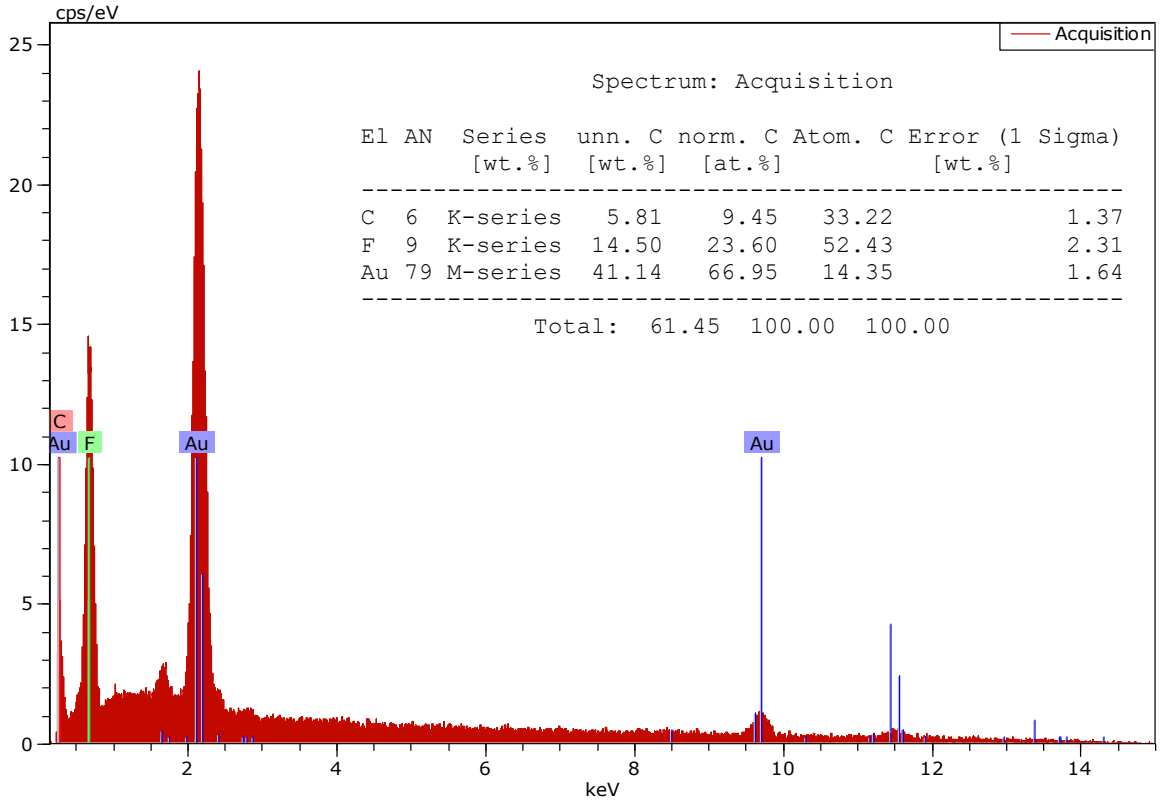

Figure 5.8 EDS analysis of the Au/PTFE membrane after treated under sonication for 40 minutes.

5.3.3 Optical characteristics and solar-thermal conversion of gold nanolayer membrane

The structure-dependent light absorption characteristics of the pristine PTFE and the designed Au nanolayer-PTFE membrane were evaluated using a UV-Vis-NIR spectrometer in the wavelength range of 300-2500 nm (**Figure 5.9a**). The inset image in **Figure 5.9a** shows the reference solar spectrum (at AM 1.5 G) [245]. The pristine PTFE displayed weak light absorption characteristics in the whole solar spectrum regions. In contrast, the coated PTFE membrane with Au nanolayer shows a much higher light absorption covering the whole solar spectrum region, with light absorption of ~ 80% in the UV region (300-400 nm), ~ 55-80% in the visible (400-700 nm), and ~ 40-55% in the NIR region (700-2500 nm). Along with good light absorption characteristics of the prepared gold nanolayer PTFE membrane, surface plasmon resonance (SPR) effect from the gold nanolayer helps to generate heat in the PTMs for effective water evaporation to occur. Plasmonic metals such as gold, due to the presence of high concentration of free carriers, enable free-carrier absorption [217]. The plasmon-induced heat generation occurs when Au nanolayer is illuminated at their resonant wavelengths, which causes oscillation of the electron cloud of free electrons. The decay of the hot electrons through electron-electron scattering creates and redistributes the hot electron energy in the form of heat, which can rapidly increase the localized surface temperature of plasmonic Au [86, 246]. Furthermore, the rough surface of the PTFE membrane and the holes with open and distributed channels play an effective role in reducing light reflection and can trap the photon capture [74]. This enhancement in the optical performance is beneficial for solar-thermal conversion for water evaporation applications. The optical performance of our Au nanolayer-PTFE membrane is comparable with some reported optical characteristics of noble metal PTMs in SWE [83, 247, 248].

After the optical properties test, we designed a simple solar evaporator consisting of a Au nanolayer membrane (Au-PTFE) placed on top of a hydrophilic porous cellulose sponge (CS) (referred to as Au-PTFE@CS). The added CS has dual-functional roles; (1) acting as thermal insulator where it can localize the heat at the air/water interface, and can reduce the downward heat losses, and, (2) it helps in supplying water to the top hydrophobic photothermal Au-PTFE. This simple combination design allowed fast and continuous water supply from the bulk water to the top hydrophobic Au nanolayer-PTFE membrane. Meanwhile, the hydrophobic Au-PTFE can repeal the salt formations resulting in excellent salt ions rejections with long-term durability and stable performance. For comparison, a pristine PTFE membrane was examined as well as a free-standing Au nanolayer membrane (without CS), and a DI water only condition. The surface temperature change of the designed solar evaporator was monitored over time using an IR camera under 1 sun (1 kW m^{-2}) irradiation. As illustrated in **Figure 5.9b** and **5.9c**, the surface temperature of the pristine PTFE membrane only showed a slight increase in temperature from 22.1 ºC to 24.8 ºC within 10 min. In contrast, the surface temperature of the Au-PTFE@CS rapidly increased from an ambient temperature of 25.2 ºC to reach 30 ºC within 3 minutes of illumination and further rose to 33.2 ºC after 10 min. In addition, without CS, the surface of the free-standing Au nanolayer membrane increased to 29.3 ºC. The surface temperature of the Au-PTFE with CS is higher compared to without CS demonstrating its excellent solar light-to-heat conversion. One reason for this is due to CS support, which acts as a thermal insulator and heat localizer at the air-water interface. To further investigate the effectiveness of the CS in localizing heat and reducing the heat transmittance to bulk water, we measured the bulk water temperature using a thermocouple. The side-view image using an IR camera was also used to visualize the heat distribution on the side of the solar evaporator. The thermal images of Au-PTFE with CS revealed that heat is localized with low transmission to the bulk water (**Figure 5.9d**). Furthermore, the bulk water change was relatively low with an

increase in temperature from 25.6 °C to 26.5 °C (i.e., 0.9 ºC difference). Meanwhile, without CS, the bulk water temperature increased from 25.6 ºC to 30.7 °C, which indicated the fast conduction of heat to the water. These observations demonstrate the effectiveness of thermal insulation in localizing the heat at the air-water interface and minimizing the downward heat losses, which is beneficial for solar water evaporation application.

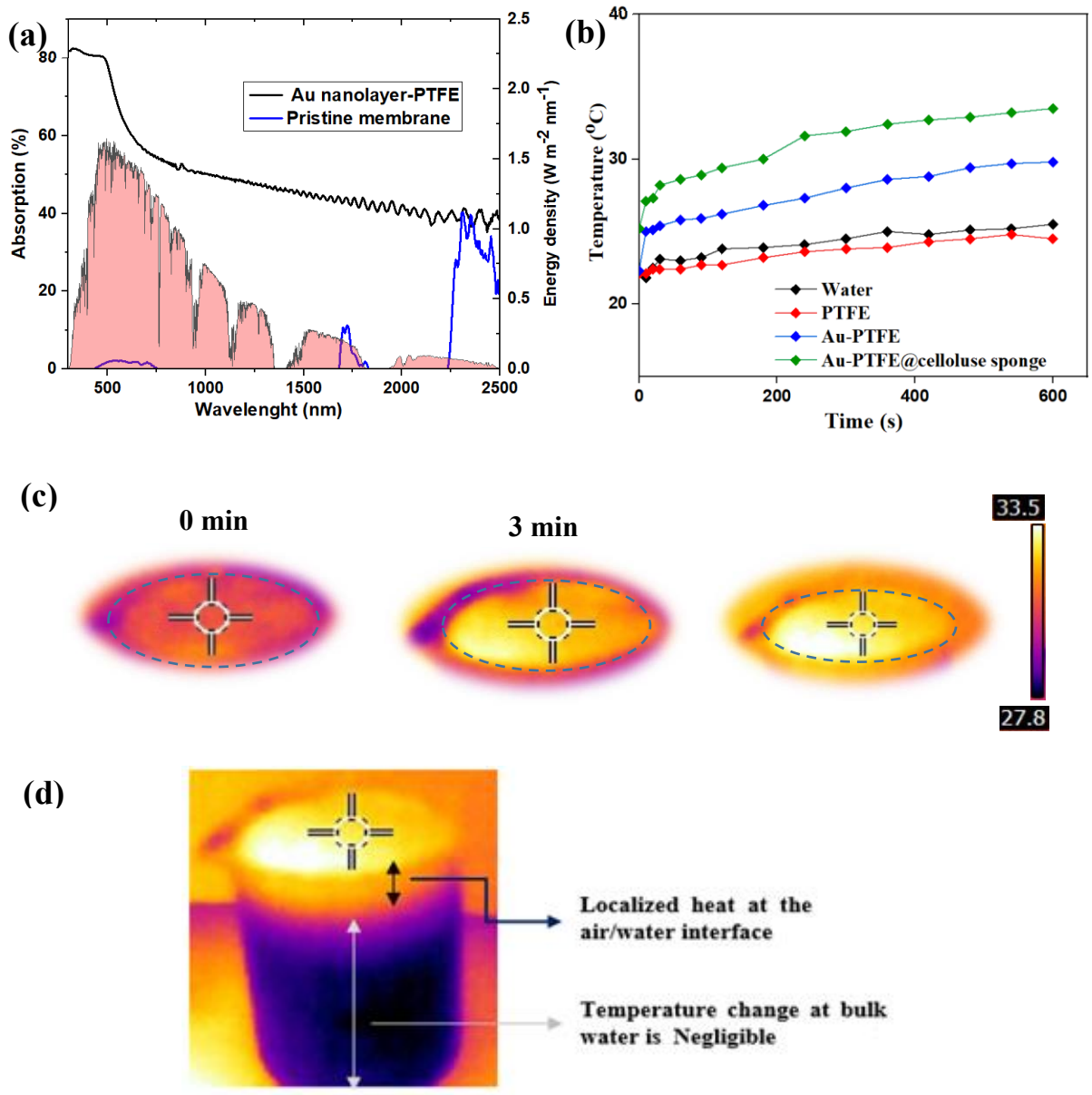

Figure 5.9 Solar absorption and solar-thermal conversion. (a) Light absorption characteristics of the pristine PTFE and Au-PTFE membrane across the UV-vis and NIR regions. (b) The temperature changes of the Au-PTFE/CS, pristine PTFE membrane, and water at 1-sun irradiation. (c) Infrared image of the heat formation after surface exposure to 1 sun-irradiation

from 0 to 10 minutes. (d) Infrared photo confirming the capability of the device to localized heat at the air-water interface.

5.3.4 Solar water evaporation performance

The solar water evaporation performance of the Au-PTFE supported CS was investigated and compared to those of DIW, and a freestanding Au-membrane (without CS support), under one sun irradiation. The solar heat-to-vapor efficiency (η) was calculated based on **Eq 3.2**. The evaporation rates at the dark condition were 0.081, 0.072, and 0.078kg m^{-2} h^{-1} for DIW, free-standing Au nanolayer-PTFE, and Au nanolayer-PTFE/CS, respectively (**Figure 5.10a**).

Under one sun irradiation, the DIW displayed an evaporation rate of 0.314 kg m^{-2} h^{-1}, corresponding to an evaporation efficiency of 14.8%. The evaporation rate was significantly increased after placing free-standing Au nanolayer membrane at the air/water interface to deliver an evaporation rate of 0.64 kg m^{-2} h^{-1}, corresponding to an efficiency of 35.6%, which is ~2 times that of pure water. The vapor generation arises from the absorption of the solar light through the gold nanolayer which generates a sufficient heat at the air-water interface. It was noticed that the evaporation rate was further improved by placing cellulose sponge below the Au nanolayer membrane to achieve an evaporation rate of 0.88 kg m^{-2} h^{-1}, corresponding to an efficiency of ~ 49.5 %. **Figures 5.10 b,c** displays the water evaporation rate and solar-heat-to-vapor efficiency results in this work. The reason for such further increase is due to the presence of underlying hydrophilic CS, which offers great heat confinement and efficient solar heat utilization. In addition, it delivers sufficient and continuous water supply to the hydrophobic Au nanolayer membrane. The spaces between the hydrophobic Au nanolayer membranes facilitate vapor escaping. Meanwhile, without CS (free-standing Au nanolayer), some of the generated heat by the Au nanolayer membrane was transmitted to the bulk water via heat conduction, resulting in lower water evaporation. Schematic illustration of the working mechanism of our designed device is illustrated in **Figures 5.10 d.** The obtained evaporation

rate in this study is comparable to some reported studies in the literature (**Table. 5.2**). The effect of the CS thickness on the water evaporation was investigated to find the optimal thickness. At 0.6 cm CS thickness, it generated a water evaporation rate of 0.82 kg m^{-2} h^{-1} at one sun intensity, while the 1.6 cm CS thickness resulted to an evaporation rate of 0.86 kg m^{-2} h^{-1}, which is similar to the 1.2 cm thickness. Hence, we chose 1.2 cm cellulose sponge as the optimized thickness in our current study (see **Figures 5.10 d**).

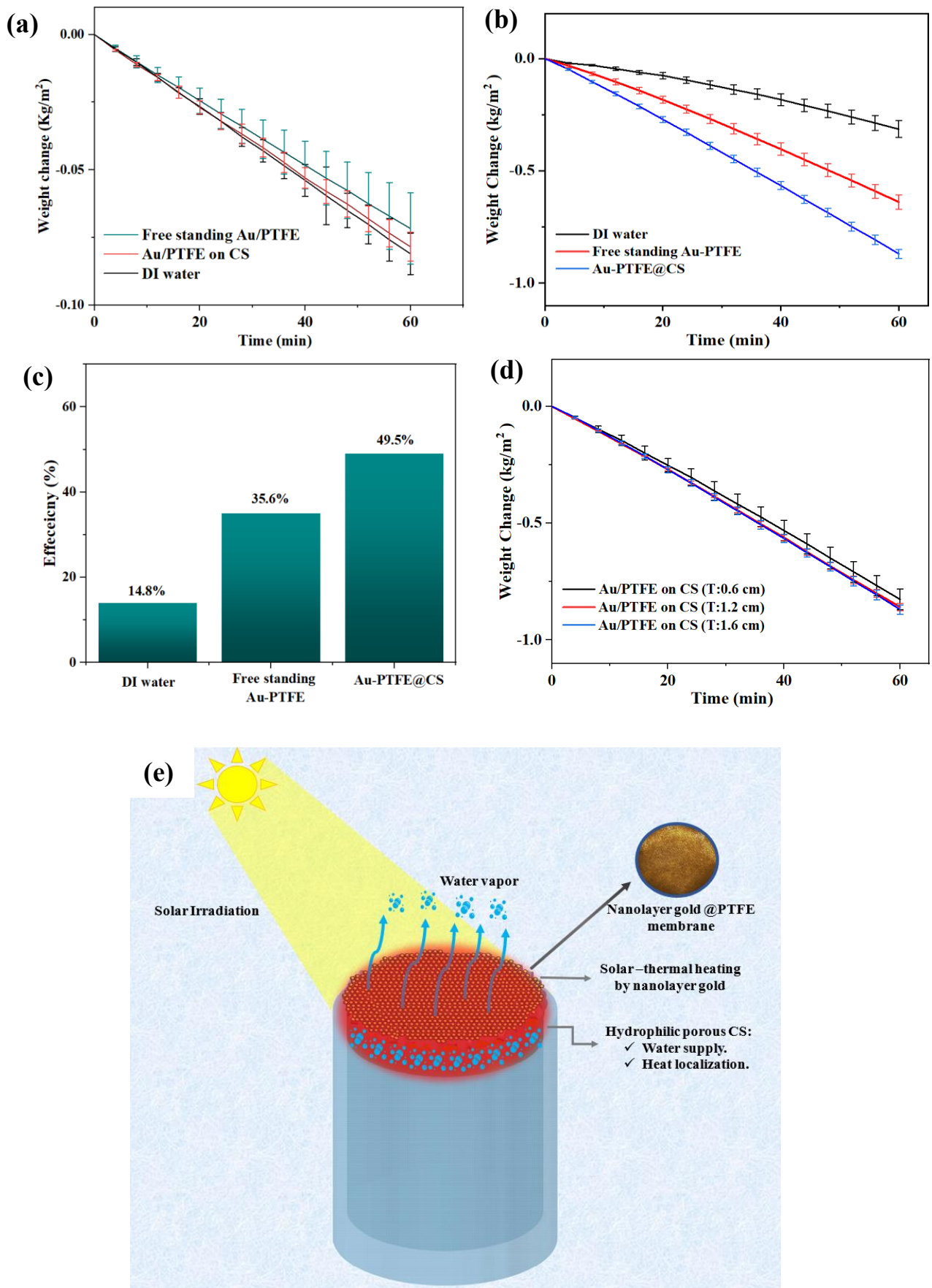
(a)
Weight change (Kg/m²)
0.00
-0.05
-0.10
0
20
40
60
Time (min)
Free standing Au/PTFE
Au/PTFE on CS
DI water
(b)
Weight Change (kg/m²)
0.0
-0.5
-1.0
0
20
40
60
Time (min)
DI water
Free standing Au-PTFE
Au-PTFE@CS
(c)
Effeceicny (%)
60
40
20
0
14.8%
35.6%
49.5%
DI water
Free standing Au-PTFE
Au-PTFE@CS
(d)
Weight Change (kg/m²)
0.0
-0.5
-1.0
0
20
40
60
Time (min)
Au/PTFE on CS (T:0.6 cm)
Au/PTFE on CS (T:1.2 cm)
Au/PTFE on CS (T:1.6 cm)
(e)
Solar Irradiation
Water vapor
Nanolayer gold @PTFE membrane
Solar –thermal heating by nanolayer gold
Hydrophilic porous CS:
✓ Water supply.
✓ Heat localization.

Figure 5.10 (a), (b) Weight change under one sun irradiation of DIW, free-standing Au-PTFE, and Au-PTFE supported CS at dark and under one sun irradiation. (c) The corresponding solar conversion efficiency. (d) Weight change under 1 sun intensity of Au-PTFE supported CS with different sponge thickness, (0.6, 1.2 and 1.6 cm), under 1 sun intensity. (e) Schematic illustration of the solar conversion and vapor generation process of Au nanolayer membrane on CS-based solar evaporator.

Table 5.1 Comparison of the obtained result with some literature report

Photothermal materials	**Water evaporation rate (kg m^{-2} h^{-1}) (at one sun** irradiation**)**	**References**
Functionalized graphene	0.47	[249]
Thin-film black gold membranes	0.67	[146]
Plasmonic Au loaded anodized alumina oxide membrane	0.63	[89]
Al nanoparticles loaded anodized alumina oxide membrane	0.92	[147]
Gold/PVDF	1.02	[148]
Black phosphorous/Collage-Polyurethane	0.89	[250]
$BiInSe_3$@NF	0.83	[251]
Plasmonic membrane	0.88	This work

5.3.5 Salt ions rejection

The feasibility of the Au-PTFE membrane for solar water desalination was also investigated. For the desalination tests, real seawater collected from Cronulla Beach, Sydney were used. In order to investigate the capability of the evaporator system for generating potable water, the evaporated water was condensed, collected and analyzed using ICP-MS and compared to the original seawater. A schematic illustration for the water condensation and collection is provided in (**Figure 5.11 a**). The results indicated that a high amount of the salt ions Na^{+}, K^{+}, Ca^{2+}, and Mg^{2+} in the purified water was significantly decreased to 7.79, 0.60, 0.62, and 0.86 mg/L, respectively compared to their respective initial concentrations of 8750, 1043.7, 348.3 and 398.3 mg/L (**Figure 5.11 b**). The obtained values are below the standard drinking water required by World Health Organization (WHO) and the U.S. Environmental Protection Agency (EPA) [214, 215]. This result proves the capability of Au nanolayer-PTFE membrane-based solar evaporator in producing drinking water.

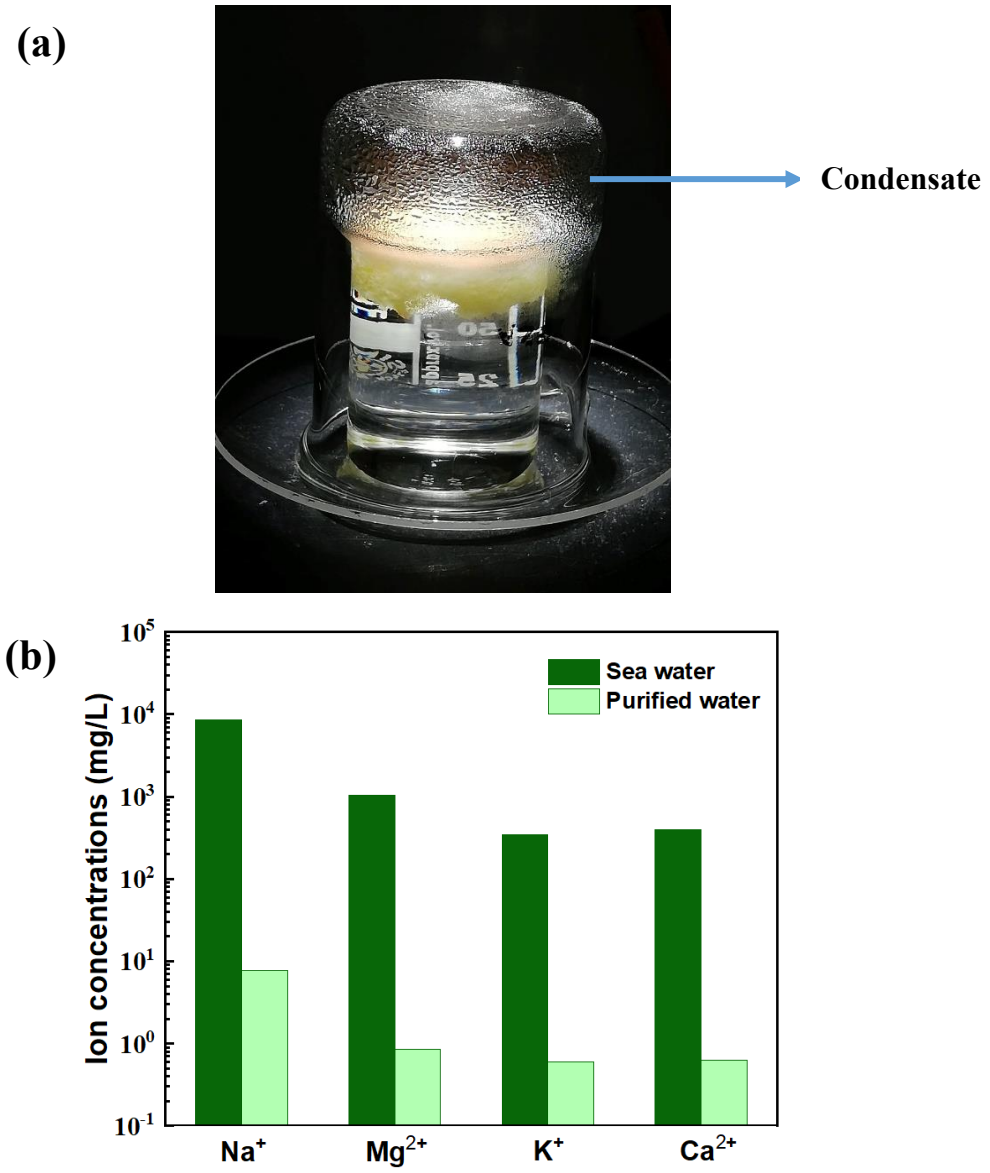

Figure 5.11 (a) Photo-image and schematic of the used device for collecting water vapor. (b) The concentrations of ions (Na^+, K^+, $Ca^{2+,}$ and Mg^{2+}) in seawater collected from Cronulla Beach demonstrate the high reductions in ion concentrations before and after the desalination process.

5.3.5 Self-cleaning, durability, and stability test

The durability and stability of the solar evaporator system are the main challenges for solar seawater desalination. The salt formations on the solar absorbers will cause a significant decrease in the light absorption, causing a lower evaporation surface [38, 39]. Therefore, it should be addressed before implementing this technology for practical application. The salt rejections capability self-cleaning of the Au-PTFE@CS evaporator was investigated by placing 2.5 g of salt on the top of the Au nanolayer membrane. After one sun irradiation, the salt gradually disappeared with continuous vapor flow through the holes between the coated fiber of the Au-PTFE membrane until no salt was observed after 2.5 hours (**Figure 5.12 a**). The self-cleaning of the designed evaporators can be ascribed to the spaces between the heated coated fibrous in Au-PTFE membranes which allows continuous vapor flow for chemical advection and diffusion induced by the salt concentration gradient, resulting in salt dissolving [252, 253]. In addition, the hydrophilic open pores CS allow the formation of the thin layer of water underneath the Au nanolayer membrane, resulting in sufficient and continuous water supply and dissolving the salt at the top.

On the other hand, the salt on pristine PTFE membrane did not change much. This is mainly ascribed to the low solar thermal conversions resulting in low surface temperature and hence low water evaporations. Besides, superhydrophobicity of the PTFE surface minimized the water penetrations from the bottom cellulose sponge, which contributed to the remaining salt on the PTFE surface for a more extended period (**Figure 5.12 b**). After the self-cleaning test, the water evaporation performance was conducted, and a solar evaporation rate of 0.87 kg m^{-2} h^{-1} was obtained. This confirms its reusability and capability to generate vapors.

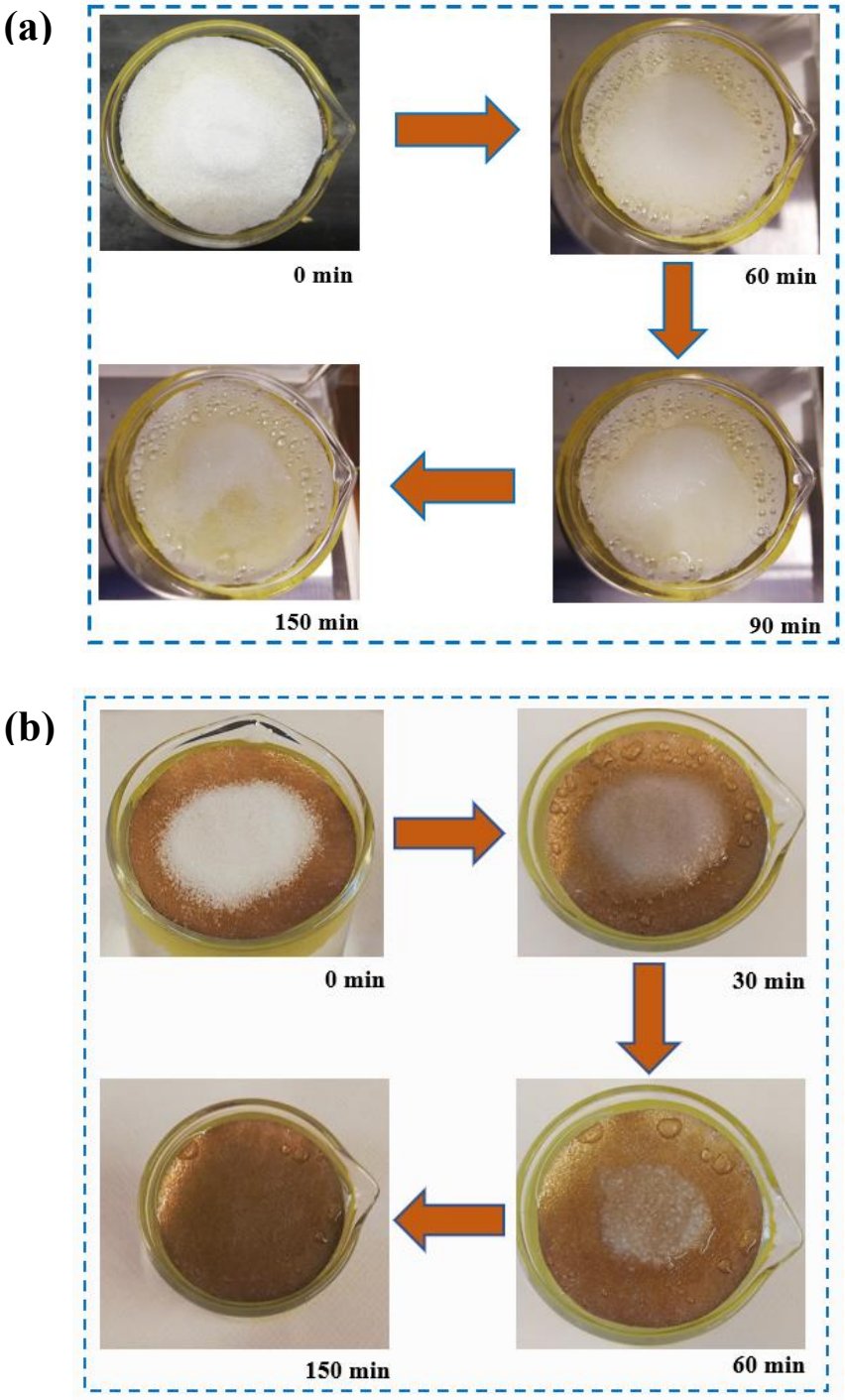

Figure 5.12 Photo-image of salt-dissolution and self-cleaning property after adding 2.5 g NaCl. (a) Pristine PTFE@CS. (b) Au-PTFE @CS.

To examine the durability of Au nanolayer-PTFE membrane for solar desalination, we conducted the evaporation test using natural seawater and high salinity brine (150 g/L NaCl) as model brine solution. The performance was carried out for 10 continuous cycles (1h/cycle) under one sun irradiation. Interestingly, excellent reusability with stable performance over ten cycles was demonstrated, with only a slight decrease in the evaporation of 0.85 kg m^{-2} h^{-1} for seawater, to 0.82 kg m^{-2} h^{-1} for the high brine 150 g/L NaCl (**Figure 5.13 a,b**). The slight reduction in evaporation rate for brine solution is attributed to the decrease in vapor pressure of brine solution [176, 254, 255]. The above-mentioned results indicate excellent salt resistance due to the continuous water supply through CS, providing a thin layer of water. In addition to that, the surface hydrophobicity of the Au nanolayer-PTFE membrane, no noticeable salt was formed. This result implies that MS technique is a reliable technology to fabricate a stable nanolayer photothermal membrane for seawater desalination, especially high-salinity with anti-fouling properties. We further extend the durability study to a harsh chemical condition, under acidic (H_2SO_4, pH = 1), basic (KOH, pH = 13), and oxidizing conditions (HNO_3). The ion concentrations of SO_4^{2-}, K^+ and NO_3^- were reduced to 0.4649, 6.41121, and 0.5434, mg L^{-1}, respectively, revealing remarkable efficiency in obtaining clean water even under harsh conditions (**Figure 5.13c**). Besides, the evaporation rate indicates that the fabricated Au nanolayer membrane possesses an excellent evaporation rate of 0.80 kg m^{-2} h^{-1} (under 0.1 M H_2SO_4), 0.85 kg m^{-2} h^{-1} (under 0.1 M KOH), and 0.85 kg m^{-2} h^{-1} (under 0.1 M HNO_3), which are close to the corresponding DI water 0.88 kg $m^{-2}h^{-1}$, suggesting its stable evaporation performances **(Figure 5.13d**). Additionally, the cycling stability was carried out for 5 cycles (1h test per 1 cycle). Ultimately, the results showed excellent reusability with stable performance (**Figure 5.13e)**. It could be deduced to three main reasons: (i) the chemical resistivity of the gold [83-85], (ii) the superior mechanical strength of the Au nanolayer-PTFE membrane, (iii) the strong adhesiveness and attachment of the thin layer Au on the PTFE

membrane. Therefore, it can be concluded that the fabricated gold membrane allowed efficient steam diffusion, minimized salt accumulation, and maintained membrane cycle stability under harsh environments.

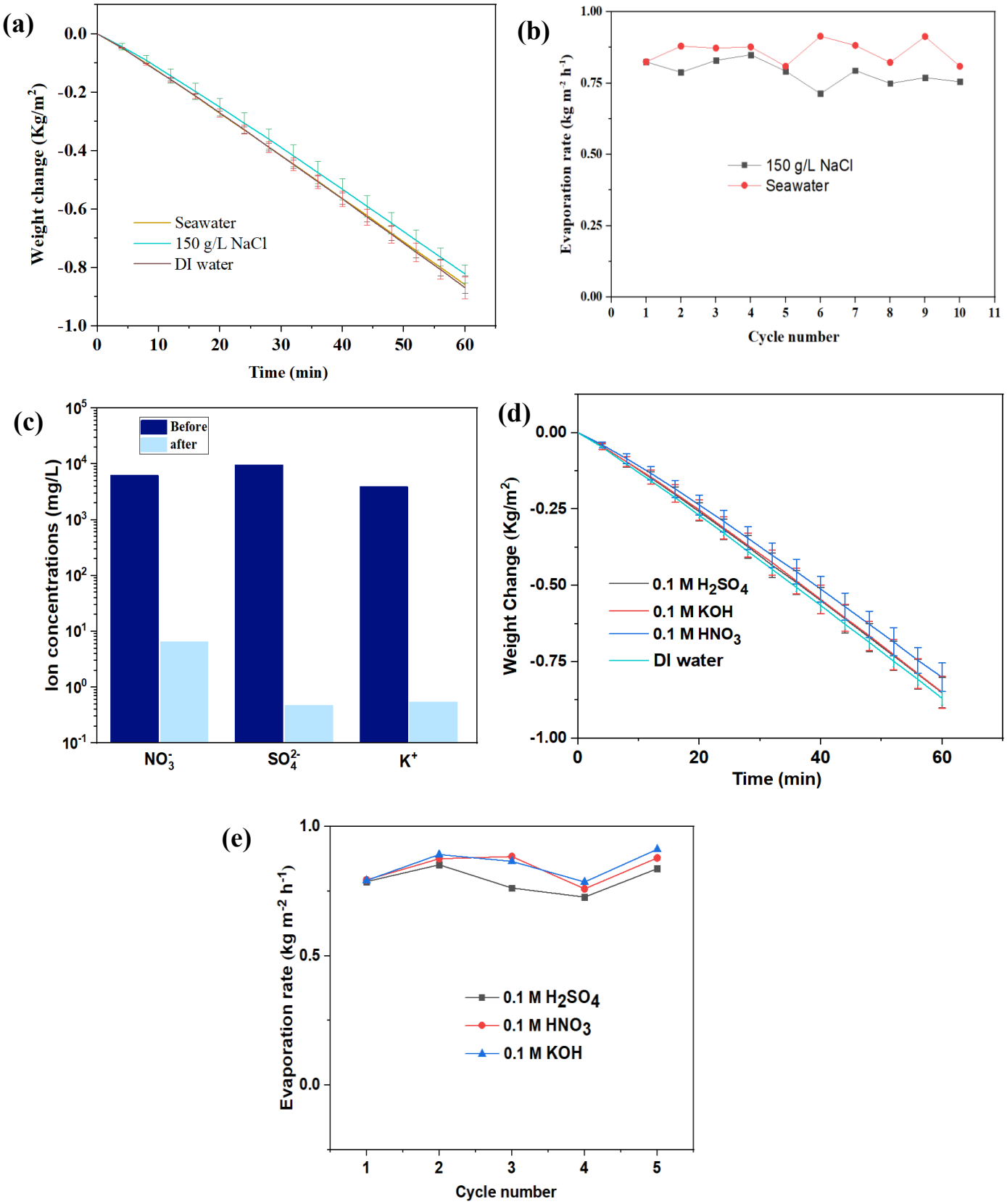

Figure 5.13 (a) Water evaporation rate of real seawater and high brine salinity (150g/L NaCl) compared to the DI water under solar irradiation of 1 sun. (b) Cycling performance of the Au nanolayer membrane using seawater, revealing stable evaporation rate for a period of 10 cycles.

(c) Ion concentrations (SO_4^{2-}, NO_3^-, and K^+) before and after the evaporation show the capability of Au nanolayer membrane for excellent ions rejections under a harsh environment. (d) Water evaporation rate of 0.1 M H_2SO_4, 0.1 M KOH, and 0.1 M HNO_3 compared to the DI water under the solar irradiation of 1 sun. (e) The cycling stability under acidic, basic and oxidizing conditions for five cycles.

5.4 Conclusion

This study demonstrates the feasibility of applying a magnetron sputtering method to fabricate a novel Au nanolayer membrane with robust mechanical strength and chemical stability for SWE applications. Detailed morphological, structural and material analysis techniques indicated that gold nanolayers were formed and homogeneously coated on the fiber of the PTFE membrane surface. The resultant Au nanolayer membranes achieved a water evaporation rate of 0.88 kg m^{-2} h^{-1}, which corresponds to an efficiency of 49.5 %, under 1-sun irradiation. Also, this system revealed a high rejection rate of salt ions of seawater with a removal efficiency of 99.9%, meeting the standard required for drinking water. Furthermore, the adhesiveness and the strong attachment of the thin film Au nanolayer on the membrane resulted in excellent durability and stability even under harsh conditions. Our proposed novel strategy may open up a new pathway for designing a highly stable nanolayer thin-film PTM for solar water purification.

CHAPTER 6

POLYDOPAMINE NANOSTRUCTURES DECORATED NICKEL FOAM TOWARDS EFFICIENT SOLAR WATER EVAPORATOR WITH ANTI-SALT PROPERTIES

This chapter is submitted in Renewable Energy. **Idris Ibrahim**, Sayed Mukit Hossain, Dong Han Seo, Andrew McDonagh, Ho Kyong Shon, Leonard Tijing*. Polydopamine nanostructures decorated a porous nickel foam toward efficient solar harvesting steam evaporator and anti-salt properties. Separation and Purification Technology. (2022): 121054.

6.1 Introduction

Recently, research efforts have focused on developing effective solar harvester PTMs with anti-salt properties [256-258]. Salt accumulation on the evaporator surface can block pore channels, causing a substantial reduction of effective surface area for solar absorption. Consequently, the water evaporation rate reduces significantly [38, 39, 259, 260].

Recently, PTMs with microporous structure and hydrophilic properties have been demonstrated as anti-salt PTMs and excellent solar thermal conversion materials. A number of substrate materials for PTMs have been studied, including porous ionic polymer [48, 189], biomass structural materials [165, 261], and porous metal foam. Among the reported materials, nickel foam (NF) has been well reported as an excellent substrate to grow versatile nano or microstructured materials [262]. It possesses a 3D porous structure with an open network and substantial surface functionality for growing different nano/microstructures materials [263]. These unique features make it highly desirable for an anti-salt and reusable solar evaporator system. To date, various NF-based materials have been reported including $CoWO_4$-x@NF [264], nickel sulfide@NF [265], graphene foam [185], graphene/MoO_3-x@NF [184], and Fe_2O_3/CNT@NF [266]. Although significant progress has been made from a material point of view, it will be a more practical idea to use a simple synthesis method to prepare NF-based PTM. Therefore, it is still of great significance to further explore novel PTMs that meet the above-mentioned criteria. Other studies have shown that bio-inspired polydopamine (PDA) is an effective PTM due to its advantages of simple synthesis methodology via *in situ* self-polymerization processes and a functionality to grow on various substrates [267-269]. PDA absorbs a broad spectrum of light due to the conjugated structure imparted by the indole-5,6-quinone units. The bonds between the 5,6-dihydroxyindole and indole-5,6 quinone units are considered to operate as electron donor and acceptor pairs, influencing the energy bandgap and light absorption properties [269-271].

Hence, in this work, we report a series of PDA nanostructures on porous nickel using a simple *in situ* synthesis method. The resultant materials exhibit excellent solar light absorption and efficient water transmission. A simple solar evaporator was fabricated, which contains cotton cloth as a 2D water transport channel to ensure a continuous water supply and cover on PS foam to act as a thermal insulator. The prepared evaporator displayed effective solar light absorption and solar-thermal conversion, with the continuous water pumping to PDA nanowires (NWs)-NF, resulting in an evaporation rate of 1.39±0.01 kg m^{-2} h^{-1} and an efficiency of 87.6 %, under 1 sun irradiation. The applications of the solar evaporator in solar seawater desalination were demonstrated with high salt rejection to obtain potable water which meets the World Health Organization (WHO) standard. Furthermore, the PDA NWs-NF displayed good reusability with stable performances for 3 days under real seawater and high brine salinity (75g/L NaCl). Finally, self-desalting capability was proven. This work demonstrated a novel, low-cost, stable, anti-salt solar evaporator system with a potential application for seawater desalination.

6.2 Experimental procedures

6.2.1 Materials

Nickel foam (Purity: 99.99%) was bought from MTI Corporation-USA. Dopamine hydrochloride (Purity: ≥ 99.0%) and Tris(hydroxymethyl)aminomethane (Tris-base) (Purity: ≥ 99.8%) were purchased from Sigma-Aldrich.

6.2.2 Synthesis methods of PDA on nickel foam

In this study, PDA nanostructures were synthesized using a modified methods from [268] to produce new and unique structural morphology. A piece of nickel foam (5 cm x 5 cm) was washed with distilled water, ethanol and immersed in 1 M HCl for 1 h to remove the oxide layer. The treated foam was then immersed in a solution (Tris-buffer pH 8.5) containing

dopamine (2 mg/mL), and the total amount of solution was 200 mL. Tris-buffer was prepared by dissolving 121.15 g/mol of Tris(hydroxymethyl)aminomethane in 1L of water, and the pH was adjusted to 8.5 by adding concentrated HCl. The solution was stirred for 2 and 6 h at ambient temperature. The as-prepared PDA nanostructures on NF were rinsed with distilled water and kept for further use. **Figure 6.1** illustrates the process of the formation of PDA nanoparticles (NPs) grown within the 2 hours reaction time. PDA nanowires (NWs) formed on NF surfaces after stirring for 6 hours.

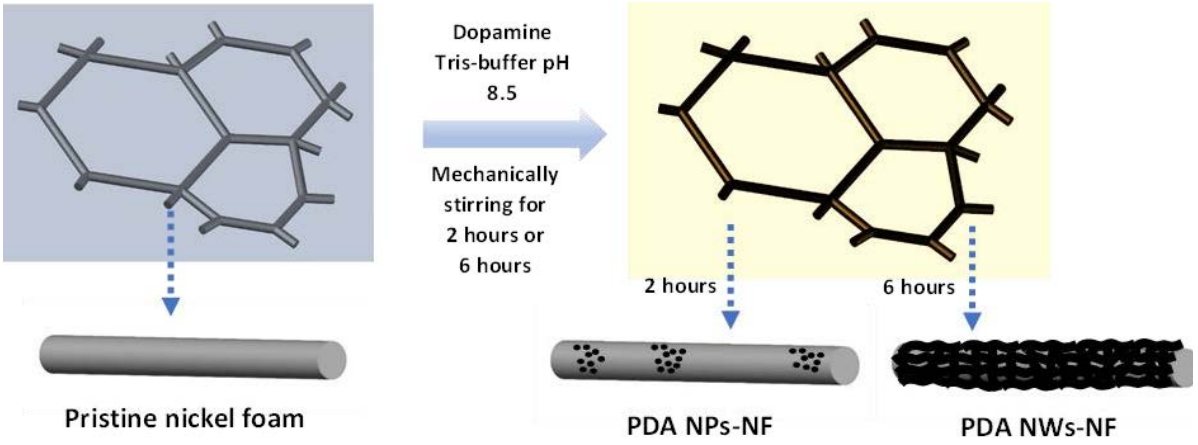

Figure 6.1 Schematic of the fabrication process of PDA nanoparticles and PDA nanowires (NWs) on NF.

6.2.3 Characterization

The surface morphology of polydopamine nanostructures on the NF surface was investigated using scanning electron microscopy SEM (Zeiss Supra 55-VP) at an accelerated voltage of 5 kV. The energy dispersive spectroscopy (EDS) and elemental mapping were measured using SEM (Zeiss EVO SEM) at 15 kV. The surface wettability of the samples was investigated by Theta Lite 100 (Attension) using a sessile drop method. The light absorption characteristics of the pristine nickel foam and prepared materials were measured using a spectrophotometer equipped with an integrating sphere (950 PerkinElmer Lambda) at wavelength range (300-2500 nm; Ultraviolet-Visible- Near-Infrared regions). The positively charged ions (K^+, Na^+, Mg^{2+}, and Ca^{2+}) concentrations of the condensate water were measured using an inductively coupled plasma mass spectrometer (Agilent 7900 ICP-MS). A Thermal Advantage SDT-Q600 thermal analyzer was used to obtain TG curve using alumina crucibles. Experiments were conducted using a flow of nitrogen gas (150 ml min^{-1}) and a heating rate of 10 °C min^{-1} over a temperature range of 25-500 °C.

6.2.4 Solar steam generation experiments

Solar water evaporation tests were conducted at ambient temperature (24 °C, humidity 60%) under solar irradiation of 1 sun. A solar simulator (Beijing perfect light) equipped with a filter (AM 1.5) was used to measure the irradiation of sunlight. Solar intensity meter was used to measure the sunlight irradiation. Solar evaporator composed of PDA nanostructure/NF was cut into a circular shape (Diameter ~ 3.4 cm) and was placed at the top of the cotton cloth (2D water channel) wrapped polystyrene foam (thermal insulator) in a beaker filled with 35 mL of Deionised water (DIW). Photo-image of the solar evaporator device is given in **Figure 6.2.** Upon sunlight irradiation on the solar evaporator, the weight change was measured using an electronic balance (Ohaus-IC-PX84/E) at an interval of 4 min and the total time of each test is 1 h (**See Figure 3.16).**

Figure 6.2 Photo-image of the designed PDA NWs driven solar evaporator.

6.2.5 Solar desalination test

The solar desalination performance was evaluated using seawater collected from Rose Bay Beach, Sydney, and similar protocols for SWE were followed. The seawater was filtered using a coarse filter, followed by a 5-micron bag filter, then treated with UV light before use. During solar desalination tests, the evaporated water was collected and analyzed using ICP-MS to measure the ions of the feedwater and the purified water. Furthermore, the cycling stability tests were carried out for 3 days and 5 cycles per day using seawater and simulated high brine solution of NaCl (at 75 g/L). Details on salt crystallization were performed using SEM and EDS analysis.

6.3 Results and discussions

6.3.1 Formations of PDA and morphological studies

Before the growing of PDA nanostructure on NF, the NF surface underwent a surface treatment to remove the oxide layer. Then, PDA was grown directly on the treated NF surface using a

straightforward process through the oxidation of dopamine using a Michael addition reaction [268]. During the reaction process, the color of the solution changed from light brown to dark brown which confirmed the oxidative polymerization of the DA to PDA [268], corresponding to an increase in amount and thickness of PDA on the NF [272]. The photographic images of the pristine NF, treated NF, and coated NF with PDA are given in **Figure 6.3**.

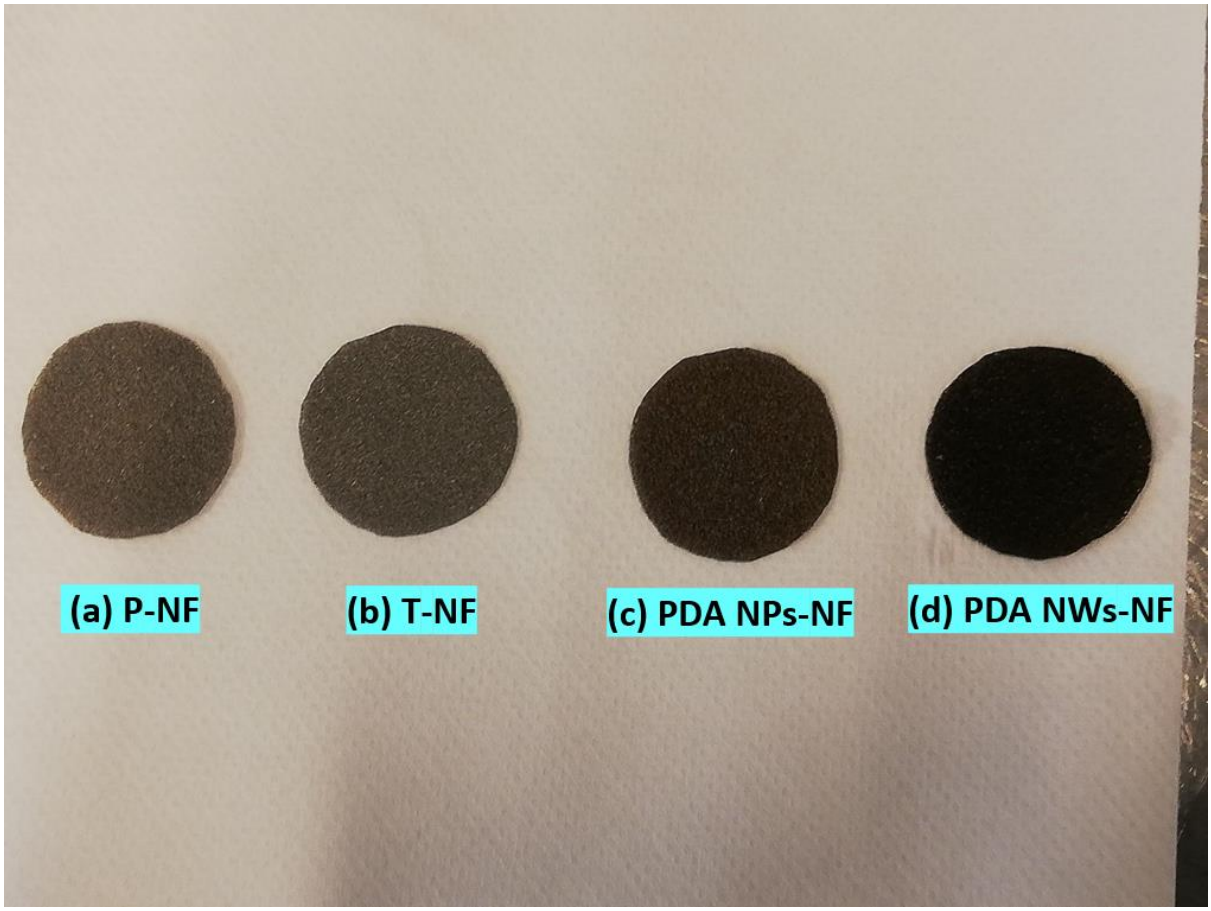

Figure 6.3 Photo-image of (a) Prsitine NF, (b) treated NF, (c) PDA-NPs-NF, and (d) PDA-NWs-NF

Figure 6.4 a,b shows the SEM images of the treated NF. After 2 h reaction, the SEM results confirmed the formation of PDA aggregated nanoparticles (NPs) with an average size of about 50 nm **(Figure 6.4 (c-e))**. After extending the reaction time to 6 h, the NPs on the surface self-assembled into NWs with hierarchical structures which were uniformly distributed on the surface of NF, as shown in **Figure 6.4 (f-h)**. Furthermore, the elemental percentages in PDA NWs-NF were higher than PDA NPs-NF. The elemental mapping of PDA NWs confirms the homogeneous distribution of C, N, and O, with more abundant on Ni foam (**Figure 6.5 b)**. Meanwhile C, N, and O within PDA NPs are less and inhomogeneously distributed, as shown in **Figure 6.5 a**. Additionally, the EDS analysis revealed the existence of the PDA elements (Ni, C, N, and O) on nickel foam (Ni). The elemental percentages of PDA NWs on NF were higher than PDA NPs on NF **(Figure 6.5 (c,d))**.

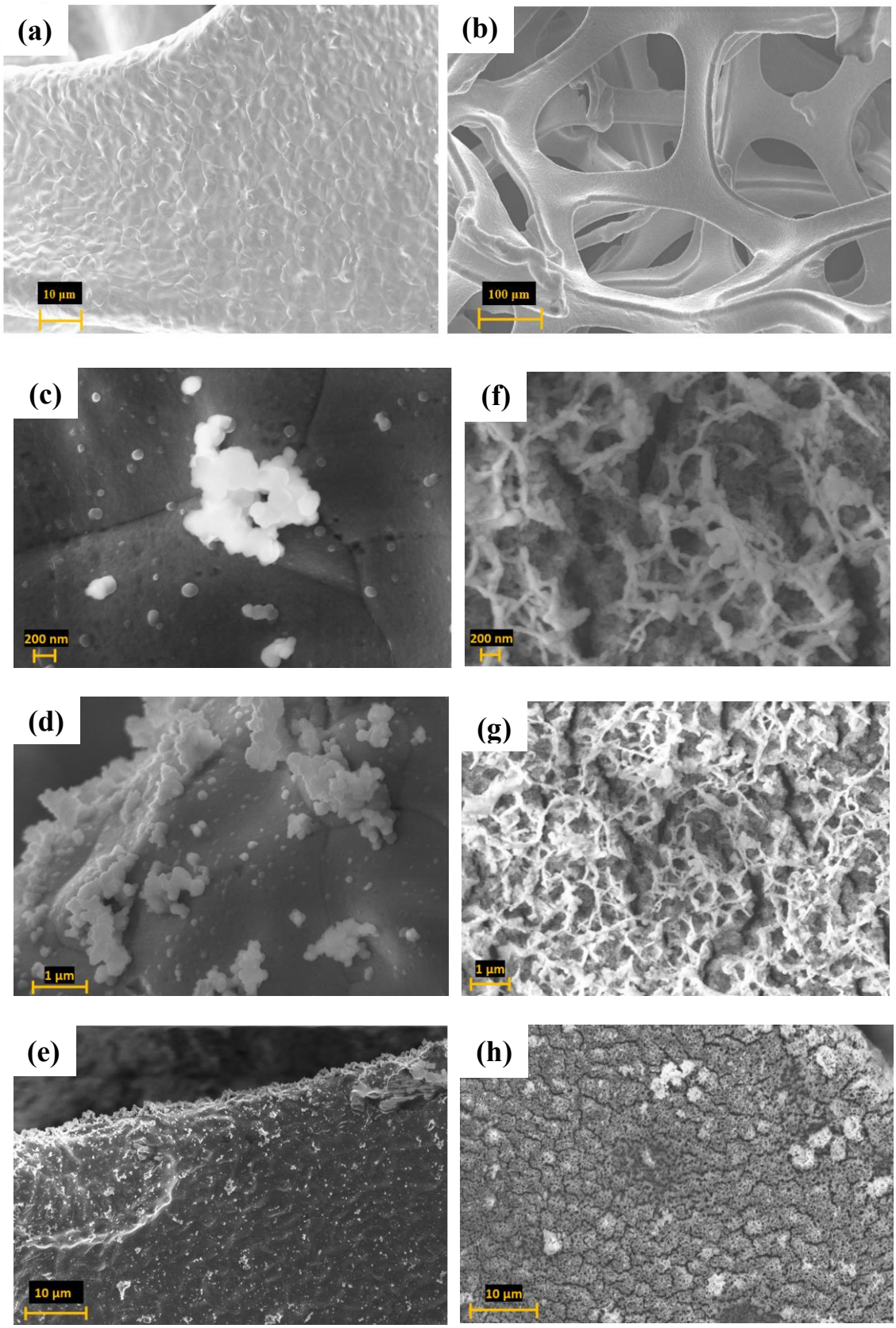

Figure 6.4 SEM images of (a,b) Treated Nickel foam (c-e) PDA NPs-NF. (f-h) PDA NWs-NF.

(a)

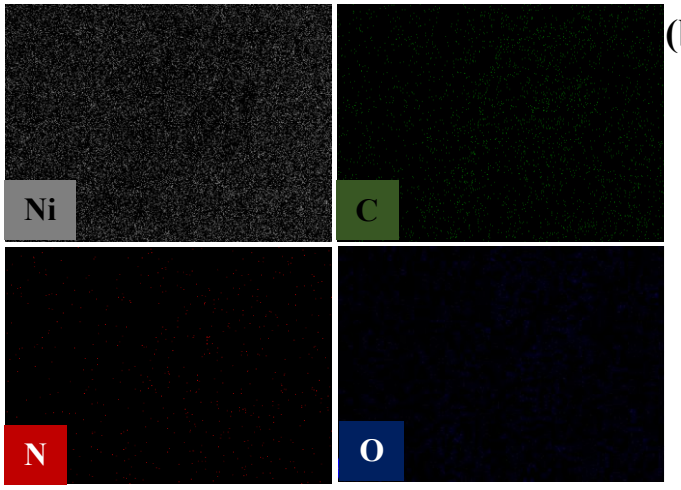

(b)

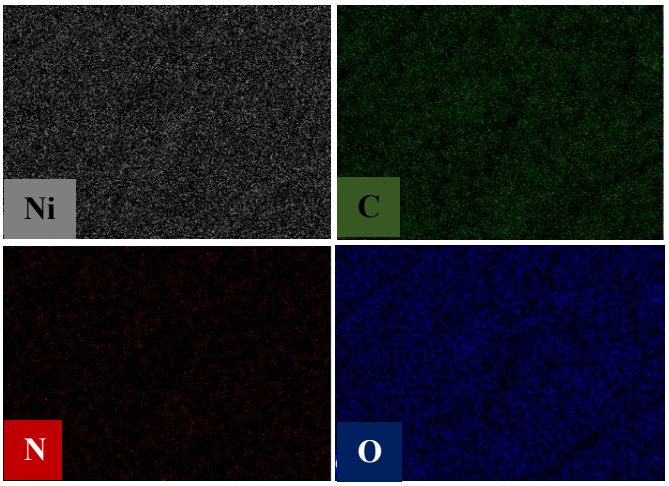

(c)

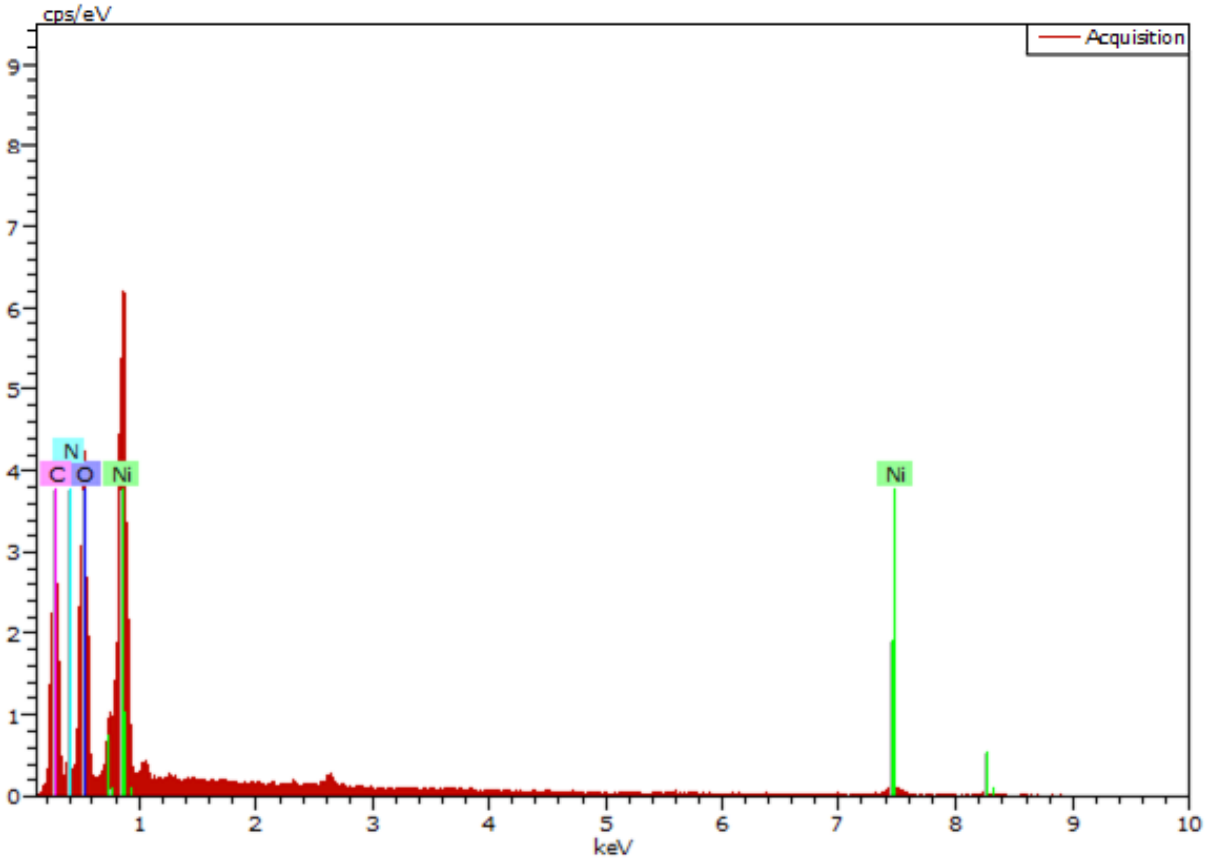

Spectrum: Acquisition

El	AN	Series	unn. C [wt.%]	norm. C [wt.%]	Atom. C [at.%]	Error (1 Sigma) [wt.%]
C	6	K-series	26.59	26.59	44.83	3.64
N	7	K-series	4.91	4.91	7.10	1.04
O	8	K-series	26.55	26.55	33.60	3.54
Ni	28	L-series	41.95	41.95	14.47	5.20
		Total:	100.00	100.00	100.00	

(d)

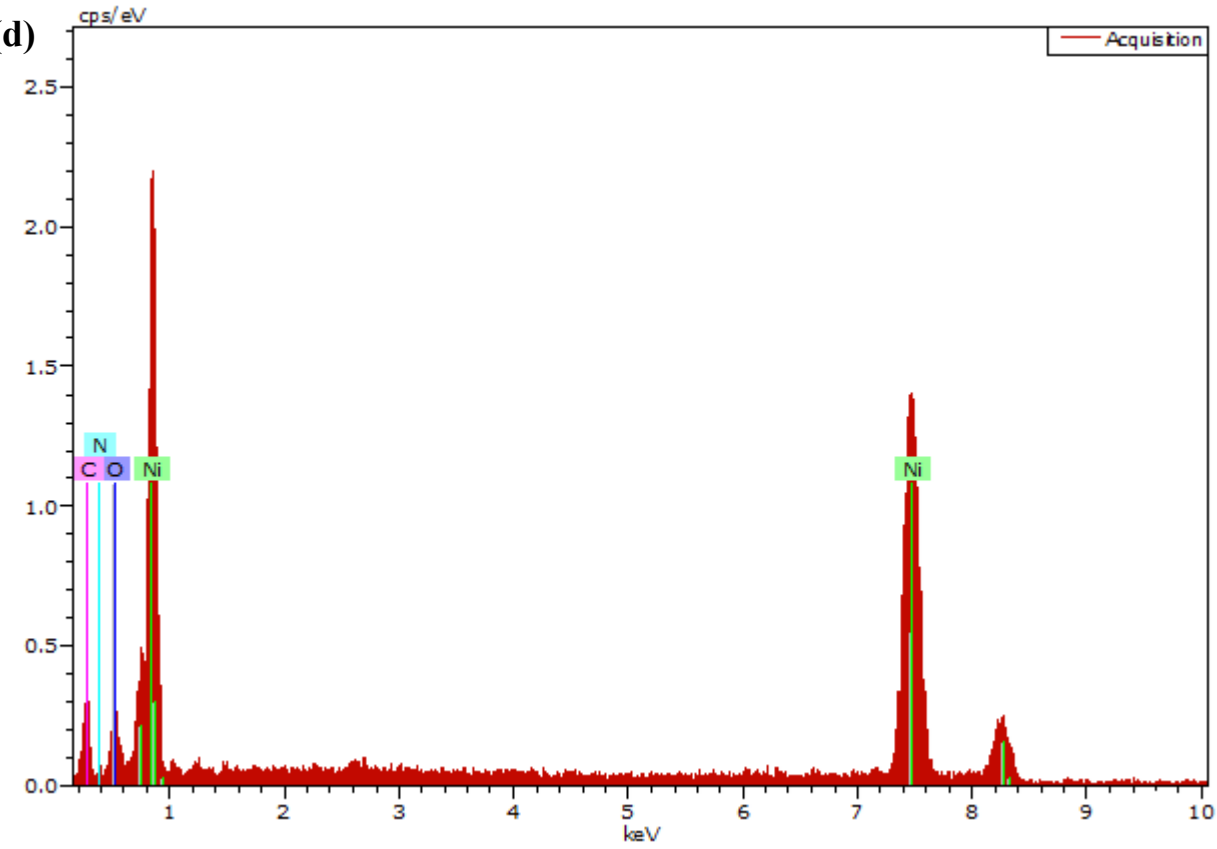

Spectrum: Acquisition

El	AN	Series	unn. C [wt.%]	norm. C [wt.%]	Atom. C [at.%]	Error (1 Sigma) [wt.%]
C	6	K-series	17.54	8.60	29.49	3.85
N	7	K-series	1.69	0.83	2.44	0.80
O	8	K-series	4.95	2.43	6.24	1.19
Ni	28	K-series	179.70	88.14	61.83	5.79
		Total:	203.87	100.00	100.00	

Figure 6.5 Elemental mapping of **(a)** PDA NPs-NF. **(b)** PDA NWs-NF EDS analysis of **(c)** PDA NWs-NF. **(d)** PDA NPs-NF

Thermogravimetric analysis (TGA) of PDA grown on NF substrate was performed from ambient temperature to 800 °C. As shown in **Figure 6.6**, the thermal loss curve displays multiple mass losses. Between 25 °C to 100 °C, the mass loss event is attributed to the removal of moisture on the surface. The curve for pristine NF was stable until 500 °C, and then it started rising owing to the conversion of pristine nickel to nickel oxide. Meanwhile, the coated NF with PDA showed a mass loss of ~ 3.08% and ~ 1.6% at 490 ºC for PDA NWs-NF and PDA NPs-NF, respectively. The higher percentage of decrease of PDA NWs is due to the higher concentration of PDA on the NF surface.

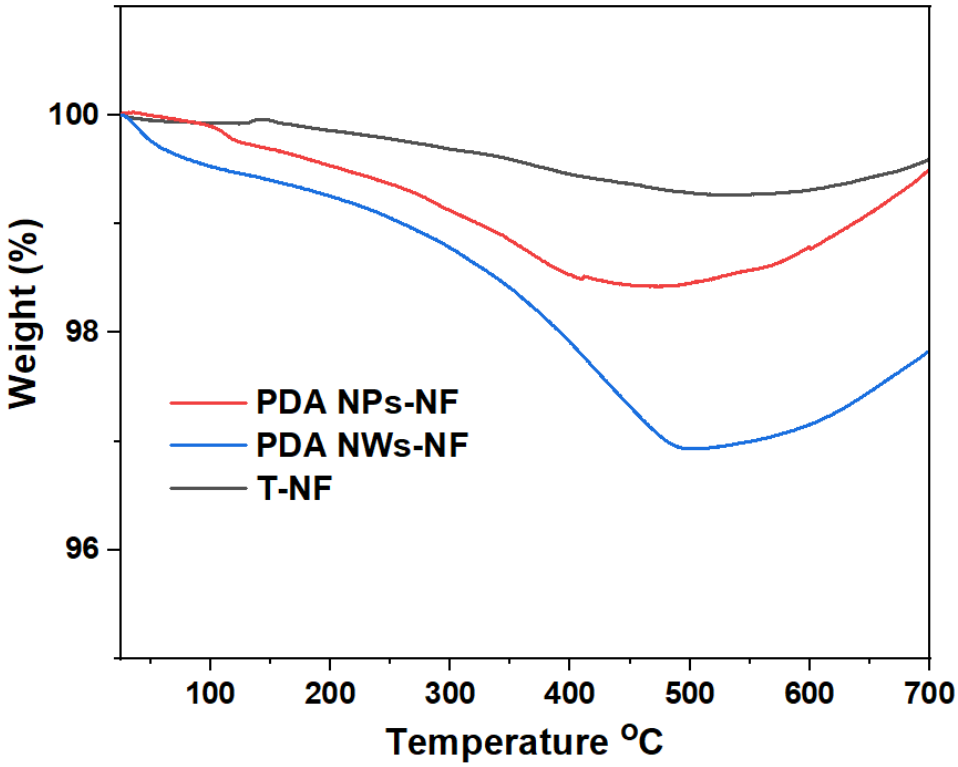

Figure 6.6 TGA analysis of NF, PDA NPs-NF and PDA NWs-NF.

6.3.2 Surface wettability and water transport

Surface wettability is an important criterion to ensure fast and effective water penetration and transportation within the structures of PTMs during the water evaporation test. A water contact angle of 131° was obtained for the pristine NF (**Figure 6.7 a)**. Upon surface treatment, the wettability was enhanced, and the water contact angle reduced to 113° **(Figure 6.7 b)**. The reduction in contact angle is attributed to the removal of the oxide layer from the NF surface. After the PDA coating process, the wettability changes from hydrophobic to superhydrophilic. Therefore, water penetrates and spreads rapidly within the surface within 1.38 s for PDA NPs-NF and 0.40 s for PDA NWs-NF **(Figure 6.7 c-d)**. This ultrafast water spreading is due to the hydrophilic hydroxyl-containing functional groups in PDA [273]. The water transport for PDA NWs-NF was faster than PDA NPs-NF due to the thicker PDA on the NF surface.

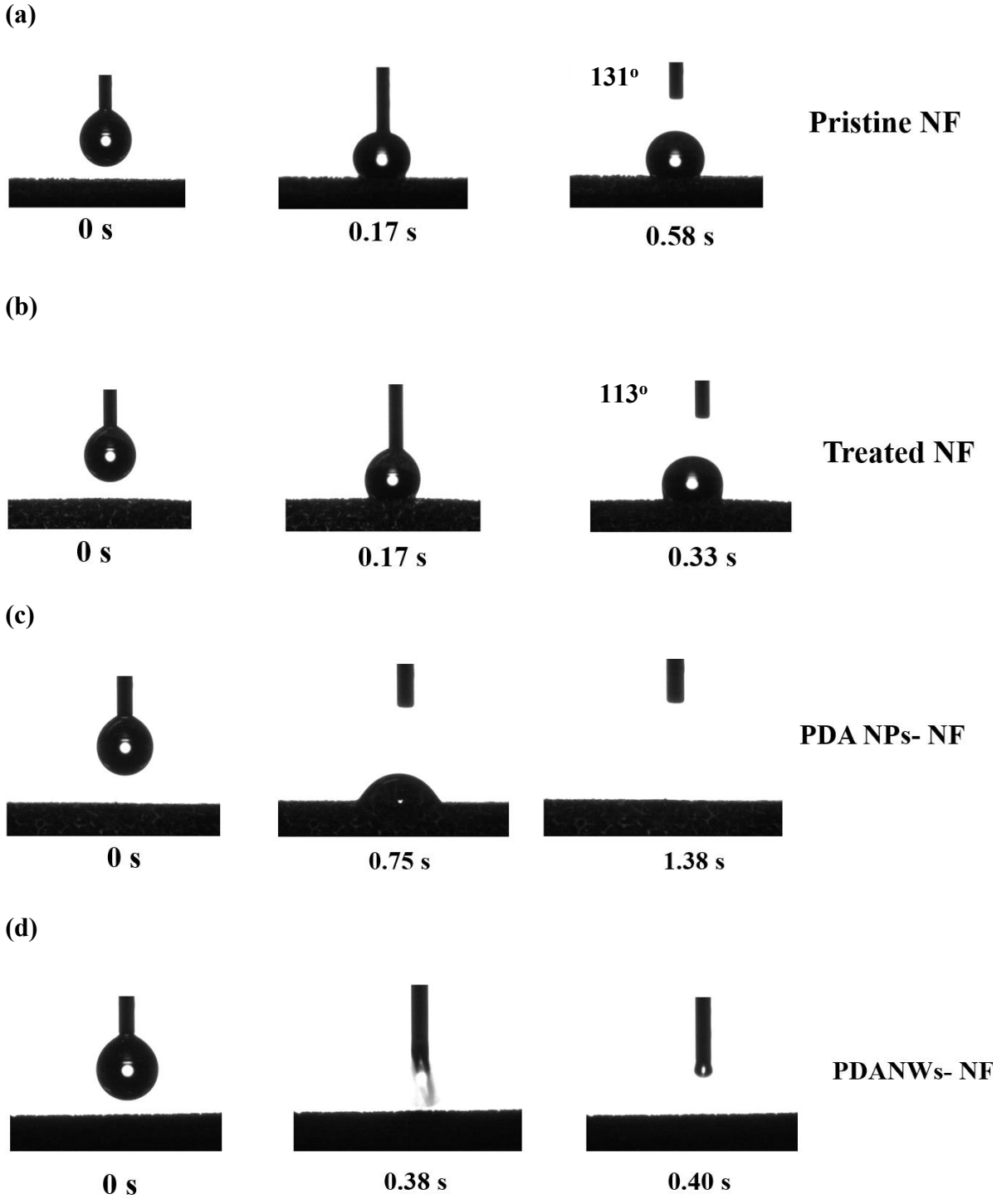

Figure 6.7 Contact angle measurement of; (a) P-NF, (b) T-NF, (c) PDA NPs-NF, and (d) PDA NWs -NF.

6.3.3 Solar-thermal-to-heat conversions

The ability of the PTMs to absorb solar light is essential for a highly efficient solar evaporator system [274]. We examined the light absorption in the dry state (**Figure 6.8 (a)**) and wet state (**Figure 6.8 (b)**) over a wavelength range covering the bulk of the solar spectrum (300-2500 nm), i.e., UV (300-600 nm), Vis (600-750 nm), and NIR (750-2500 nm). The optical absorption results clearly display the capability of NF and PDA coated NF to efficiently absorb the sunlight across the solar spectrum which is an important criterion for efficient solar-thermal conversion in solar water evaporation [274]. The superior light absorption is attributed to the high porosity and 3D interconnected structures of the foam yielding high light absorption through internal scattering and trapping that result in less reflection and transmittance [257, 275]. The pristine NF displays light absorption of ~68-73% at UV, ~56-73% at Vis, ~38-56% at NIR. In contrast, the treated NF shows better absorption capability ~73-77 % at UV, ~ 66-73% at Vis, 41-66% at NIR. The results for the pristine NF are consistent with previous investigations [183, 257, 276]. The light absorption was increased after coating NF with PDA NPs reaching ~85%, 76-85%, 52-76% at UV, Vis, and NIR regions, respectively. The improved absorption capability is attributed to the strong π-π interactions on PDA compounds [277]. The light absorptions can be further extended by increasing the thickness of PDA by forming hierarchical NWs on NF surface to finally reach ~90% at UV, ~90-88% at Vis, 59-88% at NIR. The formed porous hierarchical structures can help enhance light harvesting through multiple scattering [265]. Furthermore, light absorption was investigated at the wet state to validate the influence of the absorbed water on the light capturing ability, as the evaporation will take place under water [274]. Interestingly, the light absorption is further boosted at the wet state, mainly in the NIR regions, which could be attributed to the porous hydrophilic structures' capability to allow more water within the pores. Water replacing the air within the pores is well-known to further extend the light absorption capability in the NIR

regions [278]. To validate this, the untreated NF (hydrophobic) displayed lower light absorption compared to the treated NF. These trends in the optical performance are similar to our previous report [279] and other reported work [138, 159, 233]. The results demonstrate that the superhydrophilicity and high porosity structures are important factors for enhancing the light absorption characteristics, which is beneficial for solar-thermal conversion. A schematic illustration of the mechanism of absorption of our designed solar evaporator is provided in **Figure 6.8 (c)**.

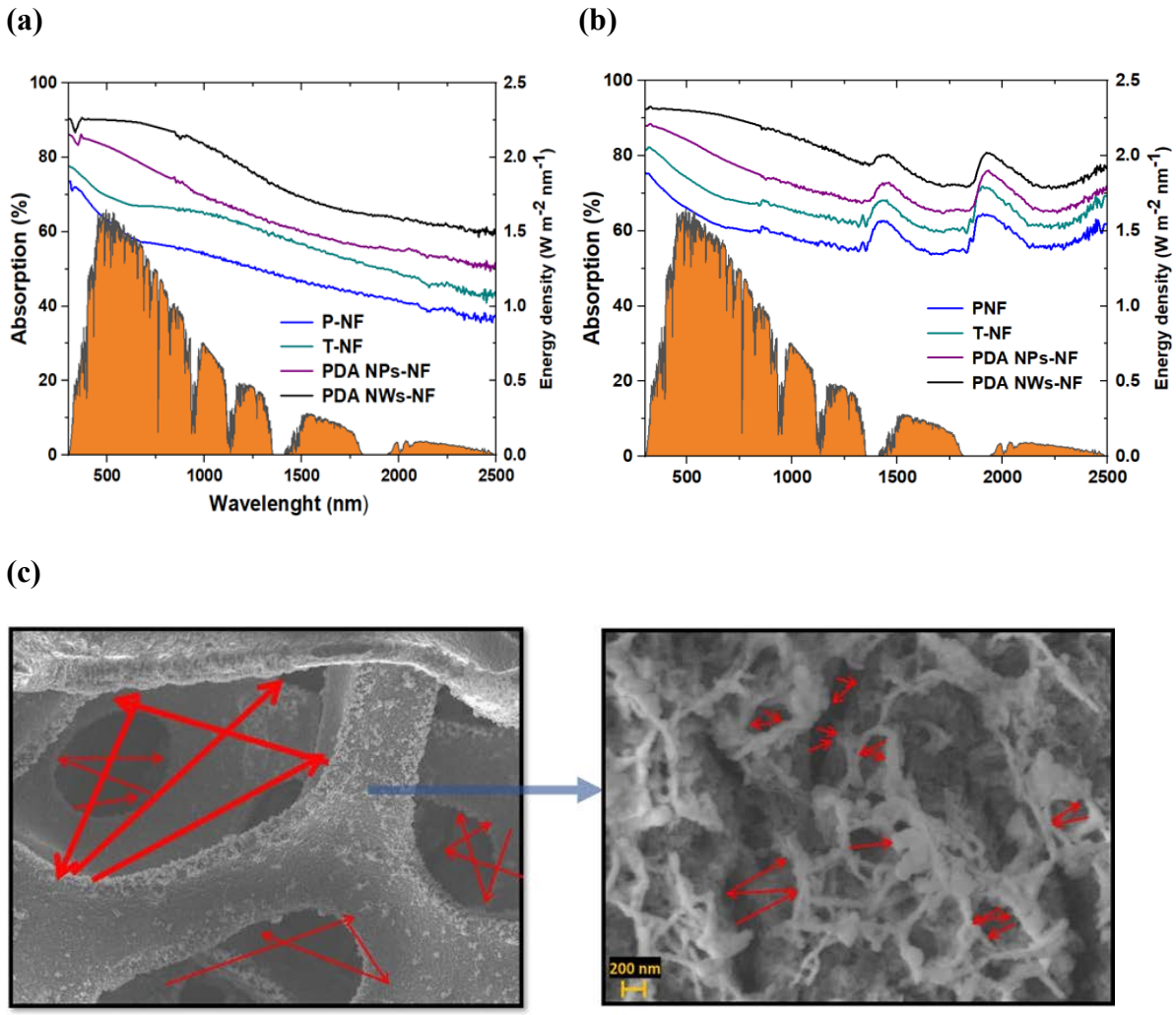

Figure 6.8 Light absorption in the UV–vis–NIR spectra (solar energy density spectrum (orange)) characteristics of NF substrates and after coating with PDA nanostructure in the dry state (a) and wet state (b) (c) SEM images showing the light reflection/scattering pathways between the pores of nickel foam (left image) and PDA nanowires on NF (right image).

A solar evaporator was constructed that was composed of a solar absorber (P-NF, T-NF, PDA NPs-NF, and PDA NWs-NF) on a top of thermal insulator PS foam wrapped with cotton cloth) as 2D water transport (see **Figure 6.9)**. The cotton cloth allowed fast water transport from the bulk water to the evaporator surface. Hydrophobic PS foam acts as a supporter and thermal insulator. The designed device allowed fast water transport and water vapor escape, while the heat is localized at the air/water interface resulting in efficient energy utilization and improved water evaporation performance.

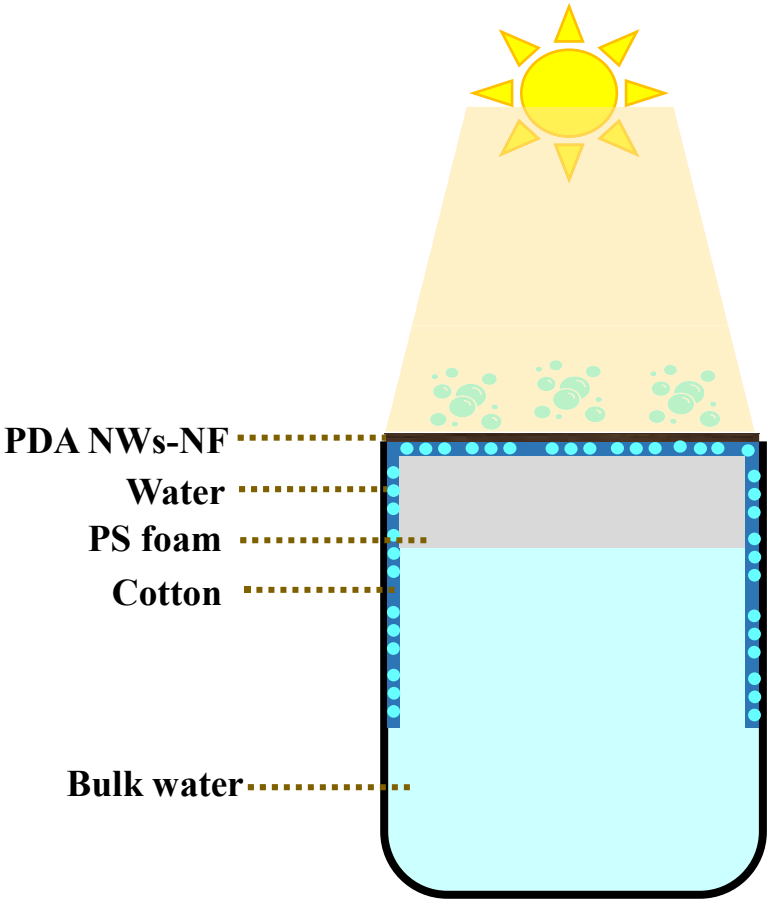

Figure 6.9 Schematic illustration of the designed solar evaporator system in this study.

An IR camera was used to investigate the solar-to-thermal conversion of the PTM and thermal insulation capability of the designed evaporator. Thermal images of the top surface were collected until it reached an equilibrium temperature within 900 s. The resultant PDA NWs-NF was compared to the PDA NPs-NF, T-NF, P-NF, and DIW. **Figure 6.10 (a,b)** show the

surface temperature of all samples rapidly increased within 4 min, then steadily stabilized after 10 min of solar illumination. In the case of the baseline DIW based evaporator, the surface temperature increased gradually from 23 to 25.7 °C within 15 min. In contrast, the surface temperature of our evaporators attained a temperature above 32 °C, which is sufficient to generate water vapor. This can be explained by the 3D interconnected porous structure of the NF which potentially results to localizing the heat in the evaporation area [257].

The surface temperature for P-NF and T-NF rose from 21.8 °C and 19.1 °C to 27.6 °C and 32.3 °C, respectively within 3 min, and goes up to 32.5 °C to 35.7 °C after 15 min. However, the coated NF with PDA displayed high solar-thermal conversion, and for the PDA NPs-NF and PDA NWs-NF, temperatures rose rapidly from 18.8 °C and 19.6 °C to 31.9 °C and 34.2 °C within 3 min and continued to increase to 36.1 °C and 39.5 °C within 15 min. The rapid photothermal response of PDA NWs-NF is 3.4 °C higher than PDA NPs-NF owing to the hierarchical nanowires structures resulting in more heat-trapping on the surface. This fast photothermal response is beneficial for reducing time for warming up the evaporator surface for vapor generation [280]. In contrast, the side-view of the PDA NWs-NF evaporator shows the interfacial heat localization at the top region and low surface temperature of the bulk water (Figure 6.10 c), which indicates good thermal insulation properties from PS foam resulting in localized heat at the top surface on the nanostructure PDA-NF surface [279]. Consequently, excellent solar-thermal conversion in a high-performance solar water evaporation system was achieved.

(a)

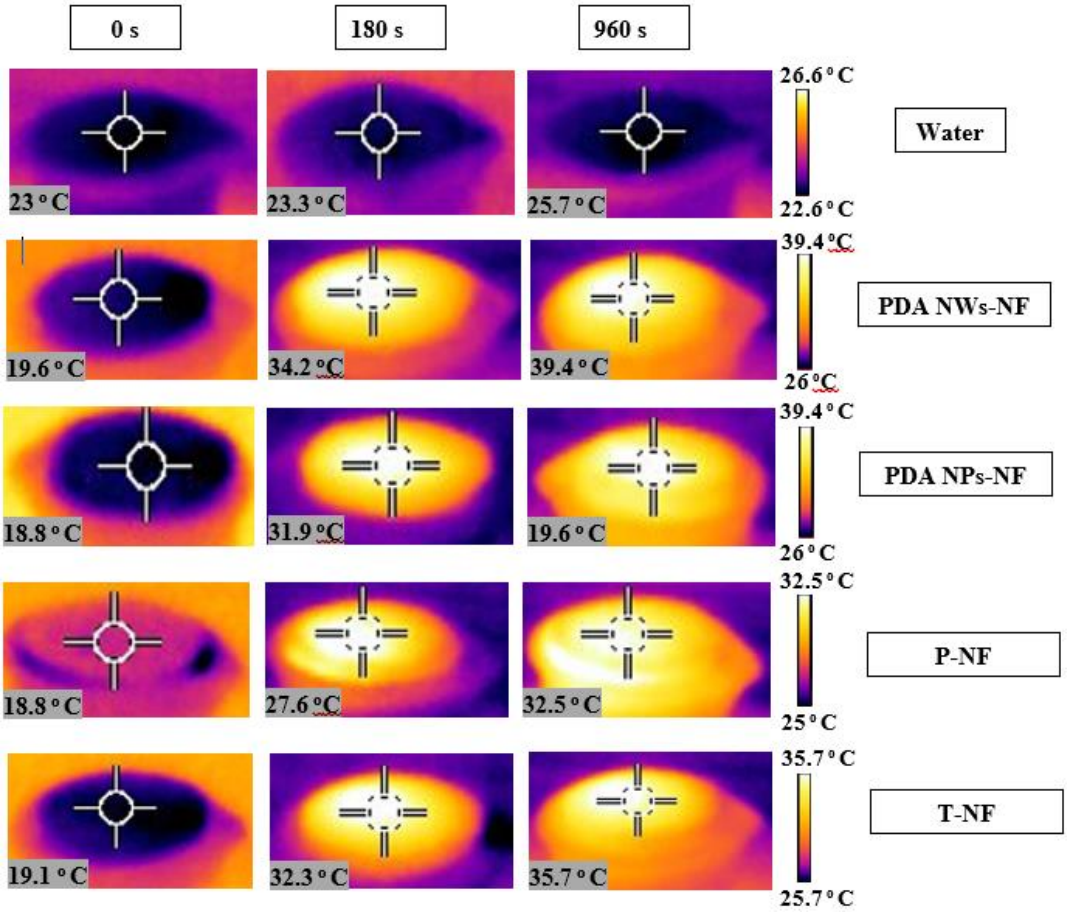
0 s
180 s
960 s
26.6 °C
22.6 °C
Water
23 °C
23.3 °C
25.7 °C
39.4 °C
26 °C
PDA NWs-NF
19.6 °C
34.2 °C
39.4 °C
39.4 °C
26 °C
PDA NPs-NF
18.8 °C
31.9 °C
19.6 °C
32.5 °C
25 °C
P-NF
18.8 °C
27.6 °C
32.5 °C
35.7 °C
25.7 °C
T-NF
19.1 °C
32.3 °C
35.7 °C

(b)

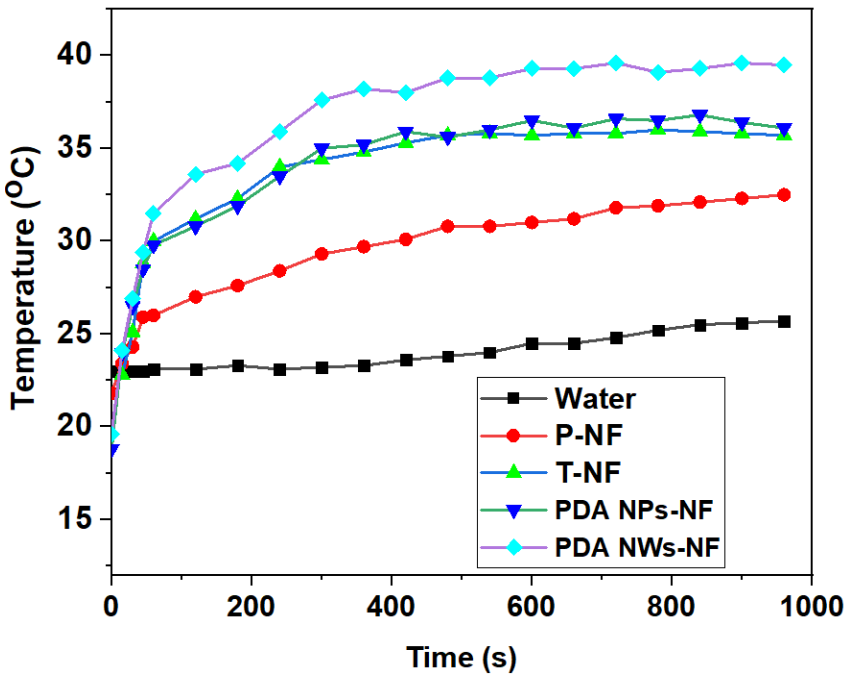
Temperature (°C)
Time (s)
40
35
30
25
20
15
0
200
400
600
800
1000
Water
P-NF
T-NF
PDA NPs-NF
PDA NWs-NF

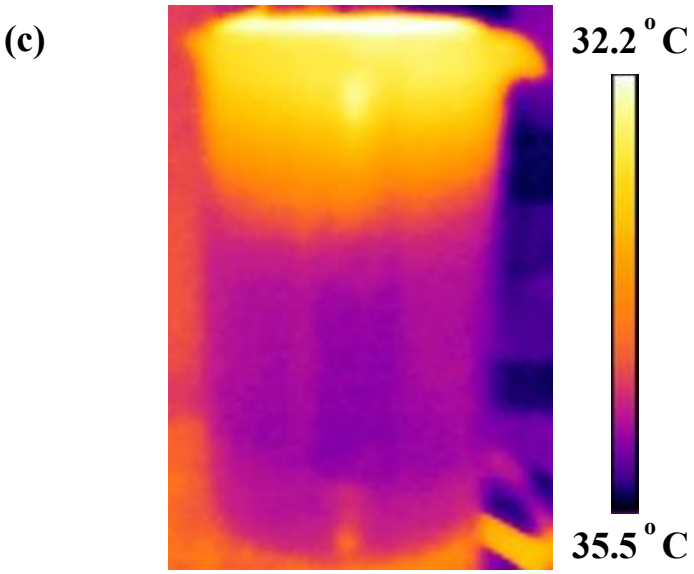

Figure 6.10 Light absorption and heat conversion characteristics of NF substrates and after coating with PDA nanostructure. (a) IR images revealed the effectiveness of PDA nanostructure-based solar evaporator in localizing heat at the air-water interface. (b) The temperature profile of heat conversion with respect to time. (c) Side photo of NWs PDA-NF-based solar evaporator system upon sunlight irradiation for 15 minutes.

6.3.4 Water evaporations performances

Water evaporations performances were evaluated under one sun irradiation and the mass change was recorded at 4 min intervals with a duration of 1 h for each test. The evaporation rate at the dark condition was subtracted before calculating the efficiency**.**

Figure 6.11 a, b show the mass loss, water evaporation rate, and calculated efficiency data results. The data show that the DIW-based evaporator has a low evaporation rate of 0.33 kg m^{-2} h^{-1}, corresponding to an efficiency of 14.4%. Our interfacial solar evaporator-based P-NF and T-NF displayed water evaporation rates of 0.79±0.11 kg m^{-2} h^{-1} and 0.92±0.02 kg m^{-2} h^{-1}, with efficiencies of 43.5% and 52.9%, respectively. The higher evaporation rate of T-NF is attributed to the enhanced surface wettability that enabled fast water transportation during

evaporation. The trends seen here also reflect those of the optical data. After coating NF with PDA NPs, the water evaporation rate was further enhanced to achieve evaporation of 1.27±0.03 kg m^{-2} h^{-1} and an efficiency of 75.9%. PDA NWs-NF showed an evaporation rate of 1.39±0.01 kg m^{-2} h^{-1}, and an efficiency of 83.3%, about 4.2 times higher than DIW. The increase in water evaporation rate of PDA NWs-NF could be attributed to the following four features:

a) The superhydrophilicity of the PDA acted as water transporter and solar-thermal converter.
b) The larger quantity of PDA NWs-NF resulted in high capability of solar-thermal conversion and faster water supply compared to the lower PDA content in PDA NPs on NF.
c) The 3D microstructures of the NF resulted in more water penetration within the pores, as a result, more water surface was available.
d) The presence of PS foam and cotton cloth led to excellent heat localization at the air/water interface and caused adequate water supply.

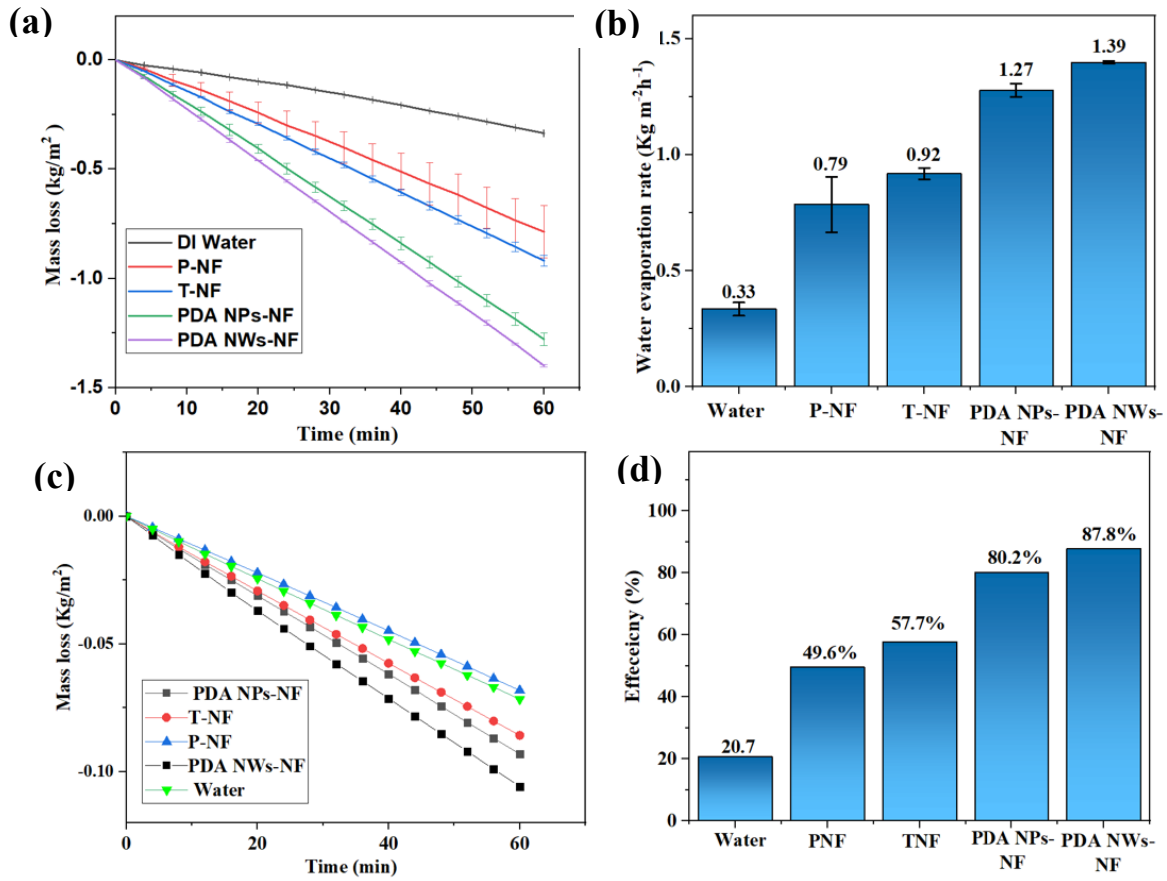

Figure 6.11 Water evaporation performances DI water, P-NF, T-NF, PDA NPs-NF, PDA NWs-NF. (a) Mass loss with respect to time (min) under 1 sun irradiation (1 kW m^{-2}). (b) Water evaporation rate under 1 sun irradiation (1 kW m^{-2}) (kg m^{-2} h^{-1}). (c) Water evaporation rate under dark conditions. (d) Water evaporation efficiency (%).

6.3.5 Solar seawater desalination

Solar desalination performance was assessed using natural seawater. For water condensation and collection performance, a purpose-built device was used (**Figure 6.12 a).** The salt ion rejections of the primary salt ions (Na^+, Mg^{2+}, Ca^{2+}, and K^+) were quantified before and after the desalination test using an ICP-MS instrument. The salt ions were significantly reduced to below 2 mg/L for seawater (**Figure 6.12 (b**)). The obtained results were far below the World Health Organization (WHO) [214] and the US Environmental Protection Agency (EPA) [281].

Hence, our designed PDA NWs-NF based evaporator displays excellent capability in salt ion rejection to produce drinking-quality water.

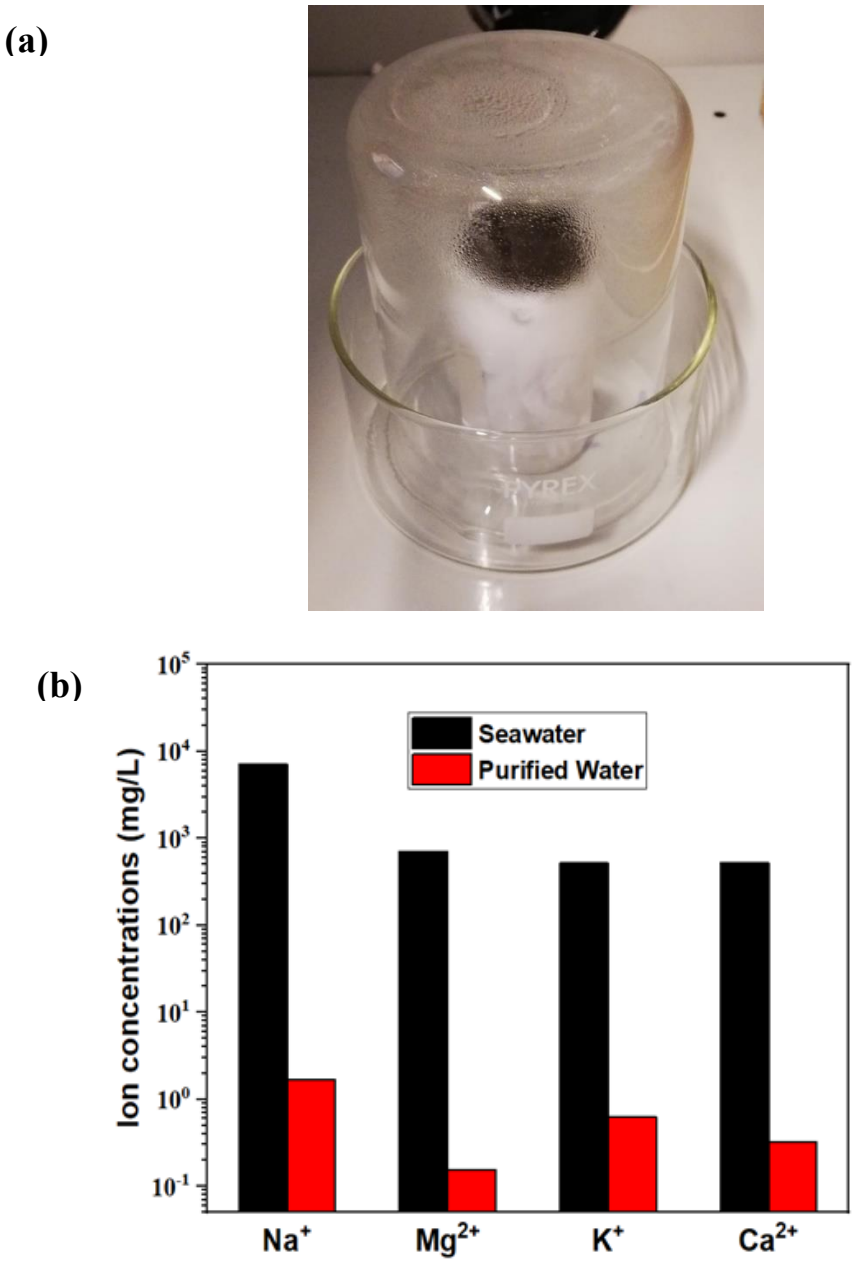

Figure 6.12 (a) Home-made device of PDA NWs-NF based evaporator for water collections. (b) ICP-MS analysis of the primary salt ion concentrations (Na^+, Mg^{2+}, Ca^{2+} and K^+) before and after solar desalination using PDA NWs-NF based evaporator.

6.3.6 Reusability and stability tests

The long-term stability and reusability of PTMs is considered vital for practical applications in solar-driven seawater desalination [38, 39]. Salt crystallization on the solar evaporation surface lowers solar-thermal conversion efficiency of PTMs, hence lowering evaporation rates and hindering practical application [282]. In this study, durability and stability tests were conducted using two types of saline water including real seawater and high salinity brine (75 g/L NaCl). Surface morphology and elemental composition of PDA NWs-NF based evaporator were further investigated after 3 days using SEM and EDS analysis. The durability and stability tests were investigated under one sun irradiation. Tests were carried out for 3 days, with 5 cycles per day (1 h/cycle); after each day, the evaporator was left overnight under dark conditions. The calculated water evaporation results displayed a rate of 1.38 kg m^{-2} h^{-1} and 1.32 kg m^{-2} h^{-1}, for seawater and high brine solution (75 g/L NaCl), respectively, which are closer to 1.39±0.01 kg m^{-2} h^{-1} of DIW.

The durability test using seawater revealed a stable performance during day 1 and 2, with very slight increase on the third day (**Figure 6.13**). Moreover, after the third day, SEM analysis revealed some salts crystalized and accumulated between PDA NWs on the NF surface, which was confirmed by EDS to be Na, Cl. Mg, Ca, Cl, and S, O, corresponding to the formation of NaCl, $MgSO_4$, $MgCl_2$, $CaCl_2$, and Na_2SO_4 on the surface **Figure 6.14 (a-c)**. Then, salt formed on PDA NWs-NF was cleaned by soaking in DIW for a period of 9 h at ambient temperature. As seen by SEM analysis, the salts were removed and the PDA NWs remained intact on the NF surface **Figure 6.15 (a-b)**. Furthermore, the EDS analysis confirmed negligible sodium and chloride content, revealing the high removal efficiency of salt crystals from PDA NWs-NF surface **Figure 6.15 (c)**.

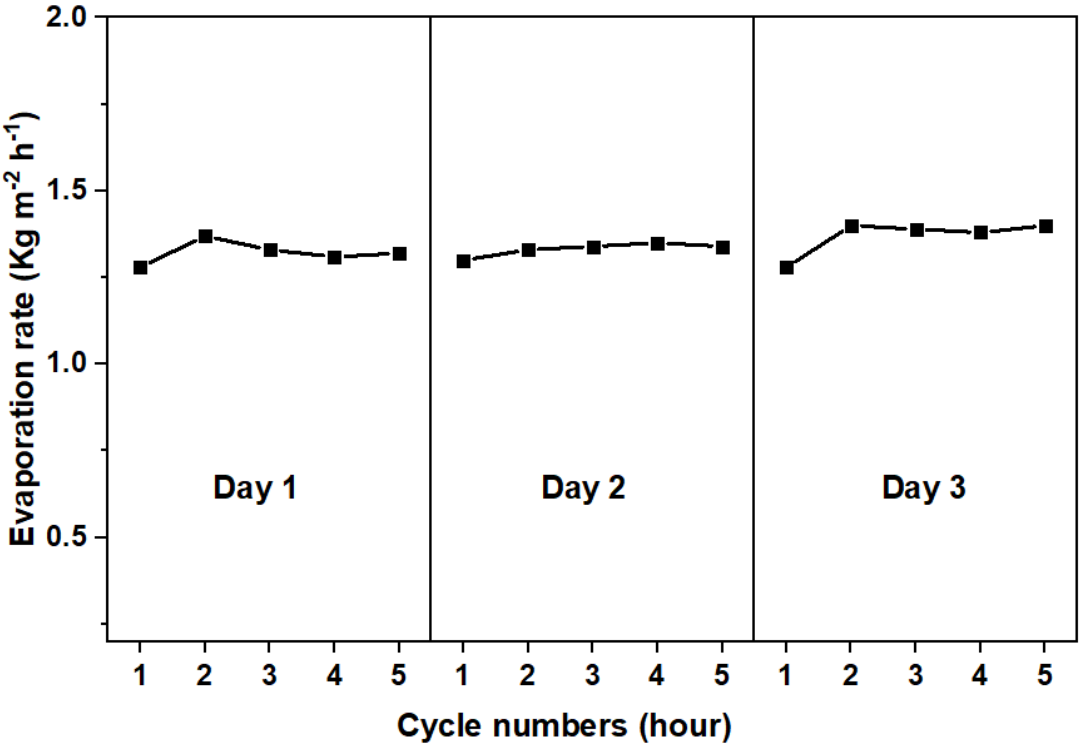

Figure 6.13 Cycling stability of PDA NWs-NF based evaporator. The evaporation rate during a static-continuous light irradiation for 3 days under real seawater.

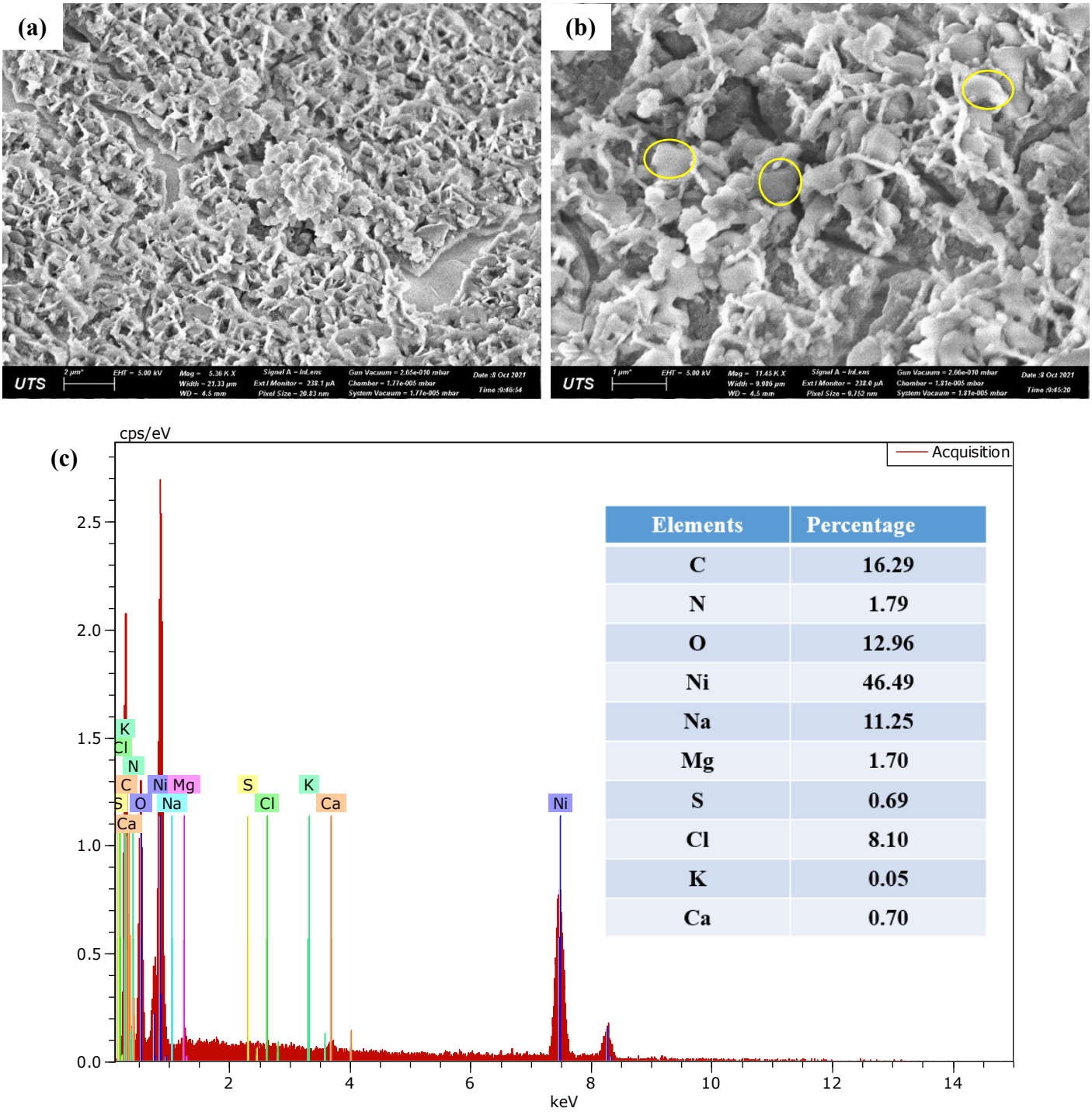

Elements	Percentage
C	16.29
N	1.79
O	12.96
Ni	46.49
Na	11.25
Mg	1.70
S	0.69
Cl	8.10
K	0.05
Ca	0.70

Figure 6.14 (a-b) SEM images of PDA NWs-NF, after 3 Days solar desalination test using a real seawater. (c) Corresponding EDS analysis.

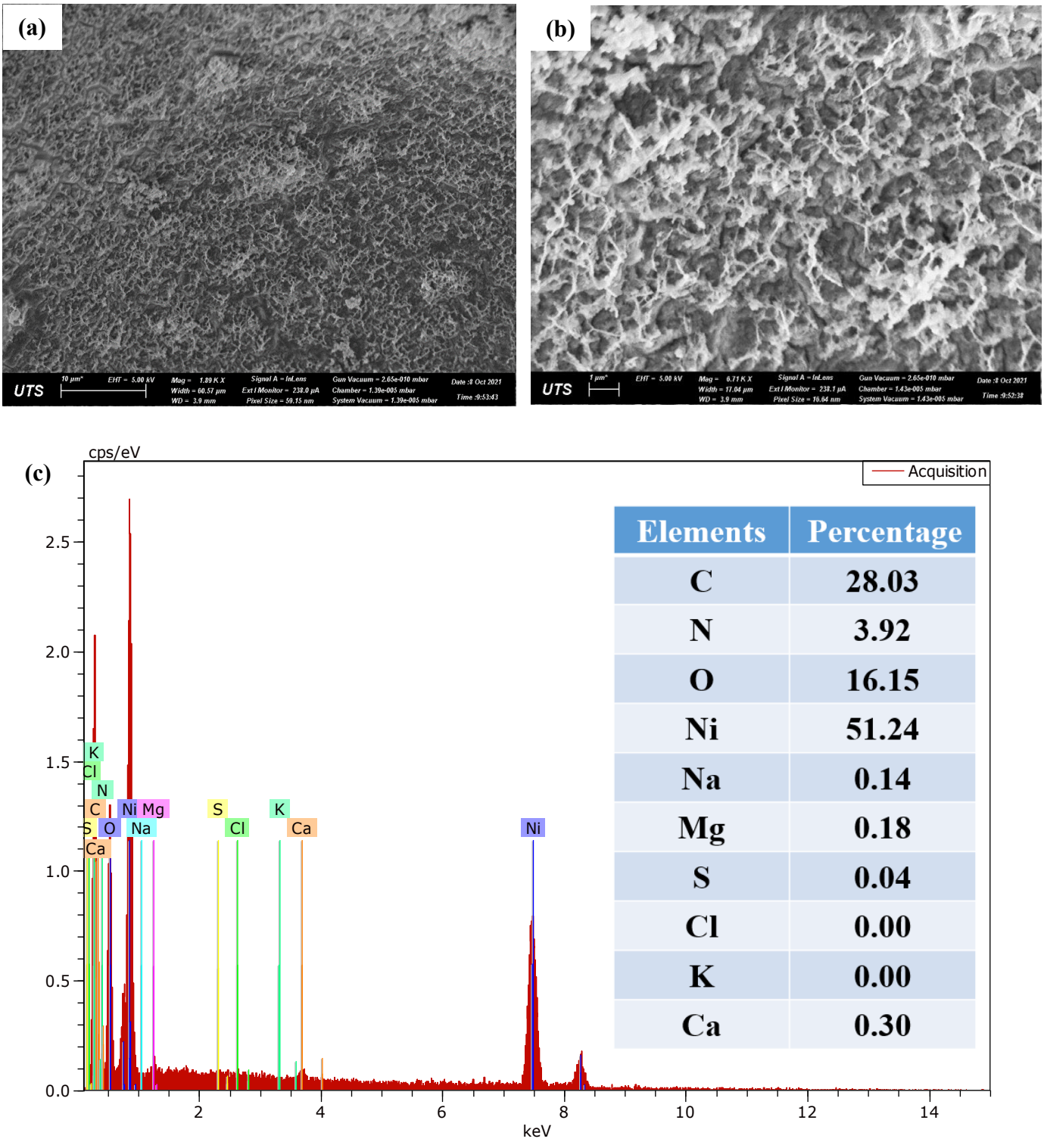

Elements	Percentage
C	28.03
N	3.92
O	16.15
Ni	51.24
Na	0.14
Mg	0.18
S	0.04
Cl	0.00
K	0.00
Ca	0.30

Figure 6.15 (a,b) SEM images of NF-PDA NWs after washing by soaking in DIW for 9 hours, after 3 Days solar desalination test using a real seawater. (c) Corresponding EDS analysis.

In contrast, the high salinity solution (75 g/L NaCl) displayed different trends; the evaporation was stable for day one and then started slightly to decrease on day 2 and then day 3 to reach an evaporation rate of 1.31 kg m^{-2} h^{-1} **Figure 6.16**. The SEM images further confirmed the presence of large NaCl crystals on the PDA NWs-NF while some parts contained the PDA NWs on the NF surface **Figure 6.17 (a-d)**. Salt was removed from the PDA NWs-NF surface by soaking it in DIW for 9 h at ambient temperature. Notably, it can be seen from the SEM images that no salt on the PDA NWs-NF surface and the PDA NWs remain almost confined on the NF surface **Figure 6.18 (a-b)**. Furthermore, EDS analysis confirmed negligible sodium and chloride content, revealing the high removal efficiency of NaCl crystal from PDA NWs-NF surface **Figure 6.18 (c)**.

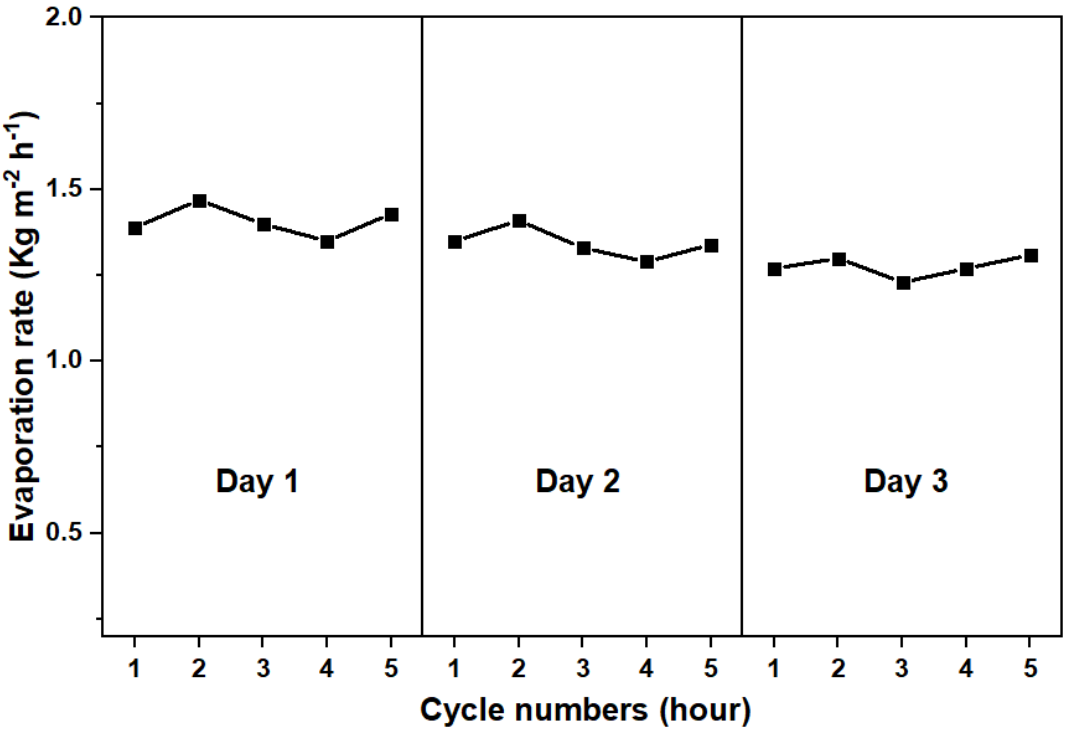

Figure 6.16 Cycling stability of PDA NWs-NF based evaporator. The evaporation rate during a static-continuous light irradiation for 3 days under high saline brine (75 g NaCl/L).

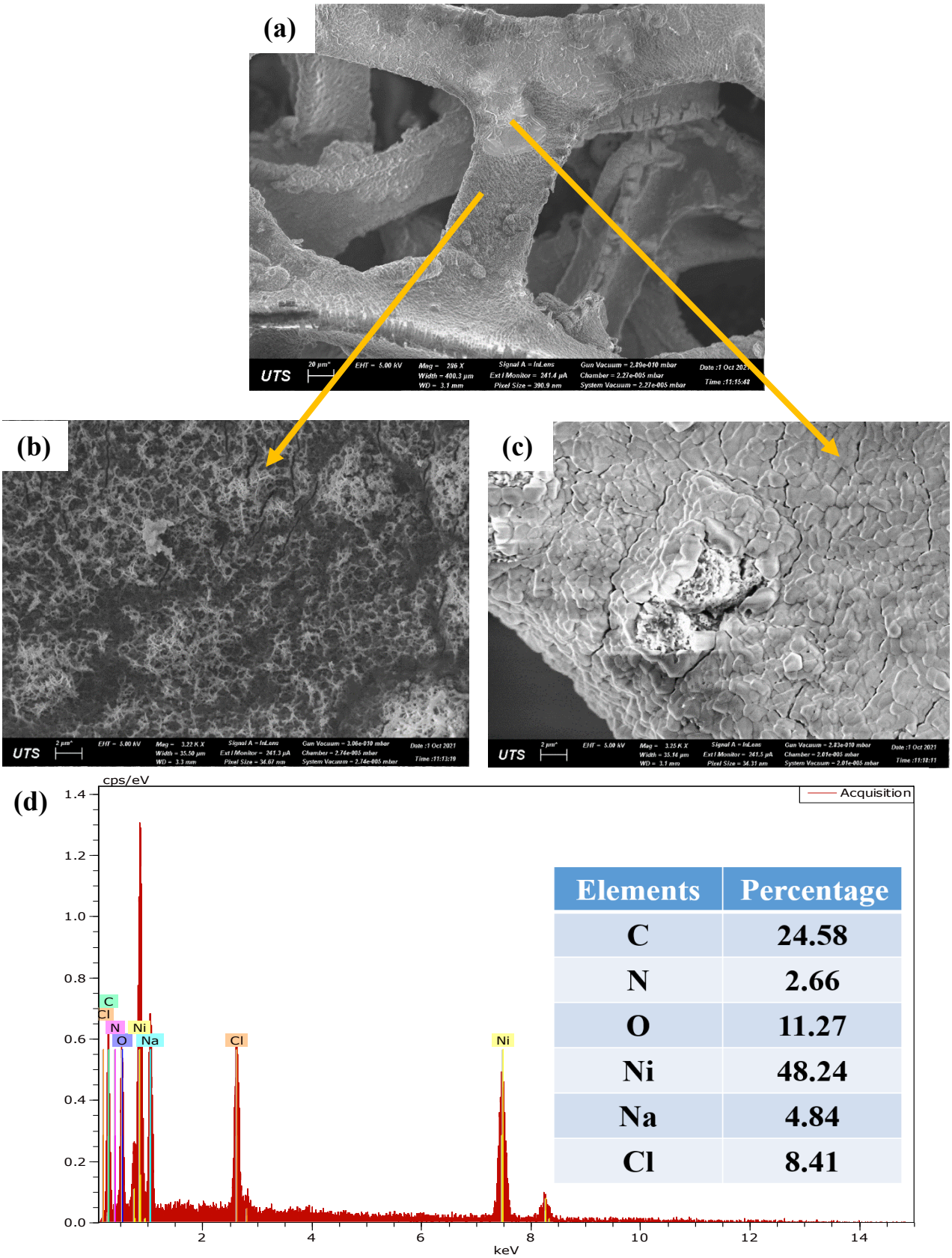

Elements	Percentage
C	24.58
N	2.66
O	11.27
Ni	48.24
Na	4.84
Cl	8.41

Figure 6.17 (a-c) SEM images of NF-PDA NWs, after 3 Days solar desalination test using (highly brine solution (75 g/L NaCl). (d) Corresponding EDS analysis.

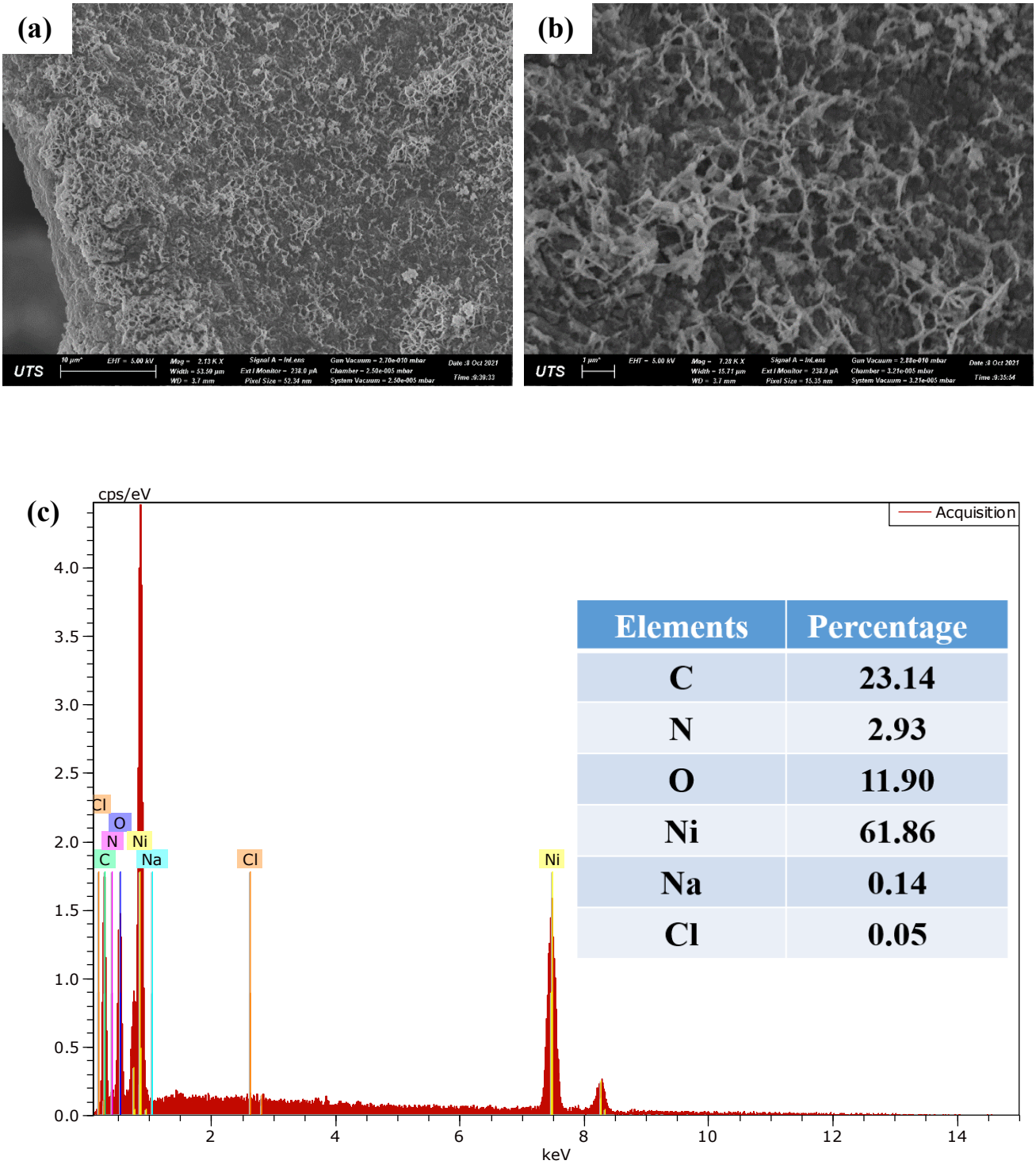

Figure 6.18 (a,b) SEM images of NF-PDA NWs after washing by soaking in DIW for 9 hours, after 3 Days solar desalination test using highly brine solution (75 g/L NaCl). (c) Corresponding EDS analysis.

The good reusability results, and excellent self-cleaning properties are attributed to; (1) the large number of hydroxyl and carboxyl groups in PDA, which absorb the water rapidly through its superhydrophilicity, leading to fast salt dissolving [283], (2) the weak adhesion between the salt crystals and PDA NWs on NF [284], and (3) the 3D porous interconnected structure of NF provides more spaces so that the concentrated and diluted brine in the pores can spontaneously form convection and diffusion. Overall, our solar evaporator displayed good salt resistance making it potentially applicable for solar seawater desalination.

6.3.7 Self-cleaning properties

The self-cleaning properties were conducted to examine the self-desalting capability of our proposed NWs PDA-NF based solar evaporator. During the test, 1 g of NaCl was placed on the NWs PDA-NF surface, and real seawater was used as a feed. The test was performed under sunlight (one sun) and dark conditions. After placing the salt at the top of NWs PDA-NF surface, the salts started to dissolve within 15 s. This could be mainly attributed to the superhydrophilicity of NWs PDA-NF, resulting in a fast water supply. Under dark conditions, most of the salt disappeared within 170 min, until no salt was realized on the surface after 270 min (**Figure 18 a**). Upon sunlight irradiation, the salt started gradually to dissolve, penetrate and diffuse within the pores of the substrate. Finally, no salt was noticed on the surface after 50 min (**Figure 18 B**). The obtained results were compared to the control sample TNF (without PDA). The amount of NaCl on the NF surface did not change much under dark conditions or sunlight (**Figure 18 c,d**). This is mainly derived from the surface hydrophobicity which reduce the water supply from the bottom surface. Besides, the absence of the coated solar absorber PDA resulting in low-solar thermal conversions and hence, low water evaporations and vapor escaping. After the self-cleaning test, the water evaporation rate was conducted to investigate the material cability for solar steam generation. Then, an evaporation rate of 1.39 kg m^{-2} h^{-1} was obtained, similar to the initial water evaporation value. The above mentioned observations

revealed the important of PDA for achieving good self-cleaning properties for solar driven seawater desalinations.

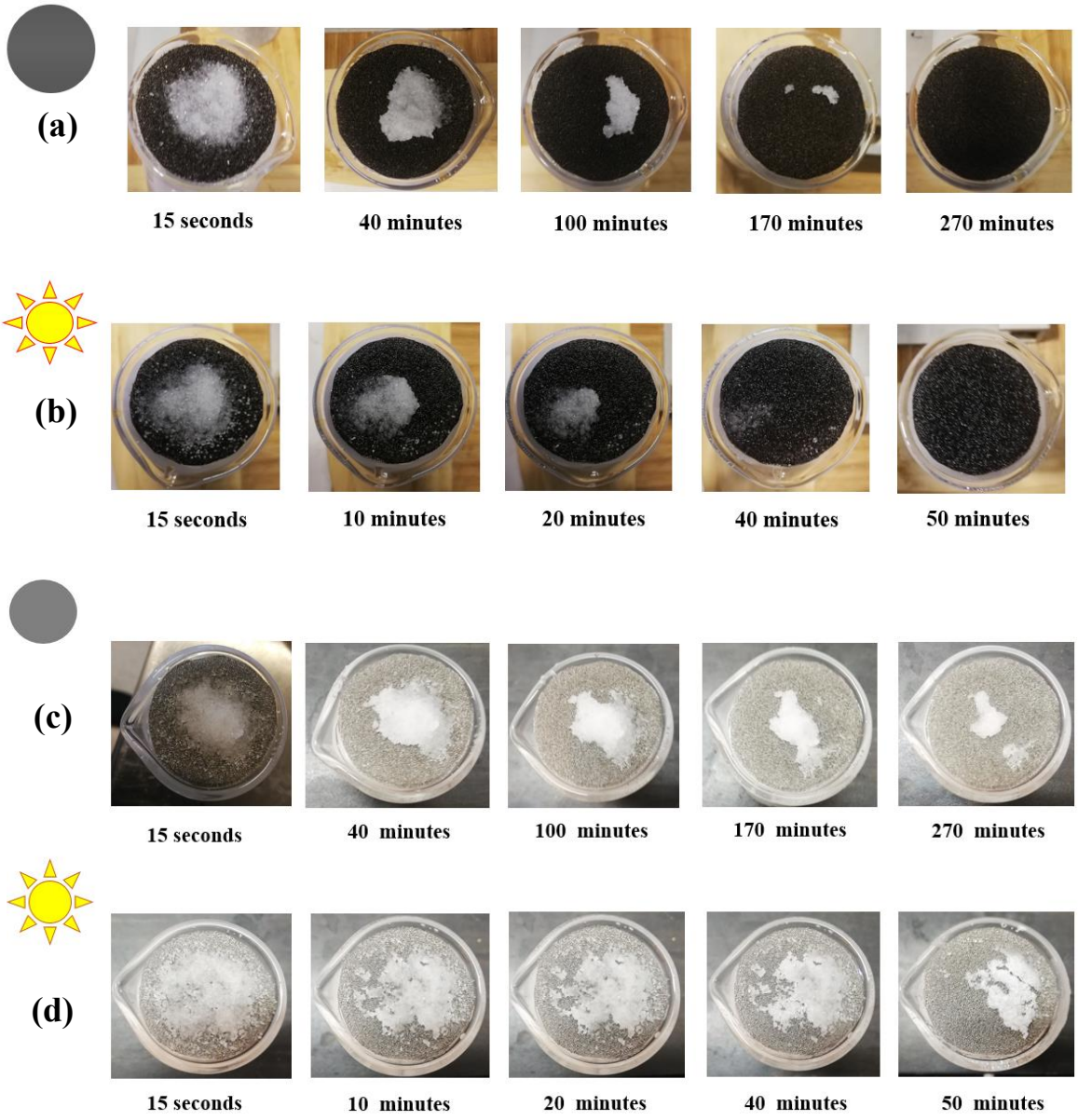

Figure 6.19 Self-cleaning properties of; PDA NWs-NF (a) at dark condition (without sunlight), (b) under one sun irradiation. Treated NF (c) at dark conditions (without sunlight). (d) Under one sun irradiation.

6.4 Conclusion

PDA NWs-NF were prepared using a straightforward and scalable *in situ* oxidative polymerization. Our work explored the superior hydrophilicity and the perks of interconnected surfaces of the 3D porous hierarchical PDA NWs. By taking advantage of the aforementioned features, excellent solar absorption capability covering the whole solar spectrum region and efficient photothermal conversion was demonstrated. PDA NWs-NF based evaporator confirms a remarkable water evaporation rate of 1.39±0.01 kg m^{-2} h^{-1} and efficiency of 87.2%, which could be achieved under one sun irradiation. Moreover, PDA NWs-NF based evaporators display excellent salt ion rejection meeting the standard required for drinking water. Notably, by taking advantage of the thicker PDA containing hydrophilic hydroxyl groups, exceptional durability and stability could be obtained using real seawater and high brine salinity. Even after 3 days (5 cycles/day), the evaporation performance was not much deviated from the initial evaporation performance. Additionally, the small amount of salt formed on the surface during desalination can be simply re-washed by immersing in DIW. The salt resistance of our designed materials could be attributed to the weak adhesion of salts on the PDA-NF surface. Besides, the self-desalting capability can be realized through chemical advection and diffusion. The aforementioned attributes suggested the effectiveness of our proposed PDA NWs-NF in seawater desalination. Our proposed approach is simple and scalable for fabricating large-scale solar evaporators for both portable solar devices for solar-driven seawater purification.

CHAPTER 7

TANNIC ACID DERIVED MULTIFUNCTIONAL HYDROGEL FOR HIGHLY EFFICIENT SOLAR STEAM GENERATION

This chapter is under review in Desalination: **Idris Ibrahim**, Qiang Fu, Andrew McDonagh, Tim Foster, Ho Kyong Shon, Leonard Tijing*. Tannic acid derived multifunctional hydrogel for highly efficient solar evaporator system. (Under review in Desalination).

7.1 Introduction

Hydrogel-derived ISSG have been recognized as a promising system to achieve a massive water evaporation rate beyond 2 kg m^{-2} h^{-1} [118, 285]. This was ascribed to their merits of three-dimensional highly porous structures which retain a large amount of water within the structure [46, 126, 218]. These features provides a solar evaporator with a good light absorption and effective heat localization. Moreover, the interior structures allow the diffusion of water internally and on the external surface, making an excellent anti-salt, reusable and stable solar desalination device [286]. Recent research findings revealed that a PVA-based hydrogel is one of the promising PTMs for highly efficient solar steam generator, due to its advantages of superhydrophilicity and good mechanical stability [125, 287]. Despite the above mentioned features, PVA-derived hydrogel displays a significant drawback of dense structures, resulting to low intermediated bond water, hence low water vaporization [125, 288]. To address this, the inclusion multiple hydroxyl groups can effectively form hydrogen bonding through a suitable cross-linker [289, 290]. Tannic acid (TA) is a naturally occurring polyphenol compound that exists widely in various plants and can be extracted easily, attracting academic and industrial interest [291-293]. TA possess several advantages which make it an excellent cross-linker that can be highlighted into three main points. Firstly, it is known that TA is a consist of multiple phenolic functionalities enabling it to interact with various materials and can act as a cross-linker through cross-linked macromolecules by hydrogen bonds, ionic bonds, coordination bonds and hydrophobic bonds [294]. Secondly, multiple hydroxyl functional groups in TA molecules provide coordinating sites for metal ions such as Fe^{3+}, hence resulting in cross-linked metal-phenolic networks. Thirdly, the resultant metal phenolic complex (TA-Fe^{3+}) possesses can turn the color to a black and led to a strong solar light absorption characteristics [295]. Fourthly and lastly, the carboxyl groups on tannic acid on the trivalent Fe^{3+} formed an ionic coordination bond. This resulted in a dynamic increase in the crosslink

density of the hydrogel. The ionic coordination displays a high binding affinity between Fe^{3+} and carboxylic functional groups in the hydrogels crosslinking [296]. It plays a vital role in enhancing the mechanical properties of the hydrogels [297, 298].

Herein, we used a low-cost, and straightforward process to fabricate a PVA@TA-Fe^{3+} hydrogel for SSG applications. TA-Fe^{3+} metal coordination with dual functions of ionic cross-linker and help transform the hydrogel to PTMs. The structural properties of the prepared hydrogel display highly porous structures. The intrinsic structural porosity resulted in efficient solar light harvesting and solar-thermal conversion capability. As a consequence, a water evaporation rate of 2.35±0.11 kg m^{-2} h^{-1} with an efficiency of 94.6 % was obtained at one sun irradiation. Moreover, a superior anti-salt property was realized with good durability and stable performance under natural seawater and high salinity brine solution (75g/L NaCl). The synergetic effect due to structural porosity of PVA@TA-Fe (*x*%) resulted in a high-water evaporation performance making it a promising for the practical applications in solar seawater desalinations.

7.2 Experimental method

7.2.1 Materials

Tannic acid was purchased from Riedel-de Haen. Iron(II) sulfate hydrate ($FeSO_4.7H_2O$) was purchased form Merck. Polyvinylalcohol (PVA) (M_w = 8.5 X 10^4-12.4, X 10^4, 87-89% hydrolyzed) was purchased form sigma Aldrich. All the reagents were used as received. Commercial cellulose sponge was obtained from Coles Supermarket.

7.2.2 Synthesis of hydrogel materials

In this work, we modified an existing method to fabricate PVA/TA hydrogel which resulted to an improved the morphology [299, 300]. First, a polyvinylalcohol (PVA) aqueous solution was prepared by dissolving 10 g of PVA powder into 100 mL deionized water under stirring at

~90°C for ~ 3 hours (solution A). Tannic acid was dissolved in deionized water under sonication to afford TA solution with different concentrations: 2, 3, and 5 wt% (Solution B). 30 mL of solution A and 20 mL of solution B were mixed under stirring. Then, 20 mL of iron sulfate ($FeSO_4$) solution (5 wt%) was added. The colour of the mixture changed from light brown to black and the mixture was left for another 2 hours. Thereafter, the resultant black hydrogel was soaked in water before being subjected to three freeze-thaw cycles. For each cycle, the temperature was lowered to -20 °C, and maintain for 8 hours, and then the temperature rose to 25 °C, standing for 2 hours. The formation process of the hydrogel is illustrated in **Figure 7.1**. In this work, we use abbreviation PVA@TA-Fe (*x*) (*x* is the TA concentration in Wt.%; *x:* 2, 3 and 5 Wt.%).

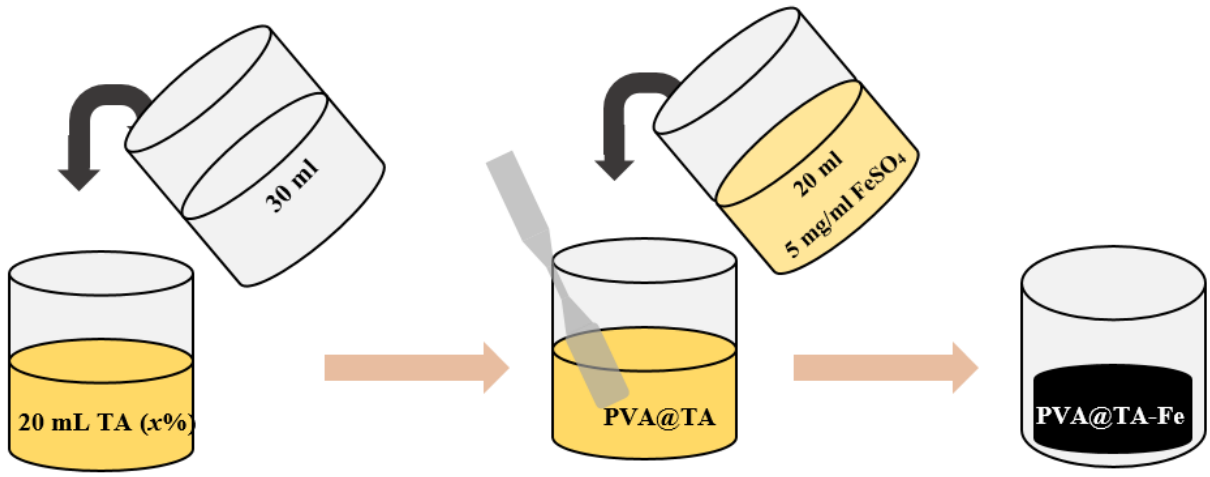

Figure 7.1 Schematic Synthesis process and structure of TA molecule and formation of the hydrogels.

7.2.3 Materials Characterization

The structure and morphology of PVA@TA-Fe^{3+} hydrogels were investigated using scanning electron microscopy SEM (Zeiss Supra 55VP, from Carl Zeiss AG) at an accelerating voltage of 5 kV. The energy dispersive spectroscopy (EDS) and elemental mapping were measured

using SEM (Zeiss EVO) at 15 kV. Before SEM analysis, the samples was sputtered-coated with Au-Pd with a thickness of 10 nm using Leica EM ACE600 Sputtering. The surface wettability of the samples was investigated using a Theta Lite 100 (Attension Theta Lite 100, Biolin Scientific) using a sessile drop method. The hydrogels were also measured using Fourier Transform Infrared (FTIR) Spectroscopy (A Bruker V70), at wavelength range from (600 to 4000 cm^{-1}). A Thermal Advantage SDT-Q600 thermal analyzer was used to obtain TG data using alumina crucibles. Experiments were conducted using a flow of nitrogen gas (150 ml min^{-1}) and a heating rate of 10 °C min^{-1} over a temperature range of 20-780 °C. The hydrogen bonding interaction between the water and hydrogel functional groups was investigated using Raman spectroscopy (RENISHAW). The light absorption characteristics were determined using a spectrophotometer equipped with an integrating sphere (950 PerkinElmer Lambda) at wavelength range (300-2500 nm; UV-Visible- Near-Infrared regions). The primary ions concentrations in seawater (K^+, Na^+, Mg^{2+} and Ca^{2+}) were quantified using an inductively coupled plasma mass spectrometer (ICP-MS), (Agilent 7900).

7.2.4 Solar water evaporation experiments

The solar evaporator designed in this study consists of PVA@TA-Fe hydrogel supported by a cellulose sponge, which was floated on deionized water (DIW) placed in a ~50 mL beaker (**Figure 7.2**). A solar simulator (Beijing Perfect Light) was positioned perpendicular to the hydrogel PTM. Simulated solar light 1 sun irradiation (1 kW m^{-2}) was illuminated to the PTM, and the mass change of water with respect to time was continuously recorded at 4 min intervals via a weighing balance (Ohaus-IC-PX84/E) connected to a laptop, and each evaporation test lasted for 1 h. The temperature variations on the hydrogel surfaces were recorded using an infrared (IR) camera (E6 Fluke, USA). All experiments were carried out at room temperature of 23 ± 3 ^oC and humidity of ~52.5%.

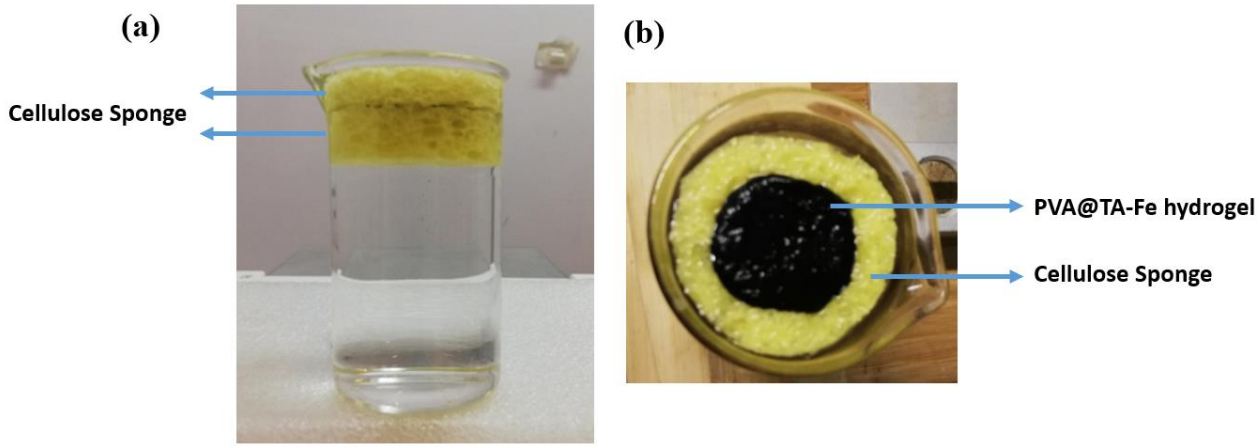

Figure 7.2 Photo-image of the designed PVA@TA-Fe (*x*%) derived solar evaporator. (a) Side view. (b) Top-view.

7.2.5 Solar seawater desalination and durability tests

The solar seawater desalination was evaluated by treating seawater collected from Rose Bay Beach, Sydney, and similar protocols for ISSG were followed. The seawater was filtered using a coarse filter, followed by a 5-micron bag filter, then treated with UV light before use. The reusability performance was also investigated for: four continues hours per day for a total of three days using both real seawater and brine 75 g/L NaCl. The capability of the PVA@TA-Fe hydrogel for salt rejections and water production was evaluated using a simple home-made device to collect the purified water. The purified water was analysed before and after desalinations test using ICP-MS.

7.2 Results and discussions

7.2.1 Formations of PVA@TA-Fe derived hydrogel

During the preparation of the hydrogel, 30 mL of 9% PVA solution was transferred into 20 mL of TA solutions (2%) and manually shake to form a viscous coagulant of PVA and TA which could transform through a physically cross-linked to form hydrogel at ambient temperature [299]. We also observed with the increase in TA concentration (3 and 5 %), more viscous coagulant of PVA and TA was formed due to the more interactions between the functional groups in PVA and TA [299]. This was followed by adding 20 mL of 5 wt.% iron sulfate solution in which the colour of the formed hydrogel turned from light brown to black (**Figure 7.3** b, c).

The hydrogel solution was left for a period of 2 hours to ensure ionic cross-linking through the catechol in TA. The coordination between TA and Fe^{3+} results in cross-linked network [301]. Thereafter, the resultant hydrogels were subjected to three freeze-thawing cycles to further enhance the mechanical property of the PVA@TA-Fe hydrogel. The prepared hydrogels with different TA contents were denoted as PVA@TA-Fe (2%), PVA@TA-Fe (3%), and PVA@TA-Fe (5%). The prepared hydrogels can be folded and back to its original state. Furthermore, it can pull a weight of up to 188 g without any damage, demonstrating its robust mechanical strength (**Figure 7.3** b, c).

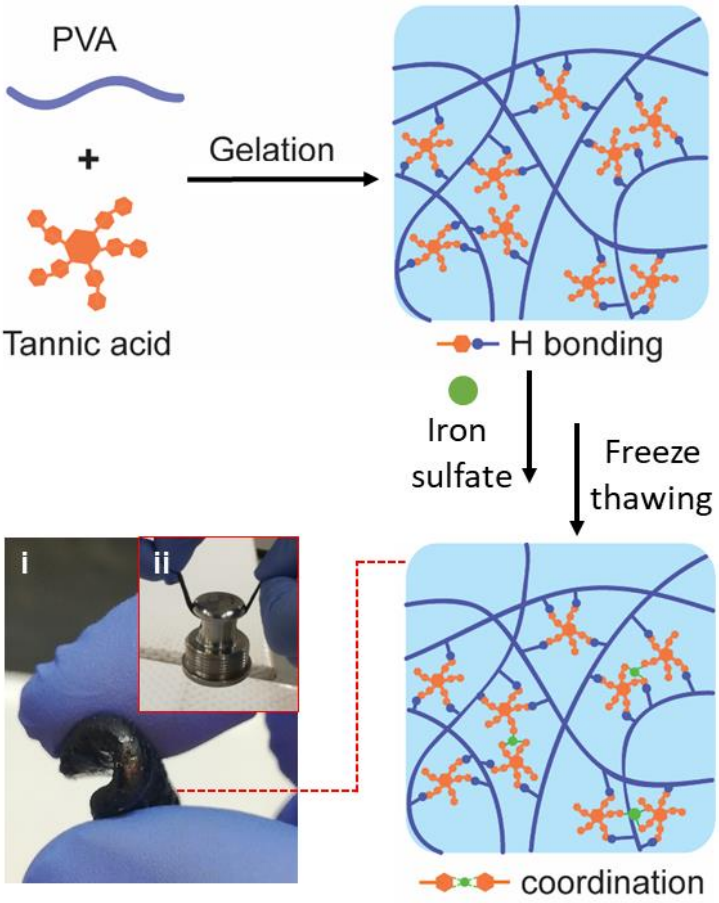

Figure 7.3 (a) Schematic illustration of the preparation of PVA@TA-Fe hydrogels. (b) Photograph of the prepared hydrogel revealing its flexibility. (c) The PVA@TA-Fe hydrogel can hold a weight of ~188 g and back its original condition.

7.2.2 Structural morphology of PVA@TA-Fe (*x*%)

The morphology of the resultant hydrogels was examined by SEM measurements. Decreasing the TA content in PVA@TA-Fe, resulted in smaller pores on the surface but were more uniform as reported in the other studies [see for e.g., 300, 302] (**Figure 7**). The surface morphology of PVA@TA-Fe (2%) revealed porous structures with rich confined nanochannels (**Figure. 7.4 a, b)**. This is attributed to the hydrogen bonding between the phenolic hydroxyl groups in the TA molecules and the alcoholic hydroxyl group in the PVA chains. This structural features provide a convenient diffusion channel which beneficial for heat localizations and a pathway channels for water vapor escaping. With the increase in TA content, fewer pores were

observed with a denser morphology as in the case of PVA@TA-Fe (3%), and PVA@TA-Fe (5%) (**Figure. 7.4 c-f)** [300]. The structural morphology of PVA@TA-Fe (3%) indicated porous structures with interconnected networks. On the other hand, with the further increase in TA contents, there were fewer but larger pores but larger with a denser and rougher morphologies as in the case of PVA@TA-Fe (5%) [300]. This can be due to the increase in TA contents resulting in more ionic covalent TA-Fe^{3+} contents within the PVA, which leads to less hydrogen bonding and further occupying more pores. Besides, there are more cross-linking formed between the -OH groups of TA and the -OH groups of PVA.

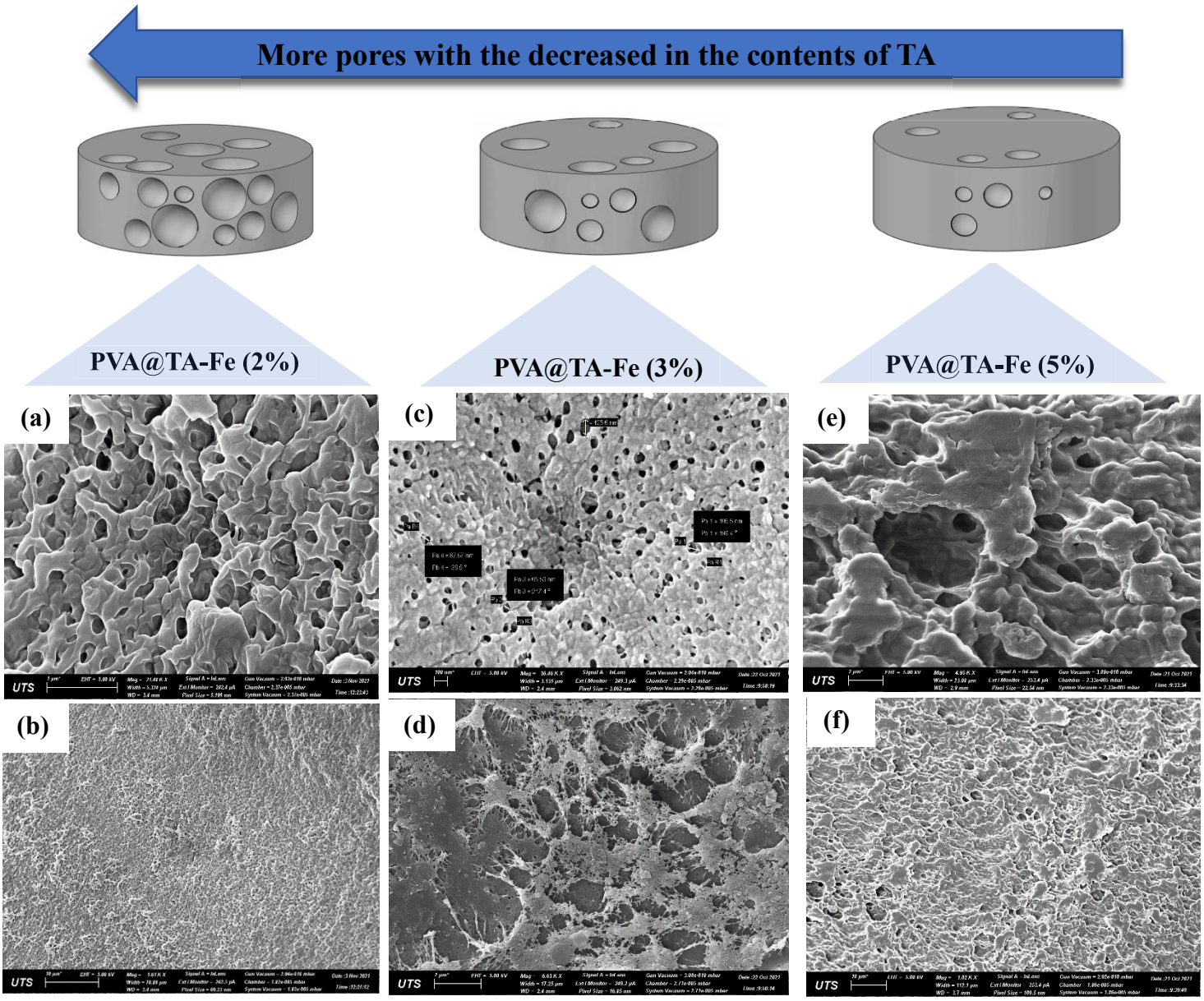

Figure 7.4 Structural morphology of PVA@TA-Fe-based hydrogel. (a-b) PVA@TA-Fe (2%). (c-d) PVA@TA-Fe (3%). (e-f) PVA@TA-Fe (5%).

FTIR spectra of PVA@TA-Fe (*x*%) are shown in **Figure 7.5a**. All three hydrogels exhibit similar spectra. The broadband peak at 3300 cm^{-1} is attributed to the –OH stretching vibrations [300, 303]. The peaks at 1712 and 1211 cm^{-1} are associated to the C=O and C–O bonds in TA [300]. The peaks at 1620 and 1527 cm^{-1} are attributed to the stretching bond C=C in the aromatic TA [303]. The peaks located at 2931 and 1195 cm^{-1} are related to the C–H, and C–O stretching of PVA [300] . The Fe_3O_4 nanoparticles exhibits a stretching band at wavelength 663 cm^{-1}, equivalent to the Fe–O and Fe–O–H bonds in Fe_3O [304]. The peak at 678 cm^{-1} is attributed to the Fe_3O_4 lattice deformation of and it is bonding with OH groups in PVA [305, 306].

Figure 7.5 b presents the TGA results of PVA@TA-Fe (*x*%) to investigate the thermal stability and measure the content of Fe in the formed hydrogel (20 ºC to 780 ºC, N_2 atmosphere). The initial mass losses to 210 ºC is due to the loss of water inside the hydrogel. The next mass loss of 75% from 210 ºC to 410 ºC are attributed to the thermal decomposition of PVA polymer networks. Meanwhile, the mass loss from 410 ºC to 490 ºC are attributed to the thermal decomposition of the TA complex [307]. After 450 ºC, the remaining residual contents (Fe and carbon) are increasing with the increase of TA concentrations, which confirm the presence of more contents of ferric tannate coordination complex.

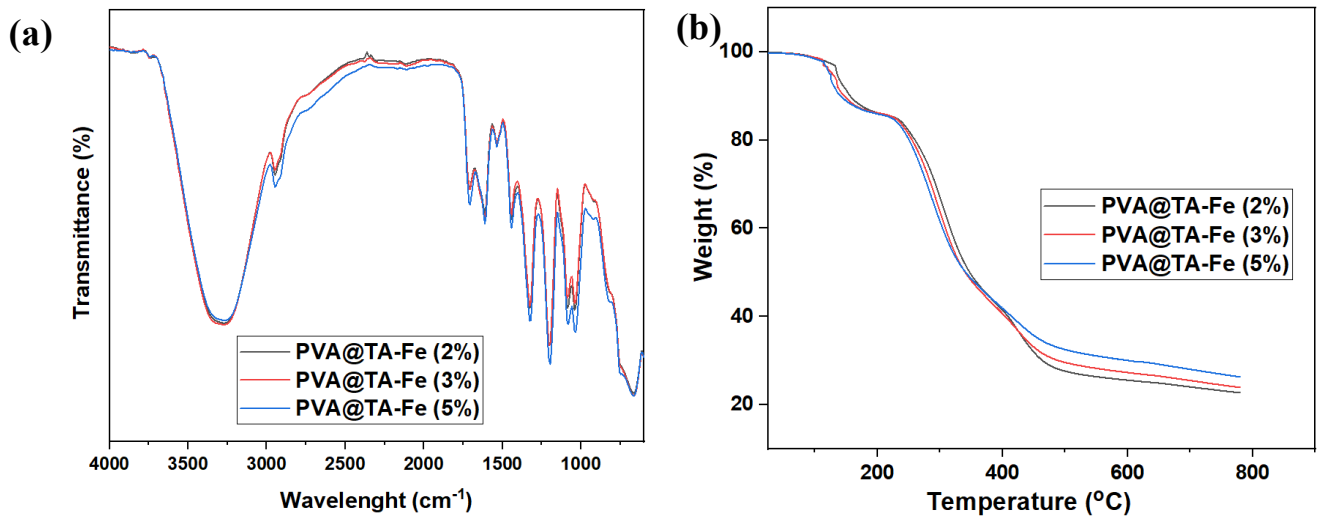

Figure 7.5 (a,b) FTIR spectra and TGA curves of PVA@TA-Fe (*x*%).

7.2.3 Surface Wettability and water bonding mechanism

The surface wettability of the PTMs is an important factor for water transport during the solar evaporation process. This ensure water penetration, release and enhancement of anti-salt crystallization within the hydrogel structures for achieving high water evaporation performance [308]. In this study, the wettability was measured using a contact angle (tensiometer) apparatus. After a water droplet (~10 μL), the whole water was quickly absorb on the hydrogel surface of PVA@TA-Fe (2%), revealing its excellent hydrophilicity (**Figure 7.6a,b)**. In comparison, contact angle values of 13^{o} and 10^{o} were attained for the surface of PVA@TA-Fe (3%) and PVA@TA-Fe (5%), respectively **Figure 7.6 c-f**. The increase in the values can be ascribed to the presence of fewer pores and an increase in surface roughness.

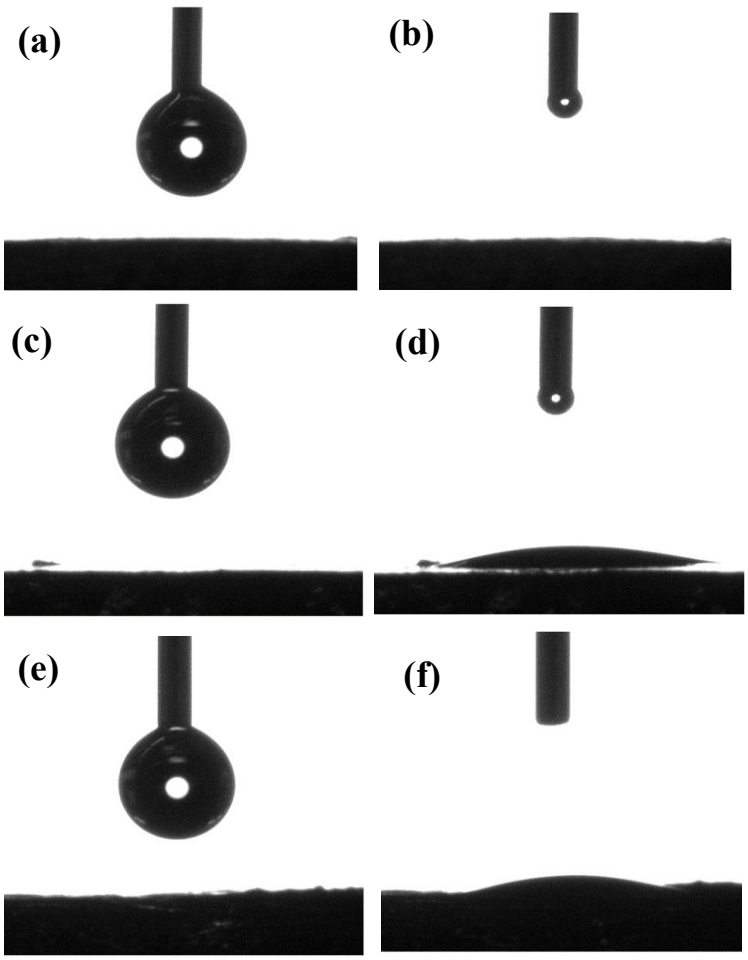

Figure 7.6 The water contact angle of PVA@TA-Fe (*x*%). (a,b) PVA@TA-Fe (2%), (c,d) PVA@TA-Fe (3%), (e,f) PVA@TA-Fe (5%).

Based on the structural properties of the hydrogel and Raman spectroscopy results. Raman spectra were used to confirm the existence of different types of water molecules. **Figure 7.7 a,** shows the spectra peaks between 3000 and 4000 cm^{-1} were curve-fitted into four peaks at 3266, 3396, 3494, and 3598 cm^{-1}. The peaks at 3266 and 3396 cm^{-1} are associated with the FW. The IW displays broader peaks positioned at 3494 and 3598 cm^{-1}. The obtained results agree well with the previously reported results in the literature [46]. Water bonding plays a vital role in water evaporations by determining the energy required for water vapor to release through the hydrogel structures. The water transportation mechanism within PVA@TA-Fe (2%) can be explained by three common states; bound water (BW) (non-freezable water), intermediate water (IW) (freezable water), and free water (FW) **Figure 7.7 b**. Besides the FW, the intermediate water interacts weakly with free water and the functional groups of the hydrogel, thus requiring less energy for evaporation [309]. It has been reported that IW requires less energy to vaporize compared to FW [310, 311]. In the case of BW possess a strong hydrogen interaction with (-OH) and (-COOH) functional groups in the PVA and TA hydrogel [46, 312]. Therefore, it will require high energy to vaporize [46].

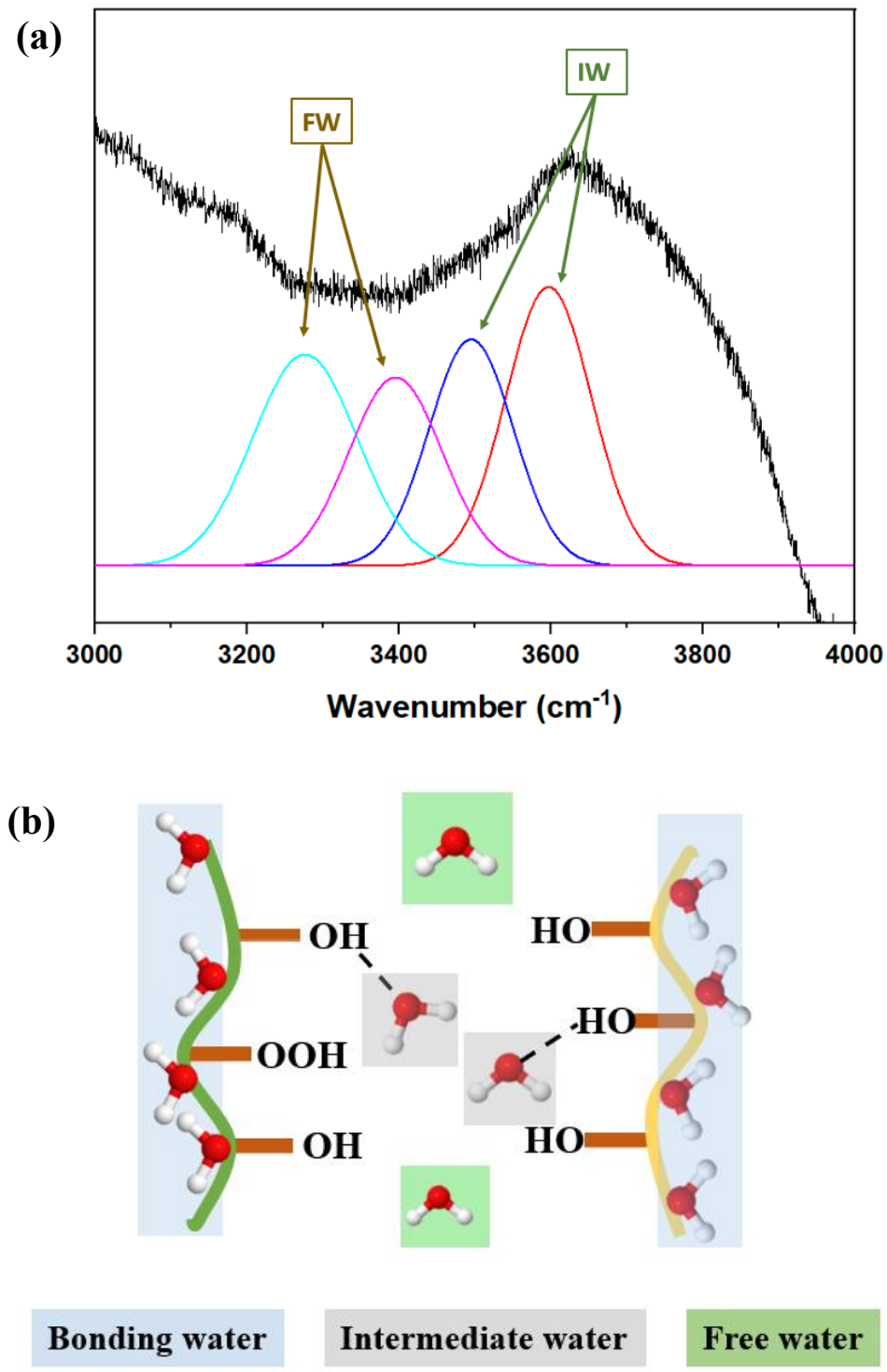

Figure 7.7 (a) Raman Spectroscopy of water bonding in PVA@TA-Fe. (b) The mechanism of water state in the PVA@TA-Fe(*x*%) derived hydrogel.

7.2.4 Solar absorption and photothermal conversion

The capability of our prepared hydrogel in harvesting sunlight was investigated using a spectrophotometer at a wavelength range from 300-2500 nm. As shown in **Figure 7.8 a**., all the presented hydrogels, PVA@TA-Fe (*x* %) displayed excellent solar light harvesting covering the solar spectrum. This is attributed to the TA-Fe^{3+} metal coordination complex, which acts as a solar harvester for the designed hydrogel. PVA@TA-Fe (2%) revealed the highest solar harvester due to the nano-size-rich pore channels, allowing more light absorption and trapping. Meanwhile, the other materials exhibited lower solar absorption due to the denser surface and irregular pores structures resulting in more light reflections. A solar evaporator device of PVA@TA-Fe (*x* %) and underneath CS, and a ring circle CS covering the hydrogel on the side. The CS has multifunctional roles of (i) allowing the floating of the hydrogel, (ii) heat localization and minimized the downward heat losses, (iii) facilitates water supply to the hydrogel PTMs. The time-dependent temperature changes were monitored using an infrared camera with corresponding time under one sun irradiation. From **Figure 7.8 b,c**, it can be observed that the initial temperature of the DIW, PVA@TA-Fe (2%), PVA@TA-Fe (3%), PVA@TA-Fe (5%) are 23.9, 24.9, 24.1, and 22.4 °C, respectively. Upon sunlight irradiation, the temperature rose rapidly to reach a temperature of 29.5, 41.6 40.7 °C, and 37.9, respectively, after 1-hour irradiation. The increase in the surface temperatures is in agreement with the optical results. Furthermore, it can suggest that the confined nanochannels in PVA@TA-Fe (2%) facilitate heat localization and utilizations by recovery of the absorbed and converted energy [52, 279]. Overall, these results suggest that a higher surface temperature would result in higher water evaporation rates, which is beneficial for the evaporation efficiency of PVA@TA-Fe (*x*%) derived hydrogel.

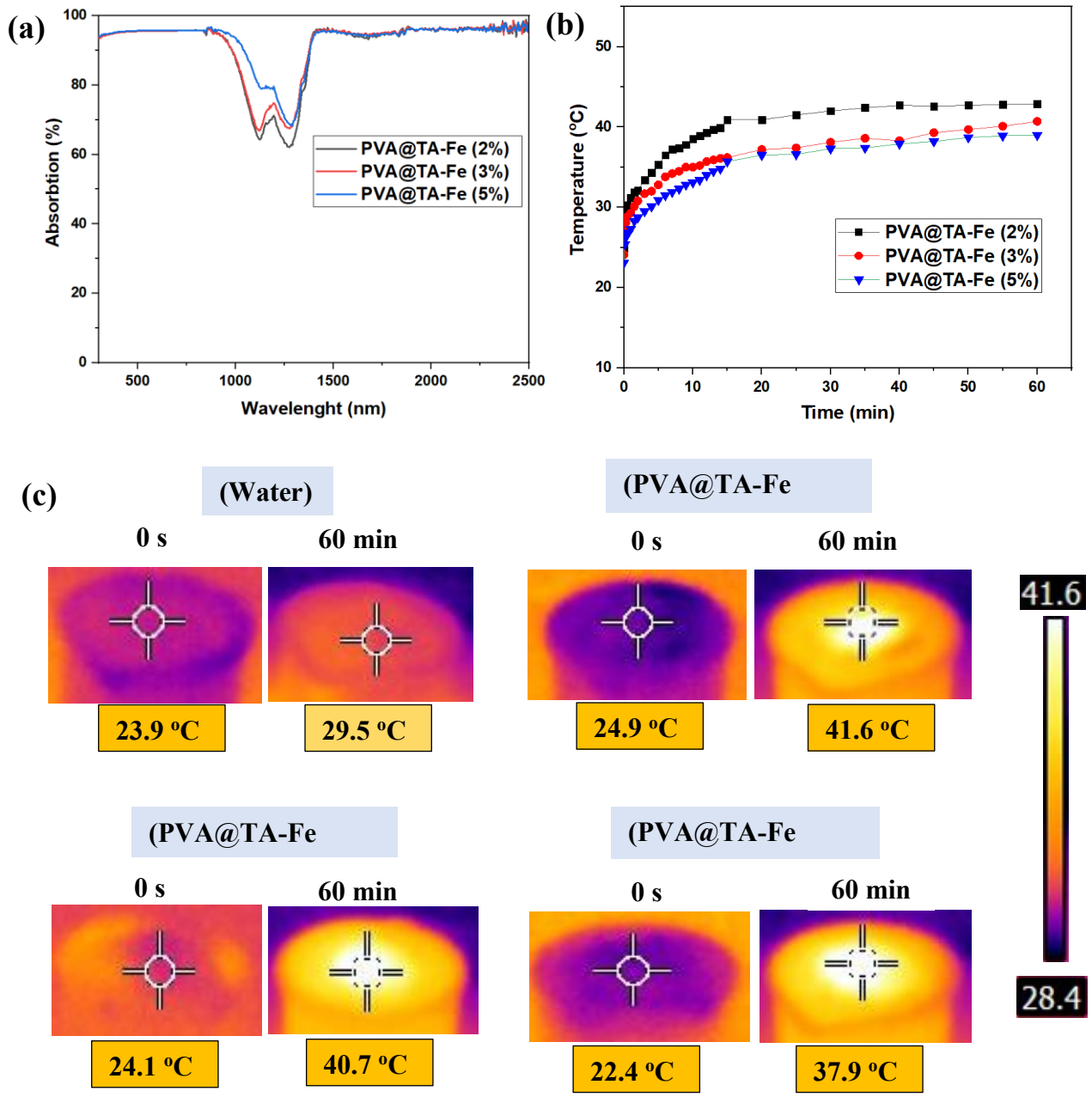

Figure 7.8 (a) Light absorption characteristics of PVA@TA-Fe(*x*%) from 300 nm to 2500 nm at dry and wet states. (b) Time-dependent Infrared images of the surface temperature light-to heat. (c) Surface temperature variations of PVA@TA-Fe(*x*%) under one sun irradiations over 60 minutes period.

7.2.5 Water evaporation performances

The water evaporation performance was examined under one sun irradiation for the prepared hydrogel (PVA@TA-Fe *x*) and de-ionized water (DIW). The inherent evaporation rates of DIW, PVA@TA-Fe (2%), PVA@TA-Fe (3%) and, PVA@TA-Fe (5%) still yield a low rate of 0.07, 0.33, 0.35, and 0.29 kg m^{-2} h^{-1}, respectively (**Figure 7.9 a**). The evaporation rate at dark conditions (without sunlight) were measured to eliminate the influence coming from the surrounding environment [313]. For the efficiency (η) calculation (Eq. 3.1) and the enthalpy vaporization of 1686 kJ/Kg of 10% PVA value was used [314]. The value was calculated based on the dark experiment test. In this work, we did not use the vaporization enthalpy of water (at 100 ºC) 2260 kJ Kg^{-1} as it will result in an efficiency >100%. As hydrogels known as high water contents and It will strongly interact with the water molecules [311, 314]. The water evaporation results under one sun irradiation displayed an evaporation rate and efficiency (in brackets) 2.35±0.11 kg m^{-2} h^{-1} (94.6%), 2.09±0.06 kg m^{-2} h^{-1} (81.4%), and 1.94±0.10 kg m^{-2} h^{-1} (77.25%) for PVA@TA-Fe (2%), PVA@TA-Fe (3%) and, PVA@TA-Fe (5%), respectively (**Figure 7.9 b-d)**. The obtained evaporation rates of PVA@TA-Fe (*x*%) are 7-8 times higher than DI water (0.29 kg m^{-2} h^{-1}). The evaporation rate and efficiency are consistent with the obtained solar-light absorption and thermal conversion. Such a high evaporation efficiency can be ascribed to the following reasons; firstly, the hydrophilic CS at the bottom acting as heat localizer and preventing the downward heat losses, additionally ensuring efficient water supply to the hydrogel. Secondly, the abundant nano-size pores on the PVA@TA-Fe-2% allowed an efficient water supply and facilitated vapor escaping during the evaporation. Thirdly, as seen from the thermal image, the hydrogel possess a temperature which relatively higher than the surrounding cellulose sponge. This allows the utilization and gaining of the gaining energy from the hydrogel to the hydrophilic CS which could enhance more energy utilizations and boost the water evaporation rate. Finally, the CS ring ensure the continuous supplying of the

water molecules to the hydrogel. Additionally, the rich free water on the hydrogel (which will continuously by supplying by the surrounding CS) which is known to require less energy for vaporizations, and reduces the energy needed to generate water vapors. In contrast, PVA@TA-Fe (5%) displayed lower evaporation rate due to the lower solar-thermal conversion and water penetration resulting from the dense structures with less pores formed due to more hydrogen bonding. Our obtained water evaporation rates outperform several classes of hydrogel-derived water evaporators [123, 218]. **Figure 7.9 e**, display the schematic illustration of the water evaporation performance through our designed hydrogel.

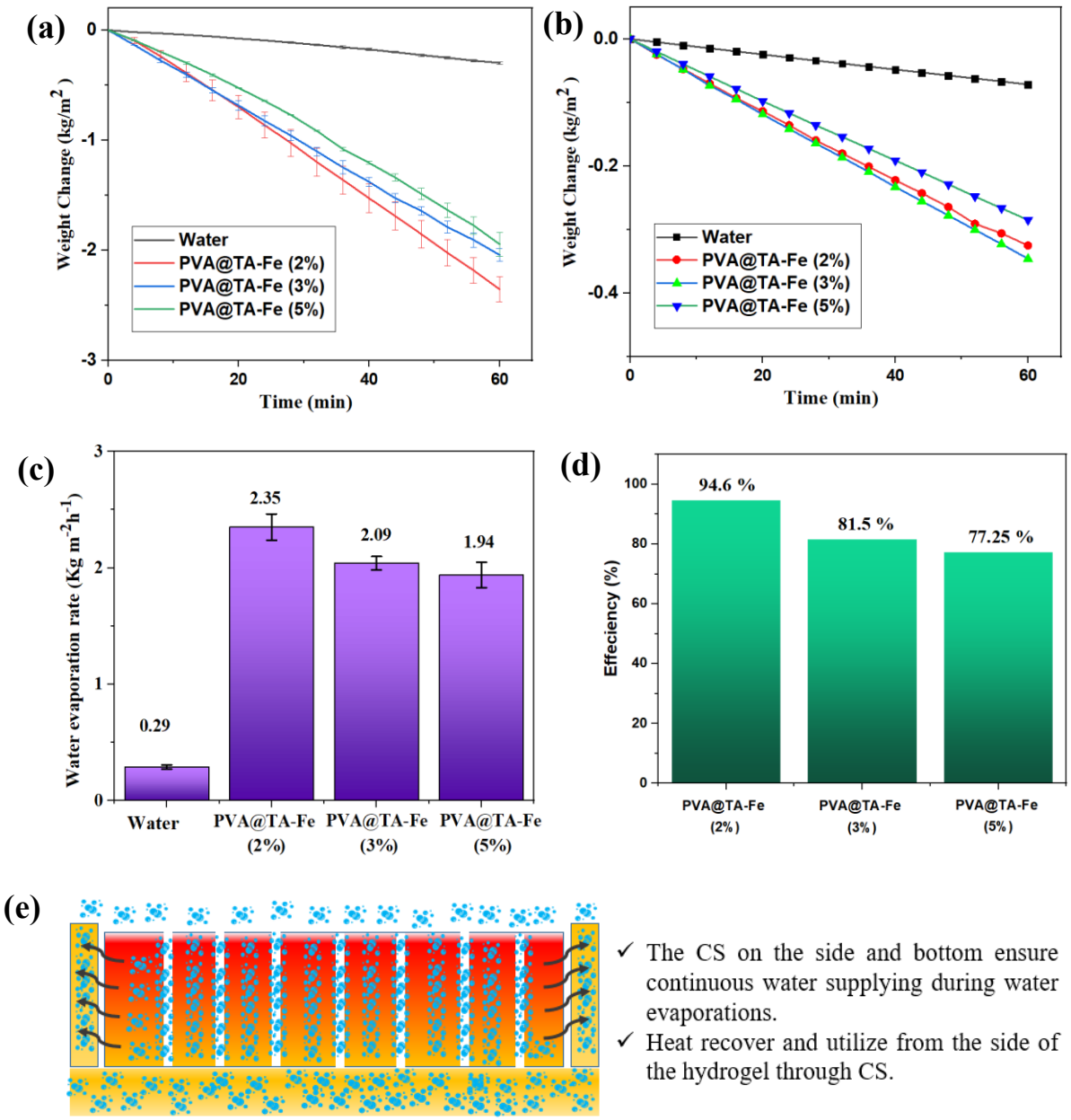

Figure 7.9 (a,b) The weight change of PVA@TA-Fe(*x%*) over a period of 1-hour under dark conditions and one sun irradiation. (**c, d**) Water evaporation rates and efficiency under one sun irradiation. **(e)** Schematic description of the heat generated recovered from the side of the hydrogel during water evaporations

7.2.6 Solar desalination performances

The capability of our designed PVA@TA-Fe (2%) for salt ions rejection of natural seawater (from Rose Bay Beach, Sydney, 33.8685° S, 151.2690° E) was conducted by measuring the concentrations of the primary ions of Na^+, Mg^{2+}, and K^+, Ca^{2+} before and after the test. A simple solar evaporator collector was made to condense and obtain the purified water (**Figure 7.10 a.**). It has been noticed that the ions concentration of the collected water has decreased from 7340.9, 913.4, 656.3 1411.56 mg L^{-1} to 0.6079, 0.2304, 0.5395, 1.4115 mg L^{-1} **(Figure 7.10 b)**. The obtained results are far below the salinity standard required by the World Health Organization (WHO) [214] and the US Environmental Protection Agency (EPA) [281]. The results confirmed the capability of our designed evaporator for obtaining drinking water from salted water.

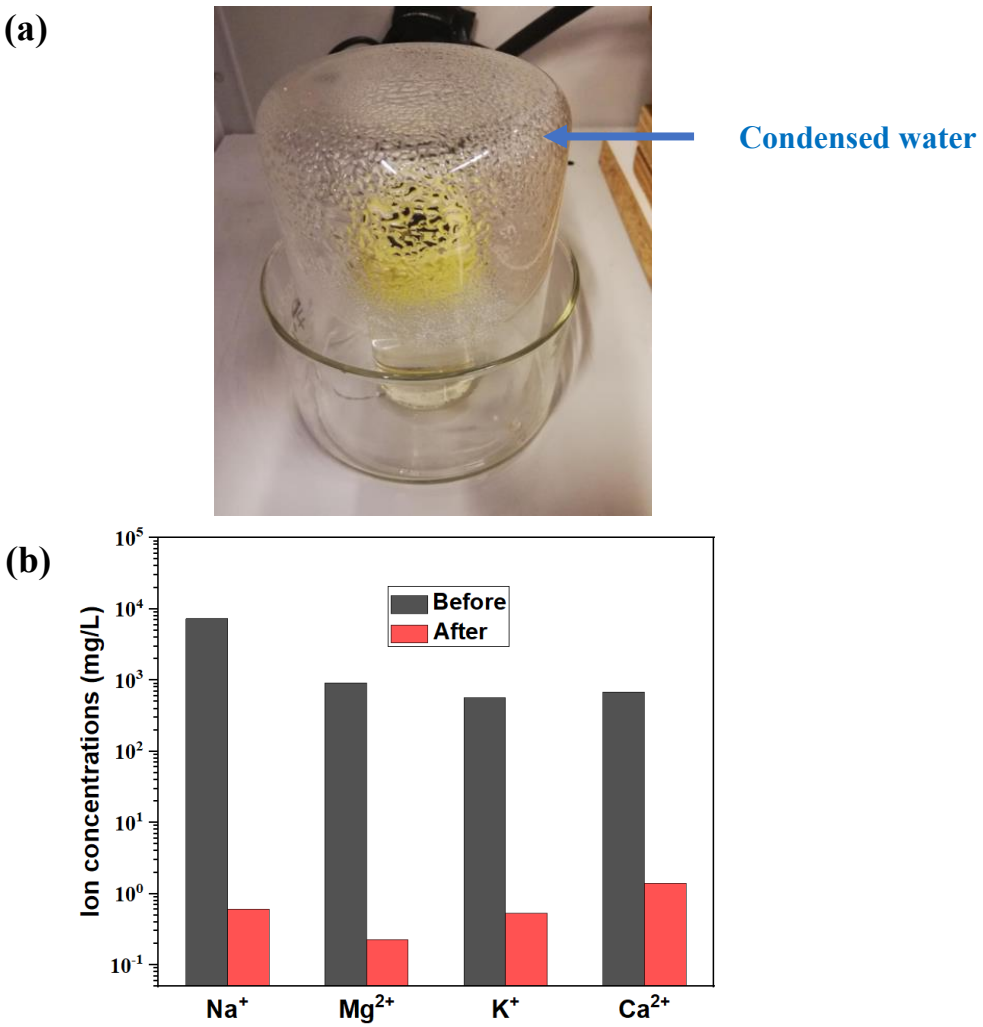

Figure 7.10 Solar desalination performances of PVA@TA-Fe (2%). (a) Home-made device for water condensations and collection. (b) Salt ions concentrations before and after seawater desalination. (b) Reusability test under three consecutive days (4 hours/day) using seawater and brine seawater (NaCl; 75 g/L).

The reusability of the PTMs under salted water is an essential criterion for the practical applications of solar evaporators in seawater desalination [315, 316]. Therefore, we assessed the reusability of the optimized hydrogel PVA@TA-Fe (2%) using natural seawater and high salinity brine (75 g/L NaCl). The experiments were carried out under day and night conditions for three consecutive days, four hours per day under one sun irradiation. The results in **Figure 7.11 a** showed that at natural seawater display stable evaporation rate of 8.98 kg m^{-2} (Day 1), 9.13 kg m^{-2} (Day 2), and 8.82 kg m^{-2} (Day 3)) were achieved. In contrast, when high salinity brine (75 g/L NaCl) is used, it does not impact the evaporation rate (9.06 kg m^{-2} (Day 1), 8.20 kg m^{-2} (Day 2), and 9.68 kg m^{-2} (Day 3)) (**Figure 7.11 b)**. We observed the formation of a little wet salts on the surface of the hydrogel. The wet salt would not block vapor escape from the hydrogel surface during the evaporation process [317]. As it has been reported that the wet salt can only possess a low light reflection in the infra-red region [317]. Additionally, recovered entirely, dissolving the formed salts on the hydrogel at night conditions to the bulk water through diffusion and advection process (**Figure 7.11 c,d**). This is ascribed to the cellulose sponge surrounded on the hydrogel, which ensures the water supply to the superhydrophilicity hydrogel surface. Besides, the self-pumping of water through the rich pore channels of the hydrogel is another reason for the self-recovery (**Figure 7.11 e**) [318]. The current results revealed the promising applications of our design hydrogel for solar desalination.

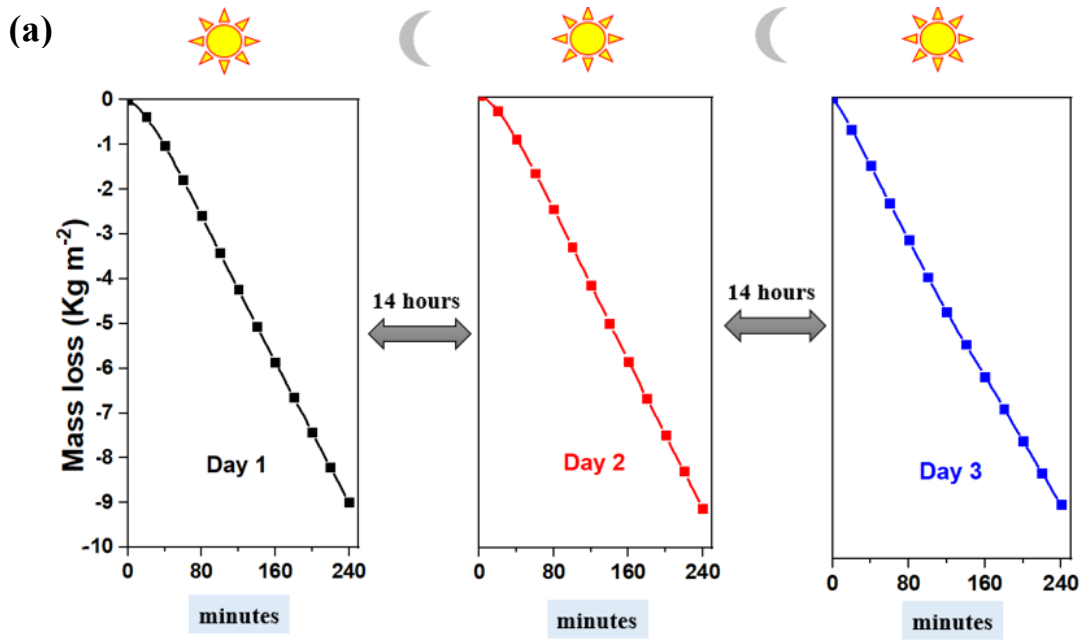
(a)
Mass loss (Kg m-2)
0
-1
-2
-3
-4
-5
-6
-7
-8
-9
-10
Day 1
Day 2
Day 3
14 hours
14 hours
0
80
160
240
minutes
minutes
minutes

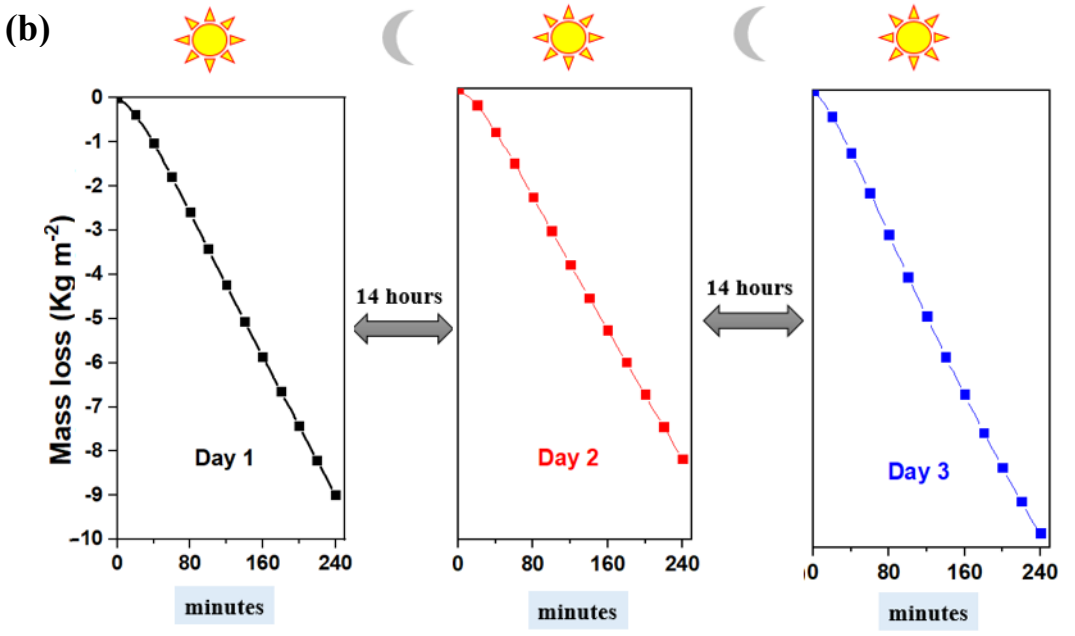
(b)
Mass loss (Kg m-2)
0
-1
-2
-3
-4
-5
-6
-7
-8
-9
-10
Day 1
Day 2
Day 3
14 hours
14 hours
0
80
160
240
minutes
minutes
minutes

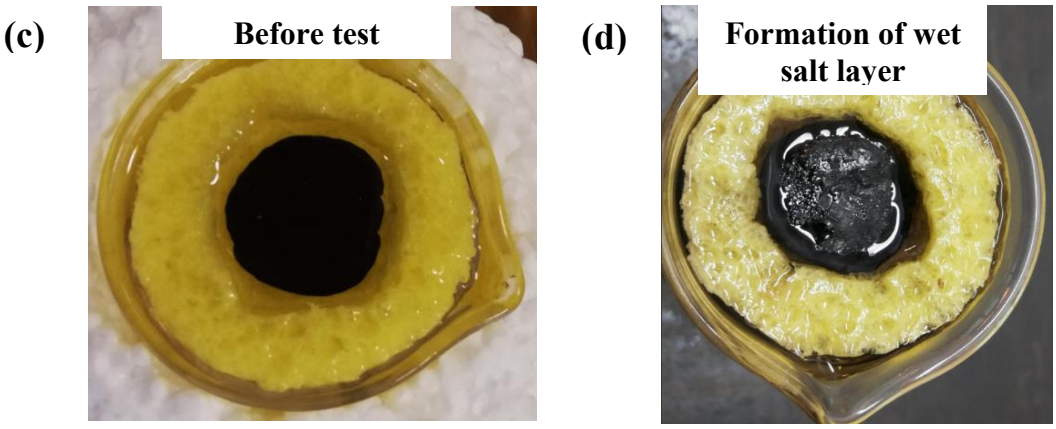
(c)
Before test
(d)
Formation of wet salt layer

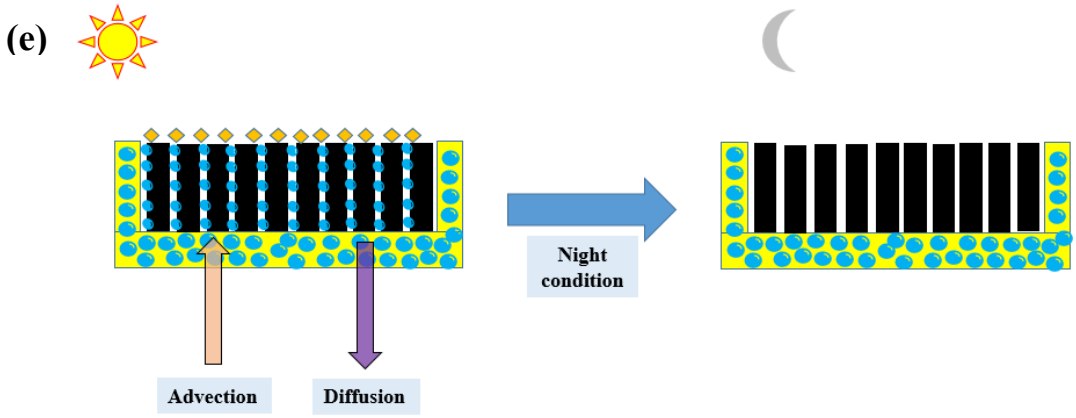

Figure 7.11 Reusability test under three consecutive days (4 hours/day) using seawater **(a)** and **(b)** high brine salinity solutions (NaCl; 75 g/L)..Photo-image of the designed PVA@TA-Fe (*2%*) after solar seawater desalinations; **(c)** before desalinations, **(d)** after desalinations.**(e)** Resistance of seawater corrosion mechanism via advection and diffusion process achieved by the covered CS form the side and bottom.

7.3 Conclusion

In summary, we have adopted a cost effective and facile approach to fabricate a versatile PVA@TA-Fe^{3+} hydrogel with controlled porosity and structural morphology for efficient solar steam generation as well as solar-driven seawater desalination. The interactions between Fe^{3+} with PVA@TA promoted the formation of catechol-complexes and achieved high solar light harvesting. By controlling the TA contents, the surface properties of hydrogel can be varied, as the pores can increase with the decrease of the TA content. The enhancement in surface properties could influence the solar-thermal conversion and water evaporation performances. As a result, the optimized PVA@TA-Fe (2%) solar evaporator can achieve a water evaporation rate of 2.35±0.11 kg m^{-2} h^{-1} with a solar-thermal conversion efficiency of 94.6%. Moreover, excellent salt rejections can be achieved meeting the standard level for drinking water. Besides, good reusability can obtain under high salinity brine solutions for three successive days. The salt formed can back flow to the bulk water through advection, and the diffusions process resulted from the uniform and confined nanochannels on the surface.

CHAPTER 8

CONCLUSION AND RECOMMENDATION

8.1 Conclusion

This doctoral study contributes to developing advanced nanostructured PTMs to harness solar energy as a means to provide an effective solution for solar vapor generations and to address salt crystallization issues. This study was keen to develop solar PTMs based on the structural engineering of nanomaterials with some modifications on various substrates and supersorbent. The detailed contributions of this study can be summarised in two major points:

- **Developing solar PTMs for efficient water evaporations**

In first study, a single-step solvothermal synthesis was proved to be an effective way to prepare a unique and novel 3D microflowers CuS/Sn_2S_3 heterostructure (3D CSS-NS MF) consisting of densely packed vertically-aligned ultrathin nanosheets and rich nanocavities formed between the nanosheets. Then, the synthesized microflowers were deposited on a hydrophilic MCE membrane, followed by coating with a hydrophobic layer (PFDTES). The unique microstructures provide a pathway for harvesting solar light through multiple reflections and scattering, achieving a high light absorption of 95% over the whole solar spectrum region. Consequently, a high solar thermal conversion was observed with a surface temperature that can reach up to ~ 41 ºC within 10 minutes under one sun irradiation. The bilayer structures resulted in a water evaporation rate of 1.42±0.04 kg m^{-2} h^{-1} under one sun irradiation, corresponding to an efficiency of 82.93 %. Such a high evaporation performance is ascribed to the rapid vapor escaping within the nanocavities and the compacted microflowers. Another avenue explored is the engineering of environmentally friendly PDA nanostructures coated on porous nickel using a simple *in situ* synthesis method. The porous NF with 3D network structures is an effective strategy for robust water evaporation with anti-salt properties. The results revealed that the fabricated hierarchical PDA NWs-NF exhibited high solar light absorption with high solar-to-thermal conversion. This could result in a high-water evaporations rate of 1.39±0.01 kg m^{-2} h^{-1} and an efficiency of 87.6 %. In another work, the

chemistry and structural relationships of the hydrogel in enhancing the water evaporation performances are demonstrated, exceeding the theoretical evaporation values (1.49 kg m^{-2} h^{-1}). This can be obtained by controlling the TA contents (2 to 5%) added to 10% PVA during the gelation process, followed by adding $FeSO_4$ solution. At low concentrations of TA (2%) [Named as PVA@TA-Fe (2%)], the structural morphology revealed a rich and uniform confined nanopores surface. This is ascribed to the hydrogen bonding formed between the phenolic hydroxyl group of catechol groups in TA molecule and the alcoholic hydroxyl group in the PVA chain. The obtained structures provide a convenient diffusion channel that is considered beneficial for solar-thermal conversion and provides pathway channels for more vapor release. After exposure to one-hour solar irradiations (under one sun irradiation), a surface temperature of ~ 41.6 ºC was obtained. Besides, remarkable water evaporation of 2.3 kg m^{-2} h^{-1} can be realized. Meanwhile, with higher TA concentrations of 5% (named as PVA@TA-Fe (5%)) less pores were obtained with a denser morphology resulting in lower solar thermal conversions and vapor generations.

- **Solar seawater desalination performances**

Solar evaporators with good durability and stability are essential for practical applications in solar desalination. In this thesis, we investigated the anti-salt by incorporating PTMs into various supersorbents or substrates for seawater or high salinity desalination. 3D CSS-NS MF/MCE coated with hydrophobic silane layer (PFDTES) demonstrated an excellent durability over 10 consecutive cycles, which maintained an almost high evaporation rate even after 10 h of operation. A slight decrease in evaporation rate 1.35 kg m^{-2} h^{-1} at the 10th cycle compared to the initial value of 1.40 kg m^{-2} h^{-1} was achieved. This observation is ascribed to the formation of tiny salts on the black 3D CSS-NS MF, which migrated and formed on the surface and clogged some surface pores. Then, we demonstrated an effective and novel strategy to fabricate a scalable gold nanolayer on PTFE membrane (Au-PTFE) using a magnetic

sputtering technique to mitigate this issue. The method has features of the cost-effective and scalable approach to coat a thin-film nanolayer. In this work, we have noticed that the coating of gold nanolayer on PTFE membrane enhanced the mechanical properties from 6.71 MPa and 33.9%, respectively, for uncoated PTFE membrane to 8.09 MPa 36.48%, for the coated Au-PTFE membrane. This was followed by designing a simple solar evaporator made of the prepared Au-PTFE membrane, which floated on a cellulose sponge. Our designed solar evaporator indicated a water evaporation rate of 0.88 kg m^{-2} h^{-1} 0.85 kg m^{-2} h^{-1} and 0.82 kg m^{-2} h^{-1} for the blank water, a natural seawater, and high salinity brine (150 g/L NaCl), respectively, under one sun irradiation. Furthermore, it demonstrated excellent stability and reusability in seawater and high salinity brine (150 g/L NaCl) for ten continuous cycles. The ideal solar desalination performances can be explained by the surface hydrophobicity of the designed Au-PTFE membrane causing salt repellents. Furthermore, the spaces between the fibrous membrane and the sufficient water supply by cellulose sponge contributed to salt dissolving through advection and convection mechanisms. Even under various pH solutions (acidic, basic, and oxidizing conditions), remarkable stability was achieved for five continuous cycles. Our findings reveal the novelty of magnetic sputtering methods for scaling up highly stable nanolayer metallic photothermal membranes for salt resistance with long-term durability and stability. Then, we prepared and developed a PDA NWs-NF to maintain high solar evaporations and achieve superior anti-salt properties. The porous NF with 3D network microstructures prevents salt blockage on the pores. Besides, the hydroxyl groups in PDA resulted in superhydrophilicity and weak salt adhesion on the substrate surface. These merits result in outstanding reusability under natural seawater and high brine salinity (7.5 % NaCl) over three days of the test (4 cycles per day). The tiny salt formed is washable by simply dipping in DW for 9 hours. Besides these features, self-cleaning properties were obtained through advection and diffusion processes. Our final strategy in this research study was to

investigate the multifunctional TA-derived hydrogel. In this work, we have observed that the formation of nanochannels with their uniform distributions pathway could combine the features of obtaining a high water evaporations rate. Besides, its self-cleaning capability during the night conditions under high salinity brine (7.5 wt% NaCl). The formed salt layer on the PVA@TA-Fe (2%) during the day conditions (at one sun irradiation) after four hours of evaporations can self-clean and dissolve back at night conditions (dark conditions). This can be explained by the surface hydrophilicity, the confined nanochannels and our designing underneath and side covered of the hydrogel by CS will ensure a sufficient amount of water supplying which are beneficial for the reusability of the proposed PVA@TA-Fe (2%) hydrogel. Overall, based on the outcomes of this study, we can conclude that polymeric hydrogel PVA@TA-Fe -derived solar evaporators can meet all the criteria for high-performance solar evaporator for solar desalination applications because of the following reasons: (1) the presence of rich nanopores porosity and the aligned nanochannels resulting in multiple internal light reflection and trapping, hence localized the heat at the air-water interfaces and minimized the heat losses; (2) the rich interconnected microchannels allow more water to penetrate and leads to efficient water suppling channel; as consequence to extraordinary anti-salt and self-cleaning properties.

In this Ph.D. study, four approaches have been utilized to fabricate four types of PTMs. The fabrication of Au nanolayer using magnetron sputtering seems to be a unique approach compared to other plasmonic methods reported in the literature. It can result in highly stable materials even under harsh environmental conditions. However, the high cost of the equipment seems might hinder it is application. The synthesis of metal sulfide (CuS/Sn_2S_3) using the solvothermal method followed by coating with silane group has the drawback of using a toxic solvent that is not environmentally friendly. Another approach to using oxidative polymerizations to grow PDA nanostructures on NF is simple and straightforward methods.

However, the water evaporation performance still needs further improvement. Our last approach to hydrogel-derived PTMs through a physical cross-linking process is considered the most promising among the reported methods. This attributes to their features of low cost, simple preparation process without requiring any expensive devices or using toxic solvents, excellent structural properties which resulted in high solar thermal conversion, and good anti-salt properties. In addition, the functionality (e.g., porosity and surface area) can be simply controlled and adjusted to achieve a desirable solar evaporation performance. Low-cost SSG devices can be built using hydrogel PTMs, which can be attractive for implementation in large-scale practical applications.

8.2 Recommendations

In this doctoral study, several classes of solar PTMs were developed which achieve an efficient solar water evaporator with anti-salt properties. Despite the good performances, further investigations are required to bring this unique technology to real-world applications. The main points are highlighted as follows:

(a) Enhancing solar thermal conversion of and selection of PTMs.

- There is a need to develop innovative solar PTMs, especially with the unique materials which exhibit low solar thermal conversion performance. Nanocomposite PTMs combine a feature of various materials and can be considered an effective method to boost the photothermal conversion efficiency should be thoroughly explored in the near future.
- Magnetron sputtering revealed a promising method for fabricating a large area of nanolayer materials. Combining 3D printing to fabricate a 3D porous substrate with magnetron sputtering to generate thin-layer PTMs will be a good direction to be investigated.
- The re-utilization of biomass waste (such as animal residues or waste) and improving their surface functionalities as effective PTM is an attractive strategy that would be more economical and environmentally friendly. This might be a potential avenue for further research as a possible PTM material for SSG.

(b) Anti-salt crystallization feature, PTMs regeneration, and stability test.

- Further studies of porous structural PTMs with regulated properties (e.g., porosity, thickness, and dimensions) are required to investigate further the material's capability for salt tolerance.
- The enhancement of the surface wettability by the surface modifications of the inner structures of PTMs with charge ions can be a promising anti-salt method that would be an attractive research direction.

- The anti-salt and durability performance of PTMs should be investigated under natural sunlight. Also, the weathering effect regarding the temperature, humidity, and the cause of sunny or cloudy weather is worth exploring. This could be a more effective method to evaluate the salt-resistant of the designed solar evaporator under realistic conditions.
- Several strategies have been developed for regenerating the PTMs highlighted as: (1) Day and night recovering through discharging salt formed during the day and back at night to the bulk saline water. This can occur by designing porous hydrophilic PTMs, allowing the salt to diffuse and dissolve back through diffusion and convection. (2) Through preparing PTMs with an abundance of hydrophilic groups (e.g., OH and $–NH_2$) resulting in a weak salt adhesion on the surface, PTMs can be recovered and reused by simply immersing in DIW. Besides the materials' functionality and structural properties, the solar evaporator components (e.g., supporter, water transport, structure design) could also play a critical role in regenerating the PTMs. The continuous water supply through the capillary effect or the supporter results in salt dissolving from the evaporator surface. Designing 3D a solar evaporator by separating the PTMs from the salted water could recover them as valuable resources instead of discharging them back. Hence, the combination of effective PTMs and evaporator systems would enable the long-term reusable for the future study. Therefore, the selection of solar evaporator components.

***(c)* Solar water evaporator design**

- The hydrophilic supporter (e.g., wood, cellulose sponge, etc.) has advantages over the hydrophobic type (e.g., polystyrene foam, expandable polyethylene, etc.). The hydrophilic supporter possesses these traits: (i) enhancing water supply due to its hydrophilicity without the need to add external wick materials. (ii) Acting as heat localizer, minimizing downward heat losses. (iii) Contributing to salt rejections from the surface of the PTMs through advection and diffusion process. Despite the capability of the hydrophobic

supporter of better photothermal conversion on the surface of PTMs due to less water supply. However, it has the drawback of requiring additional wick materials for water transport. In addition, the salt formed on the PTMs surface could be hard to recover due to insufficient water supply. Therefore, a comprehensive study on designing a hydrophilic supporter with control water suppling and maintaining high surface temperature in the evaporation area would be valuable.

- Recently, increasing studies revealed that the combination of convective heating effect and evaporative cooling technology could be a promising method to obtain highly efficient solar water evaporators. It can be achieved by designing photothermal material (solar absorber) on the top and sub-ambient cooling (solar reflector) on the bottom. evaporative cooling can be achieved by two main approaches; (1) using hydrophilic materials that allow water to pass through by capillary action and attain a cooling, and (ii) designing an evaporative cooler with materials that reflect sunlight. Creating a passive cooling capacity of up to 160 W m^{-2} remains challenging because of the high latent heat of water evaporation and should be further investigated in the future.

(d) ***Practical scale solar evaporator for seawater desalinations applications***.

Advancements in fabricating scalable solar evaporator devices (area: >1 m^2) should be explored to bring solar evaporator devices into real-world applications. However, to make it more applicable, it should possess several which can be explained as follows;

- The balance between designing cost-effectiveness, the high amount of generated water, and long-term reusability is expected to be a new research direction to dig into that need to be deeply investigated. Ideally, cost-effective materials and a high water evaporation rate are the best.

- Establishing a cost analysis standard that combines the cost of the PTMs corresponding to the concentrations used and durability under realistic conditions would be valuable for the stockholders to compare with other available technologies used in the market.

REFERENCES

1. Mekonnen, M.M. and A.Y. Hoekstra, *Four billion people facing severe water scarcity.* Science advances, 2016. **2**(2): p. e1500323.

2. Organization, W.H., *Health and environment in sustainable development: five years after the Earth Summit*. 1997, World Health Organization.

3. Politano, A., et al., *Photothermal membrane distillation for seawater desalination.* Advanced Materials, 2017. **29**(2): p. 1603504.

4. Wang, Z., et al., *Pathways and challenges for efficient solar-thermal desalination.* Science advances, 2019. **5**(7): p. eaax0763.

5. IDA, W.D.P.I.N., *22, MS Excel spreadsheet, Media Analytics Ltd*. 2010, Oxford, UK.

6. Drioli, E. and E. Curcio, *Membrane engineering for process intensification: a perspective.* Journal of Chemical Technology & Biotechnology: International Research in Process, Environmental & Clean Technology, 2007. **82**(3): p. 223-227.

7. Gao, M., et al., *Solar absorber material and system designs for photothermal water vaporization towards clean water and energy production.* Energy & Environmental Science, 2019. **12**(3): p. 841-864.

8. Zhang, P., et al., *Vertically aligned graphene sheets membrane for highly efficient solar thermal generation of clean water.* Acs Nano, 2017. **11**(5): p. 5087-5093.

9. Tao, P., et al., *Solar-driven interfacial evaporation.* Nature energy, 2018. **3**(12): p. 1031-1041.

10. Oki, T. and S. Kanae, *Global hydrological cycles and world water resources.* science, 2006. **313**(5790): p. 1068-1072.

11. Qiblawey, H.M. and F. Banat, *Solar thermal desalination technologies.* Desalination, 2008. **220**(1-3): p. 633-644.

12. Wang, P., *Emerging investigator series: the rise of nano-enabled photothermal materials for water evaporation and clean water production by sunlight.* Environmental Science: Nano, 2018. **5**(5): p. 1078-1089.

13. Anis, S.F., R. Hashaikeh, and N. Hilal, *Functional materials in desalination: A review.* Desalination, 2019. **468**: p. 114077.

14. Chen, C., Y. Kuang, and L. Hu, *Challenges and opportunities for solar evaporation.* Joule, 2019. **3**(3): p. 683-718.

15. Zhang, Y., et al., *Application of solar energy in water treatment processes: A review.* Desalination, 2018. **428**: p. 116-145.

16. Kabeel, A. and S. El-Agouz, *Review of researches and developments on solar stills.* Desalination, 2011. **276**(1-3): p. 1-12.

17. Kaushal, A., *Solar stills: a review.* Renewable and sustainable energy reviews, 2010. **14**(1): p. 446-453.

18. Zhang, P., et al., *Direct solar steam generation system for clean water production.* Energy Storage Materials, 2019. **18**: p. 429-446.

19. Chen, C., et al., *Highly flexible and efficient solar steam generation device.* Advanced Materials, 2017. **29**(30): p. 1701756.

20. Li, X., et al., *Graphene oxide-based efficient and scalable solar desalination under one sun with a confined 2D water path.* Proceedings of the National Academy of Sciences, 2016. **113**(49): p. 13953-13958.

21. Li, R., et al., *MXene Ti3C2: an effective 2D light-to-heat conversion material.* ACS nano, 2017. **11**(4): p. 3752-3759.

22. Polman, A., *Solar steam nanobubbles.* ACS nano, 2013. **7**(1): p. 15-18.

23. Mu, P., et al., *Superwetting monolithic hollow-carbon-nanotubes aerogels with hierarchically nanoporous structure for efficient solar steam generation.* Advanced Energy Materials, 2019. **9**(1): p. 1802158.

24. Liu, Y., et al., *A bioinspired, reusable, paper-based system for high-performance large-scale evaporation.* Advanced Materials, 2015. **27**(17): p. 2768-2774.

25. Long, Y., et al., *Carrot-inspired solar thermal evaporator.* Journal of Materials Chemistry A, 2019. **7**(47): p. 26911-26916.

26. Sun, P., et al., *3D-structured carbonized sunflower heads for improved energy efficiency in solar steam generation.* ACS Applied Materials & Interfaces, 2019. **12**(2): p. 2171-2179.

27. Bian, Y., et al., *Carbonized Bamboos as Excellent 3D Solar Vapor-Generation Devices.* Advanced Materials Technologies, 2019. **4**(4): p. 1800593.

28. Wang, Y., et al., *Same Materials, Bigger Output: A Reversibly Transformable 2D-3D Photothermal Evaporator for Highly Efficient Solar Steam Generation.* Nano Energy, 2020: p. 105477.

29. Wu, T., et al., *Incorporation of gold nanocages into electrospun nanofibers for efficient water evaporation through photothermal heating.* Materials Today Energy, 2019. **12**: p. 129-135.

30. Tao, P., et al., *Solar-driven interfacial evaporation.* Nature energy, 2018: p. 1.

31. Organization, W.H., *Evaluation of Certain Food Additives: Eighty-Sixth Report of the Joint FAO/WHO Expert Committee on Food Additives*. Vol. 965. 2019: World Health Organization.

32. Thapar, N. and I.R. Sanderson, *Diarrhoea in children: an interface between developing and developed countries.* The Lancet, 2004. **363**(9409): p. 641-653.

33. Gaffga, N.H., R.V. Tauxe, and E.D. Mintz, *Cholera: a new homeland in Africa?* The American journal of tropical medicine and hygiene, 2007. **77**(4): p. 705-713.

34. Chard, A.N., et al., *Impact of a school-based water, sanitation, and hygiene intervention on school absence, diarrhea, respiratory infection, and soil-transmitted helminths: results from the WASH HELPS cluster-randomized trial.* Journal of global health, 2019. **9**(2).

35. Qiblawey, H.M. and F. Banat, *Solar thermal desalination technologies Desalination.* Volume. **220**: p. 1-3.

36. Aybar, H.S. and H. Assefi, *A review and comparison of solar distillation: Direct and indirect type systems.* Desalination and Water treatment, 2009. **10**(1-3): p. 321-331.

37. Ayoub, G.M. and L. Malaeb, *Developments in solar still desalination systems: A critical review.* Critical reviews in environmental science and technology, 2012. **42**(19): p. 2078-2112.

38. Ibrahim, I., et al., *Semiconductor photothermal materials enabling efficient solar steam generation toward desalination and wastewater treatment.* Desalination, 2020: p. 114853.

39. Ibrahim, I., et al., *Biomass-based photothermal materials for interfacial solar steam generation: A review.* Materials Today Energy, 2021: p. 100716.

40. Neumann, O., et al., *Solar vapor generation enabled by nanoparticles.* ACS nano, 2013. **7**(1): p. 42-49.

41. Ghasemi, H., et al., *Solar steam generation by heat localization.* Nature communications, 2014. **5**: p. 4449.

42. Kashyap, V. and H. Ghasemi, *Solar heat localization: concept and emerging applications.* Journal of Materials Chemistry A, 2020. **8**(15): p. 7035-7065.

43. Hu, X., et al., *Tailoring graphene oxide-based aerogels for efficient solar steam generation under one sun.* Advanced materials, 2017. **29**(5): p. 1604031.

44. Ni, G., et al., *Steam generation under one sun enabled by a floating structure with thermal concentration.* Nature Energy, 2016. **1**(9): p. 1-7.

45. Li, Y., et al., *Graphene oxide-based evaporator with one-dimensional water transport enabling high-efficiency solar desalination.* Nano Energy, 2017. **41**: p. 201-209.

46. He, J., et al., *Enhanced solar steam generation of hydrogel composite with aligned channel and shape memory behavior.* Composites Science and Technology, 2021. **204**: p. 108633.

47. Chen, L., et al., *Superhydrophilic and oleophobic porous architectures based on basalt fibers as oil-repellent photothermal materials for solar steam generation.* ChemSusChem, 2020. **13**(3): p. 493-500.

48. Xiao, C., et al., *Janus Poly (ionic liquid) Monolithic Photothermal Materials with Superior Salt-Rejection for Efficient Solar Steam Generation.* ACS Applied Energy Materials, 2019. **2**(12): p. 8862-8870.

49. Jun, Y.-S., et al., *Photothermal Membrane Water Treatment for Two Worlds.* Accounts of chemical research, 2019.

50. Zhu, L., et al., *Dual-phase molybdenum nitride nanorambutans for solar steam generation under one sun illumination.* Nano Energy, 2019. **57**: p. 842-850.

51. Gueymard, C.A., *The sun's total and spectral irradiance for solar energy applications and solar radiation models.* Solar energy, 2004. **76**(4): p. 423-453.

52. Lin, Y., et al., *Solar steam generation based on the photothermal effect: from designs to applications, and beyond.* Journal of Materials Chemistry A, 2019. **7**(33): p. 19203-19227.

53. Tao, F., et al., *CuS nanoflowers/semipermeable collodion membrane composite for high-efficiency solar vapor generation.* Materials today energy, 2018. **9**: p. 285-294.

54. Zhao, Y., et al., *Plasmonic Cu2− x S nanocrystals: optical and structural properties of copper-deficient copper (I) sulfides.* Journal of the American Chemical Society, 2009. **131**(12): p. 4253-4261.

55. Coughlan, C., et al., *Compound copper chalcogenide nanocrystals.* Chemical reviews, 2017. **117**(9): p. 5865-6109.

56. Zhang, C., et al., *Shape-Controlled Synthesis of High-Quality Cu7S4 Nanocrystals for Efficient Light-Induced Water Evaporation.* Small, 2016. **12**(38): p. 5320-5328.

57. Sivula, K. and R. Van De Krol, *Semiconducting materials for photoelectrochemical energy conversion.* Nature Reviews Materials, 2016. **1**(2): p. 15010.

58. Mu, C., et al., *High Solar Desalination Efficiency Achieved with 3D Cu2ZnSnS4 Nanosheet-Assembled Membranes.* Advanced Sustainable Systems, 2017. **1**(10): p. 1700064.

59. Guo, Q., H.W. Hillhouse, and R. Agrawal, *Synthesis of Cu2ZnSnS4 nanocrystal ink and its use for solar cells.* Journal of the American Chemical Society, 2009. **131**(33): p. 11672-11673.

60. Zhang, J., et al., *Shape tailored Cu2ZnSnS4 nanosheet aggregates for high efficiency solar desalination.* Materials Research Bulletin, 2019: p. 110529.

61. Hirate, Y., et al., *Dielectric functions of Cu2ZnSnSe4 and Cu2SnSe3 semiconductors.* Journal of Applied Physics, 2015. **117**(1): p. 015702.

62. Yang, Y., et al., *Membrane assembled from anti-fouling copper-zinc-tin-selenide nanocarambolas for solar-driven interfacial water evaporation.* Chemical Engineering Journal, 2019. **373**: p. 955-962.

63. Li, Z., et al., *Broadband-absorbing WO3-x nanorod-decorated wood evaporator for highly efficient solar-driven interfacial steam generation.* Solar Energy Materials and Solar Cells, 2020. **205**: p. 110254.

64. Di Valentin, C. and G. Pacchioni, *Spectroscopic properties of doped and defective semiconducting oxides from hybrid density functional calculations.* Accounts of chemical research, 2014. **47**(11): p. 3233-3241.

65. DeSantis, C.J., M.J. McClain, and N.J. Halas, *Walking the Walk: A giant step toward sustainable plasmonics.* ACS nano, 2016. **10**(11): p. 9772-9775.

66. Cong, S., F. Geng, and Z. Zhao, *Tungsten oxide materials for optoelectronic applications.* Advanced Materials, 2016. **28**(47): p. 10518-10528.

67. Ding, D., et al., *Non-stoichiometric MoO 3− x quantum dots as a light-harvesting material for interfacial water evaporation.* Chemical Communications, 2017. **53**(50): p. 6744-6747.

68. Dey, A., *Semiconductor metal oxide gas sensors: A review.* Materials Science and Engineering: B, 2018. **229**: p. 206-217.

69. Saenger, M., et al., *Polaron and phonon properties in proton intercalated amorphous tungsten oxide thin films.* Physical Review B, 2008. **78**(24): p. 245205.

70. Chala, T.F., et al., *Melt electrospun reduced tungsten oxide/polylactic acid fiber membranes as a photothermal material for light-driven interfacial water evaporation.* ACS applied materials & interfaces, 2018. **10**(34): p. 28955-28962.

71. Sun, L., et al., *Phase-Transition Induced Conversion into a Photothermal Material: Quasi-Metallic WO2.9 Nanorods for Solar Water Evaporation and Anticancer Photothermal Therapy.* Angewandte Chemie International Edition, 2018. **57**(33): p. 10666-10671.

72. Fang, Z., et al., *A Flexible, Self-Floating Composite for Efficient Water Evaporation.* Global Challenges, 2018: p. 1800085.

73. Chang, Y., et al., *Hydrophobic W18O49 mesocrystal on hydrophilic PTFE membrane as an efficient solar steam generation device under one sun.* Journal of Materials Chemistry A, 2018. **6**(23): p. 10939-10946.

74. Lu, Q., et al., *Oxygen-Defected Molybdenum Oxides Hierarchical Nanostructure Constructed by Atomic-Level Thickness Nanosheets as an Efficient Absorber for Solar Steam Generation.* Solar RRL, 2019. **3**(2): p. 1800277.

75. Wang, M., et al., *Plasmon-Mediated Solar Energy Conversion via Photocatalysis in Noble Metal/Semiconductor Composites.* Advanced Science, 2016. **3**(6): p. 1600024.

76. Wu, N., *Plasmonic metal–semiconductor photocatalysts and photoelectrochemical cells: a review.* Nanoscale, 2018. **10**(6): p. 2679-2696.

77. Wang, J., et al., *High-performance photothermal conversion of narrow-bandgap Ti2O3 nanoparticles.* Advanced Materials, 2017. **29**(3): p. 1603730.

78. Tao, F., et al., *Copper sulfide-based plasmonic photothermal membrane for high-efficiency solar vapor generation.* ACS applied materials & interfaces, 2018. **10**(41): p. 35154-35163.

79. Li, T., et al., *Ultra-robust carbon fibers for multi-media purification via solar-evaporation.* Journal of Materials Chemistry A, 2019. **7**(2): p. 586-593.

80. Yang, X., et al., *An ultrathin flexible 2D membrane based on single-walled nanotube–MoS2 hybrid film for high-performance solar steam generation.* Advanced Functional Materials, 2018. **28**(3): p. 1704505.

81. Yao, J., Z. Zheng, and G. Yang, *Layered tin monoselenide as advanced photothermal conversion materials for efficient solar energy-driven water evaporation.* Nanoscale, 2018. **10**(6): p. 2876-2886.

82. Shang, M., et al., *Full-spectrum solar-to-heat conversion membrane with interfacial plasmonic heating ability for high-efficiency desalination of seawater.* ACS Applied Energy Materials, 2017. **1**(1): p. 56-61.

83. Kiriarachchi, H.D., et al., *Plasmonic chemically modified cotton nanocomposite fibers for efficient solar water desalination and wastewater treatment.* Nanoscale, 2018. **10**(39): p. 18531-18539.

84. Hammer, B. and J.K. Norskov, *Why gold is the noblest of all the metals.* Nature, 1995. **376**(6537): p. 238-240.

85. Badawy, A.M.E., et al., *Impact of environmental conditions (pH, ionic strength, and electrolyte type) on the surface charge and aggregation of silver nanoparticles suspensions.* Environmental science & technology, 2010. **44**(4): p. 1260-1266.

86. Linic, S., et al., *Photochemical transformations on plasmonic metal nanoparticles.* Nature materials, 2015. **14**(6): p. 567-576.

87. Kim, M., J.-H. Lee, and J.-M. Nam, *Plasmonic Photothermal Nanoparticles for Biomedical Applications.* Advanced Science. **0**(0): p. 1900471.

88. Guo, A., et al., *Diameter effect of gold nanoparticles on photothermal conversion for solar steam generation.* RSC Advances, 2017. **7**(8): p. 4815-4824.

89. Zhou, L., et al., *Self-assembled spectrum selective plasmonic absorbers with tunable bandwidth for solar energy conversion.* Nano Energy, 2017. **32**: p. 195-200.

90. Bae, K., et al., *Flexible thin-film black gold membranes with ultrabroadband plasmonic nanofocusing for efficient solar vapour generation.* Nature communications, 2015. **6**: p. 10103.

91. Wang, Y., et al., *A facile nanocomposite strategy to fabricate a rGO–MWCNT photothermal layer for efficient water evaporation.* Journal of Materials Chemistry A, 2018. **6**(3): p. 963-971.

92. Fang, J., et al., *Ag/diatomite for highly efficient solar vapor generation under one-sun irradiation.* Journal of Materials Chemistry A, 2017. **5**(34): p. 17817-17821.

93. Lee, W., *The anodization of aluminum for nanotechnology applications.* Jom, 2010. **62**(6): p. 57-63.

94. Zhou, L., et al., *3D self-assembly of aluminium nanoparticles for plasmon-enhanced solar desalination.* Nature Photonics, 2016. **10**(6): p. 393.

95. Zhu, M., et al., *Plasmonic wood for high-efficiency solar steam generation.* Advanced Energy Materials, 2018. **8**(4): p. 1701028.

96. Wang, X., et al., *Solar steam generation through bio-inspired interface heating of broadband-absorbing plasmonic membranes.* Applied energy, 2017. **195**: p. 414-425.

97. Sheng, C., et al., *Bamboo decorated with plasmonic nanoparticles for efficient solar steam generation.* Applied Thermal Engineering, 2020. **167**: p. 114712.

98. Ghim, D., et al., *Mechanically interlocked 1T/2H phases of MoS2 nanosheets for solar thermal water purification.* Nano energy, 2018. **53**: p. 949-957.

99. Wu, X., et al., *Photothermal materials: a key platform enabling highly efficient water evaporation driven by solar energy.* Materials Today Energy, 2019. **12**: p. 277-296.

100. Feast, W., et al., *Synthesis, processing and material properties of conjugated polymers.* Polymer, 1996. **37**(22): p. 5017-5047.

101. Xu, L., et al., *Conjugated polymers for photothermal therapy of cancer.* Polymer Chemistry, 2014. **5**(5): p. 1573-1580.

102. Wang, Y., et al., *Photothermal-Responsive Conjugated Polymer Nanoparticles for Remote Control of Gene Expression in Living Cells.* Advanced Materials, 2018. **30**(8): p. 1705418.

103. Lyu, Y., et al., *Semiconducting polymer nanobioconjugates for targeted photothermal activation of neurons.* Journal of the American Chemical Society, 2016. **138**(29): p. 9049-9052.

104. Jiang, Q., et al., *Polydopamine-filled bacterial nanocellulose as a biodegradable interfacial photothermal evaporator for highly efficient solar steam generation.* Journal of Materials Chemistry A, 2017. **5**(35): p. 18397-18402.

105. Wu, X., et al., *A plant-transpiration-process-inspired strategy for highly efficient solar evaporation.* Advanced Sustainable Systems, 2017. **1**(6): p. 1700046.

106. Zou, Y., et al., *A Mussel-Inspired Polydopamine-Filled Cellulose Aerogel for Solar-Enabled Water Remediation.* ACS Applied Materials & Interfaces, 2021. **13**(6): p. 7617-7624.

107. Zhang, L., et al., *Waste semi-coke/polydopamine based self-floating solar evaporator for water purification.* Solar Energy Materials and Solar Cells, 2021. **230**: p. 111237.

108. Ahmed, E.M., *Hydrogel: Preparation, characterization, and applications: A review.* Journal of advanced research, 2015. **6**(2): p. 105-121.

109. Mathur, A.M., S.K. Moorjani, and A.B. Scranton, *Methods for synthesis of hydrogel networks: A review.* Journal of Macromolecular Science, Part C: Polymer Reviews, 1996. **36**(2): p. 405-430.

110. Kumar, A. and S.S. Han, *PVA-based hydrogels for tissue engineering: A review.* International journal of polymeric materials and polymeric biomaterials, 2017. **66**(4): p. 159-182.

111. Xu, T., et al., *Sustainable self-cleaning evaporator for long-term solar desalination using gradient structure tailored hydrogel.* Chemical Engineering Journal, 2021. **415**: p. 128893.

112. Lei, W., et al., *Hierarchical structures hydrogel evaporator and superhydrophilic water collect device for efficient solar steam evaporation.* Nano Research, 2021. **14**(4): p. 1135-1140.

113. Guo, Y., et al., *Biomass-derived hybrid hydrogel evaporators for cost-effective solar water purification.* Advanced Materials, 2020. **32**(11): p. 1907061.

114. Wu, Y., et al., *Polyacid doping-enabled efficient solar evaporation of polypyrrole hydrogel.* Desalination, 2021. **505**: p. 114766.

115. Park, S.H., et al., *Simultaneous solar-driven seawater desalination and spontaneous power generation using polyvalent crosslinked polypyrrole/alginate hydrogels.* Desalination, 2021. **500**: p. 114900.

116. Bashir, S., et al., *Fundamental concepts of hydrogels: Synthesis, properties, and their applications.* Polymers, 2020. **12**(11): p. 2702.

117. Jiang, S., S. Liu, and W. Feng, *PVA hydrogel properties for biomedical application.* Journal of the mechanical behavior of biomedical materials, 2011. **4**(7): p. 1228-1233.

118. Yu, Z. and P. Wu, *Biomimetic MXene-polyvinyl alcohol composite hydrogel with vertically aligned channels for highly efficient solar steam generation.* Advanced Materials Technologies, 2020. **5**(6): p. 2000065.

119. Hao, L., et al., *High-performance solar-driven interfacial evaporation through molecular design of antibacterial, biomass-derived hydrogels.* Journal of Colloid and Interface Science, 2022. **608**: p. 840-852.

120. Xu, Y., et al., *Facile fabrication of low-cost starch-based biohydrogel evaporator for efficient solar steam generation.* Desalination, 2021. **517**: p. 115260.

121. Irshad, M.S., et al., *Semiconductive, Flexible MnO2 NWs/Chitosan Hydrogels for Efficient Solar Steam Generation.* ACS Sustainable Chemistry & Engineering, 2021. **9**(10): p. 3887-3900.

122. Yu, F., et al., *Molybdenum carbide/carbon-based chitosan hydrogel as an effective solar water evaporation accelerator.* ACS Sustainable Chemistry & Engineering, 2020. **8**(18): p. 7139-7149.

123. Yin, X., et al., *Macroporous double-network hydrogel for high-efficiency solar steam generation under 1 sun illumination.* ACS applied materials & interfaces, 2018. **10**(13): p. 10998-11007.

124. Ismail, H., M. Irani, and Z. Ahmad, *Starch-based hydrogels: present status and applications.* International Journal of Polymeric Materials and Polymeric Biomaterials, 2013. **62**(7): p. 411-420.

125. Guo, Y., et al., *Scalable carbon black deposited fabric/hydrogel composites for affordable solar-driven water purification.* Journal of Materials Science & Technology, 2022. **106**: p. 10-18.

126. Xiao, C., et al., *Ag/polypyrrole co-modified poly (ionic liquid) s hydrogels as efficient solar generators for desalination.* Materials Today Energy, 2020. **16**: p. 100417.

127. Xu, Y., et al., *Multifunctional CuO nanowire mesh for highly efficient solar evaporation and water purification.* ACS Sustainable Chemistry & Engineering, 2019.

128. Tao, F., et al., *CuS nanoflowers/semipermeable collodion membrane composite for high-efficiency solar vapor generation.* 2018. **9**: p. 285-294.

129. Shang, M., et al., *Full-spectrum solar-to-heat conversion membrane with interfacial plasmonic heating ability for high-efficiency desalination of seawater.* 2017. **1**(1): p. 56-61.

130. Tao, F., et al., *Copper Sulfide-Based Plasmonic Photothermal Membrane for High-Efficiency Solar Vapor Generation.* 2018. **10**(41): p. 35154-35163.

131. Guo, Z., et al., *Super-hydrophilic copper sulfide films as light absorbers for efficient solar steam generation under one sun illumination.* 2018. **33**(2): p. 025008.

132. Hua, Z., et al., *Designing a novel photothermal material of hierarchical microstructured copper phosphate for solar evaporation enhancement.* 2016. **121**(1): p. 60-69.

133. Wu, X., et al., *A flexible photothermal cotton-CuS nanocage-agarose aerogel towards portable solar steam generation.* Nano energy, 2019. **56**: p. 708-715.

134. Guo, Z., et al., *Super-hydrophilic copper sulfide films as light absorbers for efficient solar steam generation under one sun illumination.* Semiconductor Science and Technology, 2018. **33**(2): p. 025008.

135. Huang, W., et al., *Three-dimensional hierarchical CuxS-based evaporator for high-efficiency multifunctional solar distillation.* Nano Energy, 2020: p. 104465.

136. Yang, Y., et al., *A general salt-resistant hydrophilic/hydrophobic nanoporous double layer design for efficient and stable solar water evaporation distillation.* 2018. **5**(6): p. 1143-1150.

137. Song, C., et al., *Hydrophobic Cu12Sb4S13-deposited photothermal film for interfacial water evaporation and thermal antibacterial activity.* New Journal of Chemistry, 2018. **42**(5): p. 3175-3179.

138. Shi, Y., et al., *A Robust CuCr2O4/SiO2 Composite Photothermal Material with Underwater Black Property and Extremely High Thermal Stability for Solar-Driven Water Evaporation.* Advanced Sustainable Systems, 2018. **2**(3): p. 1700145.

139. Li, N., et al., *High-quality ultralong copper sulphide nanowires for promising applications in high efficiency solar water evaporation.* 2019. **3**(3): p. 394-398.

140. Li, W., et al., *Synergistic High-Rate Solar Steaming and Mercury Removal with MoS2/C@ Polyurethane Composite Sponges.* 2018. **8**(32): p. 1802108.

141. Guo, Z., et al., *PEGylated Self-Growth MoS2 on a Cotton Cloth Substrate for High-Efficiency Solar Energy Utilization.* 2018. **10**(29): p. 24583-24589.

142. Chen, R., et al., *A bifunctional MoS 2-based solar evaporator for both efficient water evaporation and clean freshwater collection.* 2019. **7**(18): p. 11177-11185.

143. Wang, M., et al., *A Ternary Pt/Au/TiO2-Decorated Plasmonic Wood Carbon for High-Efficiency Interfacial Solar Steam Generation and Photodegradation of Tetracycline.* ChemSusChem, 2019. **12**(2): p. 467-472.

144. Wang, X., Y. He, and X. Liu, *Synchronous steam generation and photodegradation for clean water generation based on localized solar energy harvesting.* Energy Conversion and Management, 2018. **173**: p. 158-166.

145. Sheng, C., et al., *Bamboo decorated with plasmonic nanoparticles for efficient solar steam generation.* Applied Thermal Engineering, 2019: p. 114712.

146. Bae, K., et al., *Flexible thin-film black gold membranes with ultrabroadband plasmonic nanofocusing for efficient solar vapour generation.* Nature communications, 2015. **6**(1): p. 1-9.

147. Zhou, L., et al., *3D self-assembly of aluminium nanoparticles for plasmon-enhanced solar desalination.* Nature Photonics, 2016. **10**(6): p. 393-398.

148. Li, T., et al., *Enhancing solar steam generation through manipulating the heterostructure of PVDF membranes with reduced reflection and conduction.* Journal of Materials Chemistry A, 2019. **7**(29): p. 17505-17515.

149. Yu, H., et al., *Polydopamine-Coated Natural Rubber Sponge for Highly Efficient Vapor Generation.* Polymers, 2022. **14**(7): p. 1486.

150. Zhang, C., et al., *Harnessing solar-driven photothermal effect toward the water–energy nexus.* Advanced Science, 2019. **6**(18): p. 1900883.

151. Zhao, J., et al., *A hydrophobic surface enabled salt-blocking 2D Ti 3 C 2 MXene membrane for efficient and stable solar desalination.* Journal of Materials Chemistry A, 2018. **6**(33): p. 16196-16204.

152. Xu, Y., et al., *Multifunctional CuO nanowire mesh for highly efficient solar evaporation and water purification.* ACS Sustainable Chemistry & Engineering, 2019. **7**(5): p. 5476-5485.

153. Liu, H., et al., *Narrow bandgap semiconductor decorated wood membrane for high-efficiency solar-assisted water purification.* Journal of Materials Chemistry A, 2018. **6**(39): p. 18839-18846.

154. Guo, D. and X. Yang, *Highly efficient solar steam generation of low cost TiN/bio-carbon foam.* Science China Materials, 2019. **62**(5): p. 711-718.

155. Shi, Y., et al., *A 3D photothermal structure toward improved energy efficiency in solar steam generation.* Joule, 2018. **2**(6): p. 1171-1186.

156. Zhou, J., et al., *Development and evolution of the system structure for highly efficient solar steam generation from zero to three dimensions.* Advanced Functional Materials, 2019. **29**(50): p. 1903255.

157. Huang, W., et al., *Three-dimensional hierarchical CuxS-based evaporator for high-efficiency multifunctional solar distillation.* Nano Energy, 2020. **69**: p. 104465.

158. Cao, S., et al., *Advances in solar evaporator materials for freshwater generation.* Journal of Materials Chemistry A, 2019. **7**(42): p. 24092-24123.

159. Zhao, X., et al., *Macroporous three-dimensional MXene architectures for highly efficient solar steam generation.* Journal of Materials Chemistry A, 2019. **7**(17): p. 10446-10455.

160. Yang, Y., et al., *A general salt-resistant hydrophilic/hydrophobic nanoporous double layer design for efficient and stable solar water evaporation distillation.* Materials Horizons, 2018. **5**(6): p. 1143-1150.

161. Yi, L., et al., *Scalable and low-cost synthesis of black amorphous Al-Ti-O nanostructure for high-efficient photothermal desalination.* Nano Energy, 2017. **41**: p. 600-608.

162. Yi, L., et al., *Hollow black TiAlO x nanocomposites for solar thermal desalination.* Nanoscale, 2019. **11**(20): p. 9958-9968.

163. Zeng, Y., et al., *Solar evaporation enhancement using floating light-absorbing magnetic particles.* Energy & Environmental Science, 2011. **4**(10): p. 4074-4078.

164. Wang, J., et al., *Microporous cokes formed in zeolite catalysts enable efficient solar evaporation.* Journal of Materials Chemistry A, 2017. **5**(15): p. 6860-6865.

165. Li, J., et al., *Migration crystallization device based on biomass photothermal materials for efficient salt-rejection solar steam generation.* ACS Applied Energy Materials, 2020. **3**(3): p. 3024-3032.

166. He, S., et al., *Nature-inspired salt resistant bimodal porous solar evaporator for efficient and stable water desalination.* Energy & Environmental Science, 2019. **12**(5): p. 1558-1567.

167. Finnerty, C., et al., *Synthetic graphene oxide leaf for solar desalination with zero liquid discharge.* Environmental science & technology, 2017. **51**(20): p. 11701-11709.

168. Fan, Y., et al., *Conductively monolithic polypyrrole 3-D porous architecture with micron-sized channels as superior salt-resistant solar steam generators.* Solar Energy Materials and Solar Cells, 2020. **206**: p. 110347.

169. Kou, H., et al., *Recyclable CNT-coupled cotton fabrics for low-cost and efficient desalination of seawater under sunlight.* Desalination, 2019. **462**: p. 29-38.

170. Zhao, L., et al., *Co2. 67S4-Based Photothermal Membrane with High Mechanical Properties for Efficient Solar Water Evaporation and Photothermal Antibacterial Applications.* ACS applied materials & interfaces, 2019. **11**(23): p. 20820-20827.

171. Xu, W., et al., *Flexible and salt resistant Janus absorbers by electrospinning for stable and efficient solar desalination.* Advanced Energy Materials, 2018. **8**(14): p. 1702884.

172. Zhao, Q., et al., *Solar-powered Janus membrane for one-step conversion of sewage to clean water.* Chemical Engineering Journal, 2020. **387**: p. 124131.

173. Gao, S., et al., *Bioinspired Soot-Deposited Janus Fabrics for Sustainable Solar Steam Generation with Salt-Rejection.* Global Challenges, 2019. **3**(8): p. 1800117.

174. Li, L., et al., *GO/CNT-silica Janus nanofibrous membrane for solar-driven interfacial steam generation and desalination.* Journal of the Taiwan Institute of Chemical Engineers, 2020. **111**: p. 191-197.

175. He, J., et al., *High-performance salt-rejecting and cost-effective superhydrophilic porous monolithic polymer foam for solar steam generation.* ACS applied materials & interfaces, 2020. **12**(14): p. 16308-16318.

176. Xu, N., et al., *A water lily–inspired hierarchical design for stable and efficient solar evaporation of high-salinity brine.* Science advances, 2019. **5**(7): p. eaaw7013.

177. Chen, R., et al., *Interfacial solar heating by self-assembled Fe 3 O 4@ C film for steam generation.* Materials Chemistry Frontiers, 2017. **1**(12): p. 2620-2626.

178. Chen, R., et al., *Magnetically recyclable self-assembled thin films for highly efficient water evaporation by interfacial solar heating.* RSC advances, 2017. **7**(32): p. 19849-19855.

179. Ye, M., et al., *Synthesis of black TiOx nanoparticles by Mg reduction of TiO2 nanocrystals and their application for solar water evaporation.* Advanced Energy Materials, 2017. **7**(4): p. 1601811.

180. Song, C., et al., *Hydrophobic Cu 12 Sb 4 S 13-deposited photothermal film for interfacial water evaporation and thermal antibacterial activity.* New Journal of Chemistry, 2018. **42**(5): p. 3175-3179.

181. Ye, M., et al., *Synthesis of black TiOx nanoparticles by Mg reduction of TiO2 nanocrystals and their application for solar water evaporation.* 2017. **7**(4): p. 1601811.

182. Xu, K., et al., *Salt Mitigation Strategies of Solar-Driven Interfacial Desalination.* Advanced Functional Materials, 2021. **31**(8): p. 2007855.

183. Wang, T., et al., *Three-dimensional hierarchical oxygen vacancy-rich WO3-decorated Ni foam evaporator for high-efficiency solar-driven interfacial steam generation.* Journal of Colloid and Interface Science, 2021. **602**: p. 767-777.

184. Gong, L., et al., *Highly Efficient Solar Evaporator Based on Graphene/MoO3-x Coated Porous Nickel for Water Purification.* Separation and Purification Technology, 2021: p. 119139.

185. Ren, H., et al., *Hierarchical graphene foam for efficient omnidirectional solar–thermal energy conversion.* Advanced Materials, 2017. **29**(38): p. 1702590.

186. Kuang, Y., et al., *A high-performance self-regenerating solar evaporator for continuous water desalination.* Advanced Materials, 2019. **31**(23): p. 1900498.

187. Wang, C., et al., *A Facile and General Strategy to Deposit Polypyrrole on Various Substrates for Efficient Solar-Driven Evaporation.* 2019. **3**(1): p. 1800108.

188. Zhang, J., et al., *Shape tailored Cu2ZnSnS4 nanosheet aggregates for high efficiency solar desalination.* Materials Research Bulletin, 2019. **118**: p. 110529.

189. Wang, F., et al., *Salt-Resistant Photothermal Materials Based on Monolithic Porous Ionic Polymers for Efficient Solar Steam Generation.* ACS Applied Energy Materials, 2020. **3**(9): p. 8746-8754.

190. Ghafurian, M.M., et al., *Wood surface treatment techniques for enhanced solar steam generation.* Renewable Energy, 2020. **146**: p. 2308-2315.

191. Varaprasad, K., et al., *A mini review on hydrogels classification and recent developments in miscellaneous applications.* Materials Science and Engineering: C, 2017. **79**: p. 958-971.

192. Pita-López, M.L., et al., *Physically cross-linked chitosan-based hydrogels for tissue engineering applications: A state-of-the-art review.* European Polymer Journal, 2021. **145**: p. 110176.

193. Hu, W., et al., *Advances in crosslinking strategies of biomedical hydrogels.* Biomaterials science, 2019. **7**(3): p. 843-855.

194. Batul, R., et al., *Recent progress in the biomedical applications of polydopamine nanostructures.* Biomaterials science, 2017. **5**(7): p. 1204-1229.

195. Ryu, J.H., P.B. Messersmith, and H. Lee, *Polydopamine surface chemistry: a decade of discovery.* ACS applied materials & interfaces, 2018. **10**(9): p. 7523-7540.

196. Zhou, W., et al., *Fundamentals of scanning electron microscopy (SEM)*, in *Scanning microscopy for nanotechnology*. 2006, Springer. p. 1-40.

197. Connolly, J.R., *Introduction to X-ray powder diffraction.* European Physical Society of Journal, 2007. **4**: p. p400.

198. Bunaciu, A.A., E.G. UdriŞTioiu, and H.Y. Aboul-Enein, *X-ray diffraction: instrumentation and applications.* Critical reviews in analytical chemistry, 2015. **45**(4): p. 289-299.

199. Prabhu, S., et al. *Production of X-RAYS using X-RAY Tube*. in *Journal of Physics: Conference Series*. 2020. IOP Publishing.

200. Hertz, H., *Ueber sehr schnelle electrische Schwingungen.* Annalen der Physik, 1887. **267**(7): p. 421-448.

201. Greczynski, G. and L. Hultman, *X-ray photoelectron spectroscopy: Towards reliable binding energy referencing.* Progress in Materials Science, 2020. **107**: p. 100591.

202. Engelhard, M.H., T.C. Droubay, and Y. Du, *X-ray photoelectron spectroscopy applications*. 2017, Pacific Northwest National Laboratory (PNNL), Richland, WA (US ….

203. Akash, M.S.H. and K. Rehman, *Thermo Gravimetric Analysis*, in *Essentials of Pharmaceutical Analysis*. 2020, Springer Singapore: Singapore. p. 215-222.

204. Ye, H., et al., *Silver nanoparticles-enabled photothermal nanofibrous membrane for light-driven membrane distillation.* Industrial & Engineering Chemistry Research, 2019.

205. Yao, M., *Membrane Fabrication and Modification for the Treatment of Wastewater Using Membrane Distillation*. 2020.

206. Smith, E. and G. Dent, *Modern Raman spectroscopy: a practical approach*. 2019: John Wiley & Sons.

207. Hou, X., et al., *Applications of Fourier transform infrared spectroscopy technologies on asphalt materials.* Measurement, 2018. **121**: p. 304-316.

208. https://jascoinc.com/learning-center/theory/spectroscopy/uv-vis-spectroscopy/.

209. Hamdy, O. and H.S. Mohammed, *Investigating the transmission profiles of 808 nm laser through different regions of the rat's head.* Lasers in Medical Science, 2021. **36**(4): p. 803-810.

210. Huang, Q., et al., *Study on photothermal PVDF/ATO nanofiber membrane and its membrane distillation performance.* Journal of Membrane Science, 2019.

211. Tao, F., et al., *Graphite powder/semipermeable collodion membrane composite for water evaporation.* Solar Energy Materials and Solar Cells, 2018. **180**: p. 34-45.

212. Lu, Y., et al., *Biomass derived janus solar evaporator for synergic water evaporation and purification.* Sustainable Materials and Technologies, 2020: p. e00180.

213. Zhao, H.-Y., et al., *Lotus-Inspired Evaporator with Janus Wettability and Bimodal Pores for Solar Steam Generation.* Cell Reports Physical Science, 2020. **1**(6): p. 100074.

214. Organization, W.H., *Guidelines for drinking-water quality*. 1993: World Health Organization.

215. EPA, U., *2012 Edition of the drinking water standards and health advisories.* EPA 822-S-12-001, 2012.

216. Lu, Q., et al., *Nanoconfined Water-Molecule Channels for High-Yield Solar Vapor Generation under Weaker Sunlight.* Advanced Materials, 2020. **32**(42): p. 2001544.

217. Zhao, F., et al., *Materials for solar-powered water evaporation.* Nature Reviews Materials, 2020. **5**(5): p. 388-401.

218. Sun, Y., et al., *Copper sulfide-macroporous polyacrylamide hydrogel for solar steam generation.* Chemical Engineering Science, 2019. **207**: p. 516-526.

219. Li, X., et al., *A Novel Flake-like Cu7S4 Solar Absorber for High-Performance Large-Scale Water Evaporation.* ACS Applied Energy Materials, 2019. **2**(7): p. 5154-5161.

220. Chen, J., et al., *Janus Evaporators with Self-Recovering Hydrophobicity for Salt-Rejecting Interfacial Solar Desalination.* ACS nano, 2020. **14**(12): p. 17419-17427.

221. Wei, N., et al., *Scalable and low-cost fabrication of hydrophobic PVDF/WS2 porous membrane for highly efficient solar steam generation.* Journal of Colloid and Interface Science, 2021. **588**: p. 369-377.

222. Wang, F., et al., *Salt-Rejection Solar Absorbers Based on Porous Ionic Polymers Nanowires for Desalination.* Macromolecular Rapid Communications, 2020: p. 2000536.

223. Zhao, X. and C. Liu, *Overcoming salt crystallization with ionic hydrogel for accelerating solar evaporation.* Desalination, 2020. **482**: p. 114385.

224. Zhang, J., et al., *Controllable hydrothermal synthesis of ZnO nanowires arrays on Al-doped ZnO seed layer and patterning of ZnO nanowires arrays via surface modification of substrate.* Applied surface science, 2011. **257**(23): p. 10134-10140.

225. Kushwah, R., et al., *Facile and controlled synthesis of copper sulfide nanostructures of varying morphology.* Journal of Materials Science: Materials in Electronics, 2017. **28**(7): p. 5597-5602.

226. Huo, Y., et al., *All-solid-state artificial Z-scheme porous g-C3N4/Sn2S3-DETA heterostructure photocatalyst with enhanced performance in photocatalytic CO2 reduction.* Applied Catalysis B: Environmental, 2019. **241**: p. 528-538.

227. Xue, C., et al., *Bonding CdS-Sn2S3 eutectic clusters on graphene nanosheets with unusually photoreaction-driven structural reconfiguration effect for excellent H2 evolution and Cr (VI) reduction.* Applied Catalysis B: Environmental, 2018. **222**: p. 157-166.

228. Iqbal, S., et al., *Shape and phase-controlled synthesis of specially designed 2D morphologies of L-cysteine surface capped covellite (CuS) and chalcocite (Cu2S) with excellent photocatalytic properties in the visible spectrum.* Applied Surface Science, 2020. **526**: p. 146691.

229. Zhou, S.-l., et al., *Synthesis and photocatalytic performance of copper sulfide by a simple solvothermal method.* Chemical Physics Letters, 2020. **759**: p. 138034.

230. Wei, W., et al., *Highly compact nanochannel thin films with exceptional thermal conductivity and water pumping for efficient solar steam generation.* Journal of Materials Chemistry A, 2020. **8**(28): p. 13927-13934.

231. Su, L., et al., *Synthesis of hollow copper sulfide nanocubes with low emissivity for highly efficient solar steam generation.* Solar Energy Materials and Solar Cells, 2020. **210**: p. 110484.

232. Seo, D.H., et al., *Deterministic control of structural and optical properties of plasma-grown vertical graphene nanosheet networks via nitrogen gas variation.* Optical Materials Express, 2012. **2**(6): p. 700-707.

233. Fan, H., et al., *A design of bifunctional photothermal layer on polysulfone membrane with enclosed cellular-like structure for efficient solar steam generation.* Chemical Engineering Journal, 2021. **415**: p. 128798.

234. Sun, P., et al., *3D Interconnected Gyroid Au–CuS Materials for Efficient Solar Steam Generation.* ACS Applied Materials & Interfaces, 2020. **12**(31): p. 34837-34847.

235. Yang, T., et al., *Carbon-based absorbers for solar evaporation: Steam generation and beyond.* Sustainable Materials and Technologies, 2020: p. e00182.

236. Zada, I., et al., *Superior photothermal black TiO2 with random size distribution as flexible film for efficient solar steam generation.* Applied Materials Today, 2020. **20**: p. 100669.

237. Liu, F., et al., *Low cost, robust, environmentally friendly geopolymer–mesoporous carbon composites for efficient solar powered steam generation.* Advanced Functional Materials, 2018. **28**(47): p. 1803266.

238. Zhang, X., et al., *Self-floating monodisperse microparticles with a nano-engineered surface composition and structure for highly efficient solar-driven water evaporation.* 2019.

239. Grammatikopoulos, S., et al., *Self-assembled Au nanoparticles on heated Corning glass by dc magnetron sputtering: size-dependent surface plasmon resonance tuning.* Journal of nanoparticle research, 2013. **15**(2): p. 1-8.

240. Barbosa, A.I., et al., *Development of label-free plasmonic Au-TiO2 thin film immunosensor devices.* Materials Science and Engineering: C, 2019. **100**: p. 424-432.

241. Greene, J.E., *Tracing the recorded history of thin-film sputter deposition: From the 1800s to 2017.* Journal of Vacuum Science & Technology A: Vacuum, Surfaces, and Films, 2017. **35**(5): p. 05C204.

242. Chang, Y., et al., *Hydrophobic W 18 O 49 mesocrystal on hydrophilic PTFE membrane as an efficient solar steam generation device under one sun.* Journal of Materials Chemistry A, 2018. **6**(23): p. 10939-10946.

243. Pinho, A.C. and A.P. Piedade, *Zeta potential, contact angles, and AFM imaging of protein conformation adsorbed on hybrid nanocomposite surfaces.* ACS Applied Materials & Interfaces, 2013. **5**(16): p. 8187-8194.

244. Saravanakumar, K., et al., *Synthesis and characterization of nano-chitosan capped gold nanoparticles with multifunctional bioactive properties.* International Journal of Biological Macromolecules, 2020. **165**: p. 747-757.

245. Politano, A., et al., *Photothermal membrane distillation for seawater desalination.* 2017. **29**(2): p. 1603504.

246. Kim, M., J.H. Lee, and J.M. Nam, *Plasmonic photothermal nanoparticles for biomedical applications.* Advanced Science, 2019. **6**(17): p. 1900471.

247. Chen, M., et al., *Plasmonic nanoparticle-embedded poly (p-phenylene benzobisoxazole) nanofibrous composite films for solar steam generation.* Nanoscale, 2018. **10**(13): p. 6186-6193.

248. Huang, Z., et al., *A broadband aggregation-independent plasmonic absorber for highly efficient solar steam generation.* Journal of Materials Chemistry A, 2020. **8**(21): p. 10742-10746.

249. Yang, J., et al., *Functionalized graphene enables highly efficient solar thermal steam generation.* ACS nano, 2017. **11**(6): p. 5510-5518.

250. Cai, W., et al., *Effect of crystal defects on solar steam generation performance of black phosphorous nanosheets.* Materials Today Energy, 2021. **19**: p. 100553.

251. Yao, J.D., Z.Q. Zheng, and G.W. Yang, *Alloying-assisted phonon engineering of layered BiInSe3@nickel foam for efficient solar-enabled water evaporation.* Nanoscale, 2017. **9**(42): p. 16396-16403.

252. Zhou, H., et al., *Assembling carbon dots on vertically aligned acetate fibers as ideal salt-rejecting evaporators for solar water purification.* Chemical Engineering Journal, 2021: p. 129822.

253. Irshad, M.S., et al., *Salt-resistant carbon dots modified solar steam system enhanced by chemical advection.* Carbon, 2021. **176**: p. 313-326.

254. Luo, Y.-Q., et al., *A nature-inspired suspended solar evaporator for water desalination of high-salinity brines.* Chemical Engineering Journal, 2021. **421**: p. 129824.

255. Zhang, J., et al., *Wetting and evaporation of salt-water nanodroplets: A molecular dynamics investigation.* Physical Review E, 2015. **92**(5): p. 052403.

256. Liu, F., et al., *Superwetting monolithic hypercrosslinked polymers nanotubes with high salt-resistance for efficient solar steam generation.* Solar Energy Materials and Solar Cells, 2021. **221**: p. 110913.

257. Wang, S., et al., *Potentially scalable fabrication of salt-rejection evaporator based on electrogenerated polypyrrole-coated nickel foam for efficient solar steam generation.* Desalination, 2021. **505**: p. 114982.

258. Wei, D., et al., *Ionic hyper-cross-linked polymers monoliths for efficient solar steam generation.* European Polymer Journal, 2021. **147**: p. 110281.

259. Chen, Z., et al., *Microgroove-Structured PDA/PEI/PPy@ PI-MS Photothermal Aerogel with a Multilevel Water Transport Network for Highly Salt-Rejecting Solar-Driven Interfacial Evaporation.* ACS Applied Materials & Interfaces, 2021.

260. Peng, F., et al., *A janus solar evaporator with 2D water path for highly efficient salt-resisting solar steam generation.* Solar Energy Materials and Solar Cells, 2021. **221**: p. 110910.

261. Huang, L., et al., *Laser-Engineered Graphene on Wood Enables Efficient Antibacterial, Anti-Salt-Fouling, and Lipophilic-Matter-Rejection Solar Evaporation.* ACS applied materials & interfaces, 2020. **12**(46): p. 51864-51872.

262. Cendrowski, K., et al., *The river water influence on cationic and anionic dyes collection by nickel foam with carbonized metal-organic frameworks and carbon nanotubes.* Journal of Alloys and Compounds, 2021. **876**: p. 160093.

263. Edison, T.N.J.I., et al., *A novel binder-free electro-synthesis of hierarchical nickel sulfide nanostructures on nickel foam as a battery-type electrode for hybrid-capacitors.* Fuel, 2020. **276**: p. 118077.

264. Liu, H., et al., *CoWO4–x-Based Photothermal Membranes for Solar-Driven Water Evaporation and Eutrophic Lake Water Purification.* ACS omega, 2020. **5**(49): p. 31598-31607.

265. Jiang, H., et al., *Broadband nickel sulfide/nickel foam-based solar evaporator for highly efficient water purification and electricity generation.* ACS Sustainable Chemistry & Engineering, 2020. **8**(29): p. 10833-10841.

266. Han, S., et al., *Flame synthesis of superhydrophilic carbon nanotubes/Ni foam decorated with Fe2O3 nanoparticles for water purification via solar steam generation.* ACS applied materials & interfaces, 2020. **12**(11): p. 13229-13238.

267. Zou, Y., et al., *Boosting solar steam generation by photothermal enhanced polydopamine/wood composites.* Polymer, 2021. **217**: p. 123464.

268. Lee, H., et al., *Mussel-inspired surface chemistry for multifunctional coatings.* science, 2007. **318**(5849): p. 426-430.

269. Zou, Y., et al., *Regulating the absorption spectrum of polydopamine.* Science advances, 2020. **6**(36): p. eabb4696.

270. Liu, Y., K. Ai, and L. Lu, *Polydopamine and its derivative materials: synthesis and promising applications in energy, environmental, and biomedical fields.* Chemical reviews, 2014. **114**(9): p. 5057-5115.

271. Barclay, T.G., et al., *Versatile surface modification using polydopamine and related polycatecholamines: Chemistry, structure, and applications.* Advanced Materials Interfaces, 2017. **4**(19): p. 1601192.

272. Fang, Y., et al., *Eco-friendly colorization of textile originating from polydopamine nanofilm structural color with high colorfastness.* Journal of Cleaner Production, 2021. **295**: p. 126523.

273. Zhou, W., et al., *A facile method for the fabrication of a superhydrophobic polydopamine-coated copper foam for oil/water separation.* Applied Surface Science, 2017. **413**: p. 140-148.

274. Mascaretti, L., et al., *Solar steam generation on scalable ultrathin thermoplasmonic TiN nanocavity arrays.* Nano Energy, 2021. **83**: p. 105828.

275. Shan, X., et al., *Porous reduced graphene oxide/nickel foam for highly efficient solar steam generation.* Nanotechnology, 2019. **30**(42): p. 425403.

276. Wang, P., et al., *Co3O4 nanoforest/Ni foam as the interface heating sheet for the efficient solar-driven water evaporation under one sun.* Sustainable Materials and Technologies, 2019. **20**: p. e00106.

277. Galeotti, G., et al., *Synthesis of mesoscale ordered two-dimensional π-conjugated polymers with semiconducting properties.* Nature Materials, 2020. **19**(8): p. 874-880.

278. Venz, S. and B. Dickens, *NIR-spectroscopic investigation of water sorption characteristics of dental resins and composites.* Journal of biomedical materials research, 1991. **25**(10): p. 1231-1248.

279. Ibrahim, I., et al., *3D microflowers CuS/Sn2S3 heterostructure for highly efficient solar steam generation and water purification.* Solar Energy Materials and Solar Cells, 2021. **232**: p. 111377.

280. Tian, Y., et al., *Farm-waste-derived recyclable photothermal evaporator.* Cell Reports Physical Science, 2021: p. 100549.

281. EPA, U., *Edition of the drinking water standards and health advisories.* US Environmental Protection Agency, Washington, DC, epa, 2006.

282. Li, H., et al., *Latest development in salt removal from solar-driven interfacial saline water evaporators: Advanced strategies and challenges.* Water research, 2020. **177**: p. 115770.

283. Feng, J., et al., *Low-cost and facile hydrophilic amplification of raw corn straws for the applications of highly efficient interfacial solar steam generation.* Materials Chemistry and Physics, 2021. **271**: p. 124904.

284. Peng, H., D. Wang, and S. Fu, *Artificial transpiration with asymmetric photothermal textile for continuous solar-driven evaporation, spatial salt harvesting and electrokinetic power generation.* Chemical Engineering Journal, 2021. **426**: p. 131818.

285. Xu, Y., et al., *Low cost, facile, environmentally friendly all biomass-based squid ink-starch hydrogel for efficient solar-steam generation.* Journal of Materials Chemistry A, 2020. **8**(45): p. 24108-24116.

286. Hu, N., et al., *Double-layer cellulose hydrogel solar steam generation for high-efficiency desalination.* Carbohydrate Polymers, 2020. **243**: p. 116480.

287. Tao, G., et al., *Design and performance of sericin/poly (vinyl alcohol) hydrogel as a drug delivery carrier for potential wound dressing application.* Materials Science and Engineering: C, 2019. **101**: p. 341-351.

288. Ou, K., et al., *Properties and toughening mechanisms of PVA/PAM double-network hydrogels prepared by freeze-thawing and anneal-swelling.* Materials Science and Engineering: C, 2017. **77**: p. 1017-1026.

289. Deshmukh, K., et al., *Influence of K2CrO4 doping on the structural, optical and dielectric properties of polyvinyl alcohol/K2CrO4 composite films.* Polymer-Plastics Technology and Engineering, 2016. **55**(3): p. 231-241.

290. Dai, H., Y. Huang, and H. Huang, *Eco-friendly polyvinyl alcohol/carboxymethyl cellulose hydrogels reinforced with graphene oxide and bentonite for enhanced adsorption of methylene blue.* Carbohydrate polymers, 2018. **185**: p. 1-11.

291. Ge, S., et al., *Coordination of covalent cross-linked gelatin hydrogels via oxidized tannic acid and ferric ions with strong mechanical properties.* Journal of agricultural and food chemistry, 2019. **67**(41): p. 11489-11497.

292. Lee, H.-Y., et al., *Enhancement of bio-stability and mechanical properties of hyaluronic acid hydrogels by tannic acid treatment.* Carbohydrate polymers, 2018. **186**: p. 290-298.

293. Jordan, L.G. and B.W. Booth, *HER2+ breast cancer cells undergo apoptosis upon exposure to tannic acid released from remodeled cross-linked collagen type I.* Journal of Biomedical Materials Research Part A, 2018. **106**(1): p. 26-32.

294. Feng, X., et al., *Mechanical and antibacterial properties of tannic acid-encapsulated carboxymethyl chitosan/polyvinyl alcohol hydrogels.* Engineered Regeneration, 2021. **2**: p. 57-62.

295. Yeo, Y.H., et al., *Multifunctional and thermoresponsive methylcellulose composite hydrogels with photothermal effect.* Carbohydrate Polymers, 2022. **277**: p. 118834.

296. Preston, J., *Solvent extraction of metals by carboxylic acids.* Hydrometallurgy, 1985. **14**(2): p. 171-188.

297. Shi, L., et al., *Self-healing polymeric hydrogel formed by metal–ligand coordination assembly: design, fabrication, and biomedical applications.* Macromolecular rapid communications, 2019. **40**(7): p. 1800837.

298. Huang, S., et al., *Phospholipid reinforced P (AAm-co-AAc)/Fe3+ hydrogel with ultrahigh strength and superior tribological performance.* Tribology International, 2022. **168**: p. 107436.

299. Chen, Y.-N., et al., *Poly (vinyl alcohol)–tannic acid hydrogels with excellent mechanical properties and shape memory behaviors.* ACS applied materials & interfaces, 2016. **8**(40): p. 27199-27206.

300. Hong, K.H., *Polyvinyl alcohol/tannic acid hydrogel prepared by a freeze-thawing process for wound dressing applications.* Polymer Bulletin, 2017. **74**(7): p. 2861-2872.

301. Chen, Y., et al., *Ultrafast gelation of multifunctional hydrogel/composite based on self-catalytic Fe3+/Tannic acid-cellulose nanofibers.* Journal of Colloid and Interface Science, 2022. **606**: p. 1457-1468.

302. Zhou, L., et al., *Release of polyphenolic drugs from dynamically bonded layer-by-layer films.* ACS applied materials & interfaces, 2013. **5**(9): p. 3541-3548.

303. Li, H., et al., *Macroporous polyvinyl alcohol-tannic acid hydrogel with high strength and toughness for cartilage replacement.* Journal of Materials Science, 2022: p. 1-14.

304. Zhuang, Y., et al., *Fe-Chelated polymer templated graphene aerogel with enhanced Fenton-like efficiency for water treatment.* Environmental Science: Nano, 2019. **6**(11): p. 3232-3241.

305. Bajpai, A. and R. Gupta, *Synthesis and characterization of magnetite (Fe3O4)—Polyvinyl alcohol-based nanocomposites and study of superparamagnetism.* Polymer composites, 2010. **31**(2): p. 245-255.

306. Karimzadeh, I., et al., *Effective electrosynthesis and in situ surface coating of Fe3O4 nanoparticles with polyvinyl alcohol for biomedical applications.* Materials Research Innovations, 2019. **23**(1): p. 1-8.

307. Yang, M., et al., *Highly stretchable gamma-irradiated poly (vinyl alcohol)/Tannic acid composite hydrogels with superior transparency and antibacterial activity.* Journal of Polymer Research, 2021. **28**(11): p. 1-13.

308. Sun, S., et al., *Carbon black and polydopamine modified non-woven fabric enabling efficient solar steam generation towards seawater desalination and wastewater purification.* Separation and Purification Technology, 2022. **278**: p. 119621.

309. Zhou, X., et al., *Hydrogels as an emerging material platform for solar water purification.* Accounts of chemical research, 2019. **52**(11): p. 3244-3253.

310. Zhu, F., et al., *Accelerating solar desalination in brine through ion activated hierarchically porous polyion complex hydrogels.* Materials Horizons, 2020. **7**(12): p. 3187-3195.

311. Zhou, X., et al., *Architecting highly hydratable polymer networks to tune the water state for solar water purification.* Science advances, 2019. **5**(6): p. eaaw5484.

312. Zang, L., et al., *Nanofibrous hydrogel-reduced graphene oxide membranes for effective solar-driven interfacial evaporation and desalination.* Chemical Engineering Journal, 2021. **422**: p. 129998.

313. You, D., et al., *Salt-tolerant and low-cost flame-treated aerogel for continuously efficient solar steam generation.* Solar Energy, 2021. **227**: p. 303-311.

314. Yang, F., et al., *Ni-based Plasmonic/Magnetic Nanostructures as Efficient Light Absorbers for Steam Generation.* Advanced Functional Materials, 2021. **31**(7): p. 2006294.

315. Ibrahim, I., et al., *Semiconductor photothermal materials enabling efficient solar steam generation toward desalination and wastewater treatment.* Desalination, 2021. **500**: p. 114853.

316. Ibrahim, I., et al., *Biomass-based photothermal materials for interfacial solar steam generation: A review.* Materials Today Energy, 2021. **21**: p. 100716.

317. Bian, Y., et al., *Sustainable solar evaporation while salt accumulation.* ACS Applied Materials & Interfaces, 2021. **13**(4): p. 4935-4942.

318. Zhang, L., et al., *Silicate based solar evaporator with self-cleaning and corrosion resistant properties for durable seawater desalination.* Sustainable Materials and Technologies, 2021. **30**: p. e00362.